# ON THE CUTTING OF METALS AT THE SMALL SCALE: SIZE EFFECT, FRICTION AND PLASTIC INSTABILITIES

A Dissertation

by

GAN FENG

Submitted to the Graduate and Professional School of
Texas A&M University
in partial fulfillment of the requirements for the degree of

DOCTOR OF PHILOSOPHY

| | |
|---|---|
| Chair of Committee, | Dinakar Sagapuram |
| Committee Members, | Satish Bukkapatnam |
| | Bruce Tai |
| | Arun Srinivasa |
| Head of Department, | Lewis Ntaimo |

May 2022

Major Subject: Industrial Engineering

# ABSTRACT

The "size effect" phenomenon in metal cutting – the substantial increase of the specific cutting energy with the decreasing chip size – is systematically studied. An instrumented ultramicrotome is applied to achieve two-dimensional orthogonal cutting with small depths of cut in the range of 30 nm to 3 $\mu$m. Diamond and freshly cleaved glass knives with theoretically sharp cutting edges are utilized to carry out cutting in the absence of edge radius effects.

Based on the measurements of cutting forces and specific energies with multiple metallic systems (copper, zinc, polycrystalline and single crystal aluminum), new evidence is presented in support of tool-chip friction as the primary source of the size effect. It is shown that size effect arises as a result of the non-proportional decrease of the friction component with the underlying length scale. Further direct measurements show that the non-linear dependence of the tool-chip contact length with respect to the depth of cut contributes to this phenomenon. The size dependence of tool-chip friction and contact size is interpreted and quantitatively modeled using a plastic sliding contact mechanics model in which the increased role of the intermolecular adhesion at small tool-chip contacts is shown to be the primary factor underlying the non-linear scaling of the contact length and the size effect. Cutting experiments are also carried out with tools covered with solid and liquid contaminants. These results show that contaminant films effectively diminish adhesion and lead to a drastic reduction in the size effect, suggesting practical benefits for industrial manufacturing processes. Experiments to directly measure the adhesive pull-off force at the tool-chip contact are conducted using the same ultramicrotome platform, and a framework is proposed to calculate the work of adhesion at this contact from the pull-off force. Together, these studies suggest an opportunity to use tool-chip contact in cutting to study friction and adhesion phenomenon at small scales over a broad range of contact conditions.

As a sub-focus, the thesis also studies the problem of surface instability and fold formation in chip formation in cutting of soft metals. A unified framework based on plastic buckling is presented to describe this phenomenon and capture the scaling of instability wavelength (fold spacing) on the depth of cut.

DEDICATION

To my parents

# ACKNOWLEDGMENTS

First and foremost, I would like to thank my advisor Professor D. Sagapuram. His careful guidance, constant patience, and solid support over the past five years is the foundation for this thesis. Secondly, I would like to thank Professors A. Srinivasa, S. Bukkapatnam, and B. Tai for serving in my thesis defense committee and providing valuable instructions to this study and suggestions for improvements. I would also like to thank my friends, the group members, the workshop staffs, and many other people in the Industrial and Systems Engineering Department for their help and support over the past five years. Finally, I would like to highlight my thanks to my parents and my girlfriend Chen. Their unwavering encouragements are the source of strength that sustained me through countless difficult moments.

CONTRIBUTORS AND FUNDING SOURCES

## Contributors

This work was supported by a dissertation committee consisting of Professor Dinakar Sagapuram and Professor Satish Bukkapatnam of the Department of Industrial and Systems Engineering and Professor(s) Bruce Tai and Arun Srinivasa of of the Department of Mechanical Engineering.

All other work conducted for the thesis (or) dissertation was completed by the student independently.

## Funding Sources

Graduate study was supported by the following sources: Texas A&M Engineering Experiment Station (TEES), Texas A&M's T3 program, National Science Foundation (Award No. 2102030), and Breakthrough Energy Foundation.

TABLE OF CONTENTS

Page

LIST OF FIGURES

FIGURE Page

LIST OF TABLES

# 1. INTRODUCTION

## 1.1 Introduction

Metal cutting is an unconfined plastic deformation process that is accompanied by large shear strains (1 - 10), high strain rates (up to $10^5$ per second) and complex frictional interactions at the tool-chip contact [1]. In this process, a thin layer of material near the surface is separated from the workpiece in the form of a chip by a tool with a sharp cutting edge following a pass defined by the pre-configured depth of cut (see Fig. 1.1). When compared to metal plastic deformation processes encountered in other settings (e.g., forming), cutting is different in three main aspects: (1) imposition of extremely large plastic strains in a single step, (2) intimate contact of the tool-chip interface where the apparent and real contact areas are equal, and (3) unconstrained plastic flow at the workpiece/chip free surface, which makes cutting a free-boundary value problem. Under the majority of the cutting conditions, the large plastic deformation accompanying the cutting process occurs primarily in a band-shaped zone called the primary shear zone, which extends from the cutting tool edge to the free surface of the chip. The energy consumption in cutting is primarily determined by the energy required for the plastic deformation of the material within this zone plus the energy expended in overcoming friction at the tool-chip sliding contact. Although plastic deformation in cutting is generally treated as a steady-state problem (analogous to laminar flow in fluid mechanics), a careful examination of chip morphology shows that plasticity instability at the free surface is the norm rather than the exception. Recent studies reveal that the unconstrained deformation near the free surface, coupled with large plastic strains, in fact spawns a diverse and rich variety of plastic instability modes, including shear bands, plastic buckling and fracture [2, 3, 4, 5]. As a result, in addition to conventional application as a material removal manufacturing process, the cutting framework is particularly well-suited also for studying plastic flow modes and flow instabilities in large strain deformation.

Owing to the miniaturization of electronic components and machinery, as well as the increased usage of ultra-precision and micro-machining processes in recent years, the mechanics of cutting at small scales (that is, depth of cut in the range of a few nanometers to microns) has received renewed attention [6]. Compared to metal cutting at regular length scales (depth of cut of tens to

hundreds of microns), the cutting mechanics at smaller scales can be strikingly different in several crucial aspects, most important of which is the so-called *size effect* [7, 8, 9, 10]. In contrast to conventional theories of cutting that are devoid of any length scales, there is ample experimental evidence that specific energy (i.e., energy consumption per unit volume of material removed) is not a constant, but increases substantially (by up to 10 times or more) when the depth of cut is decreased to sub-micron regimes (Fig. 1.2(a)). This phenomenon is referred to as the size effect. In terms of force profiles, this effect is manifested as non-proportional decrease in the cutting force with decreasing depth of cut or (apparent) finite intercept in the force at zero depth of cut (Fig. 1.2(b)). Although numerous theories [11, 8, 12, 13, 14] have been proposed in the literature for the size effect, ranging from microscopic theories such as strain-gradient plasticity to those that invoke surface energy arguments, a simple energy partition in terms of plastic deformation and friction components provides yet another, but a continuum-level and far more direct, interpretation for the size effect. This is based on the consideration that the plastic work scales with deformation *volume* whereas friction scales with contact *area*, which by itself introduces an inherent length scale into the problem. Although this type of volume/area scaling and its consequences for the size dependence is well-known in many areas of science, including nucleation [15] and fracture mechanics [16], it has not received attention in the context of cutting. Additionally, the fact that intermolecular adhesion [17] between the contacting solids plays an increasingly important role in determining the contact area at small scales introduces another intrinsic length scale. Adhesion may be further expected to play a crucial role especially in a contact situation such as in cutting, where the tool-chip contact is both very clean and intimate (i.e., apparent contact area $\approx$ real contact area). Given this, it is indeed surprising that adhesion has received little consideration to date in the cutting literature. The current thesis work seeks to understand the size effect phenomenon through this broad lens, namely, competition between plastic deformation resistance, friction and adhesion; and, importantly, how they scale with the underlying length scale (depth of cut).

As a sub-focus, the thesis also explores the scaling behavior of surface plastic instabilities in cutting of metals. These explorations are motivated by the fact that a comprehensive understanding of the material deformation behavior is critical to optimization of cutting processes for better machinability [3]. We specifically consider the case of cutting of ductile metals in the soft annealed condition, where the chip that forms is usually very thick, with characteristic folds on its back (free)

surface [18, 19, 20]. These folds, which appear as furrow-like undulations on the free surface running perpendicular to the cutting direction, are observed in a wide range of material systems (e.g., copper, aluminum, iron and single-phase brass) and across length scales (depths of cut ranging from a few tens of nanometers to $\sim$ 100 microns) [21, 22, 23, 24]. However, unlike well-known surface elastic instabilities typically observed in thin films coated on elastomeric substrates, this type of instability is permanent and remains after material unloading. Although the fold formation on the chip free surface has been loosely attributed to "the nonuniform deformation" of the material or adiabatic instability in the past [23], it is only recently that its formation has been explicitly characterized using *in situ* observations [18, 20]. These observations, among others, specifically show that the folds form as a result of plastic buckling and periodic folding, which occur when surfaces of soft ductile materials are subjected to large stresses well into the plastic range. Guided by these studies, the current work focuses on characterizing the scale-dependence of surface fold characteristics (morphology, wavelength, etc.) as a function of the underlying length scale (depth of cut); and its modeling using a continuum-level plastic buckling framework.

### 1.2 Problem statement

To enable a good physics-based understanding of the complex process of chip formation, it is important to have clean experimental data obtained using well-defined experiments. A special case of cutting called as orthogonal cutting, where the cutting tool edge is perpendicular to the cutting speed, is the desired framework for studying the metal cutting process from a fundamental point of view. In this framework, the variation of the chip width during the cutting process is negligible, which reduces the problem to a simplified plane-strain deformation process and enables direct comparison of the data with the cutting models (which are usually two-dimensional). However, conducting these types of experiments at the small scale (especially sub-micron depths of cut) poses considerable practical challenges, and as a result, most of the studies involving small depths of cut have been carried out under non-orthogonal cutting conditions and are often characterized by a non-constant depth of cut that varies during the cutting pass [9, 10, 25, 26, 27]. Another important experimental consideration at small scales pertains to the cutting tool edge radius. Since most of the scale effects become pronounced only in the sub-micron range, it is important that the cutting tool edge is extremely sharp ($\sim$ nanometer sharpness), for one to separate the edge

radius effects. However, cutting tools which are commonly used for small scale cutting studies are characterized by an edge radius of a few hundreds of nanometers [7, 9, 28]. Consequently, most of the investigations of the size effect on specific cutting energy attribute the effect to processes resulting from finite cutting edge radius such as ploughing around the blunt tool edge [29] or rubbing at the tool-machined surface [30]. Whether or not scale dependence exists with perfectly sharp tools remains an open question.

A novel experimental framework that overcomes the above difficulties is presented in this work. This involves the use of ultramicrotomy (a sample preparation method that is typically used to produce extremely thin material sections for transmission electron microscopy applications) to achieve controlled material removal at small scales (depth of cut in the range of 30 nm to 3 microns) under orthogonal plane-strain conditions. Another important aspect of the study is the use of freshly cleaved glass knives with atomic-scale sharpness as cutting tools, so as to minimize the uncertainties associated with the cutting edge radius effects noted earlier. The glass knives prepared using this technique are quite inexpensive, characterized by very sharp cutting edges, and could be made with different included angles. This experimental approach emerging from the early works of Ramalingam and Black [23], and Williams and Gane [31] has been refined and developed in our laboratory to include piezoelectric force sensors for direct measurement of cutting forces and energy dissipation. This experimental framework is used to explore and quantify the length scale effects in cutting of soft metals under a range of different experimental conditions (e.g., rake angle, cutting speed and a number of tool surface contaminants).

With this as an experimental backdrop, and in order to fully understand the mechanics of cutting at small scales, the following questions are considered.

1. Is size effect universal to all metals, and does it exist in the absence of cutting edge radius effects?

2. Do plastic deformation and friction components scale self-similarly with the depth of cut?

3. Does intermolecular adhesion exist at the tool-chip contact and can it be measured? Is it possible to analytically model the tool-chip sliding contact in the presence of adhesion?

4. What governs the morphology and spacing of surface folds? Is it possible to model the instability wavelength across multiple scales (nanoscale to macroscale regimes) using a unified

framework?

### 1.3 Summary of dissertation

This dissertation is divided into 8 chapters (including the current Introduction chapter). A brief summary of Chapters 2 - 8 is provided below.

**Chapter 2**: This chapter provides a basic review of mechanics of machining, along with a detailed background of the size effect and surface instability phenomena in cutting processes – the main thrusts of this thesis. Various theories that have been proposed to explain the size effect on specific cutting energy are critically reviewed and discussed from a semi-historical standpoint. Prior experimental configurations that have been used to study the mechanics of cutting at small length scales are also reviewed and compared.

**Chapter 3**: The experimental apparatus (ultramicrotome) which has been constructed to conduct controlled cutting experiments at small scales is described in Chapter 3. Two unique capabilities of the experimental system are highlighted, namely the ability to achieve orthogonal plane-strain cutting conditions and the use of glass and diamond knives as cutting tools with very sharp edges. Details related to instrumentation of the ultramicrotome with force sensors and sensor calibration are presented, along with sample force measurements. Other associated material characterization methods (such as scanning/transmission electron microscopy and atomic force microscopy) that were used to study/measure chip morphology and tool-chip contact area are also included in this chapter.

**Chapter 4**: In Chapter 4, we present detailed measurements of forces and specific cutting energy as a function of depth of cut (in the range of 30 nm to a few microns). Three ductile metals, namely, copper, aluminum and zinc, in various different states (e.g., work-hardened vs. annealed, polycrystalline vs. single crystal) are considered. A universal observation from the study is the existence of a strong size effect – manifested by multi-fold increase in the specific energy with decreasing depth of cut – even with perfectly sharp tools [32, 33]. Evidence is presented in support of tool-chip friction as the primary source of the size effect. More specifically, it shows that the tool-chip contact size and associated friction component decrease non-proportionally with the depth of cut, and this non self-similar scaling results in size effect on the specific energy at small length scales. In other words, the size effect is related to a surface area vis-à-vis volume

competition between deformation plasticity and friction. The study also highlights an interesting possibility to control or even suppress the size effect by altering the tool-chip contact boundary condition, say, by introducing foreign contaminants that alter friction conditions at this contact.

**Chapter 5**: This chapter focuses on the mechanics of plastic sliding contact that occurs between the tool and the chip, with emphasis on features that are unique to small scales. These include non-proportional scaling of the tool-chip contact area with the normal load, which is in contrast to a conventional plastic contact (contact area $\propto$ normal load) and in turn leads to non self-similar scaling of friction component discussed in Chapter 4; observations of finite contact area under zero normal load; and the occurrence of even negative normal loads (i.e., tensile tractions) at the tool-chip contact under some particular cutting conditions. A simple continuum-level model that incorporates adhesion (i.e., surface attraction forces) into the classical plastic contact mechanics analysis is presented to analytically describe this contact and explain the size dependence. The model is validated using force/contact area data obtained from the experiments. In addition to predicting all the essential experimental features (including the disappearance of scale effect in the presence of surface contaminants which diminish adhesion), the model also points to the key role of adhesion in determining the friction characteristics of small scale plastic contacts. Although the existence and influence of adhesion are well-studied and appreciated for the case of elastic contacts (both stationary and sliding) [17, 34, 35, 36], its role in contact mechanics of plastically deforming bodies has not received adequate attention in the past. This work is the first to provide a quantitative theory of adhesion for sliding plastic contacts.

**Chapter 6**: This chapter focuses on direct measurement of adhesive forces at the tool-chip contact. A simple experimental technique to measure the "pull-off" force required to break the tool-chip contact is presented. The "pull-off" force measurements are presented for various tool-material-lubricant combinations over a range of cutting depths. A "thin-film peeling" model is also presented to model the chip detachment process and predict the work of adhesion in terms of the pull-off force. The results suggest a novel and simple experimental framework to measure work of adhesion between different material systems.

**Chapter 7**: The instability mechanism leading to formation of surface folds under large-strain deformation is discussed in this chapter. We start with a general discussion of surface folds and their spacing characteristics, followed by *in situ* visualization of their development using high-

speed photography and image correlation techniques. The latter observations demonstrate how repeated buckling and folding of a thin surface layer ahead of the tool can result in characteristic folds and furrow-shaped features observed on the free surface. A buckling model is then presented to describe the fold spacing characteristics, and validated using experimental data across multiple orders of scale. The size of the plastic deformation zone ahead of the tool (which scales with cutting pressure) is shown to be the dominant length scale that governs the instability wavelength. The non-linear scaling of fold spacing with the cutting depth is shown to be intrinsically related to the size effect.

**Chapter 8**: A summary and important implications of the work are presented in this chapter. The work has demonstrated, in an unambiguous manner, how non self-similar scaling of the frictional dissipation at the tool-chip contact results in the overall size effect. This is a fundamental result that raises an important question as to whether the same underlying phenomenological principle related to frictional dissipation could also explain the size effect in other domains such as indentation [37, 38] and sliding [39], and whether all of these size effects can be described within a unified framework. This certainly warrants further study. In addition to conventional application as a material removal (subtractive) manufacturing process, the study suggests additional applications for cutting for exploring interesting materials/mechanics phenomena. These include exploration of surface plastic flow and related instability phenomena under large deformation conditions using cutting as an experimental framework; as well as the use of clean tool-chip contact in cutting as a 'nanotribology' tool for fundamental studies of adhesion and friction over a range of sliding speeds, normal loads and surface environments. Presently, the size dependence laws for sliding plastic contacts remain largely incomplete.

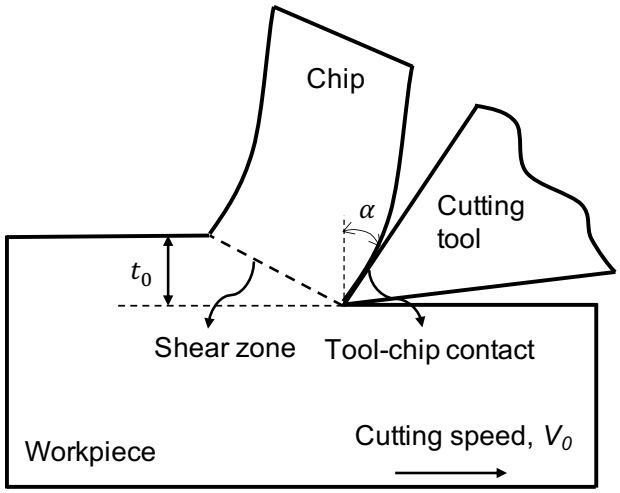


Figure 1.1. Schematic of chip formation in 2D plane-strain cutting. Process parameters $V_0$, $t_0$ and $\alpha$ are the cutting speed, depth of cut and rake angle, respectively.

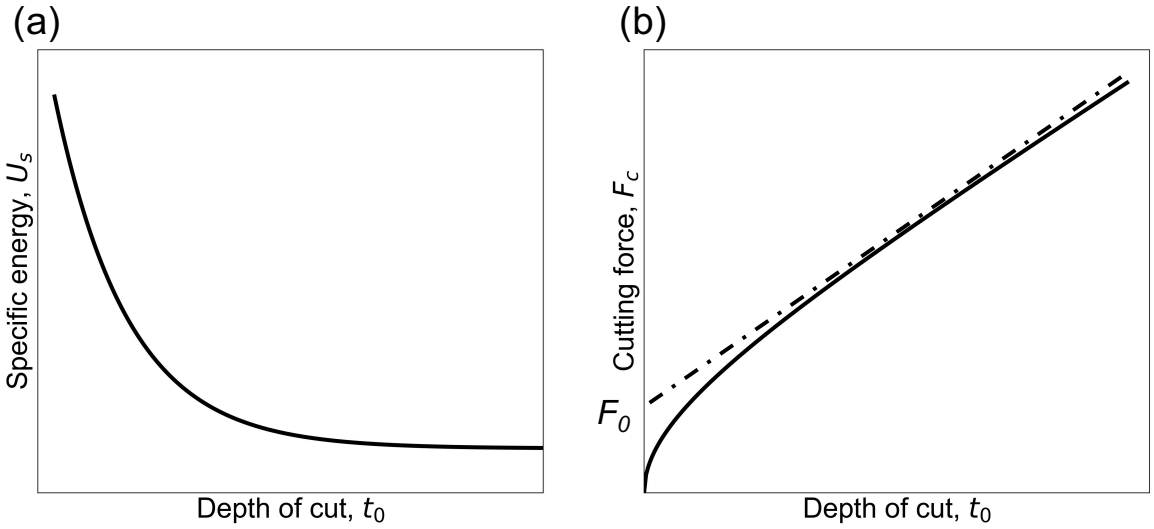


Figure 1.2. (a) Schematic representation of the size effect in cutting, characterized by specific energy $U_s$ increase with decrease in the depth of cut $t_0$. (b) Cutting force variation with $t_0$ in the presence of size effect. The solid line shows non-linear variation of $F_c$ without an intercept, while the dashed line shows linear variation with a finite force intercept $F_0$.

# 2. BACKGROUND

In this chapter, a background is presented on two important aspects of cutting of metals – the size effect on the specific cutting energy and the problem of plastic flow instability in the deformation zone. The chapter begins with a brief introduction of the mechanics of metal cutting, with particular emphasis on the energy consumption, followed by a discussion of the size effect – both experimental observations as well as various theories that have been proposed to explain the size effect phenomenon. Key experimental-related issues and limitations associated with the techniques that have been used in the past to conduct cutting experiments at small depths of cut and investigate the size effect are critically reviewed. Lastly, the role of free surface and plastic instability in determining the chip formation mode is discussed, with particular attention paid to the formation of Type 1 chip (according to Nakayama's classification).

## 2.1 Energy consumption in cutting of metals

Cutting or machining is a process in which a hard, sharp wedge-shaped tool removes material from the surface of a solid workpiece by very large strain deformation. Figure 2.1 shows a 2D schematic of the cutting process and the associated geometric parameters. The material being removed by the cutting process, namely the chip, slides over the tool surface known as the rake face. The angle between the rake face of the tool and the normal to the work surface is called the rake angle ($\alpha$). The amount of interference between the tool and the workpiece is the depth of cut or undeformed chip thickness ($t_0$) and the relative velocity between the tool and the workpiece is the cutting velocity ($V_0$). When the tool cutting edge is perpendicular to the cutting velocity and the width of cut $w$ (dimension into the plane) is large compared to $t_0$, a state of two-dimensional plane-strain deformation prevails during chip formation (as shown in Fig. 2.1). The forces experienced by the cutting tool in the two orthogonal directions are given by $F_c$ and $F_t$. The cutting force $F_c$ is the component parallel to the cutting velocity $V_0$, while the thrust force $F_t$ is the component perpendicular to $V_0$. (It may be noted that the friction force $F_f$ acting parallel to the tool rake face and the normal force $F_n$ perpendicular to it can be calculated from these two force components, given the rake angle $\alpha$.)

The specific cutting energy $U_s$, namely the energy needed for removing or cutting a unit volume

of material, is given by:

$$U_s = \frac{F_c}{wt_0} \tag{2.1}$$

Despite the seemingly simple geometry of the cutting process, a number of factors contribute to this energy expenditure. These include:

- Energy needed to create the two fresh surfaces (the chip underside and the machined workpiece surface) – or the so-called *surface energy*. This component is usually a very small fraction (0.01%) of the total energy and is therefore ignored in the cutting analyses.

- Energy associated with the plastic deformation of the material in the primary shear zone and its extension into the workpiece subsurface (see Fig. 2.2). It may be noted that in most metals, the final chip thickness $t_c$ is larger than the depth of cut $t_0$, with this shape change occurring as a result of concentrated shear in the primary shear zone. It is common to denote the chip thickness ratio $t_0/t_c$ using a symbol $r$.

- Energy associated with the tool-chip contact, which itself is made of two parts – the energy dissipation due to sliding friction at the tool-chip contact and the energy due to plastic deformation at the chip underside that is in contact with the tool (the so-called secondary shear/flow zone, see Fig. 2.2).

- Energy due to friction or "rubbing" between the tool flank face and the machined workpiece surface. This component can be especially important in the case of machining with worn tools.

- Energy associated with the momentum change as the material passes crosses the primary shear zone.

Under conditions characterized by a sharp cutting edge and low cutting speeds, the last two components (i.e., energy due to rubbing at the tool flank and machined surface, and that due to momentum change) are insignificant and can be ignored. In regards to the energy component associated with plastic deformation of the material, although it is generally difficult to precisely determine what fraction is accounted by the primary shear zone vis-à-vis secondary shear zone and

workpiece subsurface deformation, Nakayama's study suggests that the latter two components are usually small, in the range of 10-15% of the primary shear zone component. Given this, the total energy expenditure in cutting is usually treated as sum of only two parts: $U_1$ , which is the energy due to plastic deformation in the primary shear zone, and $U_2$, which is the energy associated with friction at the tool-chip sliding contact.

For a perfectly plastic material, $U_1$, represented in terms of energy per unit volume of workpiece removed, is given by:

$$U_1 = \tau\gamma_s \tag{2.2}$$

where $\tau$ is the shear flow stress of the material and $\gamma_s$ is the final shear strain imposed in the chip. For the (ideal) case of simple shear along a thin plane ($AB$ in Fig. 2.1), the shear angle $\phi$, $\tau$ and $\gamma_s$ are given by:

$$\phi = \arctan(\frac{r\cos\alpha}{1 - r\sin\alpha}) \tag{2.3}$$

$$\tau = \frac{F_c\cos\phi - F_t\sin\phi}{AB} \tag{2.4}$$

$$\gamma_s = \frac{\cos\alpha}{\sin\phi\cos(\phi - \alpha)} \tag{2.5}$$

On the other hand, the frictional component $U_2$ (energy per unit volume) can be expressed as:

$$U_2 = \frac{rF_f}{wt_0} = \frac{r\tau_f l}{t_0}, \tag{2.6}$$

where $\tau_f = F_f/wl$ is the local shear stress at the tool-chip sliding contact. (Alternatively, $U_2$ can be also obtained simply by taking the difference between $U_s$ and $U_1$.)

## 2.2 Size effect and nature of forces in cutting at small length scales

As noted earlier, in conventional analyses of cutting, the total energy expenditure is usually considered as the sum of two parts: (1) energy associated with plastic deformation of material in the primary shear zone, and (2) energy associated with friction at the tool-chip sliding contact.

Because the conventional theories of plasticity and friction are free of intrinsic length scales, this picture predicts that the specific energy $U_s$ is independent of the cutting depth or width. However, there is ample experimental evidence in the literature that shows substantial increases in the $U_s$ (up to 10-fold or more) with decreasing undeformed chip thickness $t_0$, especially when $t_0$ is in the sub-micron range [7, 9, 10]. This phenomenon, referred to as the *size effect* (Fig. 1.2(a)), has considerable implications for processes such as polishing, grinding, micro- and ultraprecision machining where material removal occurs at a fine scale.

The size effect in cutting was first highlighted by Drucker [40] and Shaw (in the context of plunge grinding of metals) at around the same time. Shaw's experimental results, in particular, clearly highlighted the non-linear dependence between the depth of cut and the primary cutting force, which brings about an increase in the specific energy when the depth of cut is reduced below $\sim$1 $\mu$m. Although length scale effects on other mechanics phenomena such as brittle fracture were relatively well-known and studied at that time, the observations of chip thickness effects in cutting were among some of the first illustrations of the size effect in the area of plastic deformation of metals.

Thereafter, size effect in cutting has been extensively investigated by various authors and shown to be a quite general phenomenon occurring across a range of material systems and material removal configurations (orthogonal cutting, grinding, etc.) [11, 7, 10, 30, 41]. In regards to the cutting force dependence on the depth of cut, an important experimental observation that has emerged during this period was the so-called "force intercept", which appears as a finite $y$-intercept in the force vs. $t_0$ plot when the depth of cut is extrapolated down to zero (see Fig. 1.2(b)). This has led to the notion of the "ploughing force" (namely force acting at the tool nose), which is often argued to be the origin of the size effect on the specific cutting energy. The basic argument is that the energy that goes into chip formation (i.e., plastic work in the shear zone plus friction work at tool-chip contact) scales down proportionally with $t_0$, while the ploughing force remains unchanged, thus producing a size effect [29, 42]. However, it should be noted that the existence of force intercept is often deduced from cutting experiments with cutting tools possessing an edge radius of at least a few microns.

It should be noted that the size effect is not just limited to cutting but has been also been reported in various other plasticity problems, including bending of thin wires, micro-pillar testing,

hardness/scratch indentation and erosion. For example, in micro-pillar compression testing of metals, the size effect is manifested by the increased material's yield strength with decreasing sample size (diameter of the pillar) [12, 43, 44], whereas in indentation, it appears in the form of increased hardness (i.e., indentation force divided by indent area) as the indentation depth is reduced below the micron scale [37, 38]. The extent of the size effect in these experiments – a two- to three-fold increase in the strength/hardness is most common – is however usually smaller when compared to that in cutting, which is characterized by up to 5 - 10X increase in the specific cutting energy. Lastly, in the case of erosion and abrasive wear [45], the size effect is manifested as the highly non-linear dependence between the particle size and the wear rate; this in fact closely resembles the cutting force trend in metal cutting at small length scales.

### 2.3 Theoretical explanations for the size effect in cutting

The origin of the observed size dependence in cutting has been the subject of considerable dispute and remains an outstanding scientific question even today. One of the earliest explanations for the size effect was given by Shaw [8] in the context of surface grinding, in terms of increase in the material's intrinsic flow stress with decrease in the specimen (chip) size. The interpretation was that when the chip size becomes small, it is less likely to find an 'imperfection' in the vicinity of the shear zone, which effectively results in an increase in the flow stress. This concept parallels with the specimen size effect on fracture strength of brittle materials, which has been satisfactorily explained using Griffith's crack and the statistical theory of Weibull [46]. Although what constitutes as a strength-limiting imperfection (dislocations) in ductile materials was left somewhat vague, Shaw used this idea to develop a description for the shear stress $\tau$ (along the shear plane) that contains characteristic chip thickness as an intrinsic length scale. The obtained $\tau \sim 1/t_0$ scaling [47] was argued to be consistent with the experimentally observed chip sizes where shear stress approaches the theoretical strength.

Over the last few decades, it has been recognized that size effects in metal plasticity can be alternatively described in terms of strain gradient plasticity, where the length scale enters the formulation in the form of strain gradient. This formulation is based on the observation that plastic strain gradients result in geometrically necessary dislocations, which contribute to the strength in addition to the common statistically stored dislocations. For instance, strain gradient plasticity-based

theories are quite extensively used to explain the size effect in nanoindentation. The application of strain gradient theory to describe the size effect in cutting was first explored by Dinesh et al. [12], wherein the average strain gradient across the shear zone is taken as $\sim \gamma_s/t_0$ (where $\gamma_s$ is the chip strain). Since the density of the geometrically necessary dislocations is proportional to the strain gradient, and flow stress scales as square-root of the dislocation density, the model predicts a $\tau \sim 1/\sqrt{t_0}$ scaling relationship. Thus, the size effect becomes appreciable when $t_0$ is small. Subsequent refinements to this theory and its implementation to a shear zone configuration with a finite thickness can be found in Ref. [13]. It is worth pointing out that strain gradient plasticity theories are most effective when the overall plastic strains are small and strain gradients are relatively large, as in nanoindentation or plastic bending of thin wires [38, 48]. Given that the deformation conditions in machining are extreme (plastic strains well over 1), the suitability of gradient-based models to the cutting problem remains a question.

Another interesting explanation for the flow stress increase with decrease in $t_0$ comes from Zorev [49], who has suggested that such an effect can arise from a potential change in the stress state of the material being deformed in the shear zone. What Zorev means by "change" here is the transition from a relatively less complex stress state (i.e., uniaxial-type) to plane-strain type conditions that are more "rigid", as the $t_0/w$ ratio ($w$ is the chip width) is reduced. The problem is similar to that of a hardness indentation where the average stress under an indenter is about three times the uniaxial yield strength of the material because of the increased constraint to the plastic flow. However, Zorev's suggestion appears to have been largely ignored in the literature.

It may be noted that all the above theories depict the size effect as an *intrinsic* effect, in that the size effect arises from flow stress increase of the material in the shear zone. Therefore, in terms of the cutting force ($F_c$), these models predict a non-linear variation of $F_c$ with respect to $t_0$. This is schematically shown in Fig. 1.2(b) using the solid black curve, where the $F_c$ vs. $t_0$ plot curves sharply and passes through the origin, but is linear at high $t_0$.

In contrast to the above size effect which comes from non-linear scaling of $F_c$ with $t_0$, an alternative possibility is the occurrence of size effect due to a positive intercept in the force at zero depth of cut. This scenario is shown using a dashed line in Fig. 1.2(b), where $F_c$ scales linearly with $t_0$ (at all $t_0$), but leaves a finite intercept $F_0$ at $t_0 = 0$. Since linear extrapolation of cutting force data from higher cutting depths, to $t_0 = 0$, almost always suggests the existence of such an intercept,

this has led several investigators to believe that size effect is a consequence of the constant $F_0$ term that does not contribute to the chip formation process. This force term is usually associated with phenomena occurring right at the cutting tool edge, although different models/theories differ in terms of their physical interpretation of $F_0$. For instance, this term has been likened to that required to 'indent' or plough the material in front of a blunt tool edge [29, 42, 50], the magnitude of which remains independent of the depth of cut. An alternative viewpoint is that the constant $F_0$ is associated with rubbing at the tool-machined surface contact, either due to flank wear [30] (in the case of worn tools) or elastic recovery of the material in the wake of the tool [7, 41]. In all these cases, the energy required for chip formation (i.e., plastic deformation work plus tool-chip friction work) is considered to scale down proportionally with $t_0$, while the energy term due to $F_0$ remains essentially unchanged, thus resulting in a size effect. In this context, a more detailed Merchant force diagram that incorporates the constant $F_0$ term has been also proposed, independently by Masuko [50] and Albrecht [29]. However, separation of this force term is complicated by the fact that local plastic flow around the tool tip, either due to indentation or ploughing, is highly difficult to isolate (let alone predict) from bulk plastic flow in the shear zone. Moreover, in regards to the suggestion of rubbing due to elastic recovery of the material, experimental studies carried out by Sarwar and Thompson [51] showed no evidence for material recovery behind the tool edge, even with extremely blunt tools.

A significant departure from above explanations for the size effect, but one that is still predicated on the existence of a finite force intercept, is the proposal of 'fracture energy' by Atkins [14]. Here, the so-called fracture energy, that is required for creating two new surfaces (chip underside and machined surface), is argued to be the origin of the force intercept. However, instead of correlating this energy with the surface free energy term, Atkins considers it as the irreversible plastic work associated with deforming a thin boundary of material on either side of the tool tip, much analogous to the Orowan's plastic work term commonly used in elasto-plastic fracture mechanics. As with the indentation and ploughing models discussed above, a significant complication is that this local plastic work term is highly difficult to separate/characterize in cutting experiments. In theory, independent measurements of the fracture toughness, under strain rates and crack-tip geometries relevant to cutting, may be used to critically test this idea, but this appears to have not been done yet. Moreover, as will be shown in this work, linear extrapolation of cutting force data

to lower depths can lead to considerable errors. Therefore, the existence of force intercept by itself is debatable, especially when the tool cutting edge is sharp.

Lastly, we draw attention to Nakayama and Tamura [11] who have presented one of the most comprehensive energy analyses of cutting and highlighted the role of plastic flow in the machined surface that is caused by penetration of the shear zone below the surface. The most important observation from Nakayama's work is the non-proportional decrease of the thickness of the deformed layer with the cutting depth. In other words, the size effect arises because of non-linear scaling of the energy associated with plastic flow in the machined subsurface layer. Although these observations contrast with more recent subsurface strain measurements [52] which show that subsurface strain profiles in cutting are self-similar and scale with the depth (much like in indentation), the experimental data provided by Nakayama and Tamura in support of the size effect argument is very convincing. In this picture of the size effect, $F_c$ variation with $t_0$ is expected to be non-linear, as shown in Fig. 1.2(b), solid curve.

From the above discussion, it can be noted that the frictional interactions at the tool-chip interface are either sidelined or not considered at all in the overall phenomenon of the size effect. This is surprising not only because interactions between the chip and the tool control to a great extent many important characteristics of the machining process (including shear plane angle, chip-tool contact length and specific cutting energy), but also because consideration of friction (which scales with surface *area*) relative to the plastic work in the shear zone (which scales with *volume*) introduces an inherent length scale into the problem. For instance, this type of volume-area scaling and the resulting size dependence is well-known in many areas of science, including nucleation [15], fracture mechanics [16] and adhesion [17]. In this regard, we also note that while several interpretations exist for the size effect in indentation, the most simple interpretation is perhaps that by Gilman [53], where the $H \sim 1/d$ ($H$ is hardness and $d$ is the indentation depth) scaling relationship is explained purely based on the consideration of the ratio between the material's frictional resistance (at indenter-workpiece contact) and plastic deformation resistance. We have no reason to doubt that size effect in cutting can be due to a similar mechanism. This hypothesis – that friction as the origin of the size effect – forms the basis of our work. A summary of the various theories that have been proposed for the size effect in cutting is given in Table 2.1.

## 2.4 Experimental issues in cutting at the small scale

Although there are several papers that analyze the size effect in cutting in significant details, except perhaps for Nakayama [11], none has been specifically able to test the various hypotheses and theories using experimental data. This is because of the considerable challenges associated with careful design of cutting experiments at small depths. First of these is the need to maintain orthogonal plane-strain conditions, which are the deformation conditions assumed in all models. However, most of the studies of the size effect have been conducted under conditions where cutting is non-orthogonal or characterized by variable depth of cut. Secondly, since the cutting depths at which size effects become pronounced are in the sub-micron to nanometer range, it is important that the cutting tool edge is as sharp as possible to separate the edge radius effects.

For instance, the experimental configurations generally used to carry out cutting experiments at small scales can be categorized into the three major types: flycutting, grooving and single point turning (Fig. 2.3). The most widely used approach among these is the flycutting (Fig. 2.3(a)). In flycutting, the cutting tool is fixed on a rotating spindle, while the workpiece remains stationary (or vice versa), and material removal is effected by engaging the workpiece against the rotating tool. The cutting tool used for flycutting is usually a semi-circular diamond cutter with a nose radius of a few mm and the material is removed following a circular trajectory (cutting direction). Therefore, the finished machined surface after the cut is actually a groove (with a cross-section determined by the specific geometry and nose radius of the cutting tool) instead of being a flat surface. More importantly, the "effective" depth of cut is not a constant, but continuously varies during the cutting process. Grooving (Fig. 2.3(b)) is a process that is analogous to flycutting, except that the cutting tool engages with the workpiece surface via a linear motion, instead of a circular cutting trajectory. This configuration overcomes the issue of variable non-constant depth of cut, but the material is still removed in the form of a groove. That is, the nature of deformation is far from the ideal plane-strain conditions assumed in the theories. A third variant of the flycutting process is single point turning (Fig. 2.3(c)). In this configuration, a disk-shaped workpiece is mounted on a rotating spindle, with a diamond tool used to remove a thin layer of material, in the form of a ribbon chip, from the workpiece surface by radially feeding the tool at a constant feed rate (i.e., constant distance per revolution of the workpiece). From the standpoint of validating

theories, single point turning is the most desirable configuration since it ensures constant depth of cut and cutting width, while replicating the orthogonal plane-strain deformation conditions. For example, this configuration has been extensively used by Komanduri and Lucca [7, 28] to quantify the cutting/thrust forces and energy dissipation in ultraprecision machining of ductile metals over a wide range of cutting depths varying from 15 $\mu$m down to 25 nm. However, the rather "large" cutting edge radius of the diamond tool – of the order of 100-200 nm and comparable to the depth of cut – is still an issue. Therefore, whether size effect occurs with perfectly sharp tools (i.e., in the absence of edge radius effects) itself remains an open question. Another key limitation of the above experimental approaches pertains to limited capability of controlling the tool rake angle, with the $0^\circ$ rake angle tool being the default option in most of the studies. The experimental approach that we propose to study cutting mechanics at small scales – to be discussed in the next chapter – overcomes most of these issues.

A summary of the experimental studies focused on the size effect problem, including material systems studied and the experimental conditions used, is provide in Table 2.2.

## 2.5 Surface plastic instabilities in cutting

An important difference between metal cutting and that of bulk deformation processes such as extrusion, rolling, and drawing is that in metal cutting, the geometry of the deformation zone is not defined *a priori* because of the free surface. It is this unconstrained plastic flow near the free surface, and related instabilities, that spawn a diverse and rich variety of chip formation modes. Nakayama [54] classified the continuous chips in cutting into four types – Type 1 to Type 4 – with each of these chip types arising from a distinct flow mode. Of these, only Type 2 chip develops via steady-state flow according to the classical Merchant model [55], i.e., via steady-state plastic shear across a well-defined and thin shear zone/plane. Type 2 chip is perhaps the most studied of all chip types, and the model presented earlier in Fig. 2.1 corresponds to this chip formation mechanism. Type 3 is the partially segmented chip, which is typically observed when cutting materials having poor workability such as hardened steel and magnesium, or under cutting conditions involving large negative rake angles. The formation of this chip type is attributed to an unsteady flow that is triggered by crack initiation at the free surface near the shear zone, followed by crack propagation towards the tool tip; the cyclic occurrence of this surface cracking then leads to the segmented

chip [56]. Type 4 on the other hand is the shear-localized chip, also referred to in the literature [2, 57, 58, 59] as the serrated or saw-tooth chip. This develops as a result of periodic thermal instability in the plastic flow [60]. The most important visual attribute that distinguishes Type 4 from Type 3 segmented chip is the intense localization of plastic flow within narrow (a few $\mu$m thick) and periodically-spaced bands, called shear bands. Type 4 chip is frequently observed under high cutting speeds, especially in materials having low thermal conductivity (e.g., Ti, Ni, steels). The final exception to the steady-state flow mode, and of particular interest to this dissertation, is Type 1 chip, which is characterized by unusually large thickness (5 - 10 times the depth of cut) and "wrinkled" morphology on its free surface. Type 1 chip is most commonly observed when cutting pure soft metals (e.g., Cu, Al, Fe) having high strain-hardening capacity. Even though the thick Type 1 chip has traditionally been explained using the classical shear zone (Merchant) model with a small effective shear plane angle, it is only recently that the flow dynamics underlying Type 1 chip formation has been explicitly characterized using *in situ* observations.

The *in situ* observations [18, 19, 20, 61] in particular show that the plastic flow leading to Type 1 chip formation in ductile metals such as Cu is far from steady-state, and in fact, is characterized by periodic material folding that is facilitated by surface (plastic) buckling instability. This type of flow has been termed as the "sinuous" flow. The principal stages involved in the initiation and evolution of material folding are reproduced in Fig. 2.4. This figure shows four images from a high-speed image sequence, where the colored lines represent the streaklines, as obtained using an image correlation technique called as Particle Image Velocimetry (PIV). The wavy streaklines clearly reveal the unsteady nature of the flow characterized by repeated folds – the sinusoidal-shaped features that make up the chip. The development of an individual fold starts with initialization of a small bump at the workpiece free surface ahead of the tool, that is pinned between two points marked by arrows, $P_1$ and $P_2$, see Fig. 2.4(a). As the tool advances, the "pinning points" approach together, with the bump growing in its amplitude, and eventually forming a fold. Subsequently, the fold is rotated and sheared as the material slides past the tool face. The process repeats and this periodic material folding then results in a series of folds, which also appear as wrinkles or mushroom-shaped structures on the free surface of the chip, as shown in Fig. 2.5(a). The above process of bump formation at the free surface and its increase in the size with the load closely resembles plastic buckling of an inelastic column. In the chip formation case, the pinning points –

or the two ends of the "column" – have been argued to be grain boundaries within the material's microstructure. *In situ* observations of the plastic flow with chemically etched samples, to facilitate direct observation of the grain boundaries [18], and finite element simulations with polycrystalline aggregates [62] have provided further support to this view. In this picture, the spacing between the folds may be expected to scale with the grain size.

A survey of the past literature on chip morphologies in small scale cutting of soft ductile metals suggests that this surface buckling mechanism leading to wrinkled Type 1 chip may be widespread, occurring across different length scales. In this regard, the early work by Phillips, Stobbs et al., Ramalingam, Black and others [21, 22, 23, 24, 63, 64], involving the use of ultramicrotomy and sharp glass/diamond tools to cut soft metals at extremely small depths of cut (50 nm to a few $\mu$m), is of particular interest. In these studies, electron microscopy (SEM and TEM) was used as a tool to observe the free surface morphology of the sectioned chips. The most important observation from these studies is the fact that the chip free surface is not smooth but is rumpled and characterized by periodic wrinkles or folds that are oriented along the direction perpendicular to the cutting velocity (i.e., along the chip width direction) [21, 22]. As an example, Fig. 2.5(b) shows an SEM image of the surface morphology of a pure Cu chip sectioned at a 300 nm depth of cut. The striking similarity with the regular Type 1 chip free surface morphology, shown in Fig. 2.5(a), may be noted despite the widely different length scales. In the absence of direct observations, the folds observed on the chip free surface have been attributed to various instability processes. For instance, Phillips [22] attributed the formation of folds on the free surface due to periodic resistance to chip flow at the tool-chip contact (analogous to stick-slip instability); the experimental observations which showed that the fold formation is minimized by the use of smooth, lubricated knife face and large rake angle – all of which reduce the tool-chip contact friction – supported this hypothesis. On the other hand, the fact that metal cutting represents a unique class of high strain, high strain-rate plastic flow, led other investigators such as Ramalingam and Black [21, 23] to view fold formation from the standpoint of thermal instability, similar to the Type 4 shear-localized chip formation mechanism. The main idea is that the severe plastic deformation in the vicinity of the shear zone produces saturation strain hardening in the material, which when coupled with the adiabatic temperature rise leads to a thermal instability in the form of localized shear. However, the fact that folds are consistently observed even under extremely small cutting speeds ($< 0.1$

mm/s) and large rake angles ($\alpha > 40^\circ$) – conditions characterized by relatively small strains and negligible temperature rise – is inconsistent with this thermal instability-based mechanism. Other micro-scale mechanisms for the fold formation, such the rearrangement and self-organization of dislocations (generated in the primary shear zone) via partial relief of compressive stresses in the chip [24, 63], also exist. It is of course extremely difficult if not impossible to verify such dislocation-level mechanisms without direct observations.

The fact that surface folds bear remarkable similarity across different length scales, coupled with their observations in a wide range of material systems and at low speeds, suggests a continuum-level buckling instability mechanism for their formation that is devoid of any intrinsic microstructural length scales and temperature effects. In this dissertation, we revisit the problem through the plastic buckling framework and seek to answer a two-fold question. First, are microstructural features such as grain boundaries necessary to initiate folding in metals, e.g., can surface folds develop in cutting of single crystals? If so, what determines the wavelength and fold spacing in the absence of microstructural effects? Secondly, is it possible to model the instability wavelength across different length scales within a unified framework? The fact that fold spacing in an ultramicrotomed chip section ($t_0 \sim$ hundreds of nm) is a few orders lower than that in a chip produced at the macroscale ($t_0 \sim 50$ $\mu$m), see Fig. 2.5, suggests self-similar scaling of the fold spacing with respect to sample length scale, $t_0$.

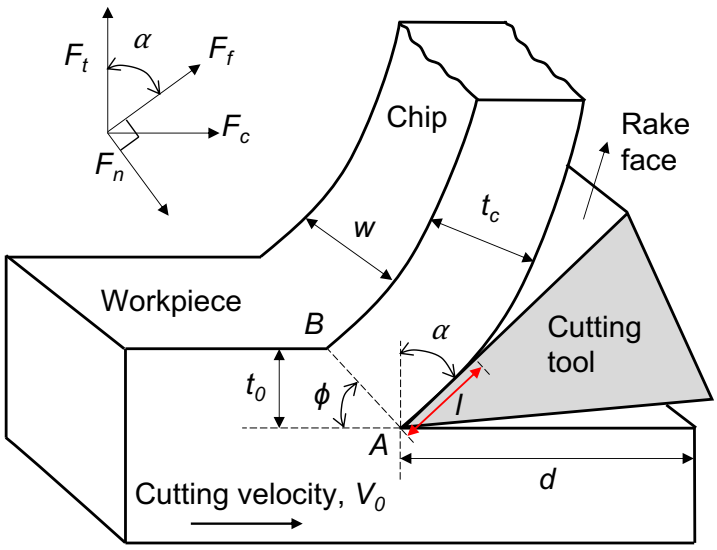


Figure 2.1. Schematic of 2-dimensional plane-strain orthogonal cutting. $F_c$ and $F_t$ are the cutting and thrust forces, while $F_f$ and $F_n$ are the friction and normal forces acting at the tool-chip contact. Cutting process parameters include rake angle ($\alpha$), depth of cut ($t_0$) and the cutting width ($w$). The tool-chip contact length is denoted by $l$.

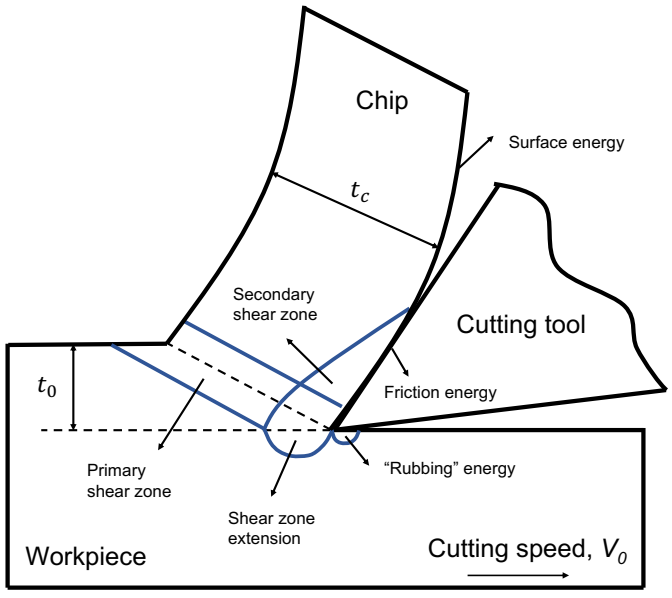


Figure 2.2. Energy consumption in orthogonal metal cutting (reproduced from Nakayama and Tamura [11]) with permission).

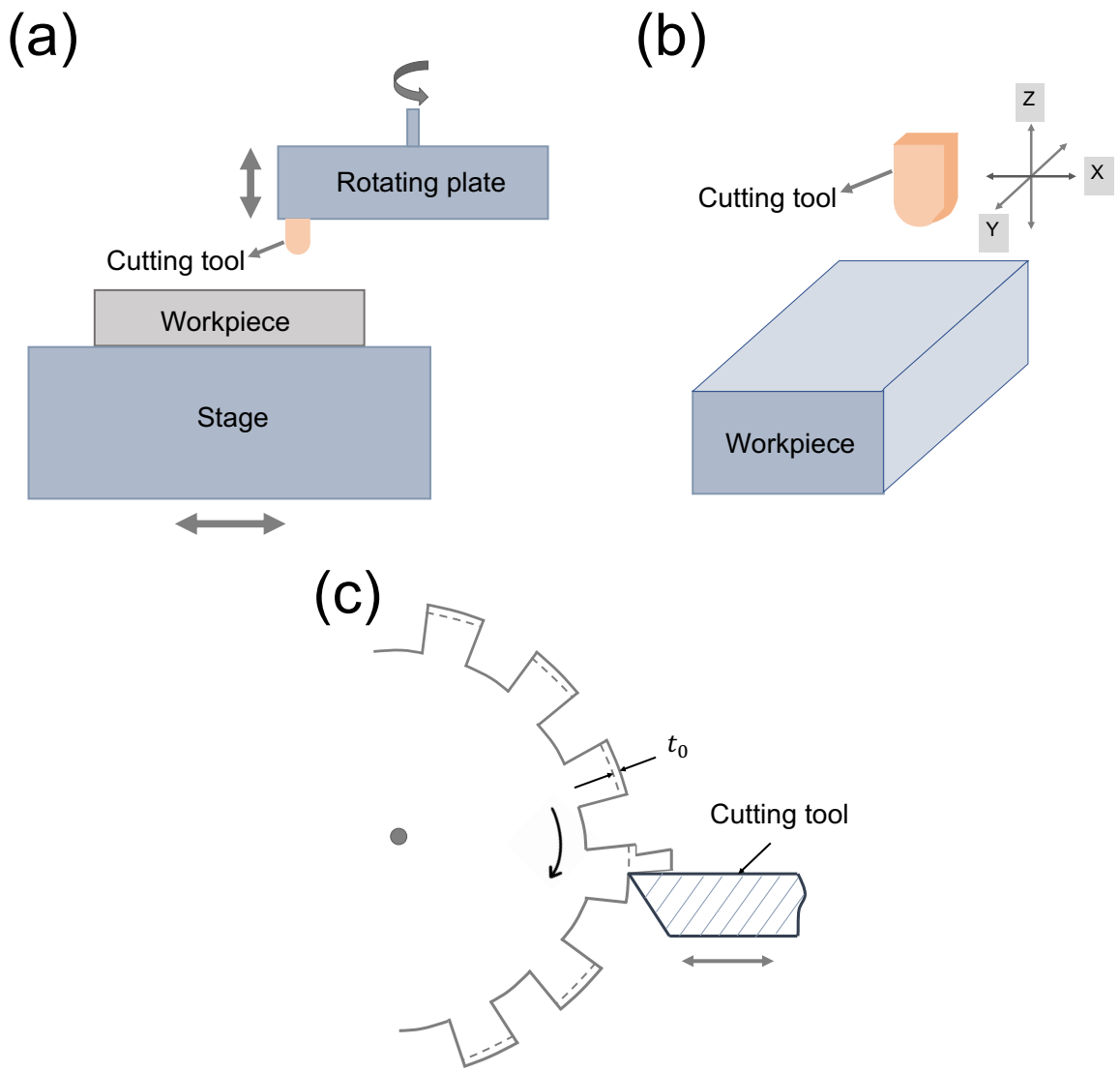


Figure 2.3. Schematic of experimental configurations used in small scale cutting studies: (a) flycutting, (b) grooving, and (c) single-point turning (reproduced from Lucca et al. [7] with permission).

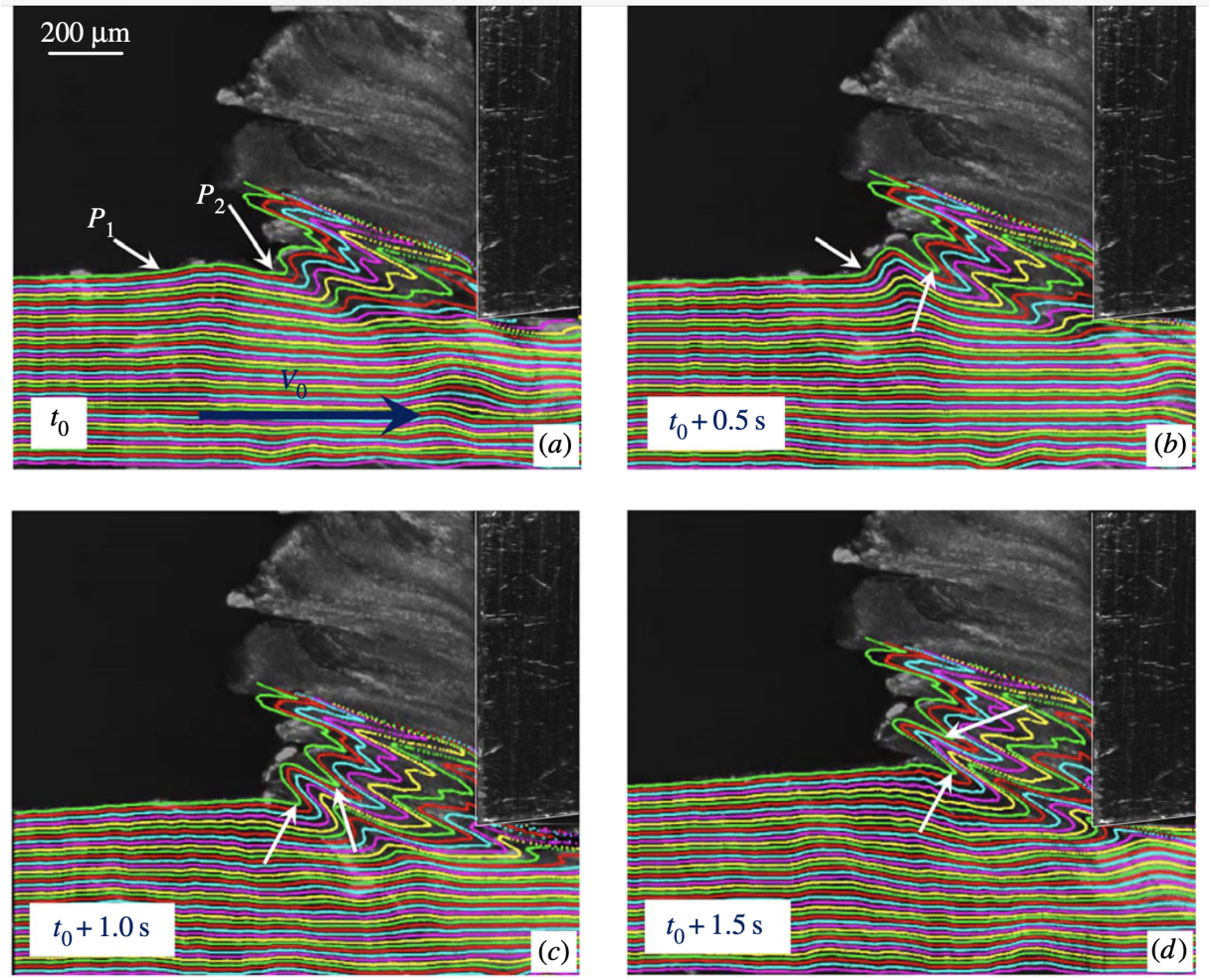


Figure 2.4. Fold formation via plastic buckling in cutting of pure copper: (a) initialization of small bump ahead of the tool edge, (b) growth of the bump through localization between two 'pinning points', (c) rotation of the bump, and (d) formation of sinusoidal-shaped fold (reproduced from Udupa et al. [18] with permission).

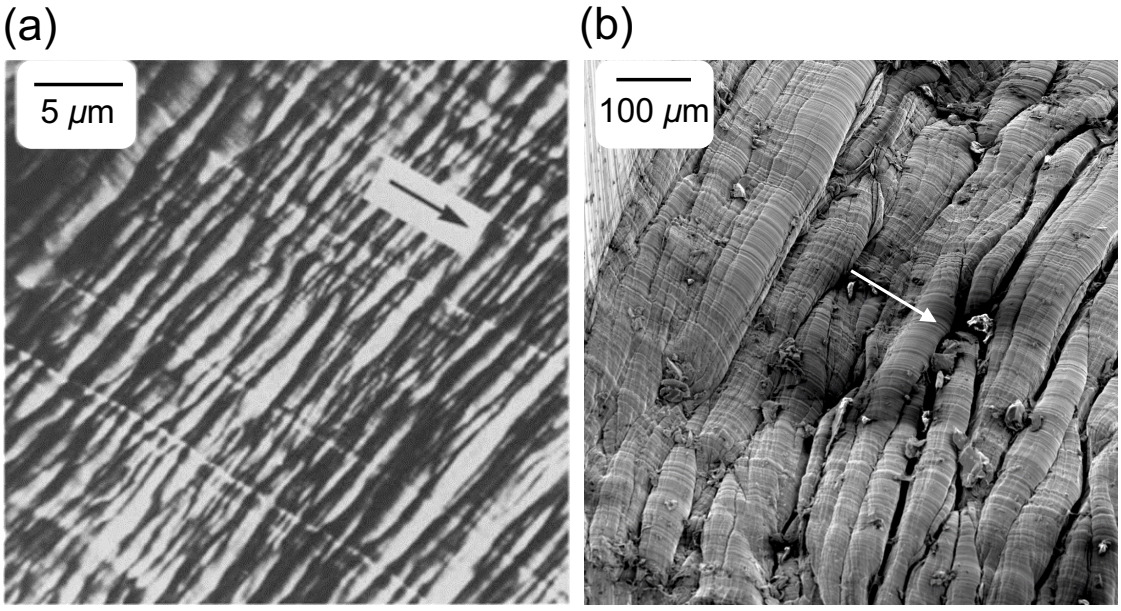


Figure 2.5. SEM images showing the free surface morphology of copper chips produced using: (a) microtomy at $t_0 \sim 1$ $\mu$m (reproduced from Williams et al. [31] with permission) and (b) conventional machining ($t_0 \sim 100$ $\mu$m). Note the similar surface fold characteristics in both the cases despite the large difference in the cutting depth. Arrows indicate the chip flow direction.

Table 2.1. Summary of the theoretical explanations for the size effect in metal cutting at small scales

| **Theory** | **Description** | **Limitation** |
|---|---|---|
| Dislocation-based [47] | Size effect arises from flow stress increase due to lower chance of encountering dislocations at small scales. | Questionable given that cutting is a large strain plastic deformation process characterized by dislocation densities exceeding $10^{15}/\mathrm{m}^2$. |
| Strain gradient theory [12, 13] | Flow stress increases at small length scales due to increased plastic strain gradient and associated geometrically necessary dislocations. | Strain gradient theory primarily applies to small deformation problem where the density of geometrically necessary dislocation is comparable to the static dislocation density. |
| Cutting edge radius effects | Size effect attributed to the non-zero force intercept that is associated with processes arising from finite cutting edge radius, e.g., rubbing at flank wear [30], ploughing [29, 42, 50]. | Does not explain the occurrence of size effect with very sharp tools. Existence of finite force intercept is also debatable for the case of very sharp tools. |
| Fracture energy [16] | Size effect attributed to non-zero force intercept due to the fracture work required to create two new surfaces. | |
| Subsurface plastic deformation [11] | Size effect attributed to non-linear scaling of subsurface plastic deformation energy with the depth of cut. | Accurate characterization of the energy component associated with subsurface plastic deformation is highly difficult at small scales. |

Table 2.2. Summary of experimental studies on cutting of metals at small depths of cut. Blank entries in the table indicate the lack of data/information.

| Experimental configuration | Workpiece material | Cutting tool | Tool nose radius (mm) | Tool edge radius (nm) | Rake angle (°) | Depth of cut ($\mu$m) | Cutting speed (m/min) | Reference |
|---|---|---|---|---|---|---|---|---|
| Flycutting (fixed workpiece) | Cu, Al | Diamond | 5 | – | 0 | 3, 7, 12 | 565, 942, 1319 | [65] |
| Flycutting (fixed workpiece) | SUS303Se | Diamond, CBN | Diamond: 1, CBN: 0.2 | – | 0 | 2 | 565 | [26] |
| Flycutting (fixed workpiece) | Al, Al-Mg-Si, Al-0.2% Fe | Diamond | – | 23 – 70 | 0 | 2 – 3 | 450 | [66] |
| Flycutting (fixed workpiece) | Annealed OFHC Cu | Diamond | 1 | – | 0 | 0.0025 – 5 | 754 – 1380 | [9] |
| Flycutting (fixed workpiece) | Cu-0.5% Te | Diamond | Flat | 220 – 920 | -30 – 0 | 0.01 – 20 | 7.6, 76.2 | [28] |
| Flycutting (fixed workpiece) | 6061-T6 Al | Diamond | Flat | 200 | 2.5 | 0.01 – 20 | 48 | [67] |
| Flycutting (fixed workpiece) | Cu-0.5% Te | Diamond | Flat | 75 – 105 | 0 | 0.01 – 10 | 47.9 | [68] |
| Flycutting (fixed tool) | OFHC Cu | Diamond | – | 500 | 0 | 1 | 138, 276 | [69] |
| Flycutting (fixed tool) | SUS303Se | Diamond | 0.8 | – | 0 | 2, 3 | 1.4 – 4.2 | [25] |
| Flycutting (fixed tool) | Al-4% Cu, OFHC Cu | Diamond | 1 | – | 0 | 3 | Al-4% Cu: 337 – 1413, OFHC Cu: 377 – 1272 | [70] |
| Flycutting (fixed tool) | Al-Mg | Diamond | – | – | – | 10 | – | [71] |
| Flycutting (fixed tool) | Cu, Al | Diamond | 3 | – | -1 | 1.25 | 16 | [72] |
| Flycutting | Al-Mg | Diamond | 2, 6, 10 | – | 0 | 15 – 20 | 0.02 | [73] |
| Single point turning | OFHC Cu | Diamond | – | 10 | – | 0.01 – 0.6 | 600 | [74] |
| Single point turning | OFHC Cu | Diamond, HSS | – | Diamond: 15 – 45 | 20 | Diamond: 0.1 – 10, HSS: 1 – 15 | 138, 276 | [69] |
| Single point turning | OFHC Cu | Diamond | 6.35 | 100 – 300 | 0 | 0.1 – 10 | 6 | [7, 75] |
| Single point turning | Fine-grained Cu | Diamond | 6.35 | 100 – 300 | 0 | 0.025 – 15 | 7.2, 107.7 | [7, 75] |
| Single point turning | Annealed 70/30 brass | HSS | – | – | 10 – 30 | 86.4, 213, 345 | 61, 122, 183 | [76] |
| Grooving | OFHC Cu | Diamond | 0.762 | – | 0 | 0.046 – 3.8 | 122 – 183 | [77] |
| Grooving | Al, Cu, Ge, $CaF_2$, PMMA | Diamond | 0.5 | – | 0 | 0.5 – 10 | 6 | [27] |

# 3. EXPERIMENTAL

As discussed in Chapter 2, one of the main challenges in understanding the mechanics of cutting at small length scales is the lack of experimental techniques suitable for conducting cutting experiments under ideal and well-controlled conditions. The present work attempts to overcome this experimental challenge by using an ultramicrotomy setup to achieve steady-state orthogonal cutting under 2-dimensional plane-strain conditions at depths of cut as small as 30 nm. A modification to the sample and knife mounting of an ultramicrotome and instrumentation of the setup with load sensors, to enable cutting and thrust force measurements during the cutting process, is described. The performance of this instrumented ultramicrotome is described in terms of repeatability of the experiments and the range of cutting depths it can achieve. Glass knife preparation procedures that have been used to achieve cutting tools with extremely small edge radius ($\sim 5$ nm) and different rake angles are also discussed, along with the material systems that were used in the study.

## 3.1 The instrumented ultramicrotome

A number of studies have been made on the cutting of metals (both polycrystalline and single crystals) at small depths of cut using an ultramicrotome. Clarebrough and Oglivie [78] were perhaps the first to use a microtome to investigate the cutting behavior of metals, who also highlighted the development of periodic folds and wrinkle-like structures on the chip free surface in their experiments with lead. Subsequent research on producing ultrathin sections of metals using the microtomy technique was explored by Phillips, Ogura, von Turkovich, Black, Ramalingam, Stobbs, Williams and co-workers [21, 22, 23, 24, 63, 79]. All of these studies were primarily concerned with the development of fine-scale structures within and on the surface of the chips, including the effects that crystallographic orientation of individual grains have on these structures. However, serious attempts to quantify forces and energy consumption during microtomy have been extremely few. The only study which attempts to measure forces in microtomy of metals appears to be that by Williams and Gane [31]. Even in this case, forces were measured only in one direction (along the cutting velocity) and the smallest depth of cut used was 1 $\mu$m.

The present work is based on the ideas of Ericson and Lindberg [80] who proposed using piezo-

electric force transducers to measure both the forces (cutting force as well as thrust force) to evaluate the fracture energies in soft polymers. A complete account of similar attempts to instrument the microtome for applications involving sectioning of soft visoelastic materials (e.g., polymers, wax, plant/human tissue, etc.) can be found in Refs. [80, 81, 82, 83]. The ultramicrotomy system used in our study is Leica EM UC7. The schematic of the ultramicrotomy setup and chip formation process therein are shown in Fig. 3.1, along with a picture of the actual experimental setup. In this configuration, a thin layer of material (chip) is removed from the workpiece as the swing arm holding the workpiece moves against the stationary glass/diamond knife edge in a pendulum-like motion. The depth of cut, $t_0$, in each cutting pass is controlled using a micro-stage on which the knife (cutting tool) is mounted. To measure the cutting ($F_c$) and thrust ($F_t$) forces simultaneously (see Fig. 3.1(b)), the ultramicrotome was instrumented with two separate single-axis piezoelectric force sensors (PCB 209C02) with a resolution of $9 \times 10^{-5}$ N. The modifications made to the knife and the workpiece holders to fit these sensors are shown in Fig. 3.2. To measure the cutting force, a customized tool holder as shown in Fig. 3.2(a)) was fabricated using aluminum (6061-T6). It was designed such that its bottom surface resembles the original knife holder supplied by the microtome manufacturer, but with a hollow internal structure to accommodate easy mounting of the force sensor. The glass/diamond knives were mounted on the sensor by applying a thin layer of superglue (ethyl cyanoacrylate) on the sensing surface and lightly pressing the knife against this surface. The knives were then fastened from the side using a set screw (Fig. 3.2(a)), and left for at least two hours until the glue is completely dry. The customized fixture design implemented for measuring the thrust force $F_t$ is depicted in Fig. 3.2(b). Here, the sensor is mounted between two flat aluminum surfaces, with the pre-load on the sensor is controlled by the two cap screws as shown in the figure. The rear aluminum part is used for mounting the fixture into the ultramicrotome swing arm, whereas the front end with a hollow structure is used for holding the workpiece. The fixture and sensor placement before the start of an experiment can be seen from Figs. 3.1(a) and (c).

### 3.2 Sensor calibration and signal processing

The two piezoelectric force sensors are connected to a multi-channel signal conditioner (PCB 482C24), which preprocesses the input voltage signals captured with a sampling frequency of 1280

Hz. The outputs from the signal conditioner was then processed by a data acquisition (DAQ) system (NI 9232) such that the voltage signals are readable by the readout device. In our experiments, a PC is used as the readout device with the output voltage profiles displayed in an interface developed using LabVIEW. Finally, the acquired data was saved as text files, and the post-processing and data visualization are completed with Python.

Because of the small forces (5 - 50 mN) involved at sub-$\mu$m cutting depths, careful calibration of the sensors was found to be extremely important. The cutting force sensor was calibrated by placing known weights (1 to 20 grams) on the flat rake surface of the glass knife with a zero degree rake angle (which itself is mounted on a sensor using superglue, shown in Fig. 3.3(a)), and measuring the corresponding voltage signal. As can be seen from Fig. 3.3(b), the readings have shown that the voltage signal from the cutting force sensor varies proportionally with the load; this proportionality constant, obtained using the linear regression analysis, was used as the calibration factor (in V/N). The smallest weight used in these calibration studies was 1 gm (10 mN); the forces smaller than 10 mN in our cutting experiments were estimated based on the above calibration factor.

On the other hand, the thrust force sensor along the horizontal direction was calibrated using an additional piezoelectric sensor (PCB 209C11, referred to as the "standard" sensor in Fig. 3.3), and a pre-compressed spring loaded between both the sensors, as shown in Fig. 3.3(c). Different force values were achieved by controlling the spring compression – by changing the distance between the force sensors using the micro-stage. The calibration constant was determined by plotting the voltage signal from the thrust force sensor (to be calibrated) against the readings of the second sensor, shown in Fig. 3.3(d). The above approach resulted in calibration constants of 4.85 V/N and 3.64 V/N respectively for the cutting and thrust force sensors. A sensitivity analysis was also carried out to ensure that the calibration constants are independent of the tool geometry or workpiece material; these constants are therefore determined only by the fixture design/configuration.

A series of experiments was conducted to test the suitability of the instrumented ultramicrotome configuration to sense forces as thin metal sections are produced and verify the measurements repeatability from experiment to experiment. Fig. 3.4 is a series of images showing the evolution of a copper chip when cutting using a glass knife at $\alpha = 15^{\circ}$, $t_0 = 500$ nm, and $V_0$ of 0.05 mm/s. These images were taken using a camera (Leica IC90 E) attached to the Leica microscope which

is configured to enable direct visualization of the knife edge. A perfectly rectangular chip can be seen from the images, with its width remaining constant with respect to the original (uncut) dimensions. This indicates that the deformation underlying chip formation is in fact close to the two-dimensional plane-strain conditions commonly assumed in the models.

Fig. 3.5 shows the corresponding cutting ($F_c$) and thrust ($F_t$) force sensor data simultaneously captured during the cutting process. Fig. 3.5(a) shows the raw voltage signals from the sensors, whereas Fig. 3.5(b) shows the force data, computed based on the calibration constants and the raw voltage signals. It should be noted it is the normalized force data in N/mm, i.e., force normalized with respect to the cutting width $w$, that is shown in Fig. 3.5(b). Throughout this dissertation, the force data is always presented in a normalized manner, to allow for direct comparison of data from different workpiece samples unless otherwise noted. From Fig. 3.5(b), it can be seen that the cutting process reaches steady-state in a relatively short time, with forces largely remaining constant during the remainder of the cut. This confirms constant $t_0$ during the entire course of the cutting experiment. It is also these steady-state forces that are reported and used in the specific cutting energy calculations.

That the force measurements are also repeatable can be seen from Figs. 3.6 and 3.7. These figures show three force traces in cutting of pure copper obtained from three repetitions of the cutting experiment under identical conditions; Fig. 3.6 shows the data obtained using a glass knife ($\alpha = 15^\circ$), whereas Fig. 3.7 corresponds to a diamond knife ($\alpha = 40^\circ$). The variation in the forces from experiment to experiment is typically no more than 15%, with this variation most likely due to the polycrystalline nature of the samples and relatively large grain sizes in the workpiece in comparison with $t_0$. The force traces in Figs. 3.6 and 3.7 also reveal that the thrust force component $F_t$ can be quite sensitive to the tool material used, with $F_t$ in fact being larger than $F_c$ in the case of glass knife. This latter observation is in contrast to conventional cutting ($t_0 \sim 10$ - 100 $\mu$m) where $F_c$ is usually the dominant component. It will be shown later that this anomalous behavior in cutting at the small scale is closely tied in with the tool-chip contact mechanics.

For each cutting condition (as characterized by tool-material combination, rake angle, depth of cut, tool surface boundary condition, etc.), at least 3-5 repetitions of the experiment were conducted, and force data from the steady-state region of the cutting trace were utilized to compute the average $F_c$ and $F_t$ values and associated standard deviations.

### 3.3 Cutting tool preparation

A unique feature of this work is the use of knives (cutting tools) with extremely small cutting edge radii. Two types of knives – diamond and glass knives – were used in the experiments. The diamond knife with a fixed knife angle of 45° was obtained from Diatome Ltd. Note that the knife angle is different from the rake angle. Knife angle represents the included angle between two faces on either side of the knife edge. The manufacturer-specified cutting edge radius for the diamond knife is 2 nm. All the experiments with the diamond knife were performed by allowing a $5^\circ$ clearance angle between the machined surface and tool flank face; this corresponds to a rake angle of $40^\circ$. Glass knives were made from soda-lime glass strips by using a conventional glass knife maker (Model No. LKB 7800). This involved first indenting scores on one side of the glass plate followed by application of a light bending load to produce a clean fracture (see Fig. 3.8(a)). A unique advantage of this approach is that glass knives with different knife angles ($45^\circ$, $70^\circ$, $85^\circ$, and $90^\circ$) could be conveniently made using this technique. Additionally, the glass knives prepared using this technique were quite inexpensive ($<$ 30 cents per knife) and were characterized by clean cutting edges that are extremely sharp. For example, Fig. 3.8(b) shows a scanning electron micrograph of a freshly cleaved knife (knife included angle = $45^\circ$) where a clean and defect-free cutting edge geometry is evident. Past work from the literature, involving the use of scanning force microscopy, has shown that the glass knives produced using the cleavage method have a cutting edge radius of about 5 nm [84], which is in fact close to the theoretical tip radius of a brittle crack [85]. Thus, the approach employed here overcomes a key experimental limitation intrinsic to cutting at small scales – that of large cutting edge radius that is comparable or even greater than the depth of cut – thereby allowing us to explore the mechanics of cutting in the absence of edge radius effects and as a function of different rake angles.

An attempt has been also made to characterize the rake face and cutting edge radius of the glass knives using an atomic force microscope (AFM). The results from AFM measurements on two glass knives, one with a $70^\circ$ included angle and other with a $90^\circ$ included angle, are shown in Figs. 3.9 and 3.10, respectively. Fig. 3.9(a) shows the measured 3D profile of the knife edge. In this measurement, the knife edge was aligned so that it is approximately centered about the vertical axis of the AFM tip. The scan area was 3 $\mu$m × 3 $\mu$m and the scanning speed was set to be 13.7

nm/s. The rake face surface roughness ($Ra$) computed from this measurement was 27.2 nm. A sectional profile of the cutting edge extracted from the 3D profile (marked by $A$-$A'$ in Fig. 3.9(a)) is shown in Fig. 3.9(b). The cutting edge radius estimated from this profile was about 25 nm. However, it should be noted that the cutting edge radius measurement using AFM, especially in the nanoscale range, is limited by the finite radius of the AFM tip. For instance, a typical AFM tip in its pristine condition has a radius of 5 - 20 nm [86], of the same order of the cutting edge radii in the present study. The consequence of the finite AFM tip size is that it overestimates the cutting edge radius; therefore, the above estimated value should be taken as an upper bound on the actual edge radius. Analysis of AFM data obtained from the glass knife with a $90^{\circ}$ angle has yielded similar roughness value $Ra$ = 15.3 nm for the rake face, although the cutting edge radius was estimated to be much larger in this case ($\sim$ 100 nm).

### 3.4 Material systems and sample preparation

The material systems that were studied in this work include: polycrystalline OFHC copper in two different starting conditions: as-received condition (obtained from McMaster-Carr) and annealed condition (annealed at 1000 °C for four hours); polycrystalline 1100 aluminum also in two different starting conditions: as-received condition (McMaster-Carr) and annealed condition (annealed at 350 °C for one hour); and polycrystalline commercially pure zinc (McMaster-Carr). These materials were mainly chosen because of their purity, softness and tendency to form continuous chips under most cutting conditions. Both copper and zinc samples had an equiaxed recrystallized microstructure in their as-received state, whereas aluminum samples (in both the as-received and annealed conditions) were characterized by an elongated microstructure; see Figs. 3.11, 3.12 and 3.13. The copper microstructure after annealing exhibited much larger and irregular-shaped grain structure, possibly due to the phenomenon of abnormal grain growth. The corresponding grain sizes, compositions and Vickers hardness values (500 gram indentation load) are provided in Table 3.1. A few experiments were also carried out with single crystalline aluminum to explore how lack of grain structure and defects (e.g., grain boundaries) influence chip formation and development of surface folds. In these experiments, the cutting was carried out on the $\{\bar{1}10\}$ plane of the crystal, with cutting direction aligned parallel to the $< 001 >$ direction.

Electrodischarge machining (EDM) was used to prepare bar-shaped samples with a small pyra-

midal tip. After EDM, the pyramidal tip of the sample was trimmed using a diamond knife to create a square-shaped cutting cross-section ($\sim 300 \times 300$ $\mu$m$^2$, see Fig. 3.8(a)) to minimize the effect of surface microstructure/property changes associated with the EDM sample preparation technique. Additionally, before each experiment, the sample surface was further subjected to several trimming passes with a very small cutting depth – about 30 nm with diamond knife and 100 nm with glass knife – to ensure that the surface is as smooth as possible and 'free' of any deformed layer from the previous cutting experiment. Experiments with the glass knives showed that high-quality sections (chips) could be produced from all the three materials (Cu, Zn and Al) over a range of $t_0$ varying from 100 nm to 3 $\mu$m. Chipping (fracture) of the cutting edge was an issue at higher $t_0$, while the chips produced at $t_0 < 100$ nm were often found to have defects in the form of tears and cracks. On the other hand, ultrathin sections ($t_0$ = 30 nm) were possible to achieve using the diamond knife; this is likely because of the smaller cutting edge radius of the diamond knife. However, the upper range with the diamond knife was limited to about 1 $\mu$m, because of the high likelihood of edge chipping beyond this value. It should be also noted that across all the cutting depths, the cutting edge radius is at least one order smaller than $t_0$. The edge radius effects are therefore negated in our study.

### 3.5 Characteristics of finished workpiece surfaces and microtomed chips

As noted earlier, before the start of each experiment, the workpiece surface was carefully prepared by several small trimming passes to ensure that it is as smooth as possible and free of any plastic deformation from the previous experiments. Figs. 3.14(a) and (b) show the AFM scans of these finished surfaces, as produced using diamond and glass knives, respectively. The scratches seen in these images, along the cutting direction, are a result of the tiny defects present on the cutting edge. Therefore, the finished surface morphology of the workpiece is extremely sensitive to the cutting edge quality. Multiple scans, taken over a typical 10 $\mu$m $\times$ 10 $\mu$m surface area, showed that diamond-trimmed surfaces are characterized by an $Ra$ of 0.784 nm and $Rms$ of 1.22 nm, whereas the typical values for surfaces produced by glass knives are somewhat higher, with an $Ra$ of 7.75 nm and $Rms$ of 10 nm; the better surface finish in the case of diamond is likely due to better edge quality and smaller edge radius of the diamond knife. However, it should be noted that even in the case of glass knives, the roughness values are still several times (by an order of

magnitude) smaller than the cutting depths (100 nm to 3 $\mu$m) used with these knives. We therefore expect the surface roughness to have only a secondary influence, if any, on the overall results. In the case of diamond, surface roughness effects should certainly be of little importance because of the very smooth finish.

The morphology of a typical chip section produced using a glass knife is illustrated in Fig. 3.15 using SEM imaging. As noted earlier, no change in width was observed with respect to the original (uncut) dimensions ($400 \times 400$ $\mu$m$^2$), indicating plane-strain deformation conditions. However, it can be seen that the final chip length is much smaller, by about a factor of 3, with respect to the original cutting length. It is important to note that while this is commonly referred to as the chip 'compression' in the microtomy literature, this change in length is actually brought about by plastic shear in the shear zone. Fig. 3.15(b) shows a higher-magnification image of the chip free surface that is characterized by periodic wrinkles. These features were observed in all our experiments with a large variety of metals, and found to always lie perpendicular to the cutting direction, regardless of the material or the cutting condition. Cutting direction in Fig. 3.15(b) can be for instance inferred from orientation of the knife marks, see at arrow.

In contrast to a flat chip, as shown in 3.15, there were several instances where extreme curling of the chip was observed, to an extent that the chip often wound up into a tight roll. Fig. 3.16 shows the evolution of such a chip. The chip curl was most prominent in Al at small rake angles, while quite the opposite for Cu wherein curling occurred only at highly positive rake angles ($\alpha = 40°$). The underlying reason for these differences is not clear at the present time. The $\alpha$ and $t_0$ conditions resulting in extreme curling of the chip are shown in Fig. 3.17, for both Cu and Al.

### 3.6 Experimental workflow

The typical experimental workflow included the following steps. A freshly cleaved glass knife was used in every experiment; whereas in the case of diamond knife, the knife edge was cleaned thoroughly using ethanol and a cotton swab to remove any contamination from the previous experiments. At least three sets of data from multiple repetitions of the experiment were obtained for each cutting condition (as determined by the combination of workpiece, tool and cutting parameters). This included collection of force traces, identification of the steady-state region of the force profiles and calculation of average values for $F_c$ and $F_t$ under each cutting condition. The chip

sections produced during the experiments were also collected by guiding them with an eyelash stick towards a sample mount with an adhesive carbon tape on its side, and subsequently observed under an optical or scanning electron microscope to measure the chip length. The chip thickness ratio, $r = t_0/t_c$ (where $t_c$ is chip thickness), was calculated based on the post-measurements of the chip length. It was taken as the ratio $l_c/l_0$ (where $l_c$ is the chip length and $l_0$ is the initial length of the cutting cross-section), based on the volume conservation and plane-strain assumption. In the case of extreme chip curl, the chip thickness ratio could not be determined since it was not possible to measure the chip length accurately. A limitation of our experimental setup is the difficulty of achieving steady-state chip formation at small rake angles ($< 15^\circ$) and larger $t_0$, greater than 1 $\mu$m, especially in Cu. Under these cutting conditions, it was often found that the chip thickness is not constant but continues to grow during the entire duration of the cut, accompanied by steady increase in the cutting and thrust forces. The chip thickness, $r$ value and force data for these conditions should be therefore treated with caution. Unless otherwise stated, all the experiments were performed in a "dry" condition (i.e., without lubricant or surface films). The cutting speed $V_0$ in all the experiments was 0.05 mm/s.

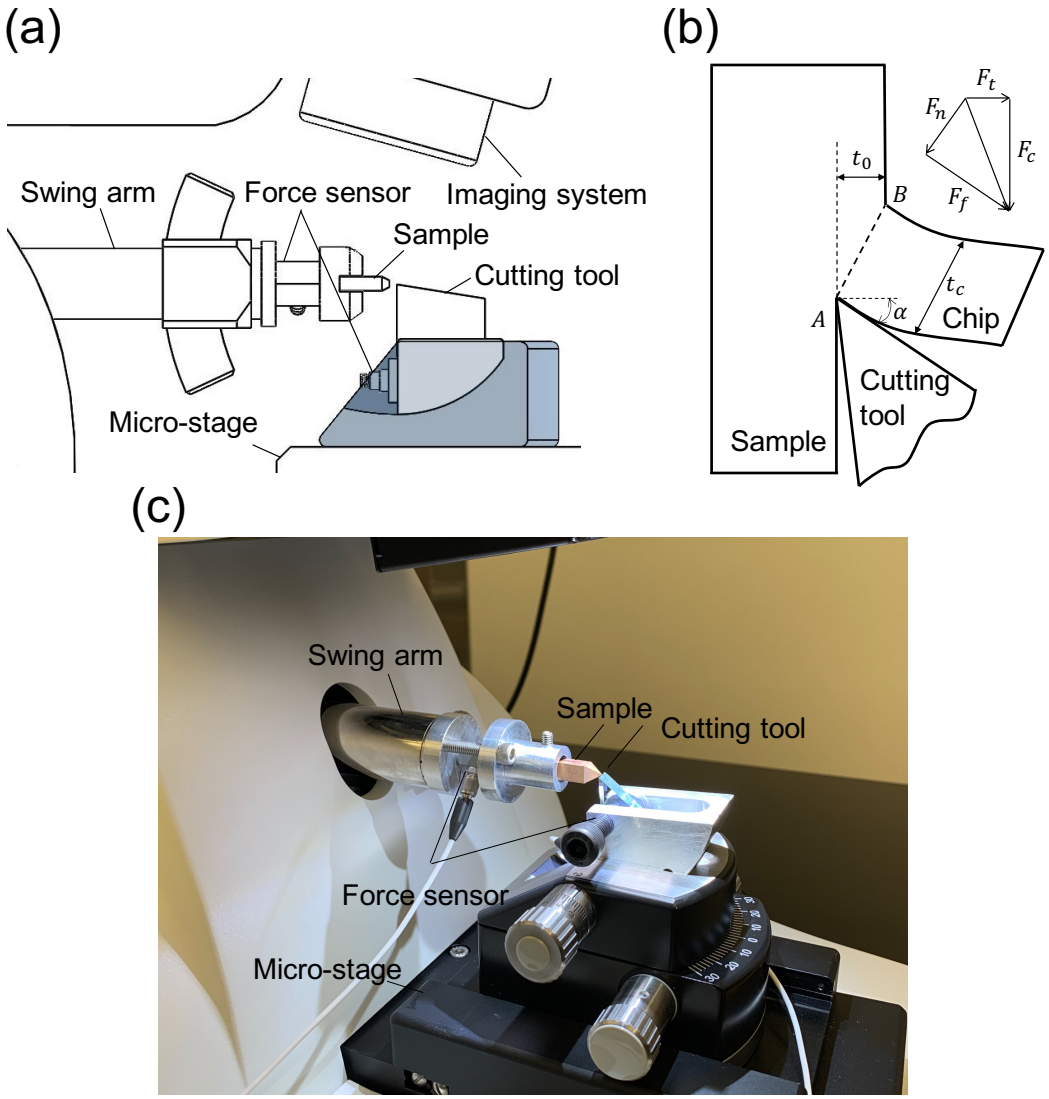


Figure 3.1. Schematic of (a) instrumented ultramicrotomy cutting setup, and (b) chip formation in 2D plane-strain cutting. $F_c$ and $F_t$ are the cutting and thrust forces measured directly by the sensors, while $F_f$ and $F_n$ are the friction and normal forces acting at the tool-chip contact. The experimental platform used in the study is shown in (c).

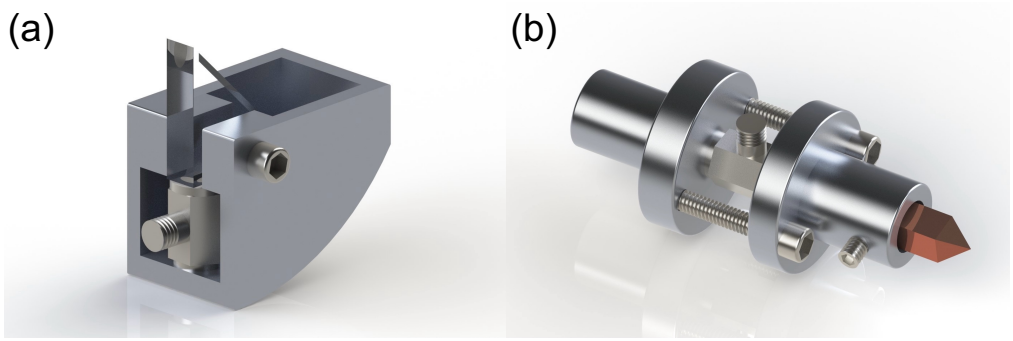


Figure 3.2. Customized fixture designs developed to measure forces in ultramicrotomy: (a) knife holder showing a glass knife mounted directly on a force sensor, and (b) workpiece holding fixture, where the sensor can be seen mounted between two flat surfaces.

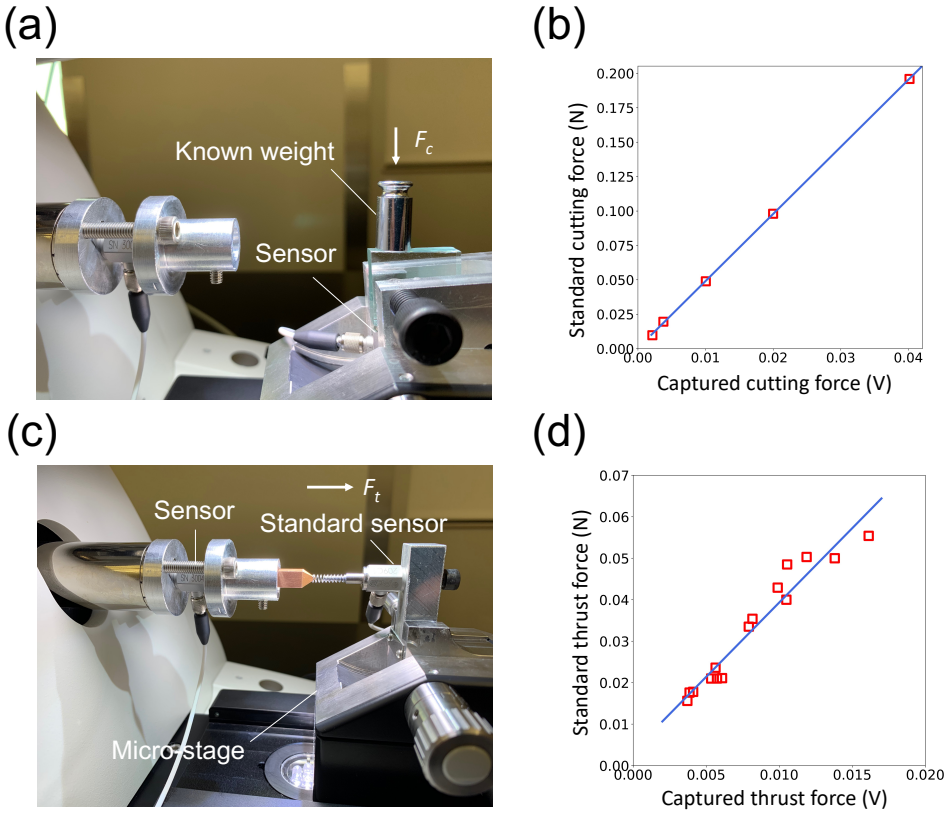


Figure 3.3. Experimental setups used for calibrating the cutting ($F_c$) and thrust ($F_t$) force sensors. (a) and (b) show cutting force sensor calibration carried out by placing known weights on top of the tool rake face. (c) and (d) show calibration of the thrust force sensor by using an additional (standard) sensor and a spring mechanism to control the load.

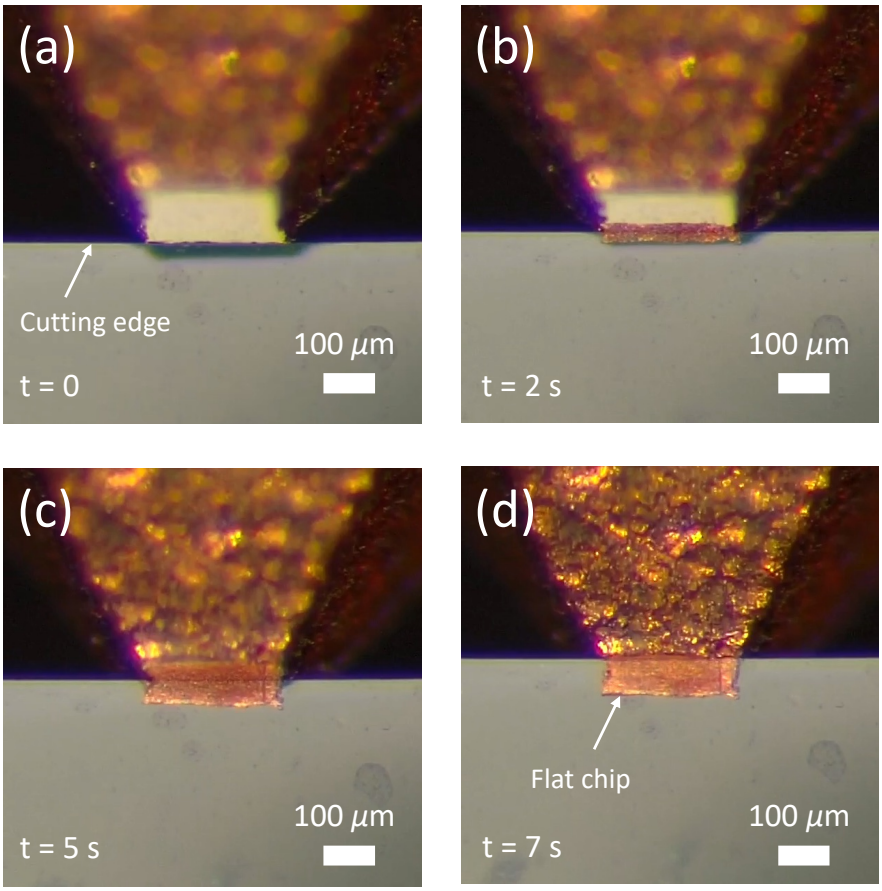


Figure 3.4. Image sequence recorded using the microscope camera showing the formation of a copper chip (glass knife, $\alpha = 15°$, $t_0$ = 500 nm).

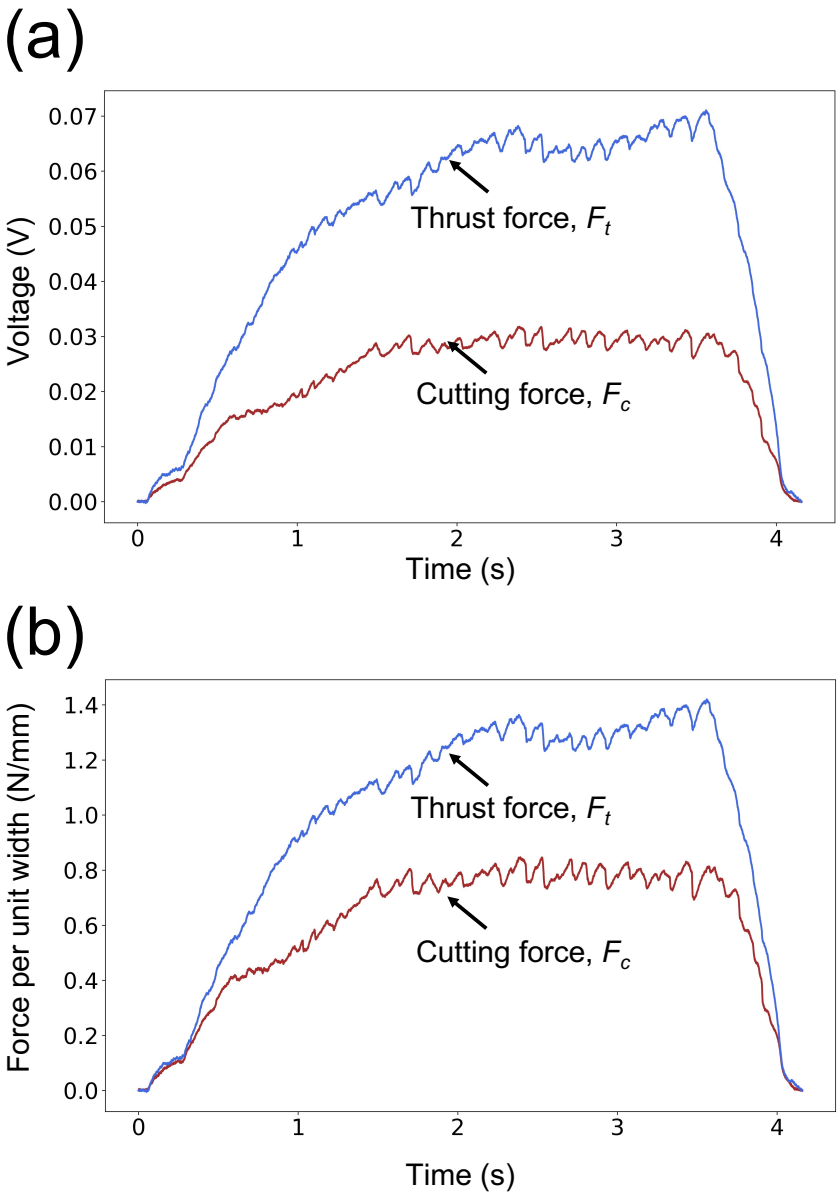


Figure 3.5. Plots showing typical sensor data obtained during cutting of copper using a glass knife ($t_0$ = 500 nm, $\alpha = 15°$, $V_0$ = 0.05 mm/s, $w$ = 0.182 mm): (a) raw voltage (V) signal from the sensors, and (b) normalized force traces (N/mm) computed based on the sensor voltage signal and calibration constants for the sensors. Force normalization is done with respect to the cutting width $w$.

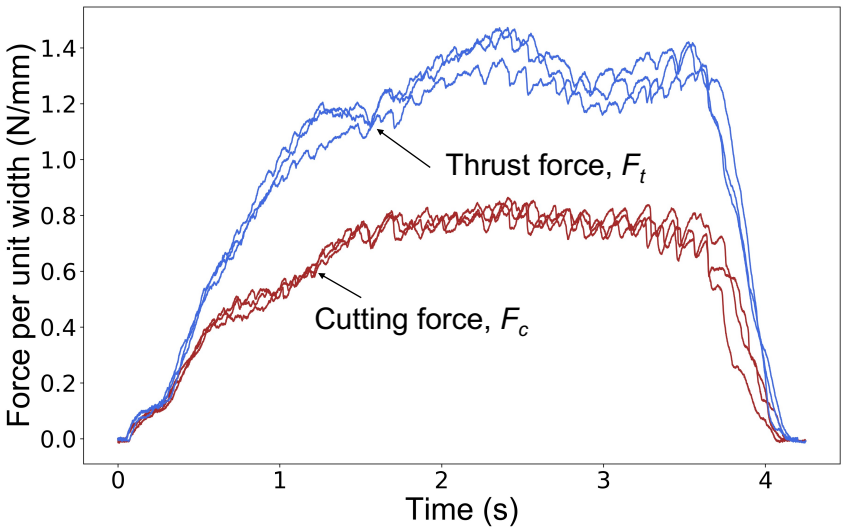


Figure 3.6. Force traces in cutting of Cu with a glass knife, obtained from three repetitions of the experiment under the following cutting conditions: $\alpha = 15°$, $t_0$ = 500 nm, $V_0$ = 0.05 mm/s. Note the good repeatability in force measurements across multiple repetitions.

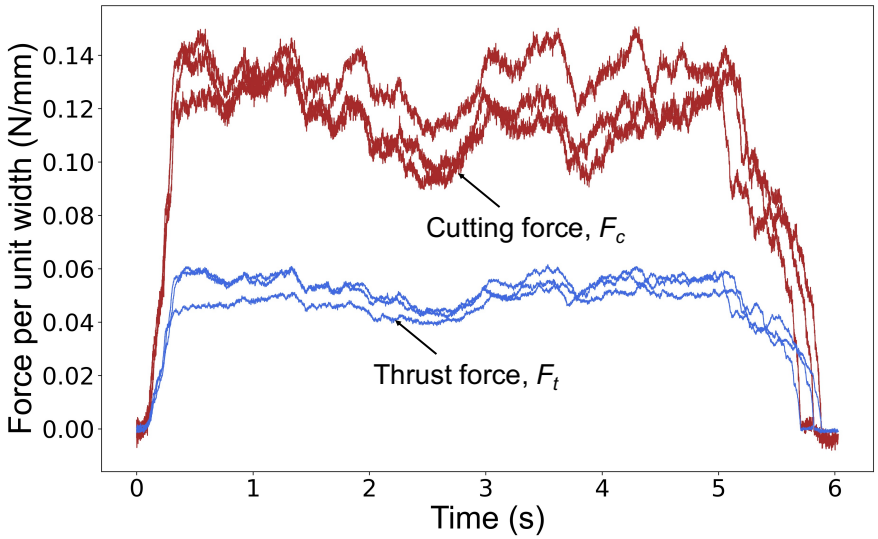


Figure 3.7. Force traces in cutting of Cu with a diamond knife ($\alpha = 40°$, $t_0$ = 100 nm, $V_0$ = 0.05 mm/s). The three force traces correspond to three repetitions of the experiment under identical cutting conditions.

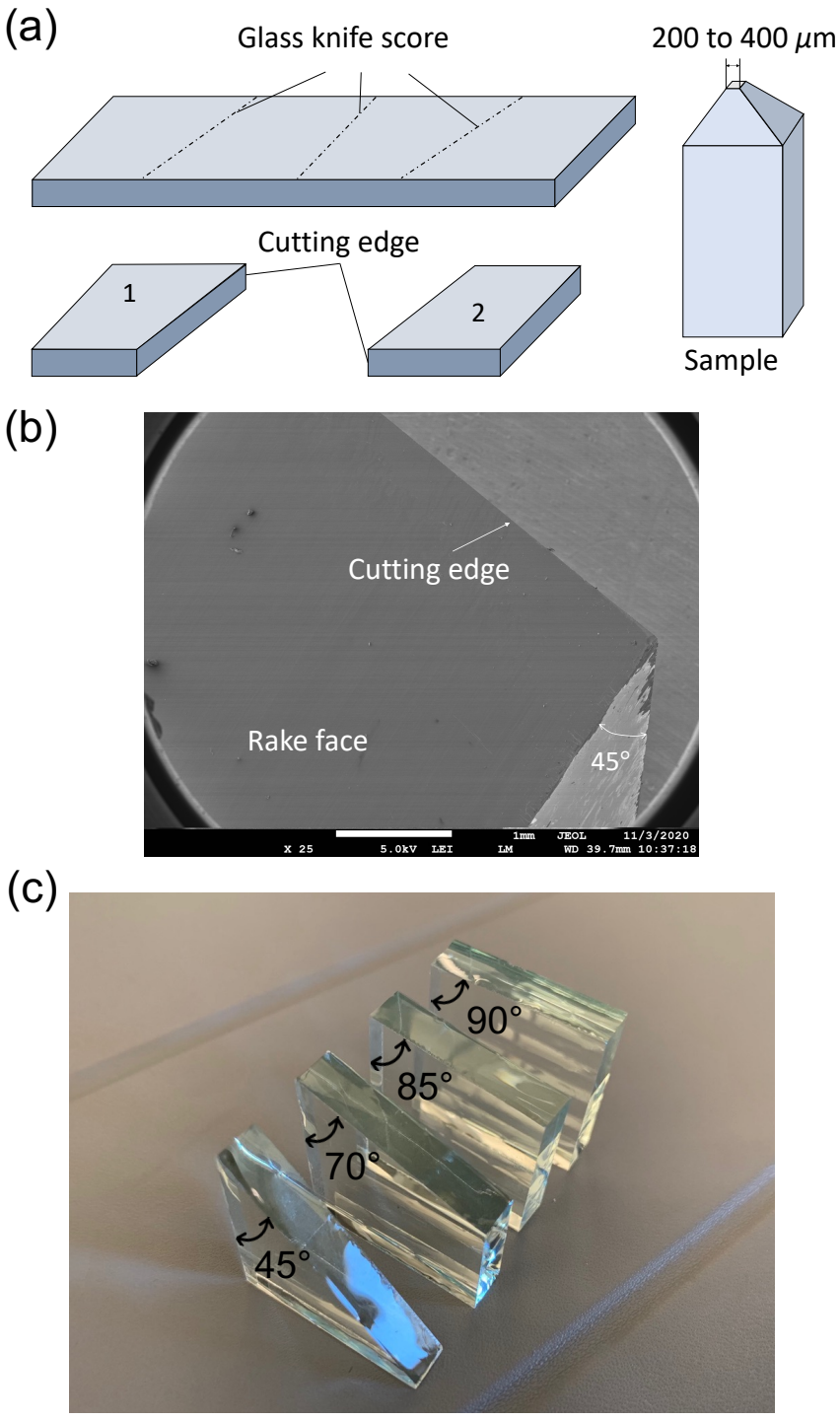


Figure 3.8. Preparation of glass knives for ultramicrotomy experiments: (a) schematic of glass knife preparation procedure, (b) SEM image of a freshly produced glass knife showing a clean and sharp cutting edge, and (c) image showing glass knives produced using the cleavage method with different knife angles.

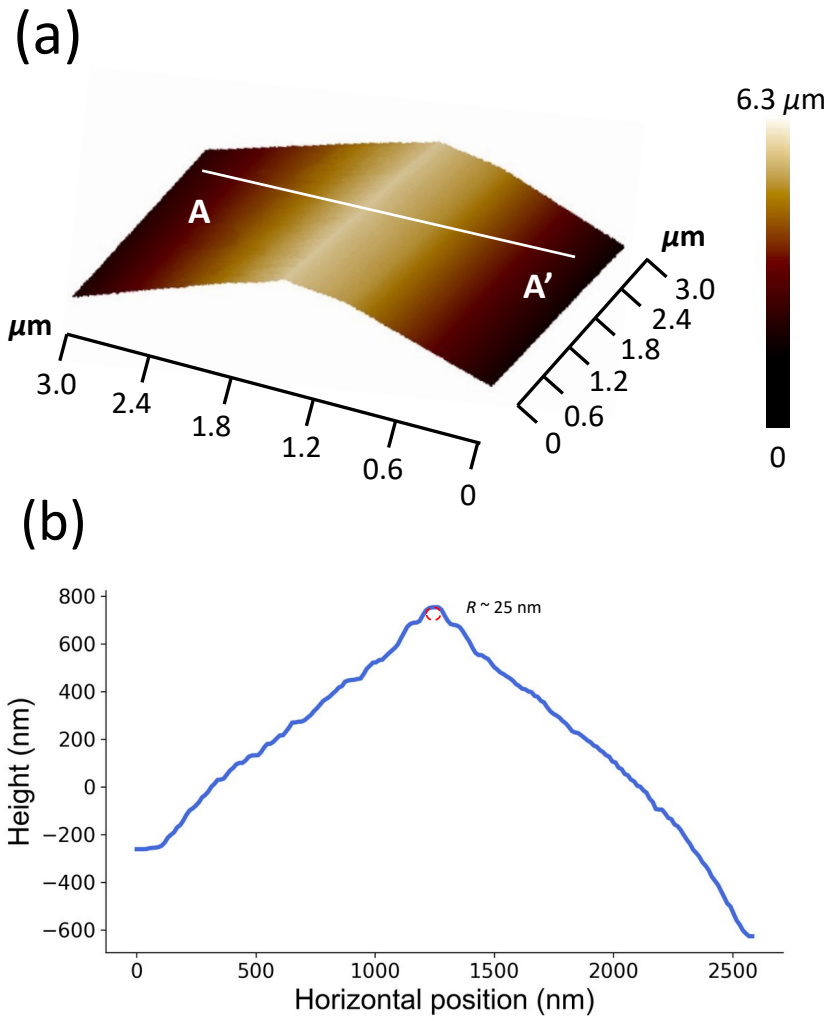


Figure 3.9. Cutting edge characterization using AFM: (a) 3D profile of a freshly cleaved 70° knife edge constructed from the AFM scan; (b) shows a 2D line profile corresponding to a single section of the cutting edge (marked by $A$-$A'$ in (a)).

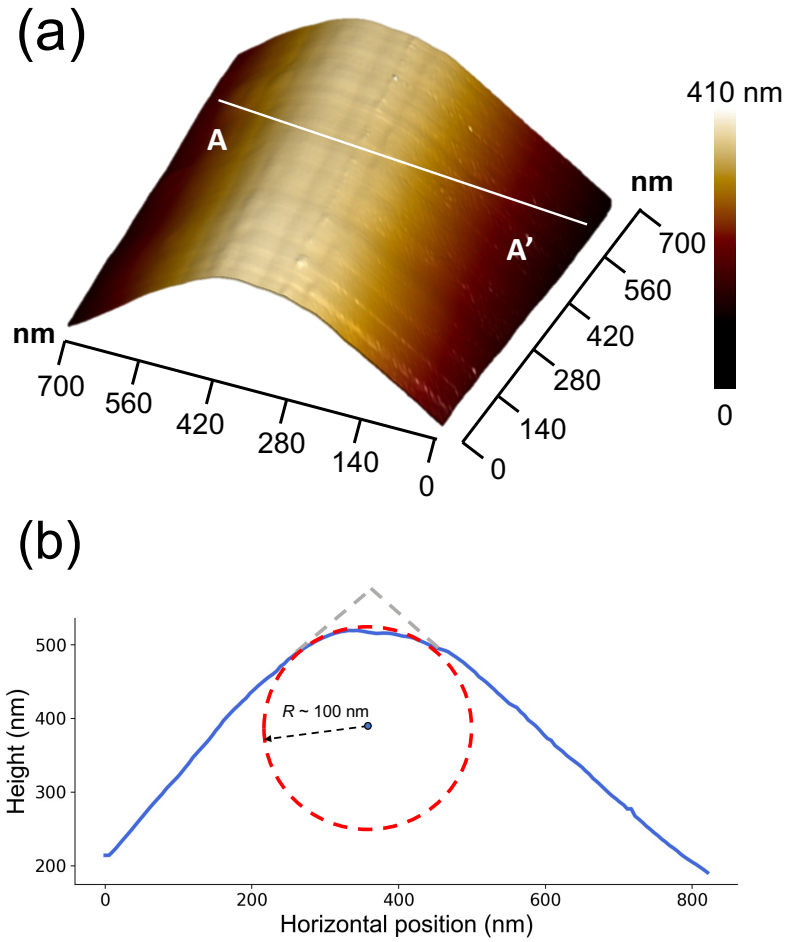


Figure 3.10. Cutting edge characterization using AFM: (a) 3D profile of a freshly cleaved $90^{\circ}$ knife edge constructed from the AFM scan; (b) shows a 2D line profile corresponding to a single section of the cutting edge (marked by $A$-$A'$ in (a)).

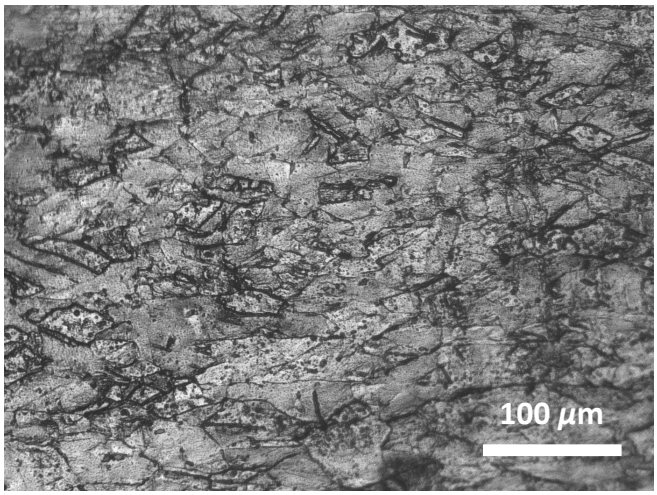


Figure 3.11. Optical micrograph showing the microstructure of as-received OFHC Cu. A partially recrystallized microstructure is evident.

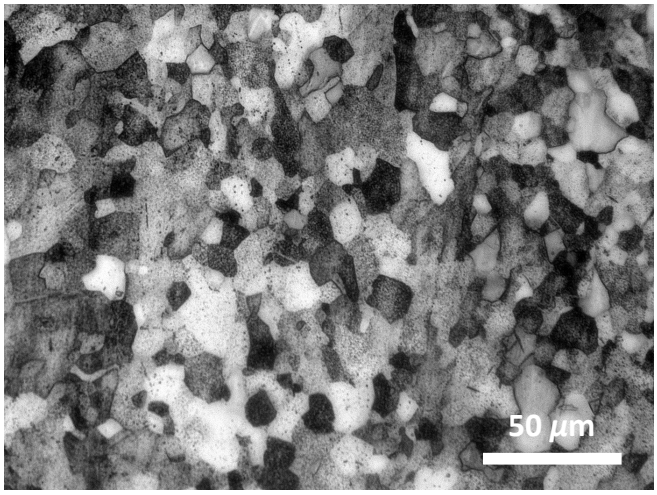


Figure 3.12. Optical micrograph showing equiaxed recrystallized microstructure in as-received commercially pure zinc.

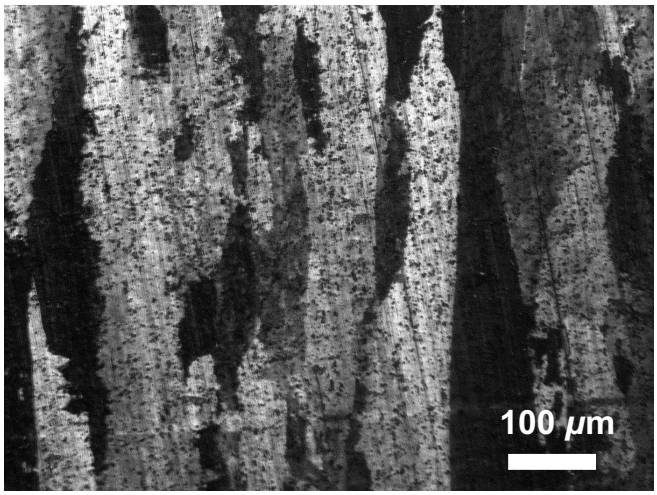


Figure 3.13. Optical micrograph showing the elongated microstructure in as-received 1100 Al.

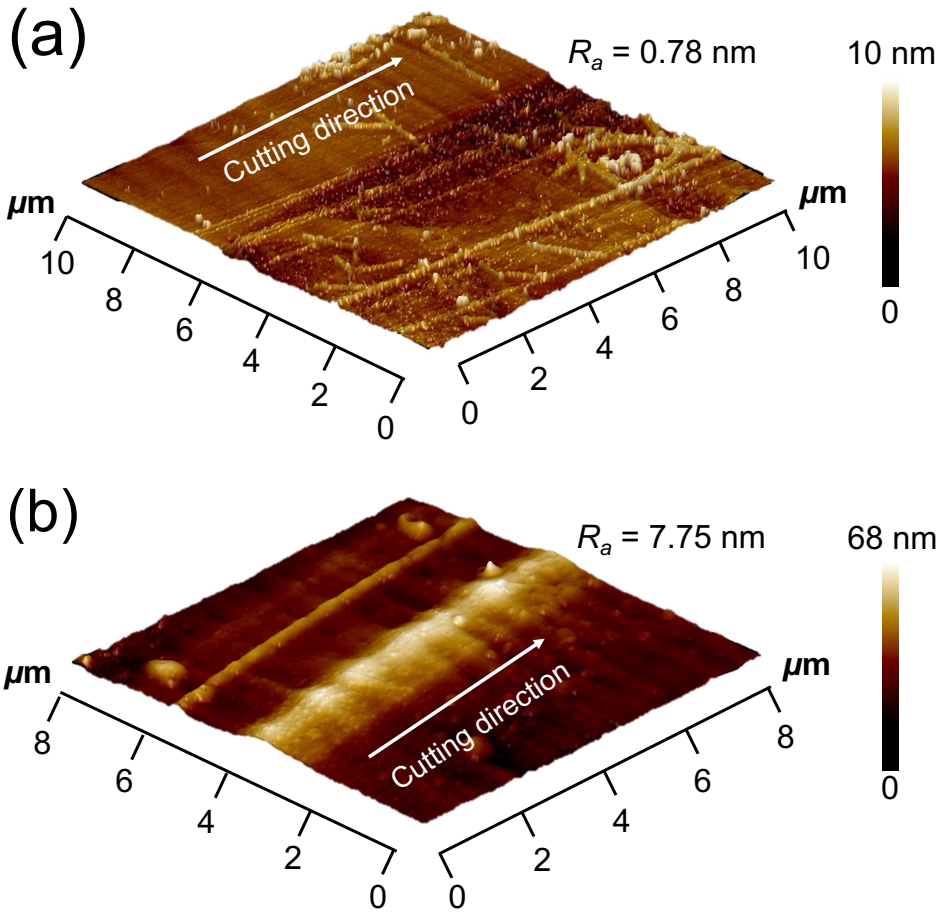


Figure 3.14. 3D AFM scans of finished workpiece surfaces created by: (a) diamond knife, and (b) glass knife.

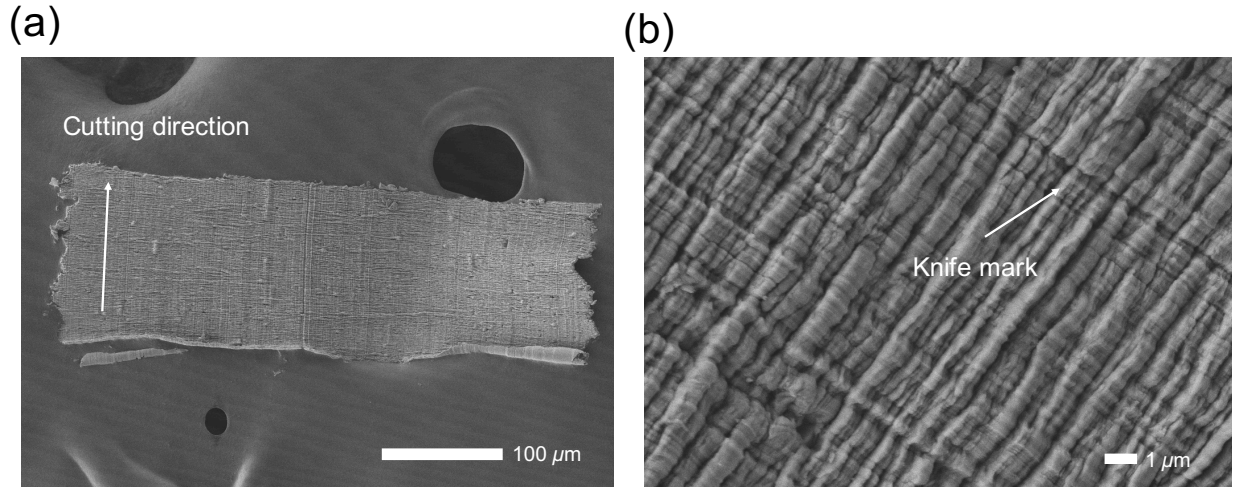


Figure 3.15. SEM images showing morphology of ultramicrotomed chip sections produced from Al ($\alpha = 40°$, $t_0$ = 1 $\mu$m). The change in dimension along the cutting direction, from an initial square-shaped uncut cross-section, can be seen from (a). The higher magnification image in (b) highlights periodic wrinkles on the chip free surface oriented perpendicular to the cutting direction and knife marks (see at arrow).

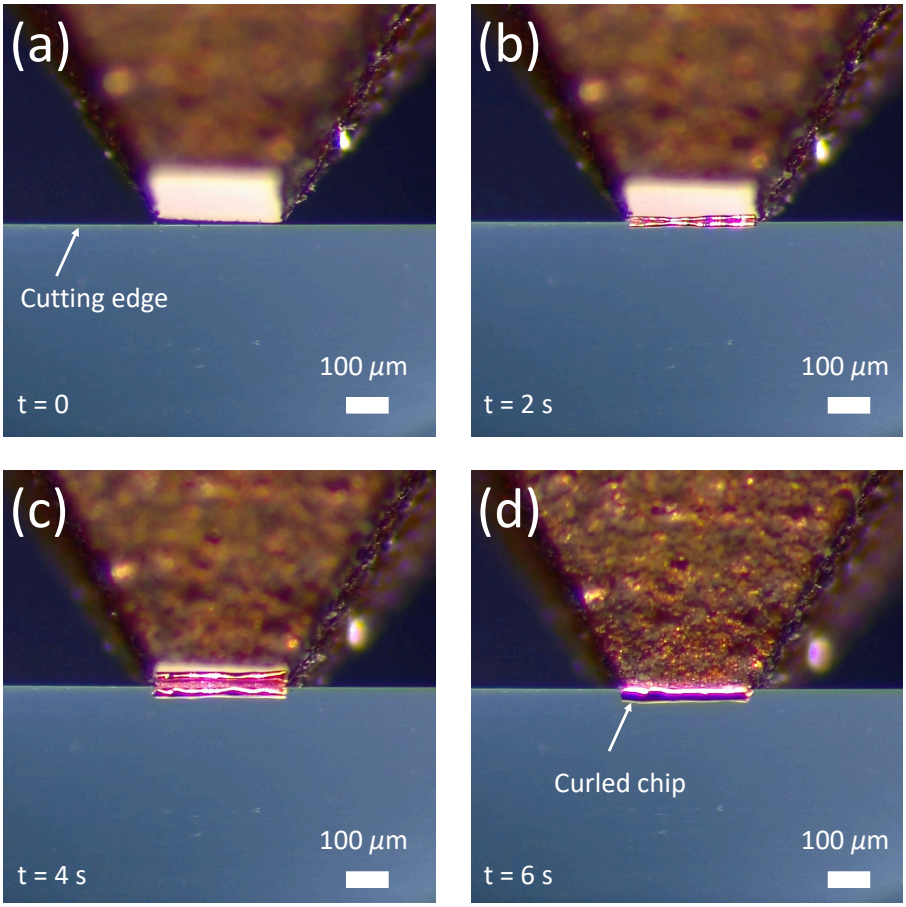


Figure 3.16. Formation of a highly curled chip in cutting of copeer with a glass knife with a rake angle of $40^{\circ}$. Depth of cut is 500 nm and cutting speed is 0.05 mm/s.

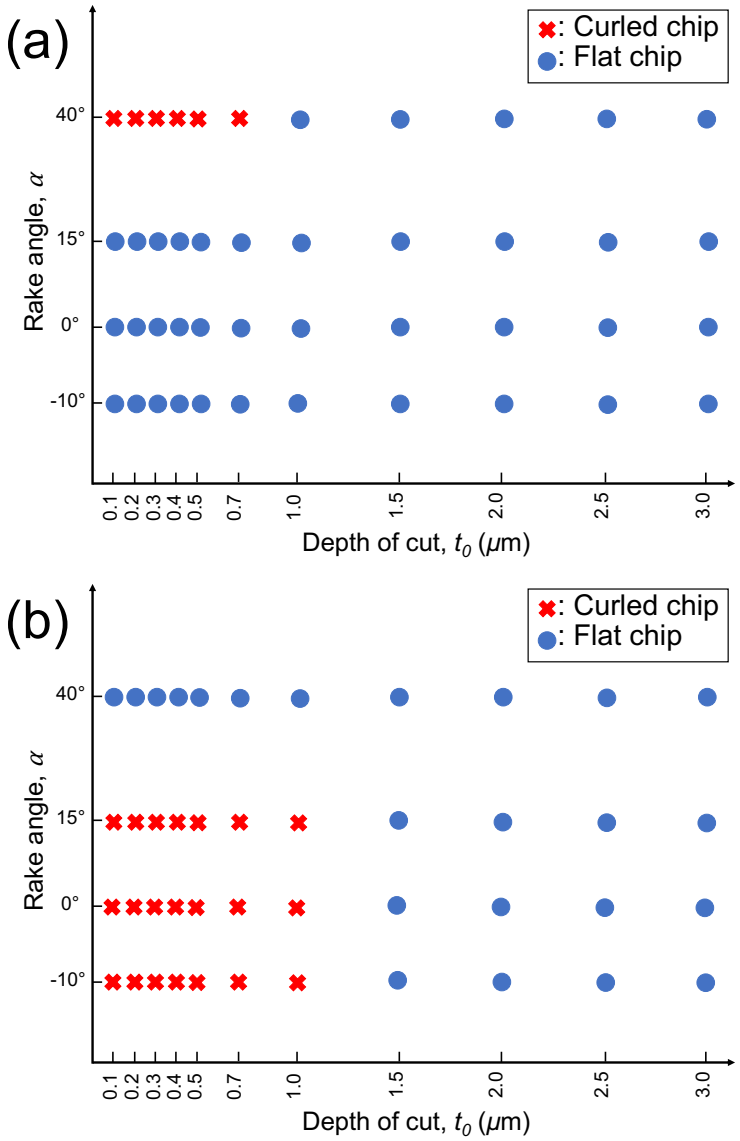


Figure 3.17. Depth of cut ($t_0$) vs. rake angle ($\alpha$) maps showing cutting conditions corresponding to curled and flat chips: (a) copper and (b) aluminum. Tool material is glass.

Table 3.1. Microstructure, composition and hardness of studied material systems.

| | **Purity** | **Grain size** | **Vickers hardness (500-gm load)** |
|---|---|---|---|
| **OFHC Cu** (as-received) | 99.99% | $37 \pm 4$ $\mu$m | 112 |
| **OFHC Cu** (annealed) | 99.99% | $\sim 400$ $\mu$m | 58 |
| **Al** | 99% Min. | $\sim$ 1 mm (along grain elongation direction),<br>$\sim 80$ $\mu$m (grain thickness) | 42 (as-received)<br>30 (annealed) |
| **Single crystal Al** | 99.99% Min. | N/A | |
| **Zn** | 99% Min. | $17 \pm 3$ $\mu$m | 37 |

# 4. SIZE SCALE EFFECT IN METAL CUTTING AT SMALL LENGTH SCALES*

A background of the size effect phenomenon in cutting of metals and various theories that have been proposed to explain this effect was given in Chapter 2. In this chapter, we explore the problem of size effect in cutting of ductile metals in the absence of cutting edge radius effects by using 'theoretically' sharp glass and diamond knives as cutting tools. Instrumented ultramicrotome is used to conduct cutting at small cutting depths ($t_0$ from 30 nm to 3 $\mu$m) under ideal orthogonal plane-strain deformation conditions, and measure corresponding cutting forces and specific energy. We show that there is a remarkable size effect even in the case of cutting with perfectly sharp tools. Based on observations with three metals (aluminum, copper and zinc), new evidence is presented in support of tool-chip friction as the primary source of the size effect. It is in particular shown that size effect arises as a result of non-proportional decrease of the tool-chip contact area and associated friction component with the underlying length scale (depth of cut). Calculation of the shear flow stress in the primary deformation zone showed that this was approximately constant for a given material, independent of the depth of cut. Size dependence of tool-chip friction and contact size is interpreted in terms of the junction growth and adhesion models. Cutting experiments are also carried out with tools covered with solid and liquid contaminants. These results show that contaminant films effectively diminish adhesion and lead to a drastic reduction in the size effect, suggesting practical benefits for industrial manufacturing processes.

## 4.1 Experimental

In the present study, we conducted experiments with three ductile polycrystalline metals: OFHC copper, 1100 aluminum in two different starting conditions: as-received condition and annealed condition, and commercially pure zinc. These materials were mainly chosen because of their softness and ability to exhibit continuous chip formation. The corresponding purities, grain sizes, and Vickers hardness values for these materials are reported in Table 3.1.

The ultramicrotome instrumented with force sensors that was described in Chapter 3 was used

*Reprinted with permission from "Size Effect and Friction in Cutting of Metals on the Small Scale" by G. Feng and D. Sagapuram, 2020. CIRP Annals, 69, 77-80, Copyright [2020] by Elsevier Ltd. and "A Strong Basis for Friction as the Origin of Size Effect in Cutting of Metals' by G. Feng and D. Sagapuram, 2021. International Journal of Machine Tools and Manufacture, 168, 103741, Copyright [2021] by Elsevier Ltd.

to conduct orthogonal cutting under two-dimensional plane strain condition over a range of depths of cut and capture the corresponding cutting and thrust forces. The cutting speed is set at a low constant value of 0.05 mm/s. The cutting tools primarily used in the experiments are glass tools ($\alpha = 40°$, $15°$, $0°$, and $-10°$) made from fresh break, with the depth of cut $t_0$ varying from 100 nm to 3 $\mu$m. This range is selected by the fact that chipping of the cutting edge was an issue at higher $t_0$, while the chips produced using glass tools at $t_0 < 100$ nm were often found to have defects in the form of tears and cracks. Experiments were also carried out using diamond knife ($\alpha = 40°$) to explore the specific energy and size effect when the cutting depth is less than 100 nm.

The effect of tool-chip contact conditions on the size effect in Cu was explored by coating the glass knives with three different types of media: vegetable oil, polybutene, and permanent marker ink. The marker ink was applied on the rake face close to the cutting edge and allowed to fully dry before the experiments were conducted. Similarly, with polybutene or oil, a thin fresh layer of lubricant was applied evenly on the rake face with a cotton swab before each experiment. After every cut, the cutting cross-section was also carefully cleaned to avoid any potential surface-related effects on our measurements.

## 4.2 Results

### 4.2.1 Cutting forces and specific energy

Figs. 4.1(a) and (b) show the cutting ($F_c$) and thrust ($F_t$) force profiles in cutting of copper ($\alpha = 15°$, $t_0$ = 200 nm) and zinc ($\alpha = 40°$, $t_0$ = 300 nm), respectively. Note that the forces shown are normalized with respect to the cutting width, and the three force traces that are shown correspond to three repetitions of the cutting experiment under same conditions. Firstly, it can be seen that the forces reach a steady state in a relatively short time, and further remain constant during the remainder of the cutting process, which is indicative of constant $t_0$ during the entire course of the cutting experiment. Secondly, good repeatability in the forces is also observed, with the force traces from different experiments (carried under same conditions) being identical to one another. This shows that the experimental platform is capable of achieving reliable measurements with diverse material systems. The slight variation in the forces from experiment to experiment, which is typically no more than 15%, is most likely due to the polycrystalline nature of the samples and relatively large grain sizes in comparison with $t_0$. In this section, data are presented for the

cutting ($F_c$) and thrust ($F_t$) forces, normalized with respect to the width $w$, and the specific energy $U_s$, calculated as $F_c/t_0$.

The $t_0$ dependence of forces and specific energy ($U_s$) for cutting of copper with glass and diamond knives is shown in Fig. 4.2. From Fig. 4.2(a) (glass), variation of $F_c$ with decreasing $t_0$ can be seen to be far from linear. The trend in Fig. 4.2(a) also suggests that with further decrease in $t_0$ below 100 nm, $F_c$ should decrease and eventually approach zero. The data collected using diamond (Fig. 4.2(b)) also support this idea, where $F_c$ is seen to approach zero at zero $t_0$. In other words, there is no cutting force intercept when cutting with sharp tools. Therefore, theories that are predicated on the finite $F_c$ intercept to explain the size effect (e.g., the fracture work concept [67]) cannot be reconciled with the current data. Equally importantly, the non-linear cutting force profiles in both the cases (Figs. 4.2(a) and (b)) suggest a strong size effect even when cutting with perfectly sharp tools. This is illustrated in Fig. 4.2(c), where the $U_s$ continuously increases with decreasing $t_0$, exhibiting a 2.5- to 3-fold increase at small $t_0$ (100 nm or below). Similar experiments with glass knives with a more positive $\alpha = 40^\circ$ revealed an even larger size effect – roughly a 5-fold increase in the $U_s$ (discussed later in Figs. 4.10 and 4.11).

At this point, a brief discussion of the unusual nature of thrust forces ($F_t$) seen in Fig. 4.2 is also in order. As seen from Fig. 4.2, $F_t$ dependence on $t_0$ is considerably different in both the cases: $F_t$ varies non-proportionally (similar to $F_c$) in the case of glass, whereas with diamond, it remains largely independent of $t_0$. For example, with diamond, varying $t_0$ over an order of magnitude increases $F_t$ only by a factor of 2 (Fig. 4.2(b)). Because the cutting edge sharpness in both the cases is roughly the same, one would get the impression that $F_t$ is highly sensitive to the tool-workpiece material combination. Another important observation from the glass knife experiments pertains to the predominance of $F_t$ over $F_c$, which is in contrast to conventional cutting ($t_0 \sim$ 10 - 100 $\mu$m) where $F_c$ is usually the dominant component. However, it is important to note that the large thrust forces observed here are not a peculiarity of the cutting setup used. Similar observations of 'larger than usual' thrust forces at small cutting depths have been also reported in diamond turning experiments for other metals (e.g., aluminum, steels) [9, 67]. As will be shown later in this study, this anomalous behavior at small scales is tied in with friction and adhesion at the tool-chip contact.

Many of the above features pertaining to size dependence are also replicated in our experiments

with Al and Zn, as shown in Figs. 4.3 and 4.4. Figs. 4.3(a) and (b) show the experimental data for the as-received and annealed aluminum, respectively, obtained using glass knives ($\alpha = 40°$). In the as-received Al ($\alpha = 40°$), $F_t$ is not only greater than $F_c$ at all $t_0$, but is also seen to approach a nearly constant value of about 0.5 N/mm at $t_0 < 500$ nm. In contrast, $F_t$ ($\sim 0.4$ N/mm) in annealed Al is seen to be roughly independent with respect to $t_0$, with a crossover between $F_c$ and $F_t$ occurring at 1 $\mu$m. In regards to $F_c$, both the plots (Figs. 4.3(a) and (b)) show that $F_c$ dependence on $t_0$ is nearly linear above 1 $\mu$m, but in the sub-$\mu$m range, the cutting force curves downwards and passes through the origin. This observation suggests that linear extrapolation of force data from larger depths of cut to zero $t_0$, as is commonly done, can lead to considerable errors. Equally importantly, it again suggests that there exists no finite force intercept at zero depth of cut when sharp tools are used. Fig. 4.3(c) shows the force plot for annealed aluminum obtained using the diamond knife, where the force dependence is seen to be similar to Fig. 4.3(b) (glass knife). Thrust force $F_t$ is seen to be nearly independent of $t_0$, whereas the cutting force $F_c$ varies non-linearly with $t_0$, with no obvious force intercept at zero depth of cut.

The specific energy increase arising from non-linear scaling of $F_c$ with respect to $t_0$ is shown in Fig. 4.3(d). The data for both the annealed and non-annealed Al obtained using glass knife overlap on top of each other, and show a strong size effect that is characterized by $\sim$ 5-fold increase in $U_s$ (from 0.25 to 1.2 J/mm$^3$) with decreasing $t_0$. It was found that the $U_s$ data in Fig. 4.3(d) could be approximately fitted using an empirical inverse power-law equation: $U_s \propto 1/t_0^n$, with an exponent $n$ of about 0.4. The extent of size effect with diamond is smaller, but still shows a more than 2-fold increase in $U_s$ as $t_0$ is decreased from 1 $\mu$m to 30 nm (see Fig. 4.2(b)).

The data for Zn (glass knife, $\alpha = 40°$) is shown in Fig. 4.4. $F_t$ is found to be always greater that $F_c$, with a tendency to approach a constant value of $\sim 0.3$ N/mm below 200 nm (Fig. 4.4(a)). This behavior is similar to that observed for the as-received Al. Likewise, the non-linear scaling of $F_c$ with $t_0$ is seen to again result in a pronounced size effect, where $U_s$ increases by some 6 times with decreasing $t_0$ (Fig. 4.4(b)). This shows that the exponential increase of the specific energy is a universal phenomenon and quite prevalent in multiple material systems. The fact that the size effect is similar in magnitude across different materials is noteworthy. Furthermore, it is interesting to note that the size effect in cutting is much more intense compared to that typically observed in indentation experiments (1 - 2X increase in hardness).

### 4.2.2 Individual contributions to specific energy

As noted earlier, the size effect has been several times (loosely) attributed to rubbing and ploughing mechanisms associated with the finite cutting edge radius. However, the lack of any indication for the cutting force intercept in all three materials and with different tools (glass, diamond), shown by Figs. 4.2, 4.3 and 4.4, suggests that the rubbing or ploughing contributions to the $U_s$ due to finite cutting edge radius are indeed negligible in the present case. This further suggests that the total specific cutting energy $U_s$ can be partitioned into two parts, the deformation component ($U_1$) due to plastic deformation in the shear zone, and the friction component ($U_2$) associated with sliding friction at the tool-chip contact. The experimental force data together with the chip thickness ratio ($r$) values are used to analyze these energy components separately to understand their relative contributions to the $U_s$, as a function of $t_0$. By treating plastic deformation as simple shear along a plane, $U_1$ is taken as $\gamma_s \tau$, where $\gamma_s$ is the shear strain imposed in the chip and $\tau$ is the shear stress along the shear plane (plane $AB$ in Fig. 3.1(b)). The measured chip thickness ratio ($r$) and force values were used in the calculations of $\gamma_s$, $\tau$ and shear angle $\phi$, as follows [3]:

$$\gamma_s = \frac{1}{r\cos(\alpha)} + \frac{r}{\cos(\alpha)} - 2\tan(\alpha) \tag{4.1}$$

$$\phi = \arctan\left(\frac{r\cos(\alpha)}{1-\cos(\alpha)}\right) \tag{4.2}$$

$$\tau = \frac{F_c\cos(\phi) - F_t\sin(\phi)}{t_0/\sin(\phi)} \tag{4.3}$$

$U_2$ on the other hand is taken as $rF_f/t_0$, with $F_f$ being the normalized friction force, i.e., the force component acting parallel to the cutting tool face (see Fig. 3.1(b)). The typical chip thickness ratios observed in our experiments are given in Table 4.1 for Cu and Zn. $r$ is seen to be nearly independent of $t_0$.

The energy profiles in cutting of Zn and Cu are shown in Figs. 4.5(a) and (b), respectively. From the plots, it is clear that friction component $U_2$ is the one that is primarily responsible for the size effect. For example, in Zn (Fig. 4.5(a)), it is remarkable that $U_1$ remains nearly constant (at $\sim 0.1$ J/mm$^3$) across the entire $t_0$ range, while $U_2$ increases by about 6 times, from 0.2 to 1.2 J/mm$^3$ with decrease in $t_0$. The constancy of $U_1$, coupled with little dependence of $\gamma_s$ and $r$ on $t_0$, also suggests a constant $\tau$. The shear stress data for Zn are shown in Table 4.2, where $\tau$ is seen to be about 40 MPa, with no systematic dependence on $t_0$. This value appears to be slightly lower than the bulk shear flow stress of 50-60 MPa reported for commercially pure Zn under relevant strains and strain rates [87]. Such a result might be perhaps expected on the general grounds that deformation in small volumes is typically characterized by unidirectional dislocation glide, whereas in bulk samples, slip is forced to take place on several slip planes. In any case, the near-constant $\tau$ shows that $U_s$ dependence on $t_0$ is not an intrinsic material effect due to increased flow stress with decreasing size. The data from Cu shown in Fig. 4.5(b) further reinforces this point. From Fig. 4.5(b), it is clear that the increase in $U_2$ (with decreasing $t_0$) is primarily responsible for the size effect. A 6-fold increase in $U_2$, from $\sim$ 0.22 J/mm$^3$ to 1.3 J/mm$^3$, is observed as $t_0$ varied from 3 $\mu$m to 100 nm. $U_1$ on the other hand remains in a narrow range of 0.5-0.75 J/mm$^3$, independent of $t_0$. The calculated $\tau$ values for Cu are around 170 MPa (Table 4.2), again close to, if somewhat lower than, the 200 MPa shear flow stress typical of bulk OFHC copper. The lower-than-expected estimates for $\tau$ at $t_0$ of 2 and 3 $\mu$m appear to be a consequence of non-steady-state chip formation under larger depths of cut. Estimation of the flow stress from the indentation hardness measurements, using the usual relationship between indentation hardness and shear stress: $\tau \approx H/6$, resulted in values of 62 MPa for Zn and 186 MPa for Cu. Given the approximations involved in estimating strength from the hardness, and considering that indentation hardness value itself depends on the indentation load, this agreement between the shear stress estimates made using cutting and indentation is considered to be satisfactory.

As for the friction component, the fact that $r$ is roughly constant at different depths of cut means that the increase in $U_2$ primarily comes from non-proportional decrease of the frictional force $F_f$ with $t_0$. This is clearly evident from the $F_f$ data provided in Table 4.3 for all the studied materials. With a 30-fold reduction in $t_0$, $F_f$ is seen to decrease by only 3-4 times in Al and Zn, whereas in Cu, this factor is about 7. For instance, in Al, this non-linear scaling between $F_f$ and

$t_0$ corresponds to 9 times increase in the $F_f/t_0$ ratio (equivalently, $U_2$) as $t_0$ is reduced from 3 $\mu$m to 100 nm. Given that, at $\alpha = 40^\circ$, $U_2 \approx U_1$ at large depths of cut, this corresponds to an overall 5-fold increase in the $U_s$ at small depths, in line with the experimental observations in Fig. 4.3(d).

### 4.2.3 Characterization of tool-chip contact length

With a slight manipulation, $U_2$ can be expressed in terms of the contact length ($l$) and shear stress ($\tau_f$) at the tool-chip interface as: $r\tau_f l/t_0$. Since $\tau_f$ is determined by the tool-chip material combination pair [88] and thickness ratio $r$ in our experiments was relatively independent of $t_0$ (Table 4.1), this necessarily implies that the observed increase in $U_2$ should arise from non-proportional scaling of the contact length $l$ with $t_0$. Experiments to directly measure the contact lengths were unsuccessful as no trace of the tool-chip contact could be deciphered on the glass knives after each cut. This problem was circumvented by using glass knives coated with a thin ($\sim$ 4 nm) layer of metallic (80% Pt - 20% Pd) coating, where upon examination of the rake face clearly revealed the tool-chip contact area where the metallic coating was removed (see Fig. 4.6). This enabled measurements of $l$ to be made as a function of $t_0$.

The acquired contact length measurements for copper and aluminum for certain cutting conditions are shown in Table 4.4 and Fig. 4.7. Figs. 4.7(a) and (c) show the contact lengths in cutting of copper at $\alpha = 40^\circ$ and $\alpha = 15^\circ$, respectively. Although the contact length dependence on $t_0$ appears to be linear, the relationship is non-proportional, as can be seen from the finite intercept at zero cutting depth. This is also clearly reflected in the normalized contact length plots ($l/t_0$), shown in Figs. 4.7(b) and (d). At $\alpha = 40^\circ$, the normalized contact length at $t_0$ = 100 nm is seen to be nearly 3 times that at the larger depth (3 $\mu$m). In the case of $\alpha = 15^\circ$, a more dramatic $\sim$ 6-fold increase in the $l/t_0$ parameter with decreasing $t_0$ is evident (Fig. 4.7(d)). Note that this dependence of the normalized contact length on $t_0$ is remarkably similar to that of $U_2$ seen earlier in Fig. 4.5, both qualitatively and quantitatively, and is therefore strongly suggestive that the size effect has its origin ultimately in how the tool-chip contact size scales with $t_0$. It is also remarkable that the contact lengths as large as 50 times $t_0$ are observed at small $t_0$, while values in the range of 2-3X are most typical of conventional cutting. This suggests that the tool-chip contact conditions at small cutting depths are such that adhesion molecular forces between two clean surfaces take an increased importance in determining the contact size. This increased 'adherence' between the

tool and chip at small scales also perhaps explains the 'anomalous' thrust forces noted earlier (Fig. 4.2).

Another interesting and counterintuitive aspect of the tool-chip sliding contact at small $t_0$ pertains to normal forces $F_n$ that act at this contact; see Table 4.3 for data. That $F_n$ is negative at $\alpha = 40^\circ$ (for both Al and Zn), especially at small $t_0$, implies that the conditions at small tool-chip contacts are such that sliding occurs under an effective "tensile" load. This can be perhaps also explained by adhesion. Furthermore, since at $\alpha = 40^\circ$, $F_t \approx \frac{1}{\sqrt{2}}(F_f - F_n)$, the negative $F_n$ is consistent with the finite thrust force intercept observed at this rake angle (Figs. 4.3 and 4.4). Note also that no $F_t$ intercept could be deciphered in the case of Cu at $\alpha = 15^\circ$ (Fig. 4.2(a)), where $F_n$ is always positive (Table 4.3).

### 4.2.4 Effect of rake angle on the size effect

To investigate the effect of rake angle on the size effect, experiments were conducted using glass knives with four different rake angles: $\alpha = 40^\circ$, $15^\circ$, $0^\circ$, and $-10^\circ$. Figs. 4.8 and 4.10 summarize the results obtained from annealed aluminum and copper, respectively. Several commonalities can be found between the data obtained with both the materials. Firstly, it can be seen that at $\alpha = 40^\circ$, $F_t$ remains roughly constant across the entire $t_0$ range, whereas $F_c$ increases non-linearly with respect to $t_0$ with no obvious intercept at $t_0 = 0$ (Figs. 4.8(a) and 4.10(a)). There is also a crossover between $F_t$ and $F_c$ that occurs at about $t_0$ = 1 $\mu$m and 100 nm for aluminum and copper, respectively. On the other hand, at smaller rake angles ($\alpha = 15^\circ$, $0^\circ$, and $-10^\circ$), both $F_c$ and $F_t$ are seen to exhibit a highly non-linear dependence on $t_0$, again with no indication of an intercept when $t_0 = 0$. Also, under these rake angles, $F_t$ is greater than $F_c$ across the entire depth of cut range of 100 nm to 3 $\mu$m, as shown in Figs. 4.8(b) - (d) and 4.10(b) - (d). It may be also appreciated that in all cases, the scaling between the forces and $t_0$ is linear for cutting depths greater than $\sim$ 1 $\mu$m.

The effect of rake angle from the standpoint of the size effect is illustrated in Figs. 4.9 and 4.11, where specific cutting energies $U_s$ are plotted as a function of $t_0$ for both the materials. At all rake angles, it can be seen that $U_s$ increases in an exponential manner in the sub-micron range, while remaining roughly constant at larger depths of cut. However, the extent of the size effect (as defined here by ratio $\frac{U_s|_{t_0=100\text{ nm}}}{U_s|_{t_0=3\mu\text{m}}}$, where 100 nm and 3 $\mu$m represent the smallest and largest depths

of cut investigated) is larger at more positive rake angles. This is especially seen in the case of copper, where a 5-fold increase in the $U_s$ is observed at $\alpha = 40^\circ$, whereas $U_s$ increases only by a factor of 2 at $\alpha = 0^\circ$. This is also reflected in the force profiles shown earlier in Fig. 4.10, where the $F_c$ dependence on $t_0$ is seen to be more linear at smaller rake angles $\alpha = 0^\circ$ and $-10^\circ$ (Figs. 4.10(c) and (d)) when compared to positive rake angles.

The energy partition analysis presented in Fig. 4.12 provides insight into this rake angle dependence of the size effect. The chip thickness ratios used in the calculation of individual energy components (i.e., $U_1$ and $U_2$) are reported in Table 4.5. In the $t_0$ range of 100 to 700 nm at $\alpha = 40^\circ$, it was not possible to measure the chip thickness ratio because of the chip curl; for these conditions, we have used an average chip thickness ratio that was calculated based on measurements at higher depths of cut (1 - 3 $\mu$m). It can be seen that at $\alpha = 40^\circ$ (Fig. 4.12(a)), the friction component is comparable in magnitude with the plastic deformation component (i.e., both $U_2$ and $U_1$ contribute equally to the overall specific energy), whereas at small rake angles the plasticity component clearly dominates the energy consumption. This result is not only consistent with the overall effect of rake angle on plasticity (smaller rake angles result in larger plastic strains and therefore higher $U_1$) but also provides a logical explanation for why size effect is reduced at smaller rake angles. Note that $U_s = U_1 + U_2$ and given that $U_1$ is several times larger than $U_2$ at small $\alpha$ and generally remains independent of $t_0$, a reduced size effect should be expected at smaller rake angles.

### 4.2.5 Effect of surface contaminants on the size effect

In view of the fact that tool-chip friction component has a disproportionately large effect on the $U_s$ at small length scales, a set of experiments was conducted with copper by coating the glass knife ($\alpha = 15^\circ$) rake face with various contaminants (permanent marker, vegetable oil, and polybutene), to achieve different tool-chip boundary conditions and explore their effects on the size dependence. The marker ink was applied on the rake face close to the cutting edge and allowed to fully dry before the experiments were conducted. Similarly, with oil and polybutene, a thin fresh layer of lubricant was applied evenly on the rake face with a cotton swab before each experiment. After every cut, the cutting cross-section was also carefully cleaned to avoid any potential surface-related effects on our measurements. In this context, the marker may be considered as a solid

contaminant, while polybutene and oil play the role of boundary lubricants. The results obtained with Cu ($\alpha = 15°$) are presented in Fig. 4.13. As can be seen, the most striking observation from these experiments is the much weaker size effect (Fig. 4.13(d)) when compared to cutting with a clean, uncoated glass tool (see Fig. 4.5(b)). For example, with the marker or oil, $U_s$ is seen to be $\sim 1$ J/mm$^3$ over the entire $t_0$ range. While $U_s$ appears to slightly increase below 200 nm, the $U_s$ at the smallest $t_0$ is still no more than 40% over the specific energy values measured at larger depths. This effect is even more prominent with polybutene, where $U_s$ remains essentially constant with respect to $t_0$. The near-constant $U_s$ is also reflected in the force plots shown in Figs. 4.13(a), (b), and (c). $F_c$ variation with $t_0$ is seen to be now much more linear, as opposed to the characteristic, highly non-linear trend observed with the clean tool (Fig. 4.2(a)). By comparing Figs. 4.13(a)-(c), one can also see that the cutting forces are significantly reduced in the presence of surface contaminants at $t_0 \leq 500$ nm. On the other hand, little effect is observed on the thrust forces.

The energy partition analysis, shown in Fig. 4.14, provides additional information on the individual energy components ($U_1$ and $U_2$) in cutting with knives coated with the marker. $U_1$ is again relatively independent of $t_0$, with an average value (0.6 J/mm$^3$) that is very close to that observed with a clean glass knife (Fig. 4.5(b)). Because the chip thickness ratio $r \sim 0.25$ was essentially the same with and without marker, this indicates that the marker has negligible influence on the material's flow stress in the shear zone. The reduction in $U_s$ dependence on $t_0$ is instead borne out by the friction component $U_2$, as clearly seen from Fig. 4.14. In contrast to the 6-fold increase in $U_2$ that was observed with a clean knife, no specific trend could be seen in the $U_2$ vs. $t_0$ data in Fig. 4.14. This observation is also consistent with the frictional force data, where $F_f$ was found to scale much more linearly with $t_0$ in the presence of marker. For instance, $F_f$ increased from 0.22 N/mm at 120 nm to 4.32 N/mm at 3 $\mu$m, close to that expected for a linear $F_f$ vs. $t_0$ relationship. This qualitative change in the frictional behavior is likely a result of reduced adhesion at the tool-chip contact in the presence of surface contaminants. Equally importantly, these observations suggest that surface contaminant can be used to suppress size effect in cutting.

### 4.3 Discussion

Ultramicrotomy experiments with three nominally pure metals (Al, Zn, and Cu) using freshly cleaved glass knives with multiple rake angles ($40°$, $15°$, $0°$, and $-10°$) have enabled us to study

cutting mechanics at small length scales in the absence of edge radius effects and under orthogonal conditions. Some universal characteristics associated with cutting at small scales are summarized below, since any explanation of the size effect should be consistent with all of these observations:

- A strong size effect occurs even when cutting with atomically sharp tools. This size effect is seen in the sub-$\mu$m range and is characterized by 3- to 6-fold increase in the $U_s$ with decrease in $t_0$ to about 100 nm.

- The extent of the size effect is higher at more positive rake angles, where the energy associated with plastic deformation in the shear zone is comparable with that of tool-chip contact friction.

- No evidence was found for the finite cutting force intercept at zero depth of cut. At $t_0 \geq 1$ $\mu$m, $F_c$ scales with the depth nearly linearly, whereas in the sub-$\mu$m range, it curves downwards and passes through the origin in every case, regardless of the material system or the rake angle.

- The magnitude of the thrust force is higher than the cutting force at small depths, $t_0 \leq 1$ $\mu$m, in all the material systems. $F_t$ is characterized by a finite intercept ($\sim$ 0.4-0.5 N/mm) at highly positive rake angle ($40^\circ$), whereas no such intercept exists at smaller $\alpha$.

- Calculation of the shear stress on the shear plane based on simple shear assumption showed this value to be a material constant, independent of $t_0$. The calculated $\tau$ values are in reasonable agreement with the bulk flow stress values reported in the literature and those obtained using indentation hardness tests.

- The friction energy component ($U_2$) associated with tool-chip interface shows a strong dependence on $t_0$, due to non-proportional decrease of the frictional force with $t_0$.

- Non-proportional variation of function arises due to non-proportional decrease of the tool-chip contact area with $t_0$.

- At highly positive $\alpha$, negative values are observed for the normal force at the tool-chip interface, indicating the possibility of tensile tractions at this contact.

### 4.3.1 A critical evaluation of the size effect

In light of these observations, we evaluate various explanations that have been proposed for the size effect. Firstly, the results show that the cutting behavior at small scales is such that $F_c$ varies in a highly non-linear manner with $t_0$, but passes through the origin as $t_0$ approaches zero. The present observations therefore lead to the conclusion that it is inaccurate to linearly extrapolate the forces measured at higher depths of cut to the sub-$\mu$m regime. Equally importantly, this calls into question the validity of models that invoke the existence of a finite cutting force intercept (based on simple extrapolation of the data) to explain the size effect. As discussed earlier, the force intercept in these models is attributed to various processes such as ploughing, indentation, rubbing (between tool and the machined surface) or "fracture". Given the sharp cutting edge radius (at least one or two orders smaller than $t_0$) employed in our study, it may be also argued on physical grounds that ploughing and rubbing are likely to be of little importance in the present case. It must be added that the intention here is not to imply that phenomena such as ploughing and rubbing do not contribute to the size effect at all, but that a pronounced size dependence exists even in the absence of these effects. Moreover, if these phenomena were important, then the tool rake angle and tool-chip boundary contamination should have a negligible influence on the size effect. From Figs. 4.8, 4.10, and 4.13, it can be seen that this is not the case.

This allows us to consider alternative explanations based on the effect of chip size on the intrinsic flow stress, be it Shaw's probabilistic theory, strain gradient plasticity or Zorev's proposal pertaining to changes in the stress state. However, the shear stress values observed in our experiments, which show little or no systematic dependence on $t_0$ (Table 4.2), directly contradict these explanations. In this context, another explanation was offered by Kopalinsky and Oxley [89] where the size effect was attributed to the strain rate sensitivity of the material. They argue that as $t_0$ decreased, the effective strain rate is increased, and this results in an increase in the material's flow stress. To evaluate the effect of strain rate on the size effect, we conducted experiments with Cu at $t_0 = 1$ $\mu$m at different $V_0$ (0.05, 0.6 and 1.2 mm/s). The specific energies ($U_s \sim 0.5$ J/mm$^3$) were quite alike in all cases and showed very little increase with the cutting speed. Although strain rate sensitivity might play an important role at high speeds, it is unlikely that it is a major contributor to the size effect at small speeds investigated here. It should be also noted that all Oxley's work

[89] was conducted at high speeds in the range of 7 m/s.

Lastly, regarding Nakayama's explanation [11] that the energy associated with plastic flow in the workpiece subsurface layer causes the size effect, it should be pointed out that according to this theory, size effect is expected to be more severe at smaller rake angles (since the shear zone is more likely to extend below the machined surface at small $\alpha$). However, our results show the opposite, that is, the overall size effect decreases with decrease in $\alpha$. Another important result, which discounts the subsurface plastic flow mechanism, comes from our experiments with knives covered with contaminants. If subsurface deformation were indeed a big contributor to the size effect, the size dependence should have persisted even under different tool-chip interface conditions.

We now return to the concept of size effect arising from tool-chip contact mechanics and friction. Using a simple shear plane model, it has been shown that the size dependence arises from an increase in the specific friction energy $U_2$ with decreasing $t_0$. The data presented in Fig. 4.5 in fact shows that under small cutting depths of $\sim$ 100 nm, $U_2$ can be as large as 5 times compared to the plastic deformation component $U_1$, which is in contrast to conventional cutting ($t_0$ of a few tens of $\mu$m) where $U_2$ is typically a small fraction of $U_1$. That is, at small scales, frictional interactions (which scale with the surface area) dominate the mechanics, in accordance with the volume-area scaling discussed earlier in Chapter 2. The fact that the calculated $\tau$ values are also in good agreement with the bulk flow stress data suggests that the simple shear plane analysis employed here is adequate for approximate determination of the individual energy components: $U_1$ and $U_2$. Moreover, the general picture that the size effect arises from tool-chip interface friction is consistent with several of our other observations. These include the drastic reduction in the size effect that is observed when the tool-chip boundary conditions are altered using the contaminants; and the fact that the size effect reduces with decreasing $\alpha$. In the latter regard, it should be noted that reduction in $\alpha$ results in higher chip strains, and accordingly, higher values for $U_1$ ($= \gamma_s \tau$). Since $U_1$ is independent of $t_0$ while $U_2$ increases with decreasing $t_0$, a smaller overall size effect on the $U_s$ ($= U_1 + U_2$) is to be expected with decreasing $\alpha$.

### 4.3.2 Size dependence of the friction component

An explanation for the $U_2$ increase with decreasing $t_0$, equivalently, non-proportional decrease of $F_f$ with $t_0$, can be found in Fig. 4.6 that shows tool-chip contact length ($l$) as a function of $t_0$.

The most significant result from this study is the unusually large contact lengths at small $t_0$. For instance, the $l/t_0$ ratio increased from a value of about 10 to 50 as $t_0$ is reduced from 3 $\mu$m to 100 nm. This is remarkable given that in conventional cutting, the contact length is no more than 5 times the $t_0$ even under extreme conditions of tool-chip friction. These observations therefore suggest that the $U_2$ increase, and consequently the size effect on $U_s$, is ultimately linked to how the tool-chip contact size scales with $t_0$. Two possible explanations for this large increase in the contact size are discussed next. The first one is based on the 'junction growth' theory [90], and another explanation is based on intermolecular adhesion between clean contacts.

Junction growth represents the case where the area of a plastic contact increases when tangential stress or sliding is introduced in addition to the normal stress. For example, let us consider a simple two-dimensional contact of a soft metal loaded against a rigid flat plane, where the initial contact area is $A_0$ and the mean contact pressure $p$ is equivalent to the yielding pressure $k$ of the softer body at the contact. Now, consider what happens to the contact area when a tangential stress $s$ is applied at the contact without altering the normal force. According to the plasticity theory, the criterion for the plastic flow under a combined stress state is given by: $p^2 + \beta s^2 = k^2$, where $\beta$ is a numerical constant that is $\sim 3$ for a two-dimensional contact. From this equation, it is evident that even the smallest tangential stress should result in an increase of the contact area from the initial $A_0$, as a result of which $p$ drops below $k$. Further increase in $s$ results in an additional increase in the area (and a corresponding drop in $p$) so that the flow condition is constantly maintained. Therefore, we see that the model predicts a steady growth in the contact (or 'junction') area as $s$ is increased. Several experimental investigations [91, 92] have confirmed the junction growth and this concept has been also successful in explaining high friction coefficients [93], quite similar to those seen in the present case. For instance, the friction coefficient, $\mu = F_f/F_n$, for the case of Cu is seen to be quite high, in the range of 2 to 5 (Table 4.3). Applying the concept of junction growth to the current tool-chip sliding contact, we see that the contact area $A \approx \frac{F_n w}{\sqrt{k^2 - \beta {\tau_f}^2}}$ and $F_f \approx \frac{\tau_f F_n w}{\sqrt{k^2 - \beta {\tau_f}^2}}$, where $\tau_f$ is the frictional shear stress at the contact. Therefore, one can perhaps conclude that the larger than expected frictional forces and contact sizes at small $t_0$ are a result of higher frictional resistance $\tau_f$ of small contacts. While this could also potentially explain how contaminants can influence the size effect (by altering $\tau_f$), the conceptual basis for $\tau_f$ dependence on the contact size is unclear. Additionally, the junction growth model by itself makes no predictions

of the negative normal contact forces observed at higher rake angles.

Perhaps a more coherent explanation may be offered from the standpoint of adhesion. By adhesion, what is meant here are the molecular attraction forces that come into picture when two flat and clean surfaces are brought into close contact with each other, and which can lead to large increases in the contact area [17]. For example, the contact area increase due to the presence of surface forces for the case of elastic contacts, beyond that predicted by the Hertzian solution, is a phenomenon that is well understood and modeled quantitatively using JKR and DMT theories [94]. The adhesion theory also explains why two smooth elastic bodies, when brought very close to each other, form a non-zero contact area even if no load is applied, and why a finite tensile force is needed to separate the surfaces apart. Now considering the clean and intimate contact conditions that exist at the tool-chip interface in cutting, it may be similarly argued that adhesion is responsible for the large contact sizes seen in the present case. A preliminary assessment of adhesive forces lends support for this argument. Treating the tool-chip contact as that of a plastically deformable cylindrical surface (chip) pressed against a rigid flat (tool), the attraction force $F_A$ can be shown as: $F_A = \gamma R w/l$ [32], where $\gamma$ is the work of adhesion and $R$ is the chip curl radius. For the case of Cu, taking $R$ to be $\sim$ 1 mm, $\gamma \sim 1000$ mJ/m$^2$ [95] and $l \sim 5$ $\mu$m [32], it can be shown that $F_A$ is about 0.2 N/mm, of the same order of $F_n$ when $t_0 \leq 300$ nm (see Table 4.3). This suggests that adhesive forces cannot be ignored at small $t_0$. Importantly, this suggests that the rather large contact areas and frictional forces observed at these length scales arise from adhesion effects. Note that, at larger depths (say, greater than 1 $\mu$m), adhesion effects become secondary since $F_A \ll F_n$.

With this description of the tool-chip boundary condition, additional observations from the study can be rationalized and interpreted with the same model. For example, the theory is capable of predicting negative (i.e., tensile) contact forces when the adhesion force exceeds the applied load, consistent with our experimental observations at highly positive rake angles. In this regard, attention should be also drawn to small scale sliding experiments carried out by Gane and Skinner [39], which demonstrate sliding under a negative normal force in the presence of adhesion. Secondly, the fact that surface contamination drastically reduces adhesion between the contacting bodies [17] is consistent with the reduced size effect seen in our study in the presence of surface films at the tool-chip interface. The role of surface contamination in reducing the size effect thus also comes out naturally from this framework.

## 4.4 Conclusion

The study provides for the first time a detailed experimental analysis of the size effect in cutting of metals with clean and atomically sharp tools. Freshly cleaved glass knives were used for this purpose and an instrumented ultramicrotomy setup was used to measure cutting forces and energy profiles at small cutting depths (100 nm to 3 $\mu$m). The experiments described here with three different metallic systems show a pronounced size effect even in the absence of edge radius effects. The size effect observed is substantial, characterized by up to 5-fold increase in the specific energy, and much greater than that typically seen in nanoindentation experiments. The major part of this effect arises from non-proportional decrease of the tool-chip contact area and associated frictional energy with decreasing size, while the plastic deformation component of cutting energy shows very little size dependence. This behavior can be explained, at least on a qualitative basis, in terms of the surface attraction (adhesion) forces which play an important role in small scale contacts.

In contrast to the common belief, no evidence was found for the cutting force intercept as depths approaching zero. This study therefore emphasizes that simple extrapolation of force data from higher cutting depths to sub-$\mu$m regimes is inaccurate and leads to significant errors. Various explanations that have been given for the size effect are evaluated in light of the new experimental evidence, and it is shown that the majority of explanations may be rejected.

Surface contaminants and films which modify the surface interactions at the tool-chip contact can exert a profound influence on the cutting forces and lead to a significant reduction in the size effect. Polybutene, oil, and contaminants such as permanent markers are shown to be effective media for suppressing the size effect. Given the inexpensive and innocuous nature of these media, they hold significant practical value. Lastly, the clean and intimate nature of (tool-chip) contact conditions in machining suggest new opportunities for using two-dimensional cutting as a means to study friction on the small scale, over a range of sliding speeds, normal loads and contact surface environments. This aspect of using cutting as a nanotribological tool remains unexplored.

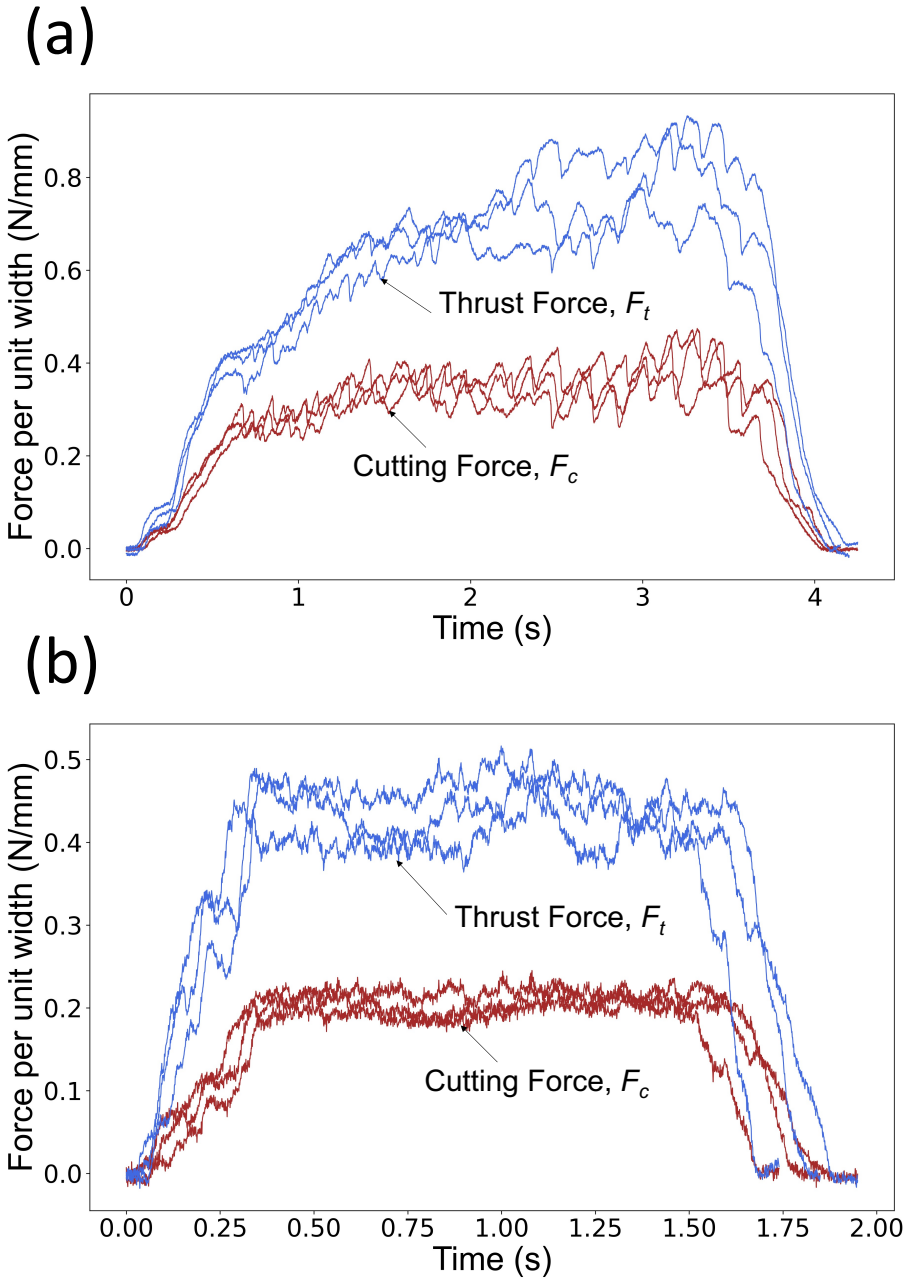


Figure 4.1. Representative force traces in cutting of (a) Cu ($\alpha = 15°$, $t_0$ = 200 nm) and (b) Zn ($\alpha = 40°$, $t_0$ = 300 nm). Forces are normalized with respect to the cutting width $w$. The three individual force traces in each plot correspond to three repetitions of the experiment under identical conditions. Note the good repeatability in force measurements.

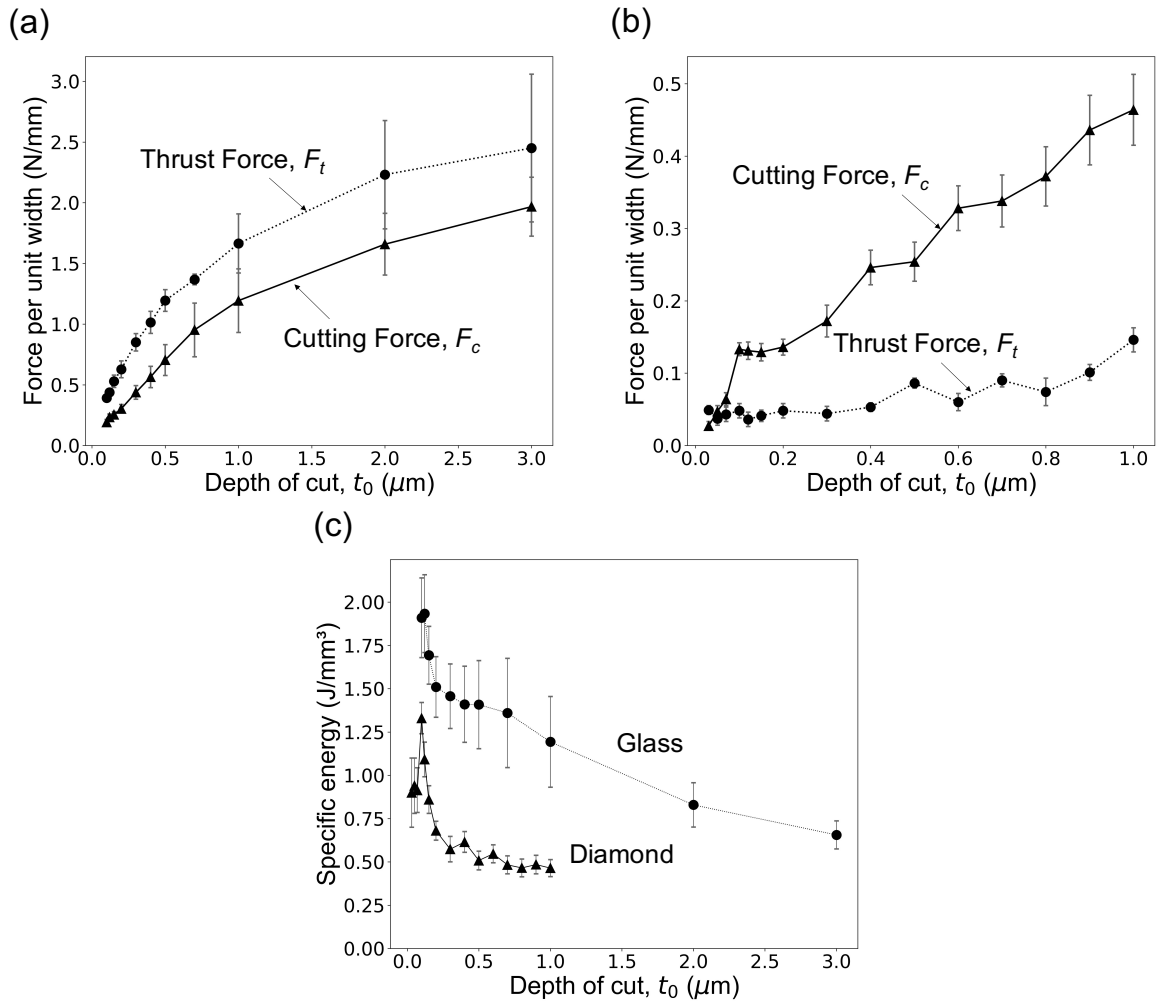


Figure 4.2. Dependence of force on $t_0$ for copper during cutting with (a) glass knife ($\alpha = 15°$) and (b) diamond knife ($\alpha = 40°$). (c) shows the corresponding variation of the specific energy $U_s$ with $t_0$. The error bars represent one standard deviation, calculated from multiple repetitions of the cutting experiment under each condition.

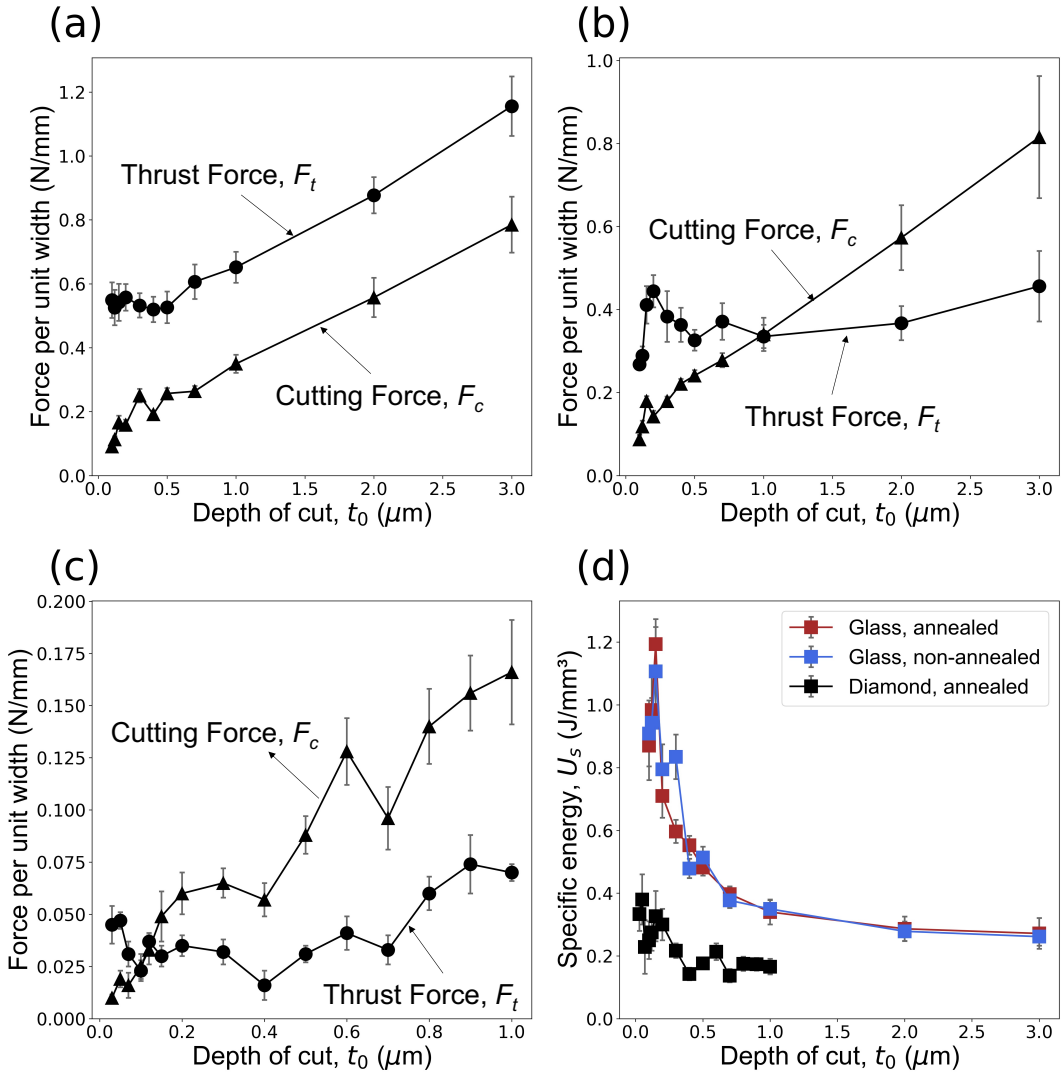


Figure 4.3. Size effect in Al. Force plots for (a) as-received Al using glass knife ($\alpha = 40°$), (b) annealed Al (1 hour at 350°C) using glass knife ($\alpha = 40°$), and (c) annealed Al (1 hour at 350°C) using diamond knife ($\alpha = 40°$). (d) Plot showing $U_s$ dependence on $t_0$ for all the cases. The error bars represent one standard deviation obtained from multiple repetitions of the cutting experiment.

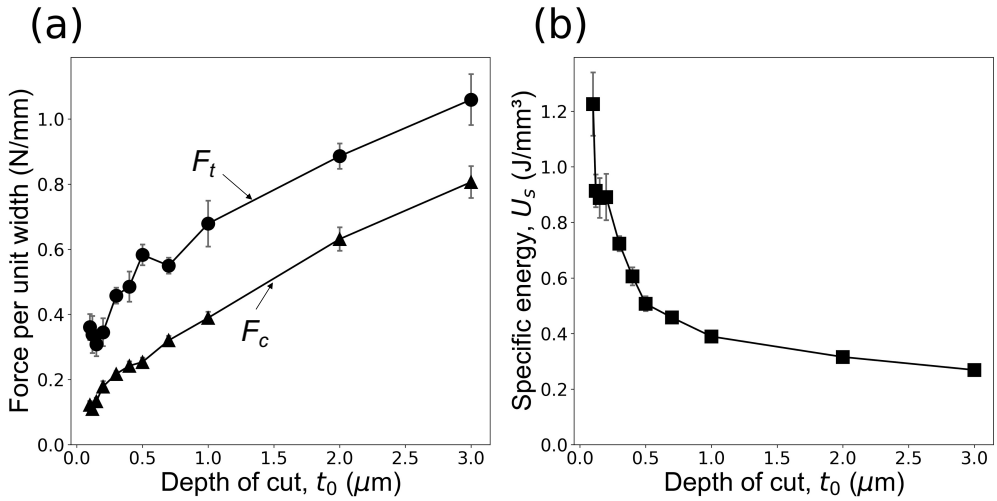


Figure 4.4. Size effect in Zn (glass knife, $\alpha = 40°$): (a) cutting and thrust forces, (b) specific energy $U_s$.

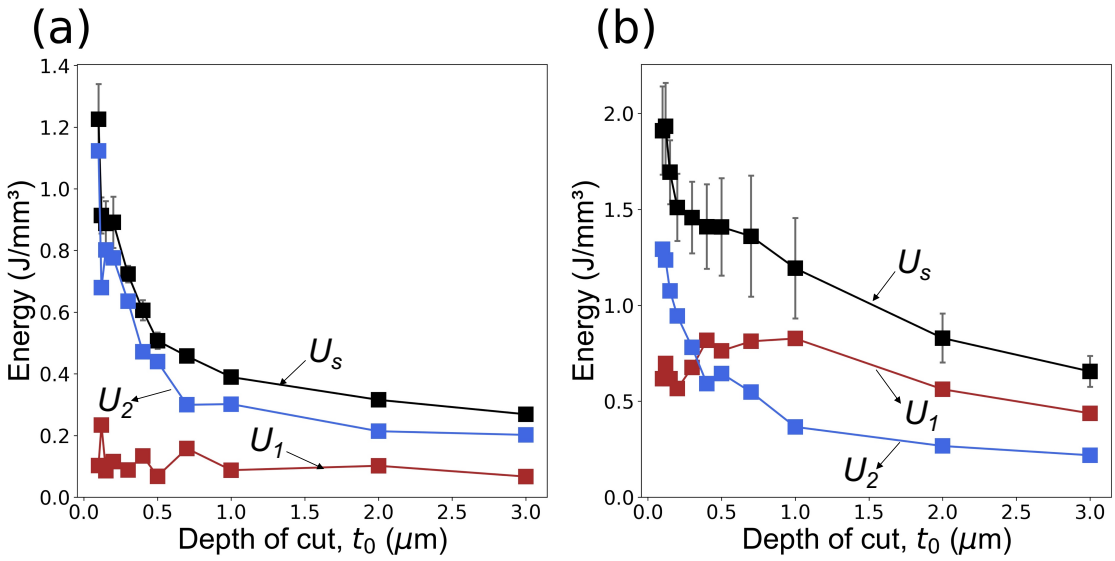


Figure 4.5. Energy partition analyses showing individual contributions to the specific energy in (a) Zn ($\alpha = 40°$) and (b) Cu ($\alpha = 15°$). $U_1$ is the energy associated with plastic deformation in the shear zone, while $U_2$ is the energy dissipated due to friction at the tool-chip contact. Note the relatively constant $U_1$ in both the cases, while $U_2$ shows a strong dependence on $t_0$. Tool material: glass.

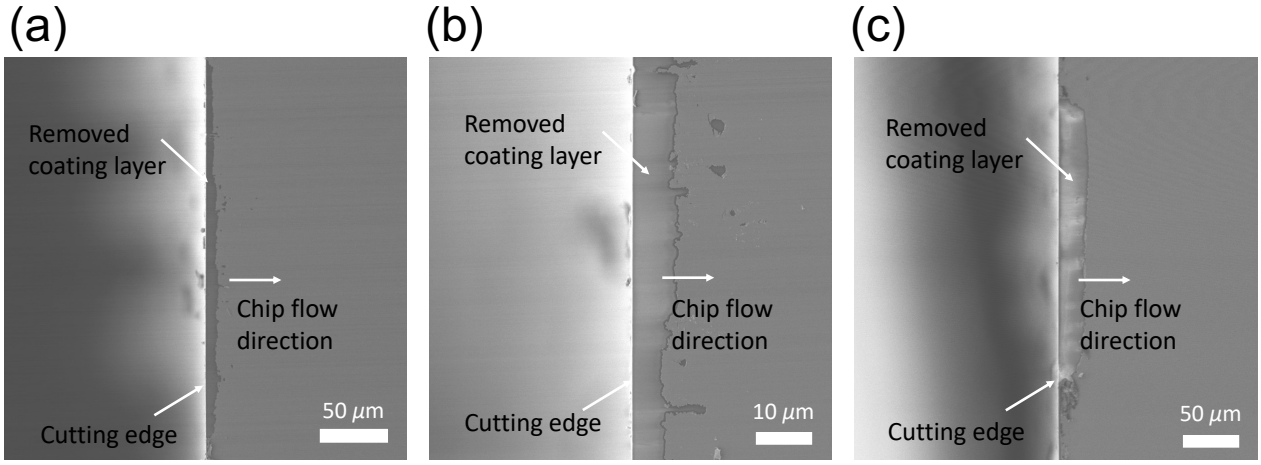


Figure 4.6. SEM images showing contact length measurements in cutting experiments with copper ($\alpha = 15^{\circ}$). (a) Rake face of the coated glass knife after the cutting experiment at $t_0$ = 100 nm. The region showing the removed coated layer demarcates the tool-chip contact area. (b) is a higher magnification image of (a), where the tool chip contact length (along chip flow direction) is seen to be about 10 $\mu$m. (c) Corresponding image of the rake face after the cutting experiment at a higher depth of cut at 3 $\mu$m.

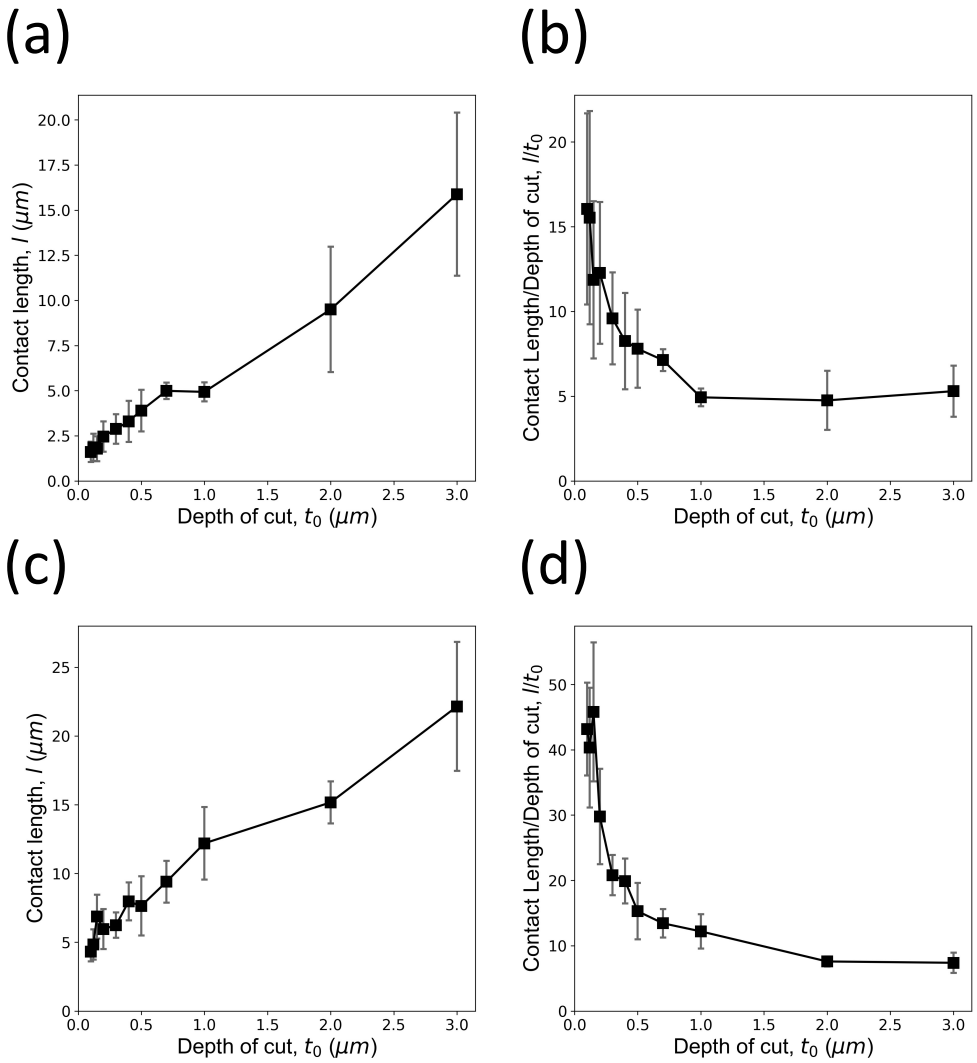


Figure 4.7. Scaling dependence of contact length ($l$) with $t_0$ shown using data obtained from copper using glass knives at $\alpha = 40°$ and $15°$: (a) $l$ vs. $t_0$ at $\alpha = 40°$, (b) $l/t_0$ vs. $t_0$ at $\alpha = 40°$, (c) $l$ vs. $t_0$ at $\alpha = 15°$, and (d) $l/t_0$ vs. $t_0$ at $\alpha = 15°$. The error bars represent one standard deviation obtained from 5 measurements of the contact length.

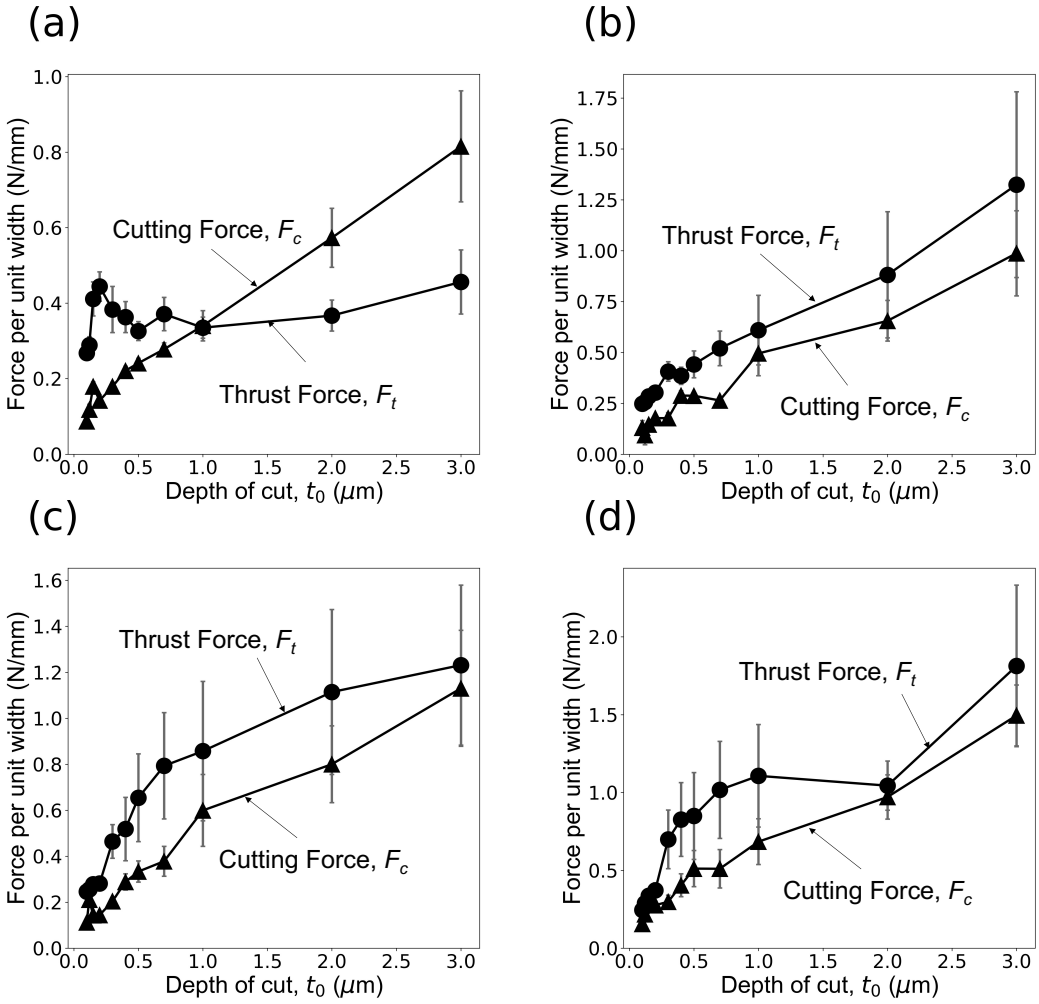


Figure 4.8. The $t_0$ dependence of cutting forces ($F_c$) and thrust forces ($F_t$) in cutting of annealed aluminum at different rake angles: (a) $\alpha = 40°$, (b) $\alpha = 15°$, (c) $\alpha = 0°$, and (d) $\alpha = -10°$. Tool material: glass.

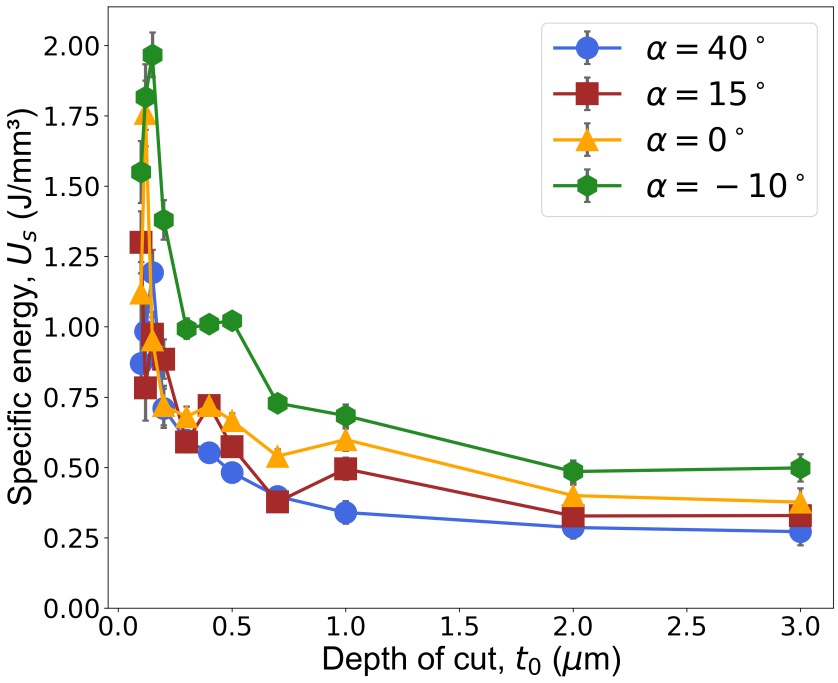


Figure 4.9. Effect of tool rake angle on the size effect in annealed aluminum. Tool material: glass.

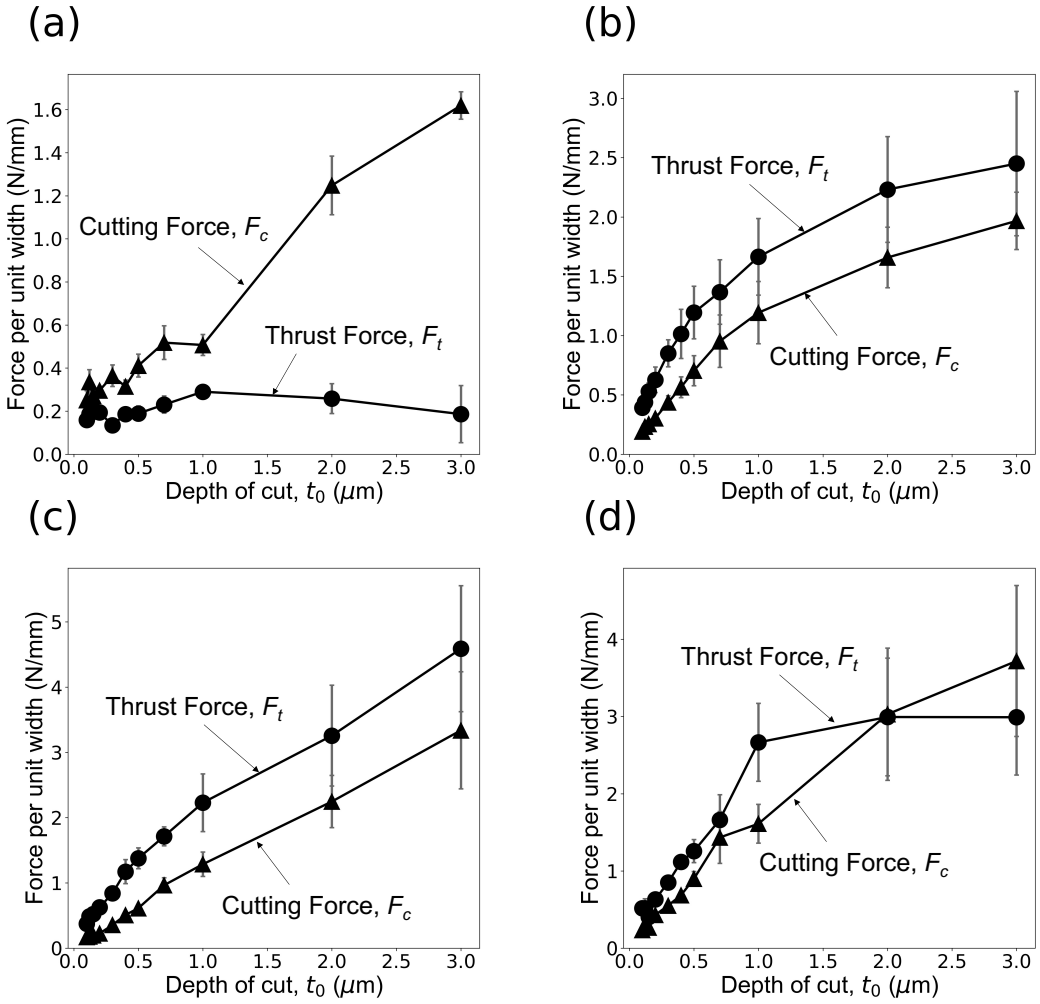


Figure 4.10. The $t_0$ dependence of cutting forces ($F_c$) and thrust forces ($F_t$) in cutting of copper using glass knives having different rake angles: (a) $\alpha = 40°$, (b) $\alpha = 15°$, (c) $\alpha = 0°$, and (d) $\alpha = -10°$.

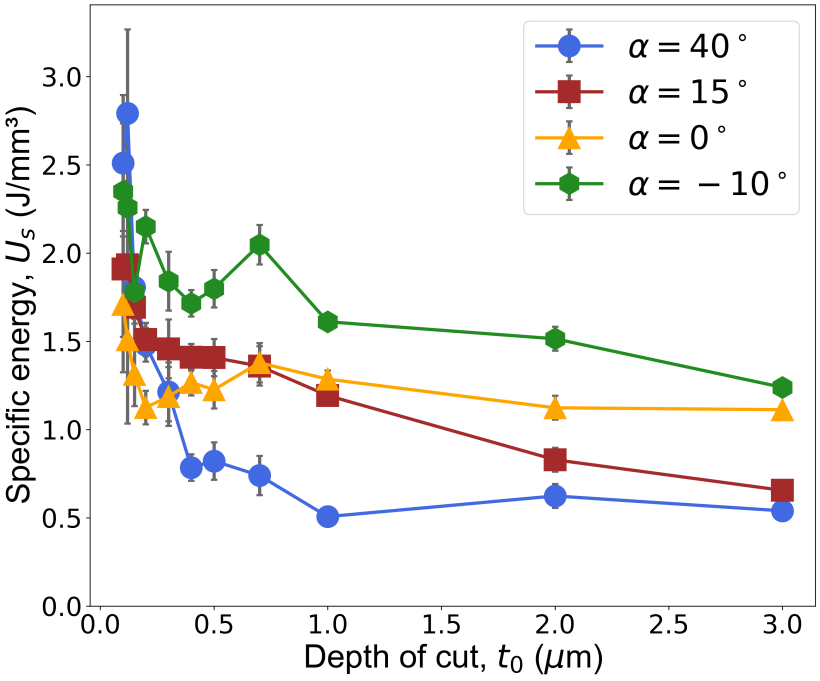


Figure 4.11. Effect of tool rake angle on the size effect in copper. Tool material: glass.

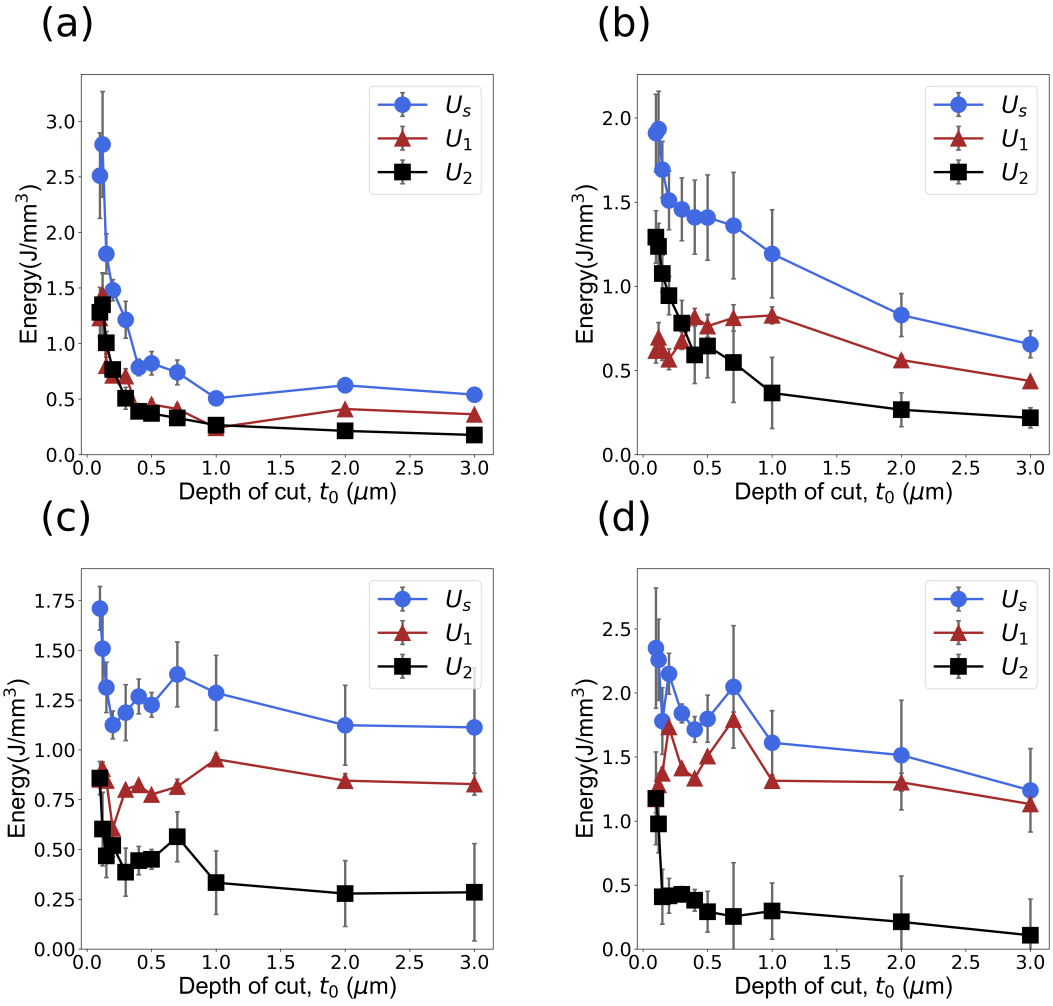


Figure 4.12. Energy partition analysis for copper at different rake angles: (a) $\alpha = 40°$, (b) $\alpha = 15°$, (c) $\alpha = 0°$, and (d) $\alpha = -10°$. $U_s$: specific energy, $U_1$: plastic deformation energy, $U_2$: friction energy.

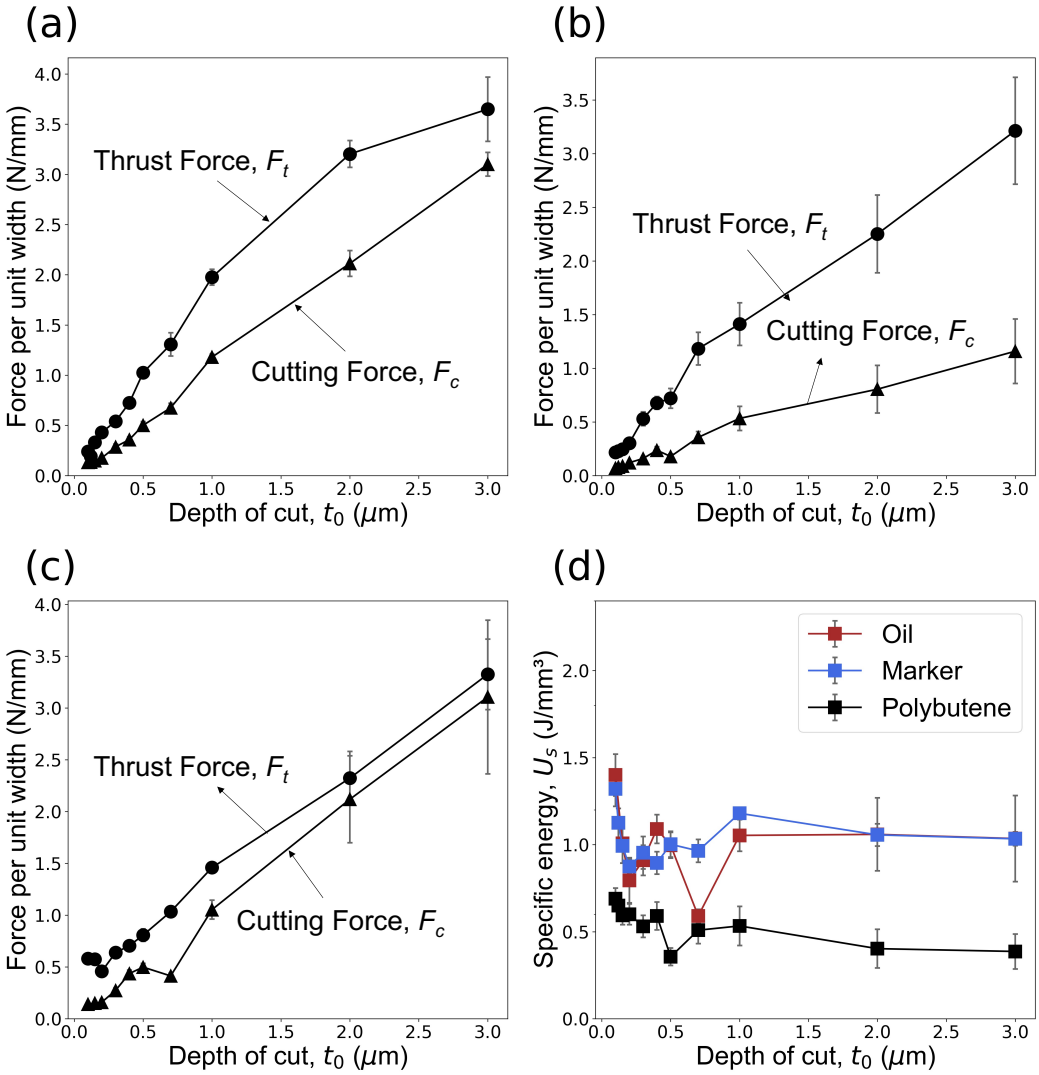


Figure 4.13. Effect of tool surface contamination on the size effect in Cu ($\alpha = 15°$). (a), (b) and (c) are the force plots obtained with glass knives coated with permanent marking ink, polybutene, and oil, respectively. (d) Plot showing the dependence of $U_s$ on $t_0$ in the presence of contaminants. Note the significantly reduced size effect when compared to that observed with clean, uncoated knives (Fig. 4.2).

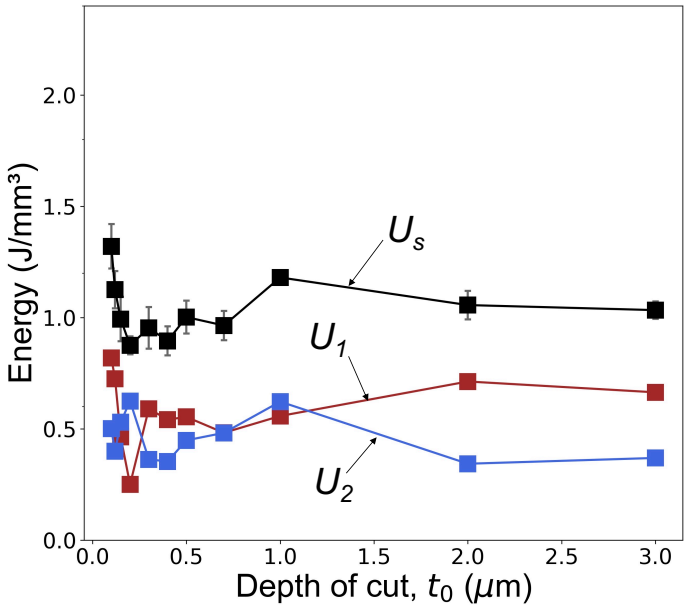


Figure 4.14. Energy partition analysis in cutting of Cu with knives coated with permanent marker. Note the relatively weak dependence of both $U_1$ and $U_2$ on $t_0$.

Table 4.1. Chip thickness ratio ($r$) values in cutting with glass. These values were calculated as the ratio of final chip length over initial cutting length.

| $t_0$ ($\mu$m) | 0.1 | 0.12 | 0.15 | 0.2 | 0.3 | 0.4 | 0.5 | 0.7 | 1 | 2 | 3 |
|---|---|---|---|---|---|---|---|---|---|---|---|
| $r$ (As-received Cu, $\alpha = 15°$) | 0.302 | 0.307 | 0.28 | 0.276 | 0.251 | 0.210 | 0.241 | 0.245 | 0.191 | 0.206 | 0.228 |
| $r$ (Zn, $\alpha = 40°$) | 0.316 | 0.248 | 0.374 | 0.410 | 0.389 | 0.358 | 0.360 | 0.334 | 0.392 | 0.394 | 0.456 |

Table 4.2. Calculated shear stress values ($\tau$, MPa) for Zn and Cu. Tool material: glass.

| $t_0$ ($\mu$m) | 0.1 | 0.12 | 0.15 | 0.2 | 0.3 | 0.4 | 0.5 | 0.7 | 1 | 2 | 3 |
|---|---|---|---|---|---|---|---|---|---|---|---|
| **Zn** ($\alpha = 40°$) | 35.85 | 59.71 | 37.25 | 56.31 | 40.32 | 54.97 | 28.12 | 59.35 | 40.47 | 47.42 | 37.50 |
| **Cu** (as-received, $\alpha = 15°$) | 192.74 | 221.06 | 178.82 | 161.73 | 175.44 | 177.76 | 190.68 | 205.74 | 162.77 | 119.81 | 103.05 |

Table 4.3. Normalized friction force $F_f$ (N/mm) and normal force $F_n$ (N/mm) data for all the three materials (Al, Zn, and Cu). Tool material: glass.

| $F_f$ (N/mm) | | | | | | | | | | | |
|---|---|---|---|---|---|---|---|---|---|---|---|
| $\boldsymbol{t_0}$ ($\mu$m) | 0.1 | 0.12 | 0.15 | 0.2 | 0.3 | 0.4 | 0.5 | 0.7 | 1 | 2 | 3 |
| **Al** (annealed, $\alpha = 40°$) | 0.26 | 0.30 | 0.43 | 0.43 | 0.41 | 0.42 | 0.41 | 0.46 | 0.48 | 0.65 | 0.87 |
| **Al** (as-received, $\alpha = 40°$) | 0.48 | 0.48 | 0.52 | 0.53 | 0.57 | 0.52 | 0.57 | 0.63 | 0.72 | 1.03 | 1.39 |
| **Zn** ($\alpha = 40°$) | 0.36 | 0.33 | 0.32 | 0.38 | 0.49 | 0.53 | 0.61 | 0.63 | 0.77 | 1.08 | 1.33 |
| **Cu** (as-received, $\alpha = 15°$) | 0.43 | 0.48 | 0.58 | 0.68 | 0.93 | 1.13 | 1.34 | 1.57 | 1.92 | 2.58 | 2.88 |
| $F_n$ (N/mm) | | | | | | | | | | | |
| $\boldsymbol{t_0}$ ($\mu$m) | 0.1 | 0.12 | 0.15 | 0.2 | 0.3 | 0.4 | 0.5 | 0.7 | 1 | 2 | 3 |
| **Al** (annealed, $\alpha = 40°$) | -0.11 | -0.10 | -0.13 | -0.18 | -0.11 | -0.06 | -0.03 | -0.03 | 0.05 | 0.20 | 0.33 |
| **Al** (as-received, $\alpha = 40°$) | -0.28 | -0.25 | -0.22 | -0.24 | -0.15 | -0.19 | -0.14 | -0.19 | -0.15 | -0.14 | -0.14 |
| **Zn** ($\alpha = 40°$) | -0.14 | -0.13 | -0.10 | -0.09 | -0.13 | -0.13 | -0.18 | -0.11 | -0.14 | -0.09 | -0.06 |
| **Cu** (as-received, $\alpha = 15°$) | 0.08 | 0.11 | 0.11 | 0.13 | 0.20 | 0.28 | 0.37 | 0.57 | 0.72 | 1.02 | 1.27 |

Table 4.4. Contact length measurements for aluminum and copper. Tool material: glass (coated with a $\sim$ 4 nm Pt-Pd coating.

| $t_0$ ($\mu$m) | 0.1 | 0.12 | 0.15 | 0.2 | 0.3 | 0.4 | 0.5 | 0.7 | 1 | 2 | 3 |
|---|---|---|---|---|---|---|---|---|---|---|---|
| Al (annealed, $\alpha = 40°$, $\mu$m) | 3.17 | 3.28 | 3.31 | 3.54 | 6.71 | 4.53 | 5.47 | 5.97 | 8.89 | 18.86 | 31.13 |
| Cu (as-received, $\alpha = 40°$, $\mu$m) | 1.60 | 1.86 | 1.78 | 2.46 | 2.88 | 3.30 | 3.90 | 4.99 | 4.93 | 9.50 | 15.88 |
| Cu (as-received, $\alpha = 15°$, $\mu$m) | 4.32 | 4.84 | 6.87 | 5.96 | 6.24 | 7.96 | 7.64 | 9.40 | 12.19 | 15.17 | 22.15 |

Table 4.5. Thickness ratio $r$ values for copper and annealed aluminum under cutting with glass knife at different rake angles. Blank represents that $r$ value could not be measured because of the chip curl.

| $t_0$ ($\mu$m) | 0.1 | 0.12 | 0.15 | 0.2 | 0.3 | 0.4 | 0.5 | 0.7 | 1 | 2 | 3 |
|---|---|---|---|---|---|---|---|---|---|---|---|
| Al (annealed, $\alpha = 40°$) | 0.319 | 0.393 | 0.383 | 0.409 | 0.46 | 0.421 | 0.477 | 0.416 | 0.484 | 0.451 | 0.430 |
| Al (annealed, $\alpha = 15°$) | - | - | - | - | - | - | - | - | - | 0.267 | 0.248 |
| Al (annealed, $\alpha = 0°$) | - | - | - | - | - | - | - | - | - | 0.163 | 0.175 |
| Al (annealed, $\alpha = -10°$) | - | - | - | - | - | - | - | - | - | 0.158 | 0.169 |
| Cu ($\alpha = 40°$) | - | - | - | - | - | - | - | - | 0.485 | 0.427 | 0.448 |
| Cu ($\alpha = 15°$) | 0.302 | 0.307 | 0.28 | 0.276 | 0.251 | 0.21 | 0.241 | 0.245 | 0.191 | 0.206 | 0.228 |
| Cu ($\alpha = 0°$) | 0.229 | 0.148 | 0.134 | 0.166 | 0.138 | 0.151 | 0.164 | 0.23 | 0.149 | 0.171 | 0.186 |
| Cu ($\alpha = -10°$) | 0.252 | 0.253 | 0.174 | 0.152 | 0.173 | 0.156 | 0.135 | 0.129 | 0.127 | 0.175 | 0.140 |

# 5. MECHANICS OF TOOL-CHIP CONTACT IN THE PRESENCE OF ADHESION

In this chapter, an attempt is made to explain the non-proportional scaling of tool-chip contact area with the cutting depth from the standpoint of adhesion. A framework to incorporate an adhesion term into conventional plastic contact mechanics model is developed. The model is shown to capture all key features of tool-chip contact mechanics at the small scale, most notably non-proportional scaling of the contact size and the occurrence of negative normal forces at the contact at very small cutting depths. The model is validated quantitatively using tool-chip contact length and force measurements obtained with aluminum and copper, with a procedure to estimate the work of adhesion at tool-chip contact established. Work of adhesion for clean glass-metal contact (2000 – 5000 mJ/m$^2$) is shown to be much higher than that for diamond-metal contacts ($\sim$100 mJ/m$^2$). Tool-chip adhesion is also shown to be drastically reduced in the presence of surface contaminants at the contact boundary. The results presented in this chapter provide quantitative support for the adhesion-based theory for the size effect in cutting of metals.

## 5.1 Introduction

In Chapter 4, the size effect, i.e., the increase in the specific cutting energy with the decrease in the depth of cut, has been studied systematically. It was shown that pronounced size effect can occur even in the case of cutting with theoretically sharp glass and diamond knives. Further investigations have revealed that the size effect is intricately associated with the tool-chip contact mechanics. It is the non-proportional decrease of the tool-chip contact length (thereby, tool-chip friction energy component) with the depth of cut that results in the size effect. This non-proportional scaling between tool-chip contact area and depth of cut in cutting at small length scales is in contrast to that typically observed at more conventional scales ($t_0 \sim 100$ $\mu$m).

This chapter explores this size dependence of tool-chip contact mechanics from the standpoint of intermolecular adhesion. In cutting of soft ductile metals, it is customary to treat the tool-chip contact as a plastic sliding contact, where the chip is plastically deformed as it is compressed against a hard (rigid) cutting tool. Given that the area for a conventional plastic contact scales with the normal load (with hardness being the proportionality constant), this picture predicts that the tool-chip contact length varies proportionally with the normal load acting at the tool-chip interface.

The fact that tool-chip contact mechanics at small length scales is far from this picture can be seen from Fig. 5.1. The figure shows the data obtained from cutting experiments with aluminum using a glass knife ($\alpha = 40°$), where the tool-chip contact length $l$ (measured using the tool-coating method discussed in Chapter 4), obtained at different cutting depths is plotted, against the corresponding normal load $F_n$ acting at the tool-chip interface. Three features of the tool-chip contact are noteworthy. First of these is the highly non-linear variation of the tool-chip contact length with the normal load. This non-linearity is particularly evident at small normal loads, with the trend at larger normal loads approaching a more linear form. Second is the existence of a finite intercept in the plot at zero normal load, that is, the tool and chip tend to adhere to each other even in the absence of applied normal load. Third relates to the observation of "negative" normal loads at very small cutting depths. The latter can be directly seen from Fig. 5.2, which shows the trace of friction force $F_f$ (force parallel to tool-chip contact) and normal force $F_n$ (force normal to the tool-chip contact) acting on the tool during cutting of aluminum with a glass knife ($\alpha = 40°$) at a small cutting depth, $t_0$ = 100 nm. $F_n$ can be clearly seen to be negative (about -0.2 N/mm) during the entire cutting duration, indicating tensile attractive forces at the tool-chip contact. The friction force $F_f$ on the tool, as expected, is greater than zero and acts along the chip flow direction. These observations show that the sliding between the chip and tool occurs under negative normal loads (i.e., tensile tractions) when the depth of cut is sufficiently small.

These distinctive characteristics of the tool-chip contact at the small scale – including non-proportional variation of the contact area with the load, finite contact size at the zero and even normal loads, and the fact that even surface contaminants have a remarkable effect on the tool-chip friction (see Chapter 4) – all suggest the presence of adhesion at the tool-chip contact. By adhesion, we mean here the molecular forces of attraction that act between two flat and chemically clean surfaces when we bring them into contact with each other, even when the two contacting surfaces are dissimilar in composition. That the adhesive attraction forces between surfaces can give rise to large increases in the contact area has been well-known for the case of lightly-loaded elastic bodies. In this case, adhesion is manifested in the form of non-zero contact area even when the applied normal load approaches zero, and further also by the fact that finite "pull-off" tensile force is actually required to separate the surfaces apart [17]. However, when the external loads are large compared to the net adhesive forces or under situations where an intimate contact between

surfaces is interrupted because of surface contamination, the contact size is well-predicted by the classical Hertzian model.

Significant experimental evidence now exists for adhesion between elastic bodies and how it affects the contact size. The transition between adhesion-dominated contact conditions and the classical Hertzian regime, as a function of the applied load, is also a problem that can be described quantitatively using the well-known JKR and DMT theories [17, 34, 96]. The JKR model considers the adhesion force as a result of short-range forces acting within the contact zone, with the surface interactions between the two objects outside the contact area being neglected. Whereas the DMT model models adhesion using van der Waals forces acting outside the contact zone; in this model, forces within the contact zone are treated in the same way as that of the Hertzian case. Both models have been shown to be quite successful in terms of quantitatively predicting/explaining the experimental observations, including deviation from the Hertzian predictions (or contact area) at small applied loads, the non-zero equilibrium contact area at zero normal load, and finally the need for a finite tensile (pull-off) force to break the contact [97, 98, 99]. The extension of the original JKR theory (which considers only normal forces at the contact) to a case where tangential load is introduced in addition to the normal load has been also demonstrated [100]. For this latter case, it was shown that the contact area is actually smaller than that predicted by the original JKR theory.

In contrast to above, adhesion interactions in the case of plastic contacts (of relevance to the current problem) have received relatively little attention, with most of the studies confined to only empirical observations. Perhaps the first direct evidence of adhesion for the case of plastic contact was provided by Golden and Rowe [101] who used radiotracers to demonstrate the transfer of material (from a hard indenter to a softer body) across the reciprocating contact. Other experimental evidence for adhesion comes from the studies by Maugis [102], Pashley and Tabor [103] and Chowdhury et al. [99] who showed that the adhesive attraction forces between the two bodies can be sometimes strong enough to cause plastic deformation. For example, it was shown that two small titanium metal particles, when brought into close contact, actually deform plastically to form a contact because of strong adhesive attraction forces, even when no external forces are applied. The study by Skinner and Gane [104] is also noteworthy for it shows that in the presence of adhesion, plastic sliding between two metal contacts could take place under a negative normal force. In contrast to these experimental observations, a quantitative framework to analyze the effect of

adhesion, and how it influences the plastic contact area dependence on the externally applied loads, is lacking. Moreover, it is important to note that the tool-chip contact of interest in metal cutting is not only plastic but is also complicated by tangential forces and sliding at the tool-chip interface.

In view of the above, this chapter seeks to develop a quantitative treatment for the sliding plastic contact in the presence of adhesion, with specific focus on the two-dimensional case of relevance to plane-strain metal cutting. The proposed model is validated using experimental data and is shown to replicate all key features of the tool-chip contact mechanics observed in our cutting experiments at the small scale. The model is shown to be also of practical utility for capturing the relative magnitude of adhesion effects between different cutting conditions, for example, across different cutting tool/workpiece material combinations and surface contaminations.

## 5.2 Experimental

To study the tool-chip plastic sliding contact mechanics and verify the continuum model, experiments under different cutting configurations were conducted using the instrumented ultramicrotome described in Chapter 3. In the present study, theoretically sharp glass tool ($\alpha = 40°$, $15°$, $0°$, and $-10°$) and diamond tool ($\alpha = 40°$) are used in the cutting experiments. The corresponding depth of cut ranges are 100 nm to 3 $\mu$m, and 30 nm to 1 $\mu$m, respectively. The material systems studied are two ductile metals: polycrystalline OFHC copper in as-received condition (obtained from McMaster-Carr) and polycrystalline 1100 aluminum in annealed condition (annealed at 350 °C for one hour). The corresponding purities, grain sizes, and Vickers hardness values are given in Table 3.1. A few experiments are also carried out using glass tools with permanent marking ink and oil lubricant to investigate how the tool-chip contact mechanics is altered by small changes to the contact boundary condition.

## 5.3 A model for tool-chip contact in the presence of adhesion

In this section, we present a continuum-level model to describe the experimental observations pertaining to tool-chip contact mechanics at the small scale. In metal cutting, it is known that the under side of the chip that is in contact with the tool undergoes plastic deformation (under a combination of normal and tangential stresses) as it slides along the tool face. The mechanics of this contact under general circumstances (i.e., without adhesion) may be modeled using the classical plasticity theory. The corresponding plasticity criterion can be given as $p^2 + \beta s^2 = k^2$.

In this expression, $p$ is the mean normal contact stress, $s$ is the tangential stress, $\beta$ is a numerical constant, and $k$ is the contact pressure at which the soft body (i.e., chip) yields in the absence of any tangential stresses. From the von Mises criterion, it is can be shown that $\beta$ should be equal to 3 for the case of a two-dimensional contact, as in a chip compressed against a rigid tool. It can be seen that in the presence of tangential stress, the material yields at a mean normal contact pressure that is lower than $k$, so that the yielding criterion is maintained.

Assuming that the tool-chip contact is as shown in Fig. 5.3(a), where $F_n$ is the normal load in N/mm (normalized with respect to width), $F_f$ is the tangential load (also normalized with respect to width), and $l$ is the tool-chip contact length under steady-state conditions, the relationship between $F_n$, $F_f$, and $l$ can be described as:

$$F_n{}^2 + \beta F_f{}^2 = (kl)^2 \tag{5.1}$$

As noted, $\beta$ in equation 5.1 is a dimensionless constant and $k$ is the critical contact pressure for yielding. If we assume the shear stress ($\tau_F = \frac{F_f}{l}$) at the tool-chip contact is approximately constant and independent of $t_0$ (an assumption that is supported by our experiments, for example, see Table 5.1 which presents data for $\tau_F$ under different cutting conditions), the contact length $l$ can be expressed in terms of $F_n$ as:

$$l = \frac{1}{\sqrt{k^2 - \beta\tau_F}} F_n \tag{5.2}$$

Clearly, the above equation predicts a linear and proportional dependence between the contact length $l$ and the normal load $F_n$ (given $\tau_F$ is a constant), as to be expected for a conventional plastic contact. Using the expression $F_f = \tau_F l$, we can further derive a relation between $F_f$ and $F_n$ as:

$$F_f = \frac{1}{\sqrt{(\frac{k}{\tau_F})^2 - \beta}} F_n \tag{5.3}$$

Similar to the contact length dependence, the model predicts that $F_f$ should vary proportional to $F_n$, which is consistent with the Coulomb theory of friction (i.e., constant friction coefficient). However, these predictions for a regular plastic contact clearly cannot explain the non-linear trend observed between the contact length (and friction force) and the normal load observed in our experiment at the small scale, nor they can explain the existence of negative normal forces that are observed in our experiments. These observations motivate us to incorporate adhesion into the model.

To quantify the effect of adhesion, the tool-chip contact in metal cutting is simplified as a half cylinder plastically compressed against a semi-infinite flat (Fig. 5.3(b)). In Fig. 5.3(b), $R$ is the radius of the chip curvature, $l$ is the contact length confined by two points A and B (same as shown in Fig. 5.3(a)), and $\delta$ is the plastic displacement (deformation) normal to the contact. Given that $\delta \ll R$ and $l$, it can be shown that $l \approx \sqrt{2R\delta}$ and full contact area, $A_{full} = 2lw = 2w\sqrt{2R\delta}$.

Two approaches (energy and force based) are considered next to estimate the adhesive force component and to understand how adhesion can alter the relation between contact length and $F_n$.

### 5.3.1 Energy-based approach

The energy balance approach presented here is similar to that of Chowdhury and Pollock [99] for the case of circular plastic contact. If we consider plastic compression of the cylinder by a small distance of $d\delta$, the total change in energy $dU_{total}$ can be written as a sum of two parts, namely the plastic deformation energy ($dU_{deform}$) and the contact adhesion energy associated with change in the tool-chip contact area.

$$dU_{total} = dU_{deform} + dU_{adhesion} \tag{5.4}$$

The energy associated with the plastic deformation of the material is taken as $HA_{full}d\delta$ (where $H$ is the material hardness under plane-strain conditions, equivalently $k$), whereas energy change associated with the contact area change is given by $\gamma dA_{full}$, where $\gamma$ is the work of adhesion (i.e., the work required to separate the two contact surfaces, unit mJ/m$^2$). If we consider the applied load to be $F_{app}$ and $dU_{total} = F_{app}d\delta$, this leads to the following equation:

$$F_{app} = 2H\sqrt{2R\delta}w - \gamma w\sqrt{\frac{2R}{\delta}} \tag{5.5}$$

With slight rearrangement of terms, we get:

$$F_N + \frac{\gamma R w}{l} = Hwl = HA, \tag{5.6}$$

where $F_N(= \frac{F_{app}}{2})$ is the normal load (in N) applied to half of the contact (namely tool-chip contact) and $A(= wl)$ is the tool-chip contact area. Note that the second term $\frac{\gamma R w}{l}$ in the above equation represents the adhesive force acting at the tool-chip contact. It is also import to note that elastic effects are ignored in the above analysis (energy balance), justified by the fact that strains involved in metal cutting are greater than 100%, where elastic strains can be safely neglected.

The above equation shows that the net normal force acting at the contact is now comprised of two components: the applied force ($F_N$) and the adhesion force $F_a(= \frac{\gamma R w}{l})$. Normalizing this net normal force with respect to width and incorporating it into the plasticity criterion results in the following:

$$(F_n + \frac{\gamma R}{l})^2 + \beta {F_f}^2 = (kl)^2 \tag{5.7}$$

As before, assuming $\tau(= \frac{F_f}{l})$ to be a constant, and let $P = \sqrt{k^2 - \beta {\tau_F}^2}$ and $Q = \gamma R$, the contact length $l$ can be expressed in terms of $F_n$ as:

$$l = \frac{F_n + \sqrt{{F_n}^2 + 4PQ}}{2P} \tag{5.8}$$

It can be seen that the above equation correctly predicts non-linear dependence of contact length $l$ under small loads (i.e., when $F_n$ is comparable to the $Q = \gamma R$ term); and near-linear

dependence on $F_n$ under large loads ($F_n \ll Q$). The equation also predicts a finite contact length at zero normal load (given by $l_{F_n=0} = \sqrt{\frac{Q}{P}} = \sqrt{\frac{\gamma R}{\sqrt{k^2 - \beta {\tau_F}^2}}}$) as well as under negative normal loads, consistent with the experimental observations. This provides strong support to the hypothesis that adhesion exists at the tool-chip contact and is responsible for non-proportional variation of the contact length with respect to the normal load and the cutting depth.

A similar relationship between $F_f$ and $F_n$ can be established by letting $S = \frac{\sqrt{k^2 - \beta {\tau_F}^2}}{\tau_F}$ and $T = \gamma R \tau_F$. This gives:

$$F_f = \frac{F_n + \sqrt{{F_n}^2 + 4ST}}{2S}, \tag{5.9}$$

which predicts the pattern shown earlier in Fig. 5.1.

### 5.3.2 Force-based approach

In this approach, the magnitude of the adhesive force is directly estimated using the DMT-type approach [36] that considers only the attraction forces outside the contact area. Assuming that a small gap $D$ exists between the tool rake face and the chip, the adhesive force involved in changing the contact area by a small $dA_{full}$ is given by:

$$\int_{\delta=D}^{\infty} \gamma_a dA_{full} = \int_{\delta=D}^{\infty} w\sqrt{\frac{2R}{\delta}} \gamma_a d\delta, \tag{5.10}$$

where $\gamma_a$ is the attraction force per unit area taken as $\frac{\pi c \rho^2}{6\delta^3}$ (according to Israelachvili [36]). This results in an equation for the adhesive force as:

$$\frac{\pi c \rho^2 w\sqrt{2R}}{6} \int_{\delta=D}^{\infty} \delta^{-\frac{7}{2}} d\delta = \frac{\pi c \rho^2 w\sqrt{2R}}{15 D^{\frac{5}{2}}} \tag{5.11}$$

Lastly, the adhesive force acting on half of the cylinder (i.e., actual tool-chip contact) is therefore $\frac{\pi c \rho^2 w\sqrt{2R}}{30 d^{\frac{5}{2}}}$. The adhesion force in this case can be seen to be independent of the contact length.

Incorporation of the adhesion term (treated as a constant $C(= \frac{\pi c \rho^2 \sqrt{2R}}{30 d^{\frac{5}{2}}})$ for a given chip curl radius and tool-chip contact) derived from the force-based approach into the plasticity criterion results in the following:

$$(F_n + C)^2 + \beta {F_f}^2 = (kl)^2 \tag{5.12}$$

Again, assuming $\tau_F$ to be an invariant leads to an expression for the contact length in terms of $F_n$ as:

$$l = \frac{F_n + C}{\sqrt{k^2 - \beta {\tau_F}^2}} \tag{5.13}$$

Similarly, the dependence of $F_f$ on $F_n$ can be given by:

$$F_f = \frac{F_n + C}{\sqrt{(\frac{k}{\tau_F})^2 - \beta}} \tag{5.14}$$

It can be seen that this approach predicts a linear dependence between the contact length and the normal load, albeit with a finite intercept (given by $\frac{C}{\sqrt{(\frac{k}{\tau_F})^2 - \beta}}$) at zero normal load similar to the energy-based approach. The model is also capable of predicting non-zero contact lengths even under negative normal loads (provided that $C$ is greater than the negative normal load). However, among the two approaches considered to calculate the adhesive force component, the energy-based approach that predicts non-linear variation of the contact length with respect to load is in better alignment with the experimental observations. In the following, we validate this energy-based approach using experimental data and show how it can be used to (qualitatively) predict the work of adhesion ($\gamma$) for different tool-material combinations.

## 5.4 Model comparison with experiments

As noted earlier, the contact mechanics model incorporating a non-constant adhesion force term (derived from the energy balance approach) is qualitatively consistent with the experimental observations. In the following, we explore quantitative validation of this model using direct experimental data obtained from aluminum and copper under different cutting configurations (tool material, boundary condition).

Note that the main parameters in the model (described by equation 5.8) are $\beta$, $k$, $\tau_F$, $\gamma$, and $R$. In our study, $\beta$ is treated as a free parameter given that for a general three-dimensional contact, $\beta$ has no theoretical value but depends on the actual ratio between the yield pressure at the contact and the shear strength of the material; for example, when the yielding pressure $k$ is five times the material's shear strength, $\beta$ has a value of 25. Even though for a perfect two-dimensional case, $\beta$ should be equal to 3, experiments with polished platinum [91] showed that a $\beta$ value of about 12 best fit the experimental data. In view of this, $\beta$ is treated as a fitting parameter.

The parameter $k$ represents the contact pressure at which the softer body at the contact yields. In our model, the contact between the tool and chip is simplified as a ductile half-cylinder compressed against a rigid plane (Fig. 5.3) under plane strain deformation. To determine the value of $k$ for this configuration, the method proposed by Green [105] is adopted (see APPENDIX A for more details). This method utilizes the Hertzian solution [35] for contact between a cylindrical workpiece and a rigid plane, and the critical contact pressure and the contact length at the elastic-plastic transition is obtained using von Mises yielding criterion. This method enables the critical pressure at yield $k$ to be expressed in terms of materials yield stress $Y$ as $k = C_k Y$, where $C_k$ is a constant depending on the Poisson's ratio ($\nu$) given as $C_k = 1.164 + 2.975\nu - 2.906\nu^2$. Based on the Poisson's ratios of 0.33 for 1100 aluminum [106] and 0.355 for pure copper [107], and by using Tabor's [108] relation between the uniaxial yielding stress $Y$ and the Vickers hardness $H$ ($Y \approx H/3$), $k$ values for aluminum and copper are estimated as 179 MPa and 677 MPa, respectively.

In our experiments, the shear stress $\tau_F$ at the tool-chip contact showed no specific dependence on the cutting depth $t_0$ (see Table 5.1). Therefore, $\tau_F$ is treated to be a constant independent of the normal load: 70 MPa and 128 MPa are obtained for aluminum and copper, respectively. Lastly, the radius of curvature of the chip $R$ is treated as a constant again based on experimental observation.

Fig. 5.4 shows the side view of a typical chip (aluminum, $t_0$ = 3 $\mu$m) captured using SEM, where the radius of curvature is seen to be around 0.1 mm. Since chip curl radius showed no specific dependence on depth of cut or tool material, a $R$ value of 0.1 mm is assumed for all the cases.

Finally, work of adhesion $\gamma$ is treated as a fitting parameter in addition to $\beta$. Model fitting to the experimental data was done by minimizing the sum of squared residuals (difference between the prediction and observed data) using the Gauss-Newton algorithm that is frequently used to solve the non-linear regression problem.

Fig. 5.5 shows the model comparison with experiments for the cases of aluminum and copper. The highly non-linear trend between contact length $l$ and the normal load $F_n$ in the case of aluminum can be seen to be clearly captured by the model. The model also correctly predicts non-zero contact length at $F_n \approx 0$ and also under negative loads. It is worthwhile to note again that both the conventional contact mechanics model and the model incorporating a constant adhesion term, which predict linear dependence between $l$ and $F_n$, are not consistent with the experimental data. For the curve fitting shown in Fig. 5.5(a), the inferred magnitude of the work of adhesion $\gamma$ is 5753 $\mathrm{mJ/m^2}$, whereas the inferred $\beta$ is 7.84. $\gamma$ value estimated based on the measured contact length ($l_{F_n=0} = \sqrt{\frac{\gamma R}{\sqrt{k^2 - \beta {\tau_F}^2}}}$) at $F_n \approx 0$ also resulted in work of adhesion close to 6000 $\mathrm{mJ/m^2}$.

In contrast to aluminum, the contact length and normal load data for copper-glass tool combination exhibits a more linear trend, with no obvious intercept as the normal load approaches zero (see Fig. 5.5(b)). Nor a negative normal load observed in these experiments even under very small cutting depths. This suggests that tool-chip adhesion for the case of copper-glass contact is significantly smaller than aluminum-glass contact. For example, from Fig. 5.5(b), it can be seen that the data can be fit (equally well) either using a straight line passing through origin (i.e., $\gamma$ = 0) or a curved line using a small $\gamma$ value of 2000 $\mathrm{mJ/m^2}$ that is about 60% smaller than that of aluminum-glass contact. These observations clearly demonstrate that the work of adhesion highly depends on the tool-material combination. The inferred $\beta$ constant for the case of copper is 6.51, close to the inferred $\beta$ of 7.84 in aluminum cutting experiments. This suggests $\beta$ is a constant that depends on the contact geometry independent of the material system.

As seen from Eq. 5.9, the proposed model can be also used to capture the dependence of $F_f$ on $F_n$. This feature is especially useful to predict work of adhesion under situations where it is difficult to make tool-chip contact length measurements. Examples include cutting experiments

conducted with boundary contaminant or lubricants and experiments involving the diamond knife where the metallic coating method (demonstrated earlier with glass tools) to calculate contact lengths is infeasible because of the expensive nature of diamond tools. To investigate the work of adhesion for diamond-metal contacts, Eq. 5.9 is fitted to the $F_f$ vs $F_n$ data obtained from aluminum and copper using diamond knife, as shown in Fig. 5.6. Note that $\tau_F$ is treated as a third fitting parameter in addition to $\beta$ and $\gamma$. From Fig. 5.6, it can be seen that model accurately captures the experimental trend both in aluminum and copper.

The $F_f$ vs. $F_n$ dependence is seen to be roughly linear at large $F_n$ (namely large $t_0$), but very non-linear at smaller $F_n$, which is accurately captured by the model. Non-zero $F_f$ under zero or even negative $F_n$ can also be seen from the figure, especially in the case of aluminum. This is generally consistent with the observation made using glass knives. The inferred $\gamma$ values for aluminum-diamond and copper-diamond contacts are 132 $\mathrm{mJ/m^2}$ and 98 $\mathrm{mJ/m^2}$ respectively, which are about one order lower than the corresponding $\gamma$ values obtained for glass-metal contacts. This is consistent with the literature reports which show smaller adhesion for the case of diamond-metal interfaces when compared to glass-metal interfaces. This suggests that in addition to providing direct support for adhesion at tool-chip contact, the model can also be used to assess the work of adhesion for different tool-material combinations.

Table 5.1 summarizes the data for $\gamma$ across different materials along with the corresponding $\beta$ and $\tau_F$ values. $\beta$ values obtained respectively for aluminum and copper using diamond knife are 5.43 and 9.36, which are fairly close to the $\beta$ values obtained with glass.

This again suggests that $\beta$ is mainly governed by the contact geometry. That $\tau_F$ for diamond-metal contacts can be strikingly smaller compared to the glass-metal contacts can also be seen from Table 5.1. Similarly, the extrapolated $F_f$ at zero $F_n$ in the case of cutting of aluminum and copper with diamond knife are 0.040 N/mm and 0.053 N/mm, significantly smaller than the corresponding 0.458 N/mm ($\approx$ 0.0071 mm $\times$ 70 MPa) and 0.295 N/mm ($\approx$ 0.0017 mm $\times$ 128 MPa) observed in cutting using glass tools.

### 5.5 Effect of surface contamination and rake angle on tool-chip contact mechanics

In the previous section, the proposed model that incorporates adhesion into a conventional contact model has been shown to be capable of predicting the non-linear dependence between the

contact length $l$ (or friction force $F_f$) and the normal force $F_n$ as well as negative normal loads under certain conditions. It is also shown that the deviation from the linearity and size of the tool-chip contact at zero normal loads depend on the magnitude of $\gamma$ term, the work of adhesion. With this as a basis, we explore the influence of tool surface contamination and rake angle on tool-chip contact mechanics. The $F_f$ vs. $F_n$ data is presented for multiple cutting conditions and interpreted using the above modeling framework.

Fig. 5.7 shows the $F_f$ vs. $F_n$ data obtained with aluminum using glass knife ($\alpha = 40°$) coated with a thin layer of permanent marking ink and oil. From the figure, it can be seen that in the presence of the tool-chip surface contaminants, the scaling between $F_f$ and $F_n$ is much more linear, roughly passing through the origin. This is in direct contrast to the highly non-linear trend observed with clean glass knife (Fig. 5.1), and suggests that the adhesion is greatly reduced ($\gamma \approx 0$) by introduction of contaminants at the tool-chip interface. Moreover, no evidence for negative normal load can be found in cutting experiments with surface coated glass knives even under very small cutting depths. This again shows that adhesive forces are highly sensitive to the contact boundary conditions and can be nearly eliminated even with a slight amount of surface contamination. The role of surface contamination in reducing adhesion in the case of elastic contacts is well-known in the literature.

The effect of rake angle on friction force plots is shown in Figs. 5.8 and 5.9 for aluminum and copper. Glass knives with four different rake angles ($40°$, $15°$, $0°$, and $-10°$) were considered in this study, and experiments were conducted under clean contact conditions. At $\alpha = 40°$ (Figs. 5.8(a) and 5.9(a)), the friction force plots in both the materials are seen to be similar, characterized non-linear variation with $F_n$ at small loads. The inferred $\gamma$ values obtained from the curve fitting to the data are 14473 $\mathrm{mJ/m^2}$ and 4345 $\mathrm{mJ/m^2}$ for aluminum and copper, respectively. These values are similar to those obtained from the direct contact length measurements (Fig. 5.5).

However, when $\alpha$ is made less positive ($\alpha = 15°$, $0°$, and $-10°$), the force plots are seen to be much more linear in line with the conventional plastic contact model, with no obvious sign of the intercept at zero normal load. Also, no negative normal loads were observed at these small rake angles. Even though this transition in the behavior resulting form the rake angle effect is not fully understood, the fact that it is observed in both aluminum and copper suggests that is is not material dependent. From the observations made so far, it should be clear the non-linear

dependence between $F_f$ and $F_n$ arising from adhesion is noticeable particularly under conditions where deformation forces are comparable or smaller than the adhesive force component acting at the tool-chip contact, as in cutting at very large (positive) rake angles or small depths of cut. Given that cutting deformation at smaller rake angles such as $0^\circ$ and $-10^\circ$ is characterized by large plastic strains (much greater than 1000%), the higher deformation forces associated with this severe plastic deformation dominate the contact mechanics at these rake angles, with adhesive forces playing a negligible role.

## 5.6 Discussion

A model is presented to capture the size dependence (non-linearity) of tool-chip contact size and friction energy that is consistently observed in our cutting experiments at small cutting depths. The main feature of the model is the incorporation of the attractive adhesive force term to correctly predict the non-linear relationship between the contact size and normal load at small normal loads. The linear relationship at high normal loads (i.e., large cutting depths) that is expected for a conventional plastic contact is also reproduced by the model. These observations provide a new interpretation of the size effect in machining in terms of tool-chip adhesion. The 'larger than usual' contact areas observed at small cutting depths, and which cause a prominent size effect, are due to the intermolecular attractive forces at the tool-chip contact. In situations where these attractive forces are much smaller compared to the applied deformation forces, e.g., at higher cutting depths, the size effect is negligible. The fact that size effect is reduced in the presence of lubricants and surface contaminants (which reduce tool-chip adhesion) and under small rake angles (large deformation forces) are quite consistent with this picture of the size effect. Given that surface attraction forces are intrinsic to all contacts, adhesion potentially provides a unified framework to analyze the size effect phenomenon across multiple applications (nanoindentation, sliding, erosion, etc.).

More generally, the present study also highlights the need for incorporating adhesion effects into machining models. Although the pristine and intimate nature of tool-chip contact, which promote adhesion, has been well-known [109, 110], it is surprising that adhesive forces have received little consideration to date in machining studies. The present study shows, for the first time, how adhesive forces can explain both the non-linear dependence of tool-chip contact length on the cutting depth as well as the existence of negative normal loads at tool-chip contact in machining at

sub-micron length scales. Another phenomenon that is of relevance is the so-called "seizure", first highlighted by Trent and co-workers [111, 112]. Under conditions of seizure, the tool-chip contact is such that the chip underside fully sticks to the tool; in other words, zero relative sliding at the tool-chip contact. Seizure is believed to occur as a result of solid-phase weld formation between two chemically clean surfaces (tool and the chip) under large contact pressures, and this "weld" between chip and the tool is sometimes so strong that it causes chip fracture or damage the tool when the chip is pulled to break the contact. Seizure therefore appears to be an extreme case of adhesion that is characterized by high work of adhesion. The fact that surface contaminants like grease have a significant effect in terms of reducing the occurrence of seizure is in line with this idea. Despite several phenomenological observations of seizure over the last few decades, a quantitative treatment for the occurrence of seizure in terms of surface attraction forces is currently lacking.

The experimental-modeling approach described in this chapter provides a convenient way for comparing the relative magnitude of tool-chip adhesion between different tool/material combinations. For example, it has been shown that the inferred work of adhesion $\gamma$ for glass-metal contacts is much higher (by about an order of magnitude) than that for diamond-metal contacts. Similarly, aluminum-glass contact is shown to be characterized by much higher $\gamma$ value when compared to the copper-glass contact, consistent with the literature reports [95]. Therefore, $\gamma$ can be used as an indicator to quantify tool-chip adhesion. This should be of significant practical value for assessing and quantifying the efficacy of various tool materials, coatings and lubricants to reduce adhesion in machining applications.

When compared to the literature values reported for $\gamma$, it is found that the values inferred from the present study are generally much higher. For example, the estimated $\gamma$ for glass-aluminum contact is about 6000 mJ/m$^2$, which is about one order of magnitude greater than the work of adhesion reported using AFM studies [86]. This discrepancy between the current and literature values might be a result of the fact that tool-chip contact in chip formation is intrinsically clean and free of roughness artefacts (i.e., real area of contact at the interface is equal to the apparent area of contact). These conditions are extremely difficult to achieve in conventional surface characterization studies, including AFM. This also suggests new opportunities of using this cutting chip formation as a novel experimental tool to study friction and adhesion in the absence of roughness effects, and

over a range of speeds, normal loads, and surface environments.

Lastly, it should be noted that while the contact mechanics model presented in this chapter is developed with particular reference to metal cutting, the proposed framework to incorporate the adhesion term is quite general and can be extended to different plastic sliding contacts (including non-plane-strain contacts) to predict the relationship between the contact area, friction force and normal force as a function of material properties and work of adhesion between the contacting materials. Likewise, elastic effects (ignored in the present study) can be easily incorporated into the energy-balance Eq. 5.4 to further generalize the model for elasto-plastic sliding contacts.

## 5.7 Conclusion

A continuum-level contact mechanics model that accounts for adhesion is presented for the tool-chip plastic sliding contact in machining. The model shows that at small cutting depths, surface attraction (adhesive) forces at this contact are comparable to the deformation forces and therefore cannot be ignored. The model correctly predicts the non-proportional reduction of tool-chip contact length with the cutting depth at the small scales and provides a basis for the size effect in machining that is rooted in tool-chip adhesion. Furthermore, the model also explains how tool-chip sliding can occur under negative (i.e., tensile) normal forces at very small cutting depths. The model is validated with experiments, and work of adhesion (surface energy) at the tool-chip contact predicted for different tool-material combinations (e.g., metal-diamond and metal-glass) and in the presence of various surface contaminants. The observations explain why size effect is highly reduced in the presence of tool-chip surface contamination and the critical role of adhesion in controlling the tool-chip contact mechanics and friction at small scales. Besides providing a better understanding of the tool-chip contact mechanics in machining applications, the proposed experimental-modeling framework also suggests a possibility to utilize cutting chip formation as a controlled means to study friction, adhesion and size dependence of plastic sliding contacts over a range of material combinations, normal loads (from millinewtons to kilonewtons) and sliding speeds.

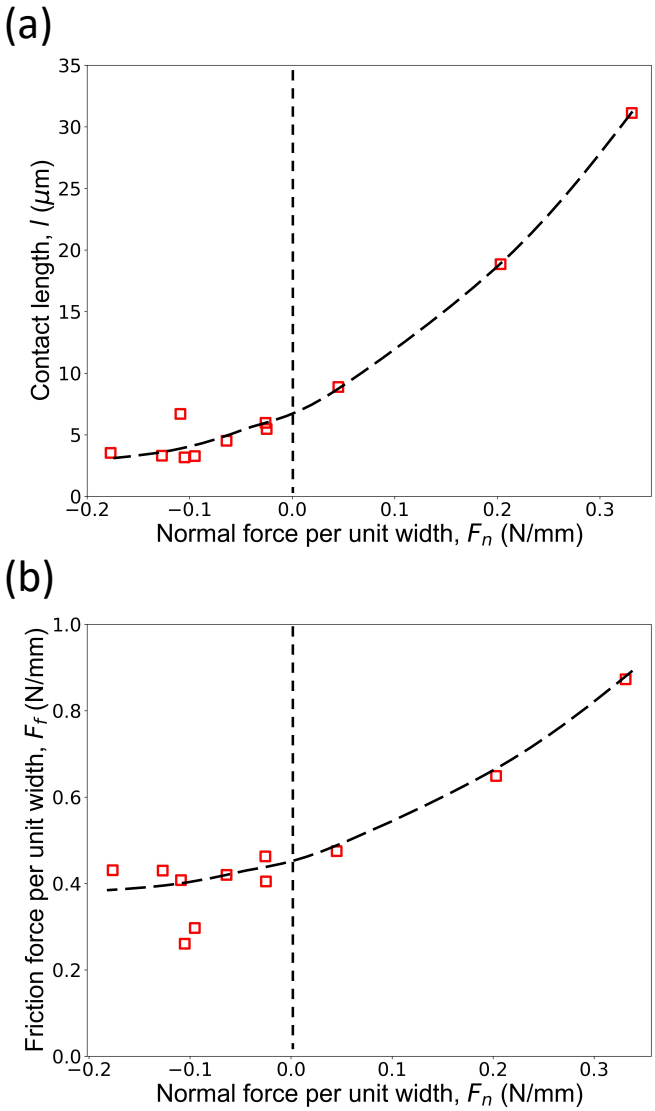


Figure 5.1. (a) Tool-chip contact length and (b) friction force dependence on the normal force in cutting of aluminum (annealed) using a glass knife at $\alpha = 40°$. The individual data points correspond to different cutting experiments conducted at different $t_0$.

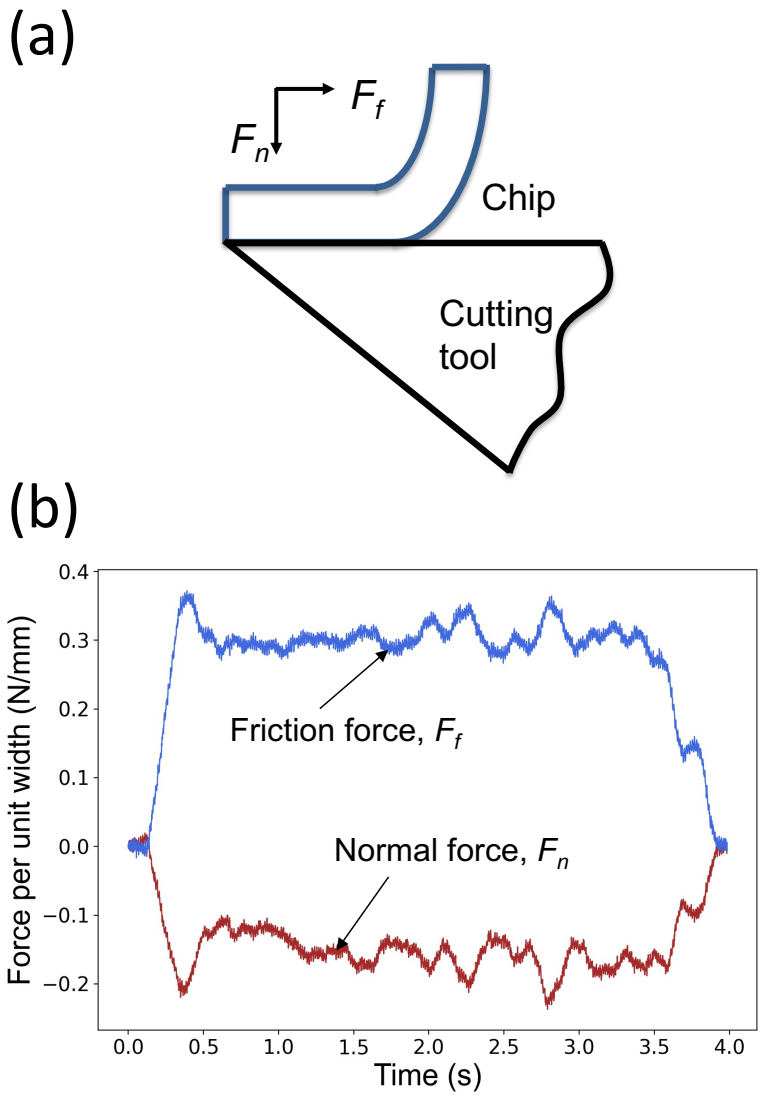


Figure 5.2. (a) Metal cutting schematic showing the directions of friction force $F_f$ and normal force $F_n$. (b) Plot showing the friction force ($F_f$) and normal force ($F_n$) traces during cutting of aluminum at $t_0$ = 100 nm (glass knife, $\alpha = 40°$). Note the negative sign of the normal force $F_n$ in (b).

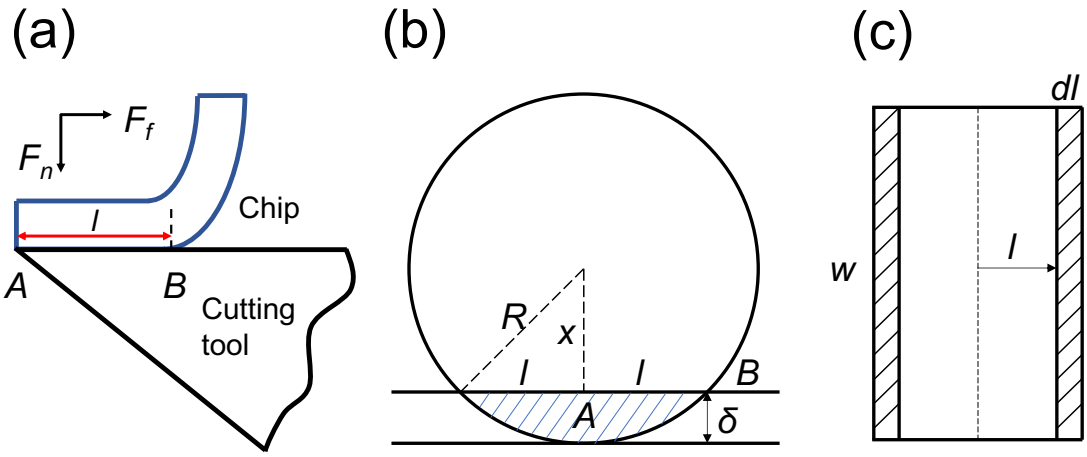


Figure 5.3. (a) Schematic of the actual tool-chip contact. (b) and (c) show the side view and top view of the tool-chip contact simplified as a half cylinder plastically compressed against a semi-infinite flat.

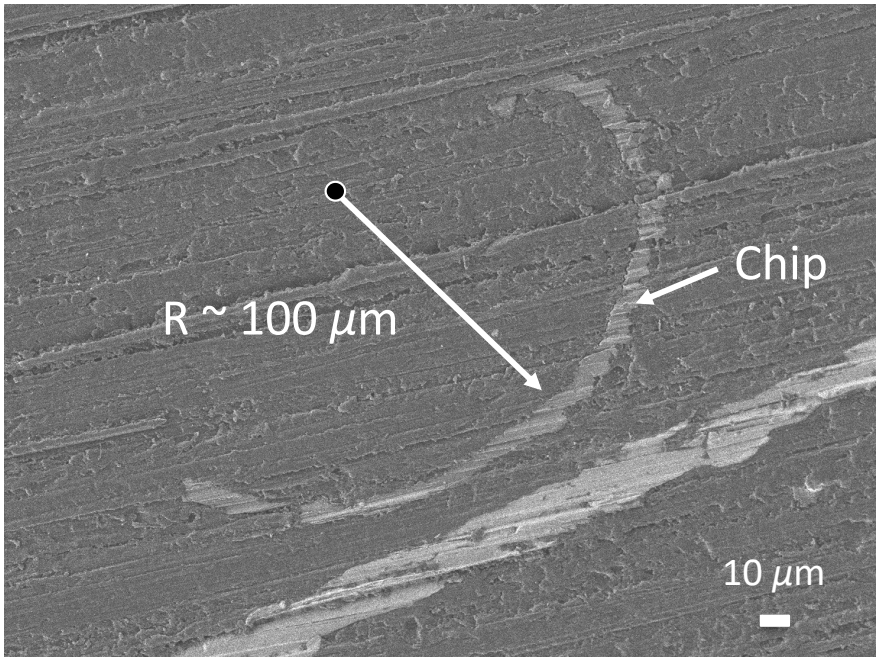


Figure 5.4. Cross-sectional view of a microtomed aluminum chip showing a radius of the curvature of about 100 $\mu$m ($\alpha = 40°$, $t_0$ = 3 $\mu$m).

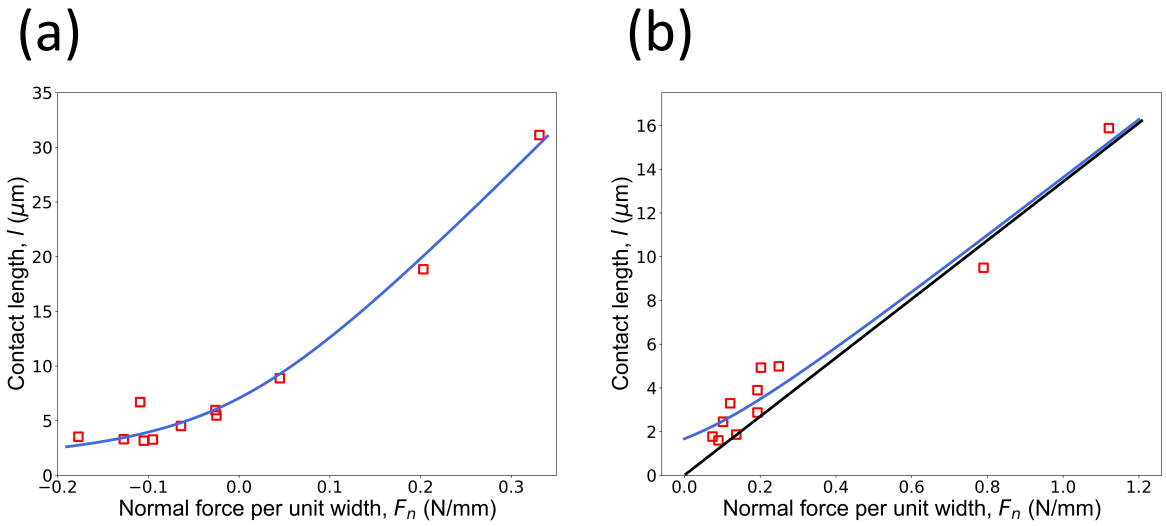


Figure 5.5. Contact length $l$ vs. normal load $F_n$ plots showing model comparison with experimental data for: (a) aluminum ($\alpha = 40°$) and (b) copper ($\alpha = 40°$). Red squares are experimental data and the fitted curves are shown in blue color. The black straight line in (b) corresponds to $\gamma = 0$.

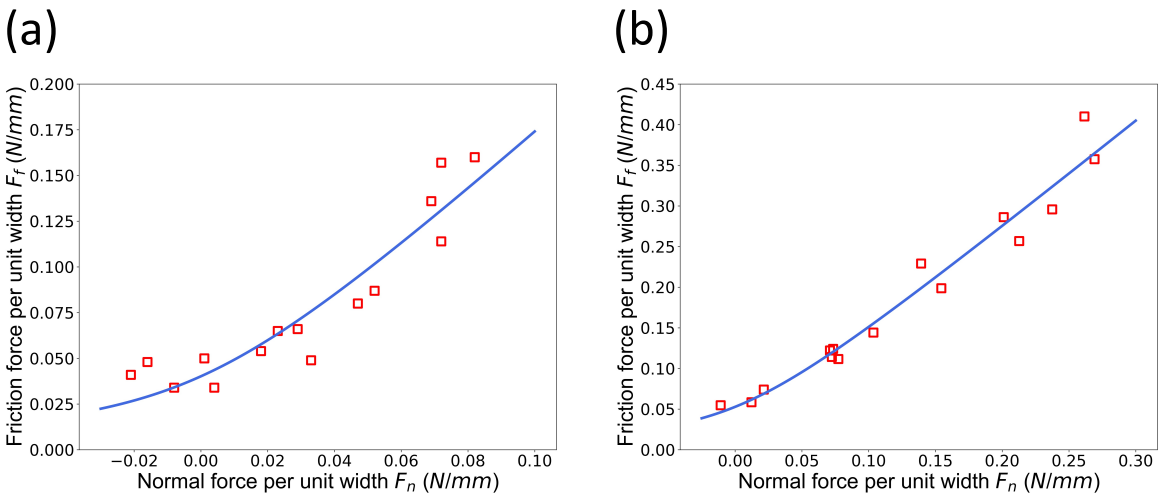


Figure 5.6. Dependence of friction force $F_f$ on the normal force $F_n$ in cutting with diamond knife: (a) aluminum ($\alpha = 40°$), (b) copper ($\alpha = 40°$). Red squares are experimental data points.

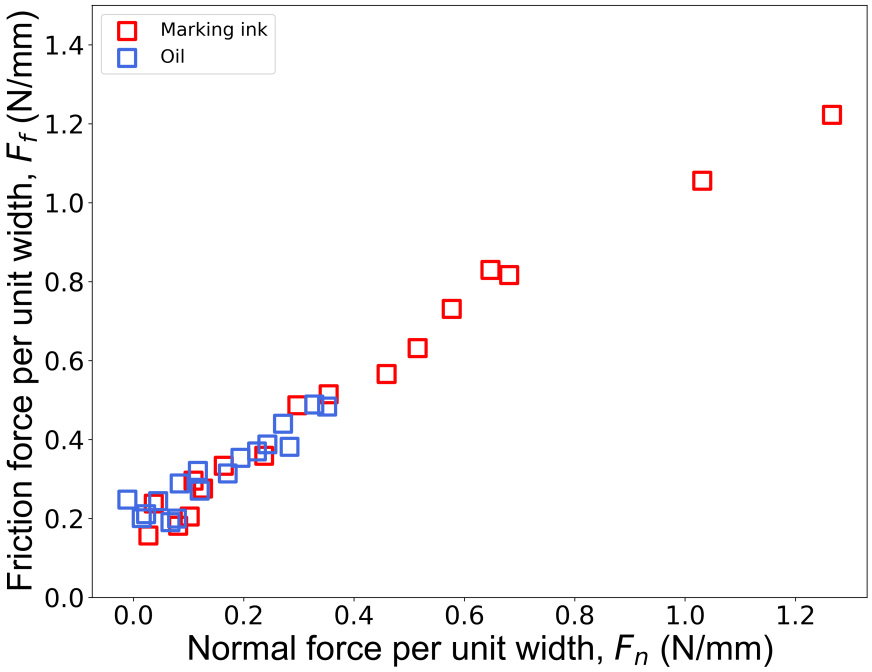


Figure 5.7. Friction force $F_f$ vs. normal force $F_n$ plot for cutting using glass knife ($\alpha = 40°$) coated with two surface contaminations: permananent marking ink and oil.

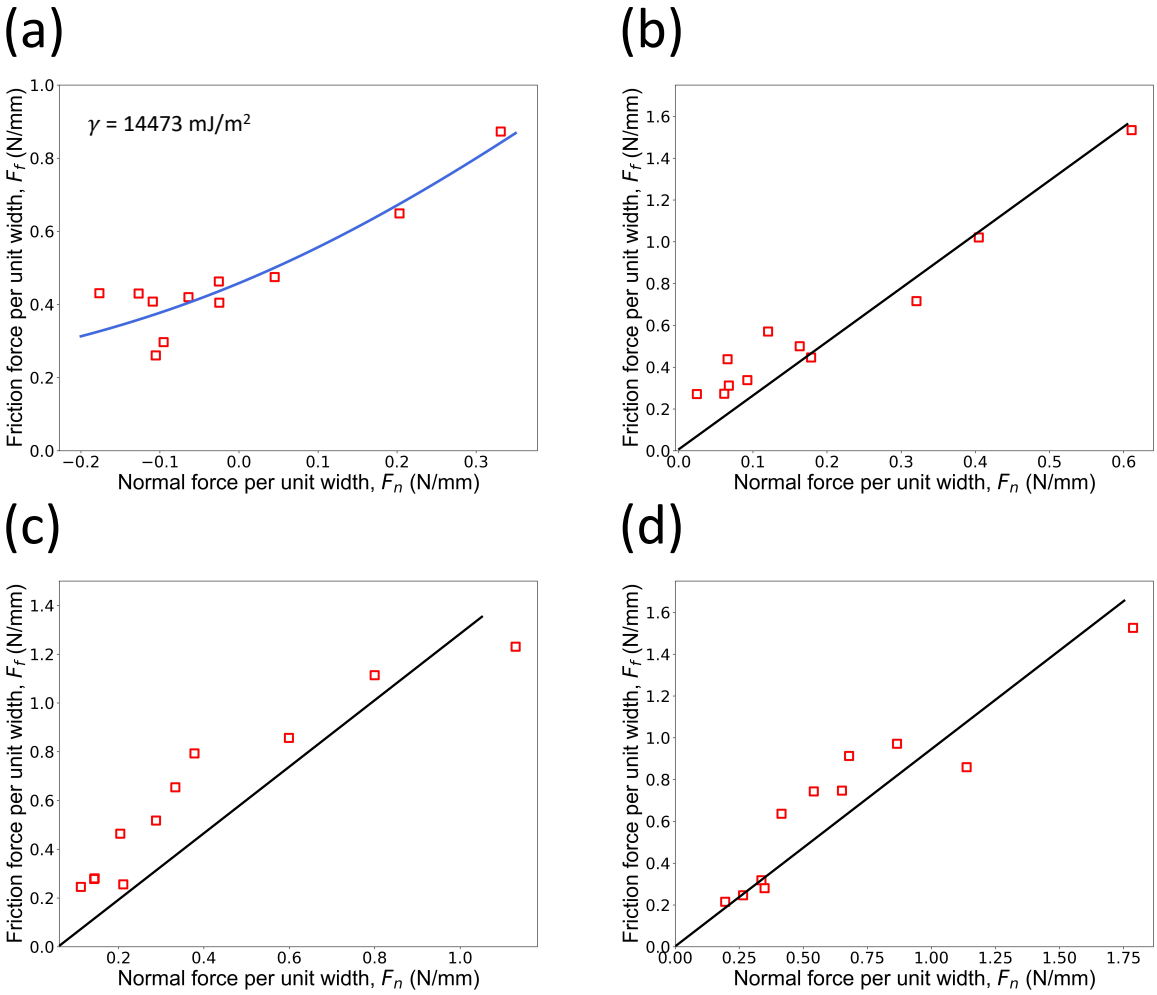


Figure 5.8. $F_f$ vs. $F_n$ plots for cutting of aluminum at different rake angles: (a) $\alpha = 40°$, (b) $\alpha = 15°$, (c) $\alpha = 0°$, and (d) $\alpha = -10°$.

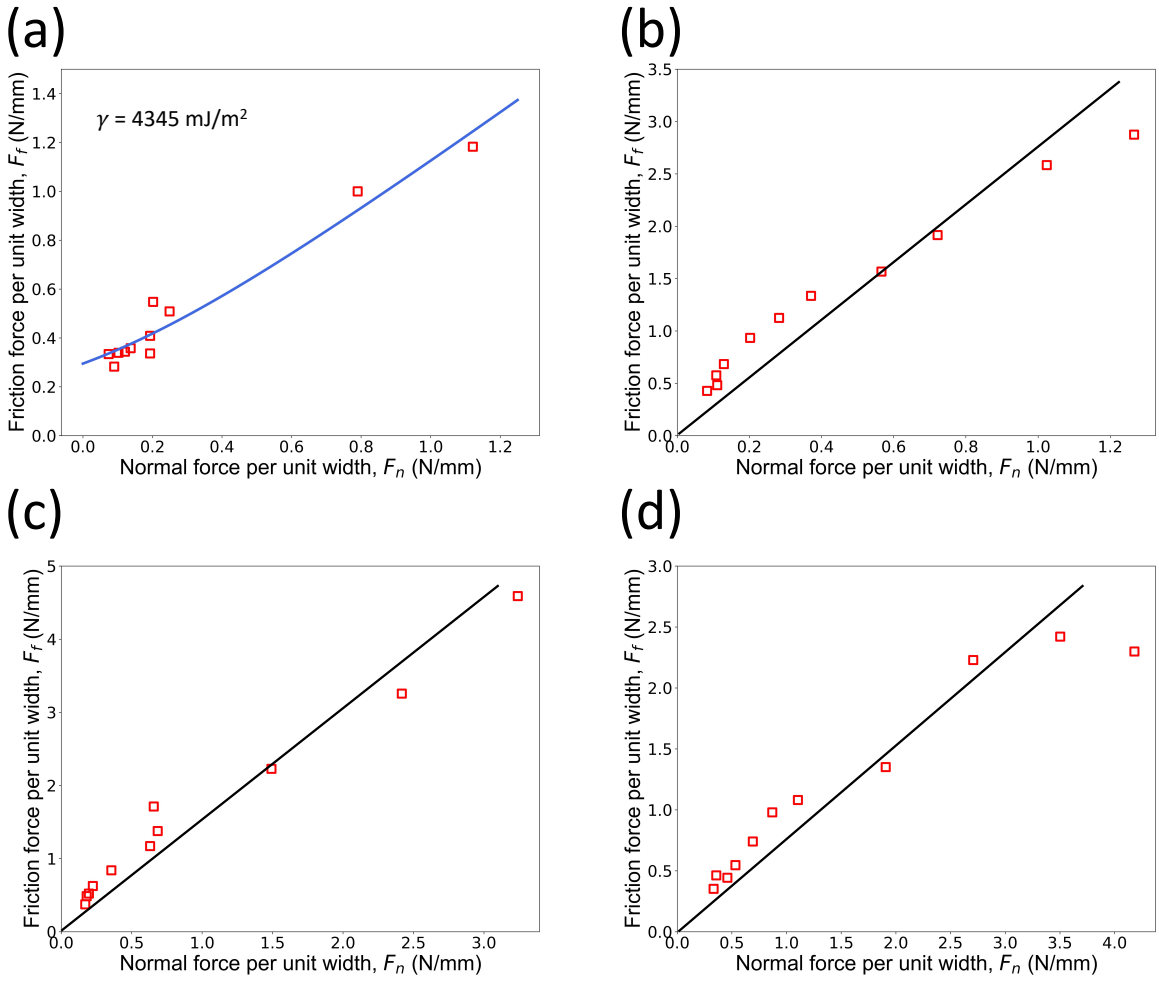


Figure 5.9. $F_f$ vs. $F_n$ plots for cutting of copper at different rake angles: (a) $\alpha = 40°$, (b) $\alpha = 15°$, (c) $\alpha = 0°$, and (d) $\alpha = -10°$.

Table 5.1. Tool-chip contact shear stress values ($\tau$, MPa) for Al and Cu.

| $t_0$ ($\mu$m) | 0.1 | 0.12 | 0.15 | 0.2 | 0.3 | 0.4 | 0.5 | 0.7 | 1 | 2 | 3 |
|---|---|---|---|---|---|---|---|---|---|---|---|
| **Al** (annealed, $\alpha = 40°$) | 82.28 | 90.62 | 129.88 | 121.86 | 60.87 | 92.74 | 73.97 | 77.54 | 53.45 | 34.44 | 28.05 |
| **Cu** (as-received, $\alpha = 40°$) | 176.50 | 191.97 | 187.42 | 138.06 | 117.01 | 104.31 | 104.95 | 102.08 | 111.14 | 105.25 | 74.50 |
| **Cu** (as-received, $\alpha = 15°$) | 99.14 | 99.82 | 83.97 | 114.74 | 149.67 | 141.34 | 174.79 | 166.67 | 157.14 | 170.31 | 129.85 |

Table 5.2. $\gamma$ (mJ/m$^2$), $\beta$, and $\tau_F$ (MPa) values predicted by the model. $\tau_F$ for aluminum-glass and copper-glass contacts are experimental measurements.

| Material | Tool | Rake angle | $\gamma$ (mJ/m$^2$) | $\beta$ | $\tau_F$ (MPa) |
|---|---|---|---|---|---|
| Al | glass | 40 | 5753 | 7.84 | 70 |
| Al | diamond | 40 | 132 | 5.43 | 74 |
| Cu | glass | 40 | 2082 | 6.51 | 128 |
| Cu | diamond | 40 | 98 | 9.36 | 215 |

# 6. DIRECT MEASUREMENT OF THE TOOL-CHIP CONTACT ADHESIVE FORCE

This chapter describes a novel experimental approach to directly measure and quantify the magnitude of adhesion at the tool-chip contact in small scale cutting of metals. The existence of adhesive forces at the tool-chip contact is demonstrated for the first time by measuring the tensile "pull-off" force needed to break the tool-chip contact. A systematic investigation is carried out to understand the dependence of the pull-off force on depth of cut, tool-chip boundary contamination, rake angle, and different tool-material combinations. In addition to the experimental study, a thin film peeling model is presented to describe the mechanics of tool-chip contact disengagement process. The model not only captures the experimental observations but can be also used to estimate the work of adhesion from the measured pull-off force. The work of adhesion values inferred using this method are shown to be consistent with our previous results. Besides providing direct experimental evidence for adhesion at the tool-chip contact in cutting, the study also opens an interesting possibility to utilize cutting chip formation as an experimental means to quantify contact adhesion between different materials in the absence of surface roughness effects.

## 6.1 Motivation

In the previous chapter (Chapter 5), a hypothesis has been put forward that intermolecular attraction forces (i.e., adhesion) acting at the tool-chip interface are responsible for the anomalous non-linear scaling between the depth of cut and tool-chip contact area under small cutting depths. A simple analytical model for the tool-chip plastic sliding interface incorporating adhesion was developed to capture this non-linear dependence and successfully predict other unique experimental observations at the small scale, namely, tool-chip sliding under effectively negative normal forces and the existence of a finite contact size between tool and the chip at zero normal loads. An interesting observation from the model is the very large work of adhesion ($\gamma$) for the tool-chip interface order of a few thousand mJ/m$^2$, especially in the case of cutting of aluminum with clean glass tools. Model estimates of the adhesive force magnitude suggest that at small cutting depths ($\leq$ 500 nm), adhesive forces become comparable to the bulk deformation forces and begin to influence the overall mechanics.

While the model provides an accurate description of the tool-chip contact mechanics at small

scales, including how the contact behavior is altered in the presence of surface contamination, its application to quantify the adhesive force at the tool-chip interface requires information about the work of adhesion and local geometry (chip curl radius) of the contact. In this regard, a direct experimental means for characterizing the adhesive force and its dependence on the cutting process conditions and tool/workpiece combination will be useful since this information is critical to understanding the mechanics of cutting at small scales, in addition to regular cutting force and thrust force data.

The objective of this chapter is to systematically characterize the tool-chip adhesive force and how it is influenced by material factors as well as the contact conditions. A new experimental approach to directly characterize the adhesive force by measuring the force profiles during the chip disengagement from the cutting tool is presented. This is based on first establishing an intimate contact between tool and the chip via steady-state chip formation, followed by controlled unloading and pull-off of the chip away from the tool so as to break the contact junction. The measured forces were found to clearly delineate the finite tensile "pull-off" force that is needed to break the tool-chip contact. A series of experiments is also conducted to systematically investigate the pull-off force and general force characteristics during the pull-off stage across various cutting configurations (tool-material combination, boundary condition, rake angle and depth of cut). Based on experimental observations, a thin film peeling model is develop to quantitatively describe the tool-chip detachment process and calculate the work of adhesion from the measured pull-off force. The work of adhesion values obtained using this approach are shown to be quite consistent with those predicted earlier in Chapter 5. Lastly, we also briefly discuss the possible application of chip formation by cutting as a tool for characterization of adhesion between various materials.

## 6.2 Experimental

The instrumented ultramicrotome described in Chapter 3 was used to measure the adhesive force at the tool-chip contact. This measurement involved two steps: establishing a clean contact between the tool and the chip, followed by measurment of the "pull-off" force that required to break the contact. The first step of establishing an intimate contact between the chip and the tool rake is done by engaging the workpiece with the tool, as in a regular cutting experiment (Fig. 6.1(a)). In this step, the swing arm (on which the workpiece is fixed) traverses against the

cutting tool edge until chip formation process reaches a steady-state characterized by constant chip thickness and cutting/thrust forces. It should be noted that, during this process, the tool rake face is continuously cleaned up as a result of chip flowing over it, resulting in a contact interface that is free of contaminants or oxide layers. The subsequent step of the experiment involves gently disengaging the workpiece from the cutting tool by moving it in the direction opposite to the cutting direction, so as to break the tool-chip contact and measuring the force profiles during the tool-chip contact disengagement process (Fig. 6.1(b)). In the present study, both the engagement (step 1) and disengagement (step 2) steps of the experiments were carried out by manual control of the microtome's swing arm. The workpiece speed during both the steps were maintained to be close to 1 mm/s.

As described in Chapter 3, two sensors are mounted perpendicularly (one under the cutting tool and another behind the workpiece) to measure the forces during both the regular cutting period as well as the tool-chip detachment period. In particular, this arrangement enables measurement of forces in two orthogonal directions ($F_c$ and $F_t$, see Fig. 6.1(a)) acting on the workpiece. The adhesion effect at the tool-chip contact is expected to manifest as a finite pull-off force (or negative $F_c$) during the tool-chip disengagement step. In the present study, experiments were carried out to characterize the pull-off force as a function of tool-chip material combination, initial cutting depth, rake angle, and in the presence of surface contamination. The cutting tools used were glass knives ($\alpha = 40^\circ$ and $15^\circ$) and diamond knife ($\alpha = 40^\circ$), with initial depth of cut in the range of 100 nm to 3 $\mu$m and 30 nm to 1 $\mu$m, respectively for glass and diamond tools. The material systems studied in this chapter are: polycrystalline OFHC copper in as-received condition (obtained from McMaster-Carr) and polycrystalline 1100 aluminum in annealed condition (annealed at 350 °C for one hour), see Table 3.1. The surface contamination effects on the pull-off forces are explored using glass knives coated using permanent marking ink and vegetable oil.

## 6.3 Results

### 6.3.1 Pull-off experiments with glass

The typical force traces obtained from pull-off experiments with aluminum and glass knife ($\alpha = 40^\circ$) at three different depths of cut are shown in Fig. 6.2. Note that the forces ($F_c$ and $F_t$) shown here correspond to forces acting on the workpiece/chip in two orthogonal directions.

Positive $F_c$ is aligned in the direction opposite to the original cutting velocity, whereas positive $F_t$ is aligned normal to the machined surface into the workpiece (see Fig. 6.1). During the cutting period (step 1), $F_c$ and $F_t$ initially increase as the workpiece engages with the cutting edge, and reach a steady-state in a relatively short period ($\sim$ 0.3 s). This is consistent with the regular cutting experiment and suggests steady-state chip formation. However during the pull-off period (step 2, starting at $t$ = 1.6 s in Fig. 6.2(a)), it was observed that both $F_c$ and $F_t$ do not drop down to zero immediately (as one would expect), but reach another steady-state for a short period (of $\sim$ 0.15 s), where the two force traces remain roughly constant again before dropping back to zero. For example, during the pull-off period, $F_c$ can be seen to be characterized by a negative value, meaning that a finite tensile force is actually needed to disengage the chip from the tool. This tensile pull-off force is denoted by $P_c$ in Figs. 6.2(a) - (c). Moreover, the fact that the forces remain roughly constant during the pull-off period demonstrates that the separation between chip and tool does not happen instantly, but occurs incrementally via a steady-state process.

Interestingly, experiments also demonstrate that the pull-off force $P_c$ is independent of the depth of cut. For example, from Figs. 6.2(a), (b), and (c), it can be seen that $P_c$ is $\sim$ -0.05 N/mm at all the three depths of cut of 100 nm, 500 nm, and 2 $\mu$m. This constant $P_c$ despite order of magnitude difference in the depth of cut is remarkable. Given that the applied normal load (perpendicular to the rake face) and the contact length during the regular cutting period are quite different for different depths of cut (see Tables 4.4 and 4.3), it appears that $P_c$ is relatively insensitive to the normal load under which tool-chip contact was established, initial tool-chip contact length before the pull-off, as well as the chip thickness or initial depth of cut. A summary of the pull-off force measurements for the clean aluminum-glass contact ($\alpha = 40^\circ$) at different depths of cut (100 nm to 3 $\mu$m) is given in Table 6.1. As noted earlier $P_c$ is the pull-off force, whereas $P_t$ is the steady-state force in the horizontal (thrust) direction captured by the sensors during the detachment period. It can be seen is caused by the elastic relaxation of the workpiece upon reversal of the loading direction. A few SEM observations of the chip underside and tool rake face have been also carried out to investigate whether any material transfer (from chip to tool) had occurred during the pull-off period. No trace of material transfer could be found.

To investigate the effect of surface contamination on the pull-off force, experiments were conducted with glass knives ($\alpha = 40^\circ$) coated with the permanent marking ink and oil. The cor-

responding force traces obtained with aluminum are shown in Fig. 6.3, with more detailed data provided in Table 6.1. It can be seen from Fig. 6.3 that the tensile pull-off force is observed even in the presence of surface contamination. However, in the presence of marking ink, $P_c$ is about 0.02 N/mm, which represents $> 60\%$ reduction in the pull-off force when compared to the clean aluminum-glass contact at the same depth of cut ($t_0$ = 1 $\mu$m). In contrast, the reduction in the pull-off force with oil boundary lubricant is marginal, if not insignificant. These observations are consistent with the fact that adhesion is greatly altered (reduced) by introduction of surface contamination. Another interesting observation from experiments with surface contaminants is the absence of pull-off force at a larger cutting depth of $t_0$ = 3 $\mu$m. This phenomenon – appearance of adhesion effects at small cutting depths but their (apparent) absence at larger depths – is analogous to why adhesion is typically not observed for macroscale contacts. At higher depth of cut, when load is reversed, the elastic stresses within the chip are released and the resulting displacement may be large enough to immediately break the tool-chip contact.

When compared to how surface contamination affects the pull-off forces, the effect of tool rake angle appears to be far more intricate. For instance, from Table 6.3, it can be seen that the $P_c$ in the case of clean aluminum-glass contact at $\alpha = 15^\circ$ is not only higher than the corresponding pull-off force magnitude at $\alpha = 40^\circ$, but also shows a monotonic dependence on the cutting depth. $P_c$ in this case ($\alpha = 15^\circ$) increases by about 4 times as $t_0$ is increased from 100 nm to 3 $\mu$m.

A similar trend is also observed in our pull-off experiments with copper and glass tools (data shown in Table 6.1). Fig. 6.4 shows the force traces obtained from the pull-off experiment with copper using a clean glass knife of $\alpha = 40^\circ$, where virtually no pull-off force could be detected. In this case, during the pull-off period, both $F_c$ and $F_t$ drop sharply to zero without any sign of the steady-state forces that were observed in experiments with aluminum. The absence of pull-off force (i.e., $P_c$ = 0) was found to be consistent across all the cutting depths ($t_0$ from 100 nm to 3 $\mu$m) at $\alpha = 40^\circ$ (Table 6.1). However, the behavior with the smaller rake angle tool ($\alpha = 15^\circ$) is quite different, where a finite tensile pull-off force is seen, which also increases from 0.086 N/mm to 0.67 N/mm as the cutting depth is increased from 100 nm to 3 $\mu$m. Although the absence or reduction of the pull-off force in experiments with copper at $\alpha = 40^\circ$ can be rationalized in terms of lower adhesion associated with the copper-glass contact (when compared to aluminum-glass contact), it appearance at the smaller rake angles cannot be explained at the present time.

### 6.3.2 Experiments with diamond

That the pull-off force is quite sensitive to the tool-chip material combination is brought out quite clearly in our experiments with the diamond knife. Fig. 6.5 shows the force traces obtained from the pull-off experiments using diamond knife with aluminum and copper. In both the cases, no pull-off force could be observed, with both $F_c$ and $F_t$ dropping to zero immediately after the reversal of workpiece direction. Additional experiments showed that $P_c \approx 0$ in the case of metal-diamond contact across all the cutting depths in the range of 30 nm to 1 $\mu$m. This observation is consistent with the smaller work of adhesion ($\gamma$) for the metal-diamond contacts when compared to metal-glass contacts. Equally importantly, this also suggests that the pull-off force observed in experiments with the glass tool is not an experimental artifact but is directly correlated with the tool-chip adhesion.

The measurements of pull-off forces under various conditions are generally consistent with the picture of adhesion presented in the previous chapters. For example, the factors that results in reduction of $P_c$ such as tool-chip surface contamination and metal-diamond combination are exactly those conditions characterized by more linear trend between the friction force and cutting depth, smaller work of adhesion, and the overall size effect. This suggests that the pull-off force that is needed to break the tool-chip contact can be taken as a proxy for the adhesion level at this contact.

### 6.3.3 A model for the tool-chip detachment process

To explore quantitative relationship between the pull-off force $P_c$ and work of adhesion, we treat the detachment between the tool and chip to occur as shown in Fig. 6.6, where a thin adhesive film (chip) is gradually peeled away from a rigid flat surface (cutting tool). This model for tool-chip detachment process is primarily based on the experimental observation that the tool-chip contact detachment does not happen instantly but occur incrementally in a steady-state-like manner. Fig. 6.6(a) shows the initial geometry of the chip before the pull-off period, where $L_0$ is the initial tool-chip contact length and angle $\theta$ represents the relative angle between the chip and the tool rake face outside the contact area. Upon retraction of the workpiece in the direction opposite to the original cutting direction, the tool-chip detachment and incremental reduction in the contact length is treated to occur such that the geometry of the peeling zone ($OA$, Fig. 6.6(b)) is always

preserved. In other words, $\theta$ remains constant and the final geometry of the chip at the end of the peeling process when it is fully detached from the tool is as shown in Fig. 6.6(c). This chip thickness is assumed to remain constant during the detachment process. Under this configuration, when the end of the chip is elevated by a distance of $dh$ under the action of a constant pull-off force $P_c$, the length of the exposed tool face or equivalent reduction in the contact length, $dL$, is given by $dL = dh/[\sin\alpha - \sin(\alpha - \theta)]$, where $\alpha$ is the tool rake angle.

Conservation of energy during the pull-off then leads to:

$$dW_t = dW_a + dW_p, \tag{6.1}$$

where $dW_t$ is the total work done on the workpiece/chip when moving it by a distance of $dh$, $dW_a$ is the work associated with tool-chip adhesion (i.e., in reducing the tool-chip contact length by $dL$), and $dW_p$ is the plastic energy term due to local plastic deformation of the chip in the vicimity of the peeling zone ($OA$, Fig. 6.6(b)).

Since the length of the swing arm ($R_s \sim 30$ cm) on which workpiece is mounted is at least four orders of magnitude larger compared to the tool-chip contact length ($< 30$ $\mu$m), $P_c$ can be treated as a point load. The total external energy can be therefore given in terms of the torque ($P_c w R_s$*) that rotates the swing arm by a small angle ($dh/R_s$) that corresponds to the chip vertical distance $dh$. The external work is therefore:

$$dW_t = (P_c w R_s)(\frac{dh}{R_s}) = P_c w dh \tag{6.2}$$

The adhesion term $dW_a$ as before is given in terms of work of adhesion for the contact $\gamma$ and change in the tool-chip contact area ($wdL$) as:

$$dW_a = \gamma w dL = \frac{\gamma w}{\sin\alpha - \sin(\alpha - \theta)} dh \tag{6.3}$$

Lastly, the plastic term $dW_p$ is calculated by assuming plastic deformation is accommodated by simple shear (analogous to that in the cutting primary deformation zone). $dW_p$ can be therefore given in terms of the shear strain $\gamma_s$, shear flow stress of the material $\tau$ and volume of the plastic zone ($wt_0 dL$) as:

*Note that $P_c$ is the normalized pull-off force (with respect to width) given in N/mm

$$dW_p = \gamma_s \tau w t_0 dL \tag{6.4}$$

Before proceeding further, an order of magnitude analysis for the adhesion and plastic energy terms is appropriate. Taking aluminum-glass contact at $\alpha = 40^\circ$ and $t_0$ = 100 nm as an example, the adheison energy term per unit area ($wdL$) can be seen to be simply given by $\gamma$, which has been deduced to be about 6000 mJ/m$^2$ for the case of clear aluminum-glass contact. On the other hand, the equivalent plastic energy term ($\sim \gamma_s \tau t_0$) may be obtained by taking $\tau = \frac{HV}{3\sqrt{3}} \approx 56$ MPa for aluminum and $\theta$ to be $10^\circ$ (based on SEM observation of the chip geometry after the pull-off, see Fig. 6.7 for reference), which corresponds to $\gamma_s$ of 0.17. This results in an estimation for the plastic energy term of about 900 mJ/m$^2$, which is much smaller (at least by a factor of 5) when compared to the adhesion term. This suggests that at small cutting depths, the plastic term can be ignored and the energy balance equation can be expressed as:

$$P_c w dh = \gamma w \frac{1}{\sin\alpha - \sin(\alpha - \theta)} dh, \tag{6.5}$$

which results in an expression for $P_c$ in terms of $\gamma$ as:

$$P_c = \frac{\gamma}{\sin\alpha - \sin(\alpha - \theta)} \tag{6.6}$$

It can be seen that the expression predicts that the pull-off force $P_c$ scales proportionally with respect to the work of adhesion $\gamma$, without intrinsic dependence on the depth of cut or contact length. This is consistent with our general observations from the pull-off experiments, including the constant pull-off force across a range of depths of cut at $\alpha = 40^\circ$ and the reduced pull-off force magnitude in the presence of surface contamination (i.e., low $\gamma$). The above expression also enables estimation of $\gamma$ given the measurements of the pull-off forces and angle $\theta$.

The $\theta$ measurements for aluminum-glass contact under different boundary conditions and the corresponding work of adhesion $\gamma$ estimated from the model are given in Table 6.4. The pull-off force used in these calculations is the average $P_c$ value measured across $t_0$ from 100 nm to 3 $\mu$m. From the table, it can be seen that the estimated $\gamma$ value for aluminum-glass clean contact is around 6422 mJ/m$^2$, which is remarkably consistent with the $\gamma$ (5753 mJ/m$^2$) predicted by the sliding contact model in Chapter 5. This not only provides additional validation of the model, but

also demonstrates the possibility of using the proposed pull-off experiment framework to quantify adhesion ($\gamma$) between two contacting bodies. From Table 6.4, it is also seen that $\gamma$ is reduced by about 50% when the tool-chip contact is coated by a thin layer of permanent marking ink. Note that this is also consistent with the more linear dependence between the friction force $F_f$ and normal force $F_n$ observed under this condition (see Fig. 5.7, Chapter 5). However, it should be noted that the work of adhesion estimated from the model for aluminum-glass contact is higher than the values reported in the literature [113].

Note that the expression for the pull-off force in terms of $\gamma$ as given by Eq. 6.6 applies only under small cutting depths or chip thicknesses where the plastic deformation term ($dW_p$) can be ignored. However, when the chip thickness is $\geq$ 600 nm, the plastic deformation term becomes comparable to the adhesive term and therefore enters the energy balance equation (Eq. 6.1). Under these conditions, the pull-off force should be expected to increase with the cutting depth or chip thickness. Some supporting evidence for this dependence of $P_c$ on the cutting depth can be seen from clean aluminum/glass experiments at $\alpha = 40^\circ$ (Table 6.1), where $P_c$ is seen to increase with $t_0$ when $t_0 \geq 1$ $\mu$m. A similar scaling between $P_c$ and $t_0$ can be also seen from experiments carried out with $15^\circ$ rake angle glass tools (Table 6.3).

## 6.4 Discussion

The pull-off force measurements made using the instrumented ultramicrotome provide first-of-a-kind demonstration of adhesive forces at the tool-chip contact and how they are influenced by different contact conditions. Considering that adhesive forces govern the tool-chip contact size and friction dissipation at small cutting depths (see Chapter 5), our results suggest that accounting for adhesion is essential to fully understand the mechanics of cutting at small scale, including the size effect phenomenon. In this regard, the proposed pull-off method presents a convenient method to characterize adhesion for different tool-material combinations and in the presence of various types of surface contamination. It is interesting to also note that adhesion in metal cutting has been discussed in the past primarily in the context of 'seizure' which involves atomic bonding at the tool-chip interface [111]. While seizure perhaps represents an extreme case of adhesion, the present study clearly demonstrates the existence of adhesion effects even under very mild cutting conditions, e.g., $\alpha = 40^\circ$ and slow cutting speeds ($< 0.1$ mm/s) where temperature effects are

minimal.

The predictions from the thin film peeling model presented for the chip detachment process during the pull-off are largely in agreement with the experimental observations. For instance, the steady-state nature of the chip detachment process is accurately captured by the model, so is the reduction in the pull-off force magnitude in the presence of surface contamination (given that the work of adhesion $\gamma$ is expected to reduce in the presence of surface contamination when compared to a clean contact). Similarly, the model predicts that the pull-off force is independent of the tool-chip contact length and cutting depth, provided that the plastic dissipation during the pull-off is small which is satisfied at small cutting depths, $t_0 \leq 1$ $\mu$m. It is only at the higher cutting depths, plastic deformation term enters the model and under these conditions, the pull-off force is expected to increase with $t_0$. These predictions are in general agreement with the experiments.

The model reveals an additional and important insight about the relationship between the pull-off force magnitude and the fundamental property that governs contact adhesion, $\gamma$ (see Eq. 6.6). This suggests that the proposed chip pull-off method described here can be used as a more general experimental means to quantify the work of adhesion between two contacting bodies, including different material combinations (e.g., metal-ceramic, metal-metal, metal-polymer, metal-diamond, etc.). In this regard, a brief comparison with the other methods that are (have been) used to estimate the work of adhesion is appropriate.

Atomic force microscopy (AFM) is perhaps the most widely used method to estimate the work of adhesion [114, 115]. In this approach, a tip with a small radius of the order of a few nanometers is brought into controlled contact with a flat surface under a light load, followed by gradual retraction of the tip away from the surface. The force profiles measured during the loading and unloading periods are used to infer the work of adhesion between the AFM tip and workpiece surface. In particular, the work of adhesion is usually estimated using the classical JKR model [96] assuming that both the tip and the workpiece undergo pure elastic deformations (note that the pure elastic deformation assumption is in contrast to that assumed in our case). By treating the flat workpiece as a sphere with infinite large radius, the work of adhesion $\gamma$ is expressed as $\gamma = -\frac{2F_p}{3\pi R_t}$ [96], where $F_p$ is the maximum negative pull-off force measured during the unloading period and $R_t$ is the finite radius of the tip. For instance, using this method, the work of adhesion for the contact between aluminum and a Si-based AFM tip (Si, $Si_3N_4$) was reported to be in the

range of 200 – 1000 mJ/m$^2$ [86, 116], which is about one order of magnitude smaller compared to the work of adhesion obtained for clean aluminum-glass contact in the present study. The discrepancy between the two methods can be attributed to at least two factors. Firstly, the surfaces that form contact between the AFM tip and the workpiece are likely not representative of the bulk material because of the formation of surface layers when surfaces are exposed to environment, for example, due to oxidation. The contact adhesion that is estimated therefore applies to the surface layers and not the bulk materials that AFM tip and workpiece are primarily made of. Secondly, even though the surface roughness effects are minimized in AFM-based adhesion measurements because of the microscopic nature of the contact, they cannot be entirely eliminated, which means that the real contact area can be different from the apparent contact area that is estimated from the JKR or Hertzian model. As a result, an intrinsic limitation of AFM-based measurements is the uncertainty associated with AFM tip and sample surface preparation, which governs the roughness levels. In contrast, the tool-chip contact in cutting chip formation is not only pristine but is also free of surface roughness effects considering that the contact conditions at the tool-chip interface are such that the real contact area is equal to the apparent contact area [110, 117]. This perhaps explains why the work of adhesion estimated in our study is much larger than those reported from AFM-based measurements. More importantly, this also suggests a unique opportunity to study adhesion in the absence of roughness and surface layer effects using cutting chip formation.

In addition to adhesion measurements using the AFM apparatus where the deformations are primarily elastic, it is also worth recalling some early measurements on adhesion of metals that are subjected to large-strain plastic deformation at the contact. The pioneering work in this area should be attributed to Tabor and co-workers [118, 119, 120] who studied adhesion between ductile metals (e.g., indium, nickel and tungsten) by first plastically compressing them together against each other under different compression loads (from 0.5 $\mu$N to several hundred $\mu$N) and then recording the pull-off forces that are needed to separate the two metal surfaces as a function of the initially applied normal load. A characteristic observation that has emerged from these studies is that the captured pull-off force scales with the initial applied load. While this dependence is not perfectly linear, studies have shown that larger the applied load, larger the pull-off force required to fully separate the two metal surfaces for the same apparent contact area. The surface roughness and asperities on the metal surfaces is argued to be the primary cause for this phenomenon. More

specifically, higher the applied load, larger will be the true contact area (i.e., the sum of individual contact areas supported by plastically deformed asperities), and thus the larger pull-off force during the contact separation. Although these studies provide a remarkable demonstration of adhesion effect in the case of mesoscale plastic contacts, they are still qualitative and cannot be used to quantify the work of adhesion $\gamma$ because of the lack of knowledge of the true contact area supporting the adhesive force.

When compared to AFM or the above method involving plastic compression of two metal surfaces, the proposed chip formation technique provides clear benefits from the standpoint of measuring adhesion. As noted earlier, the chip formation is a process that involves continuous generation of fresh metal surface and simultaneous plastic sliding of this metal surface against the cutting tool face under a large compressive force, during which there is a high likelihood of breaking any surface layers or oxides formed on the tool face. This ensures that the tool-chip interface is intrinsically clean and also characterized by an intimate contact. Moreover, under small cutting depths as demonstrated using the ultramicrotome technique (say, $t_0$ less than 1 $\mu$m), the elastic stored energy in the chip is sufficiently small to maintain steady-state peeling during the chip pull-off period. In other words, by keeping the deformed chip volume (equivalently, elastic stored energy) small, the 'snap-back' effect that is typically seen in mesoscale contacts [121] can be also overcome and the work of adhesion characterized using the proposed thin film peeling model (Eq. 6.6). The fact that the $\gamma$ values predicted using the chip pull-off method agree quite well with those independently inferred from the sliding contact model in Chapter 5 lends further support for using cutting as means for characterizing the work of adhesion. Moreover, when compared to the AFM-based approach, where the measurements are limited by the choice of the sample-tip combinations, cutting enables study of contact adhesion between diverse material systems, including metal-metal, metal-ceramic/glass/diamond and metal-polymer contacts. Lastly, $\gamma$ can be characterized over a range of different surface environments (lubricants, solid contaminants, etc.), which is highly challenging to achieve using other experimental methods.

## 6.5 Conclusion

The chip pull-off experiments carried out using the instrumented ultramicrotome platform have enables direct characterization of surface attraction adhesive forces at the tool-chip interface. The

adhesion effect is clearly manifested as a negative pull-off force during the tool-chip detachment process. The experiments have characterized the pull-off force for different tool-material combinations and contact conditions (both clean and in the presence of surface contaminants), and a good correlation is found between conditions characterized by a high pull-off force and tool-chip adhesion. The tool-chip disengagement process is modeled as that of a thin film being peeled away from a rigid flat, and a method is proposed for calculating the work of adhesion in terms of the measured pull-off force. The work of adhesion values derived from this method are shown to be quite consistent with our earlier predictions (Chapter 5). The study highlights an opportunity to use tool-chip contact in cutting as a novel means for exploring friction and adhesion phenomena under contact conditions that are hard to replicate using conventional methods.

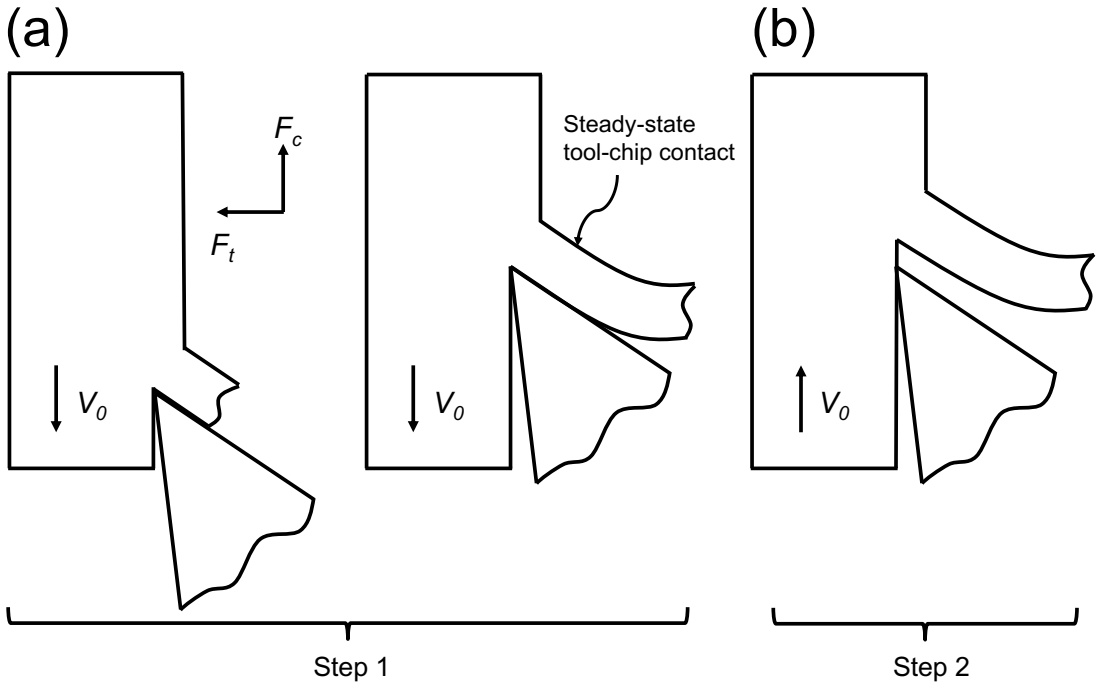


Figure 6.1. Schematic showing the pull-off force measurement: (a) step 1 where an intimate tool-chip contact is established via steady-state chip formation, and (b) step 2 where tool-chip contact is released by pulling the workpiece in the opposite direction. $F_c$ and $F_t$ are the orthogonal forces acting on the workpiece/chip.

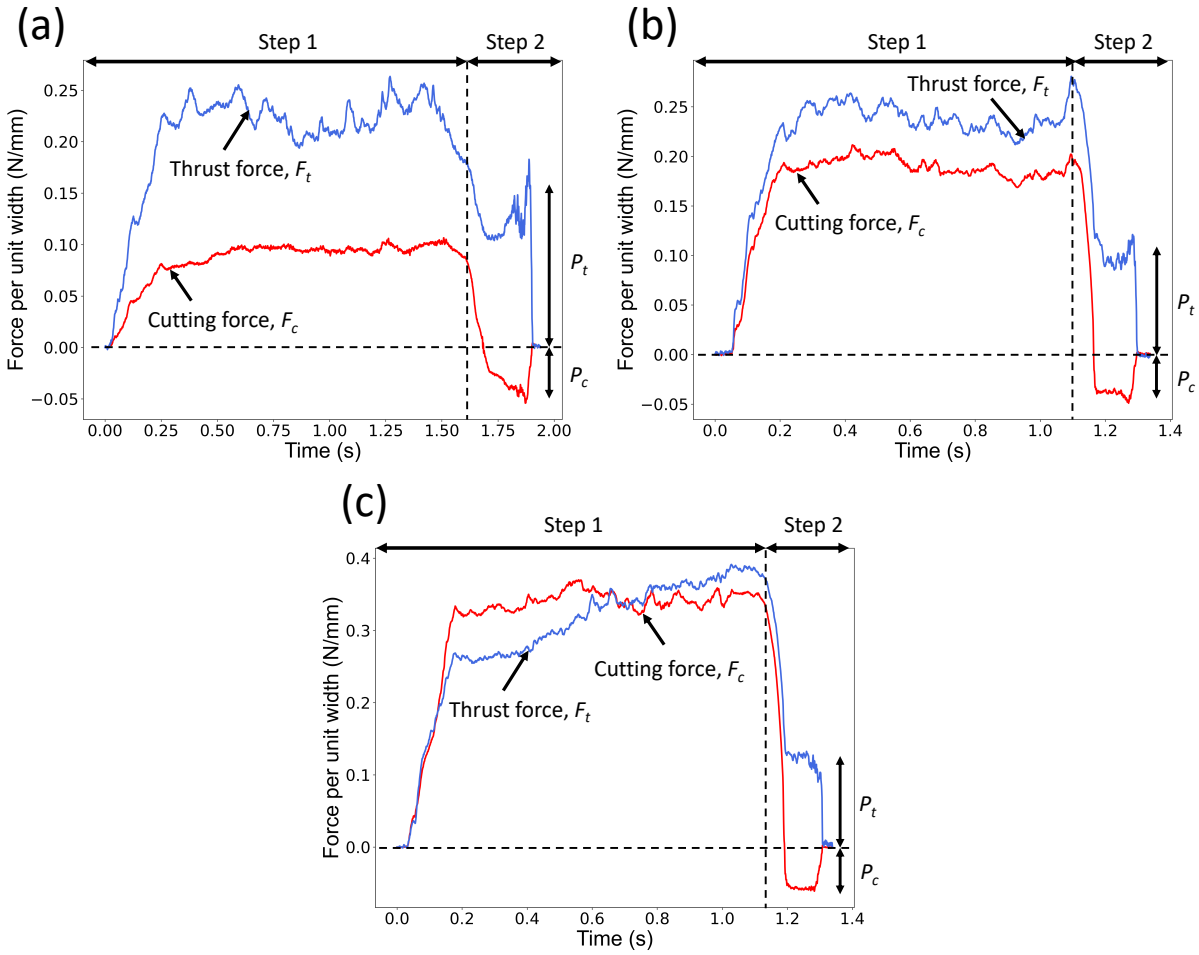


Figure 6.2. Force traces during the pull-off experiments with aluminum and glass tool ($\alpha = 40°$) at: (a) $t_0$ = 100 nm, (b) $t_0$ = 500 nm, and (c) $t_0$ = 2 $\mu$m. Step 1 is the cutting period corresponding to steady-state chip formation, and step 2 is the pull-off period. Reversal of $F_c$ to a negative value during the tool-chip detachment period is evident.

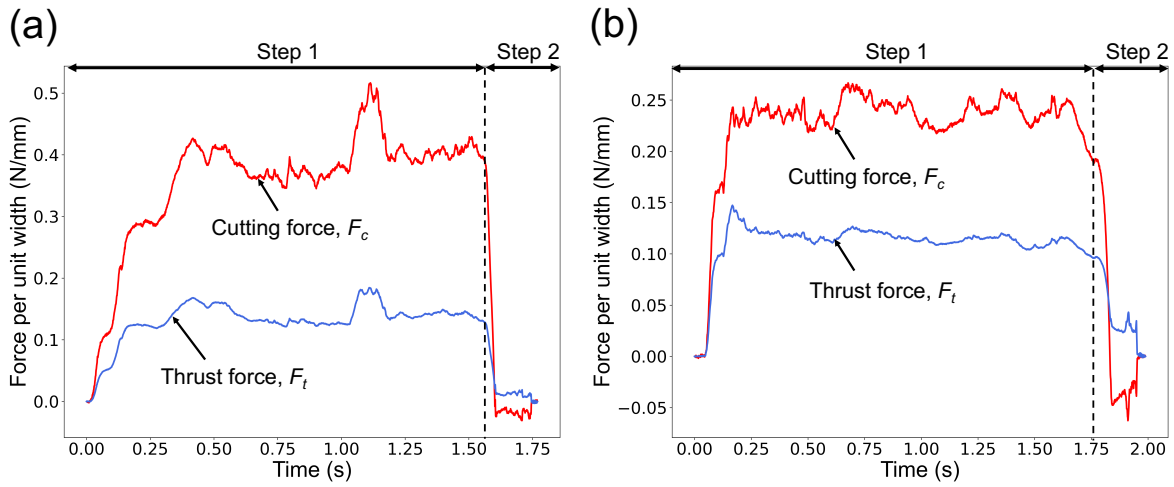


Figure 6.3. Force traces during the pull-off experiments with tool-chip surface contamination: (a) marking ink and (b) oil. Workpiece material: aluminum, tool: glass knife, $\alpha = 40°$, $t_0$ = 1 $\mu$m.

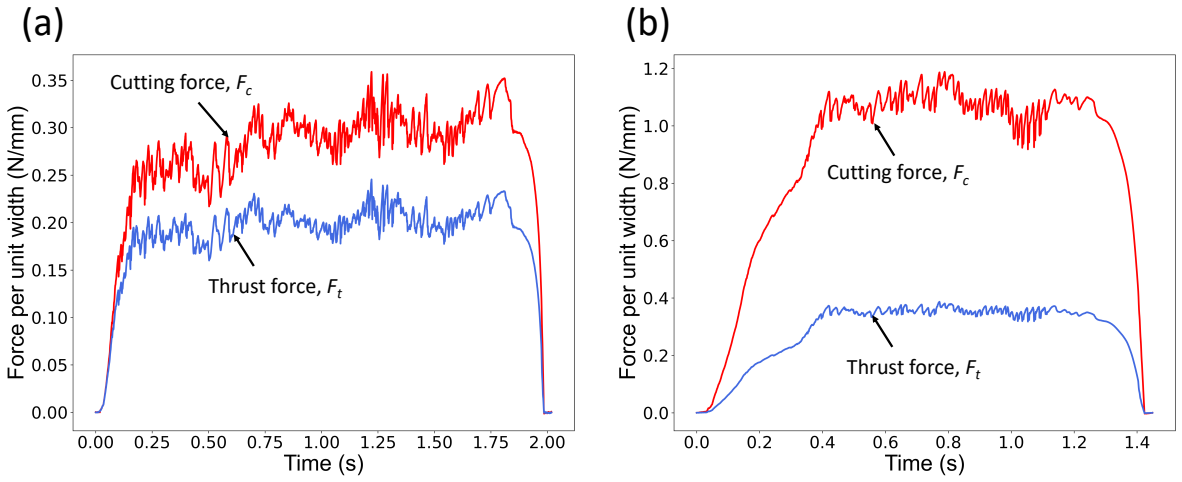


Figure 6.4. Force traces during the pull-off experiments with copper and glass tool ($\alpha = 40°$) at: (a) $t_0$ = 100 nm and (b) $t_0$ = 2 $\mu$m. No obvious pull-off force can be seen in both the cases.

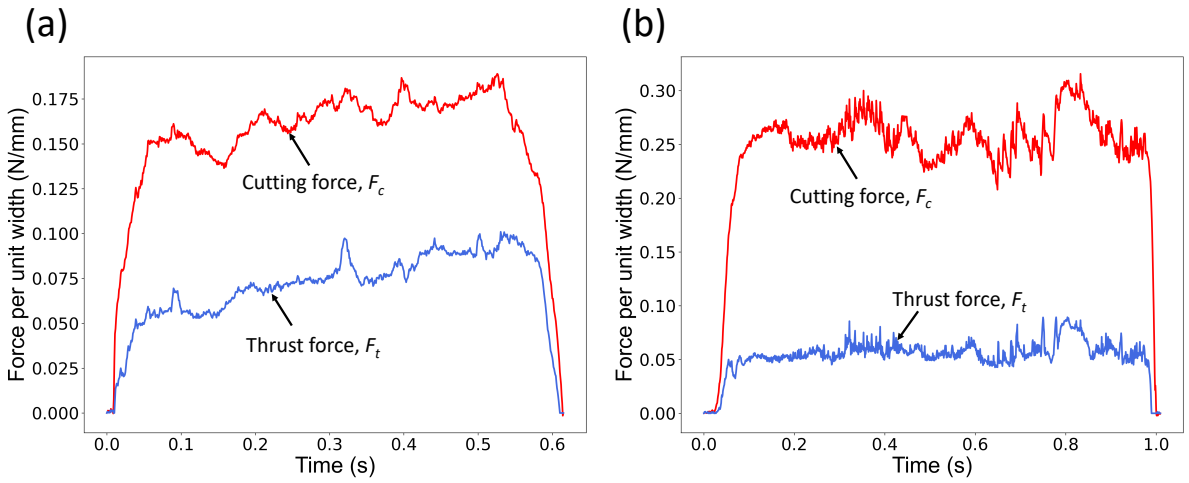


Figure 6.5. Force traces obtained from the pull-off experiments with the diamond knife ($\alpha = 40°$) at $t_0$ = 500 nm: (a) aluminum and (b) copper.

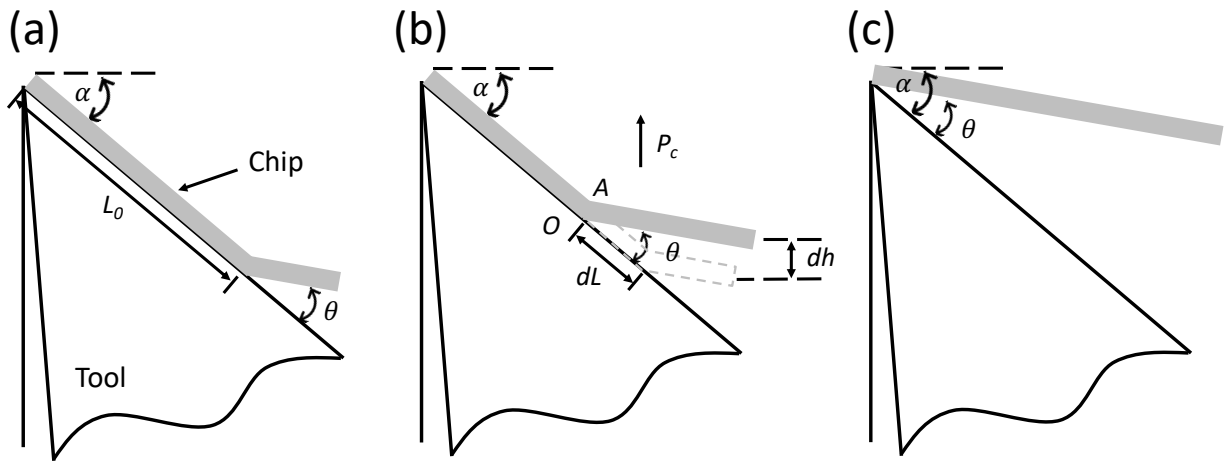


Figure 6.6. Schematic of the tool-chip detachment process in a pull-off experiment. (a) Initial state of the chip where the chip makes an angle $\theta$ with respect to the rake face outside the contact, (b) incremental decrease of the contact length during the pull-off period, and (c) final state of the chip when it is fulling detached from the tool face.

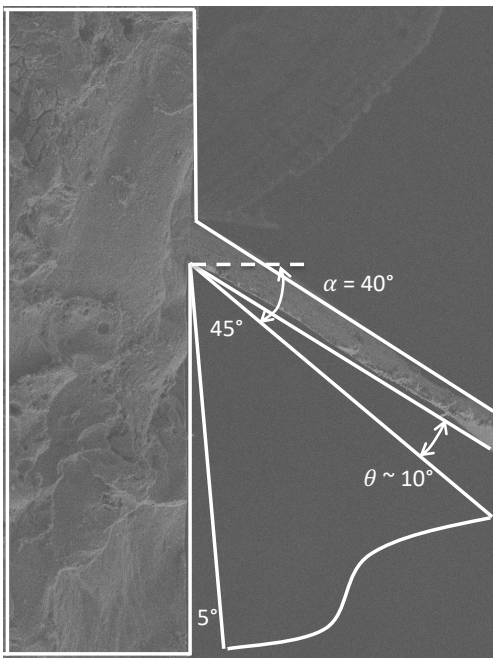


Figure 6.7. SEM image showing the final chip geometry after the pull-off experiment with aluminum and glass knife ($\alpha = 40°$, 1 $\mu$m).

Table 6.1. Pull-off force measurements with glass tool ($\alpha = 40°$) with different materials (Al and Cu) under different contact boundary conditions and cutting depths ($t_0$). $P_c$ is the pull-off force (negative value represents the tensile force) whereas $P_t$ is the average thrust force during the pull-off period.

| Material: Aluminum, Glass tool ($\alpha = 40°$) | | | |
|---|---|---|---|
| | $t_0$ ($\mu$m) | $P_c$ (N/mm) | $P_t$ (N/mm) |
| Clean contact | 0.1 | -0.035 | 0.118 |
| | 0.2 | -0.037 | 0.098 |
| | 0.3 | -0.042 | 0.108 |
| | 0.4 | -0.039 | 0.095 |
| | 0.5 | -0.039 | 0.100 |
| | 0.7 | -0.045 | 0.102 |
| | 1 | -0.055 | 0.119 |
| | 2 | -0.057 | 0.123 |
| | 3 | -0.064 | 0.135 |
| Contact coated with marker ink | 0.1 | -0.021 | 0.031 |
| | 0.5 | -0.034 | 0.023 |
| | 1 | -0.018 | 0.012 |
| | 3 | 0 | 0 |
| Contact coated with oil | 0.1 | -0.065 | 0.055 |
| | 0.5 | -0.029 | 0.020 |
| | 1 | -0.039 | 0.028 |
| | 3 | 0 | 0 |
| Material: Copper, Glass tool ($\alpha = 40°$) | | | |
| | $t_0$ ($\mu$m) | $P_c$ (N/mm) | $P_t$ (N/mm) |
| Clean contact | 0.1 – 3 | 0 | 0 |

Table 6.2. Pull-off force measurements with diamond tool ($\alpha = 40°$) with aluminum and copper across different $t_0$. No surface contamination was introduced in these measurements.

| Diamond knife ($\alpha = 40°$) | $t_0$ | $P_c$ (N/mm) | $P_t$ (N/mm) |
|---|---|---|---|
| Aluminum | 30 nm – 1 $\mu$m | 0 | 0 |
| Copper | 30 nm – 1 $\mu$m | 0 | 0 |

Table 6.3. Pull-off force measurements with a smaller rake angle glass tool ($\alpha = 15°$) with aluminum and copper in the absence of any surface contamination. Note the increase in pull-off force with the cutting depth.

| Glass tool ($\alpha = 15°$) | $t_0$ ($\mu$m) | $P_c$ (N/mm) | $P_t$ (N/mm) |
|---|---|---|---|
| Aluminum | 0.1 | -0.049 | 0.150 |
| | 0.5 | -0.075 | 0.290 |
| | 1 | -0.124 | 0.410 |
| | 3 | -0.185 | 0.480 |
| Copper | 0.1 | -0.086 | 0.091 |
| | 0.5 | -0.236 | 0.328 |
| | 1 | -0.380 | 0.634 |
| | 3 | -0.670 | 0.914 |

Table 6.4. Estimated work of adhesion ($\gamma$) in pull-off experiments with aluminum and glass knife ($\alpha = 40°$).

| Contact condition | $P_c$ (N/mm) | $\theta$ | $\gamma$ (mJ/m$^2$) |
|---|---|---|---|
| Clean | 0.0459 | 9.81° | 6422 |
| Marking ink | 0.0183 | 11.33° | 2975 |
| Oil | 0.0333 | 13.89° | 6739 |

# 7. ON THE MECHANICS OF SURFACE INSTABILITIES IN CUTTING AT SMALL SCALES

This chapter focuses on the origin of the surface instability that results in the formation of periodic folds on the chip free surface during the cutting of soft ductile metals. We start with a review of this phenomenon and possible mechanisms that have been proposed to explain fold formation. The surface instability is then systematically revisited via the ultramicrotomy platform, complemented by electron microscopy and AFM characterization of the chip free surface morphology across different cutting depths. A recently proposed plastic buckling mechanism is shown to accurately model the evolution of the surface folds and analytically describe the scaling behavior of the fold spacing with respect to the cutting depth. This work shows that the evolution of the chip surface morphology at small scales is driven by a purely mechanical mechanism and a continuum-level buckling mechanism, in direct contrast to previously proposed microscopic or thermal based mechanisms.

## 7.1 Introduction

Metal cutting is a plastic deformation process where a thin layer of material is removed in the form of chip from the workpiece, accompanied by the large shear strain and shear strain rate. Compared with some other deformation processes (extrusion, rolling, drawing, etc), the deformation zone geometry in metal cutting is not defined *a priori*, because of the existence of a free surface during the chip formation. The consequences of this unconfined plastic flow are the multiple chip formation mechanisms and the near surface instabilities. While the chip itself is considered as the by-product of the manufacturing process, its formation mechanics critically determines the nature of forces on the cutting tool, energy consumption, heat generation, and integrity of the finished surface. This provides motivations to study and understand how different chip morphologies arise and explore the fundamental mechanism of the plastic flow during the chip removal process.

For regular metal cutting at the deformation sizes from tens to hundreds of $\mu$m, the chip formation mechanisms have been systematically explored by Nakayama [54], where the formation modes of the chips are classified into types. The recent advances in *in situ* observations using high-speed imaging and digital image correlation techniques (e.g., particle image velocimetry)

have also provided more direct observations of the plastic flow dynamics underlying different chip formation mechanisms. However, for the cutting experiments conducted at a smaller scale (sub-$\mu$m to nm), a direct study of the plastic flow is still lacking, with most of the studies relying on *ex situ* observations of the formed chips.

The ultramicrotomy technique (coupled with sharp diamond/glass tools) has been extensively used by the researchers to generate very thin metal chips at sub-$\mu$m to nanometer scales [21, 22, 23, 24, 63, 64]. Ultramicrotomy experiments have been conducted with various polycrystalline (Cu, Al, Ag, Te, stainless steel, Ag-Sn alloy, Cu-Ge alloy, etc.) and single crystal (Cu, Al, Ag) materials, with an undeformed chip thickness varying from 50 nm to more than 10 $\mu$m. The morphology (free surface, cross-section) of the microtomed chips were primarily investigated using electron microscopy techniques (SEM, TEM), based on which possible chip formation mechanisms have been hypothesized.

The first and most noteworthy observation of metal chips at sub-$\mu$m to nanometer cutting scale is the highly heterogeneous plastic flow, manifested as the periodic folded patterns on the free surface of the sectioned chips distributed along the direction perpendicular to the cutting velocity [21, 22]. The rounded fold features exhibit striking similarities with the Type 1 chip described in Chapter 2, while being substantially different from the Type 3 and Type 4 chips that demonstrate serrated-like patterns at the free surface. This phenomenon seems to be universal across a variety of material systems. This phenomenon was also shown by Black and Ramalingam [21, 23] to be self-similar, where the folds bear similar resemblance across different cutting depths. Black and Ramalingam also identified that the formation of the patterns can be very sensitive to the tool rake angle and the tiny defects on the cutting edge.

Since the discovery of this phenomenon, various theories have been proposed based on the microscopy observations aiming to explain the formation mechanism of the chip at small scales and the cause for these surface instabilities. The initial explanation given by Phillips [22] was that the surface folds arise because of the resistance to smooth chip flow across the rake face due to the friction at the tool-chip contact. Phillips also concluded that the surface fold characteristics highly depend on the cutting edge quality (sharpness, defects, etc.), rake angle, boundary condition at the tool-chip contact, deformation size, as well as the material being cut. It was also reported that the surface instabilities can be mitigated by reducing tool-chip contact friction, either by using

lubricant or a more positive rake angle. In contrast to Phillips, Black and Ramalingam [21, 23] approached the problem from a standpoint similar to what has been proposed for Type 4 (shear localized) chip, and modeled the formation of the surface instability as a consequence of thermally assisted mechanism. In this theory, the heat generated ahead of the tool is said to result in shear bands and localized slipping within the bands. The repeated occurrence of shear banding then leads to the formation of the periodic surface structures. The electron micrographs showed the existence of the slip lines and partially justified their hypothesis. In another viewpoint, the formation of the folds is governed by the atomic-level imperfections (dislocations) generated during the machining process [24] and their partial rearrangement after the continuous shear. This theory claims that the instability formation relies on the rich dislocations in machining, which are generated around the cutting tool edge and the entire region affected by the high shear stress. Given that the lower part of the chip (that is in contact with rake face) experiencing a compressive stress is likely to have considerably larger strength than the surface region, it is argued that the chip will attempt to relieve the stresses plastically towards the surface, resulting in a rearrangement of the dislocations activated in the primary shear zone [63]. The crystalline plane originating from the tool edge towards the free surface and the plane confined by the local crystal orientations were believed to be potential slip directions for the single and polycrystalline systems, respectively [24].

While these theories partially explain the formation of the surface instabilities in small scale metal cutting, they fail to explain several key experimental observations in a self-consistent manner. For example, the size of the instability features (folds) is very sensitive to the defects of the cutting edge, which cannot be explained by the adiabatic shear theory. Moreover, the fact that folds are observed in experiments conducted at low cutting speeds ($< 0.05$ mm/s) and large positive rake angle ($\alpha > 40^{\circ}$), where thermal effects should be negligible, casts doubt on the adiabatic shear theory. Lastly, the fact that the surface folds can traverse a long distance along the cutting width direction, spanning across multiple grains, also is in contradiction with the microscopic theories established based on the rearrangement of the imperfections generated ahead of the tool during the primary shear. It should also be noted that such dislocation-level mechanisms are extremely difficult to verify without the direct observations.

While these past theories fail to explain the nature of this phenomenon, the recent studies [18, 19, 20, 61] highlighted the role of periodic plastic buckling in the Type 1 chip formation in

metal cutting with a deformation size more than 100 microns. Through the *in situ* observations using high-speed imaging and image correlation technique (PIV), the formation of the folds was concluded to begin with the initialization of small bump ahead of the tool edge, followed by the growth of the bump through the localization between two 'pinning points'. Finally, the bump rotates such that its orientation changes from horizontal to almost normal to the rake face.

The survey of the past literature on chip morphologies in small scale cutting of soft ductile metals suggests that this type of surface buckling mechanism leading to folded Type 1 chip may be widespread, and can occur across different length scales. This is because of the fact that the surface folds across different length scales bear remarkable similarity (showing rounded morphological surface features), which when further coupled with their observations in a wide range of material systems and across cutting speeds, provides strong support in favor of a continuum-level buckling instability mechanism for the instability formation that is devoid of any intrinsic microstructural length scales and temperature effects.

In this chapter, we revisit the surface instability in small scale metal cutting through the plastic buckling framework and seek to answer a two-fold question. Firstly, the plastic buckling theory [18, 20] emphasized how grain boundaries act as the pinning points for the initiation and development of a buckle (which eventually turns into a fold). A question we seek to answer is: are microstructural features such as grain boundaries a requirement to initiate folding in metals? For example, can similar surface folds form in single crystals? If so, what determines the distance between pinning points and the fold in the absence of microstructural effects? Secondly, considering that the fold morphology of ultramicrotomed chips and that of the Type 1 chip generated at a much larger deformation scale bear striking similarities, can we model the instability wavelength across different length scales using a unified framework? Can we model/predict the distinctive scaling behavior of fold wavelength with respect to cutting depth using this framework?

## 7.2 Experimental

In this study, the surface instability mechanism leading to fold formation at the chip free surface was studied using polycrystalline OFHC copper (as-received condition), polycrystalline 1100 Al (annealed condition) and Al single crystal as material systems. In the case of single crystal Al, cutting was conducted on the $\{\bar{1}10\}$ plane of the crystal, with the cutting direction aligned parallel

to the $< 001 >$ direction. The corresponding purities, grain sizes, and Vickers hardness values for these materials are reported in Table 3.1. The instrumented ultramicrotome described in Chapter 3 was used to generate chips under orthogonal and two-dimensional plane strain conditions over a range of cutting depths. The cutting speed was kept constant at 0.05 mm/s. The cutting tools used in this study were primarily made of glass knives ($\alpha = 40°$, $15°$, and $0°$), although a limited set of experiments were also carried out with diamond knife ($\alpha = 40°$) to explore the surface instability characteristics at cutting depths less than 100 nm.

The surface morphology of the chips produced using the microtomy technique were characterized using scanning electron microscopy (JEOL JSM-7500F) and atomic force microscopy (Bruker Dimension Icon). SEM was used to analyze the instability features in terms of fold distribution and spacing, while AFM provided the amplitude/shape information for the folds. The AFM measurements are performed under the conventional tapping mode with 25 to 100 $\mu$m$^2$ being the typical scanning area. The step size was chosen in the range of 10 nm to 40 nm, depending on the scanning area and the number of samples (data points). These techniques were complemented with bright-field transmission electron microscopy (JEOL JEM-2010) wherever possible. For example, the chips produced using the diamond knife at very small cutting depths of 20 to 50 nm were found to be thin enough (electron-transparent) to be directly imaged under a TEM 200 kV accelerating voltage without additional sample preparation. The greater magnification capability of the TEM provided a point resolution of 0.23 nm, making it suitable for characterization of very small features.

To directly visualize the fold-development process at the chip free surface, a set of experiments was also conducted with OFHC Cu (annealed at 1000 °C for 4 hours) at larger cutting depths in the range of 50 to 100 $\mu$m. These larger cutting depths enabled direct time-resolved observations of the chip formation process using high-speed imaging and quantitative analysis of the underlying plastic deformation field using an image correlation method. For these experiments, a two-dimensional plane strain cutting configuration as described in Refs. [122, 123, 4] was used. In this configuration, chip formation is effected by translating a rectangular plate sample (75 $\times$ 25 $\times$ 2 mm), mounted on a linear slide, at a controlled velocity $V_0$ against a stationary wedge-shaped cutting tool that is preset to result in an *a priori* specified engagement (cutting) depth, $t_0$. In our experiments, the tool was of ground high-speed steel with a sharp cutting-edge radius of about 5

$\mu$m, and $V_0$ was kept constant at 4.0 mm/s.

Plastic deformation of the material in the vicinity of the chip formation zone was observed *in situ* using a high-speed camera (pco dimax HS4) coupled with an optical microscope and a 10X objective lens. Any "side-flow" of the material during cutting (i.e., material displacement along to the chip width direction) was restricted by lightly constraining the workpiece/chip side surface using a transparent soda-lime glass piece and imaging the chip formation zone through the glass. This ensured plane strain condition at the side surface that is being imaged, and that the captured flow field is representative of the material flow through bulk of the chip. Images were captured at 2000 frames per second, which resulted in a temporal resolution of 0.5 ms. The spatial resolution of the imaging was 0.98 $\mu$m per pixel. Full-field displacement data was obtained by analyzing the images using an image correlation technique called Particle Image Velocimetry (PIV) [124, 125]. This displacement data was then used to analyze the deformation field and dynamics of fold development in terms of plastic strain, strain rate and streaklines. Details pertaining to PIV analysis and its application to analyze plasticity problems (including unsteady ones) can be found in Refs. [4, 61, 122, 123]. As with the microtomy experiments, the forces along and perpendicular to $V_0$ were measured concurrently with high-speed imaging. This was done using a 3-axis piezoelectric plate dynamometer (Kistler 9129AA, 3.5 kHz natural frequency) mounted directly underneath the cutting tool.

### 7.3 Results

In this section, the experimental results pertaining to chip surface morphology at different scales are presented. We start by re-visiting the chip free surface morphology in ultramicrotomy and highlight the universality of this phenomenon across different material systems. The scaling behavior of the instability features (fold spacing) is then explored and characterized as a function of depth of cut. With the aid of PIV analysis and direct observations of fold formation at large cutting depths, we establish a buckling-based framework over a wide range of cutting depths to model the fold formation and spacing. The model predictions are validated using the experimental data.

### 7.3.1 General characteristics of surface folds

Ultramicrotomy experiments with polycrystalline copper, polycrystalline aluminum, and single crystal aluminum (for properties, see Table 3.1) are conducted using the experimental setup described in Chapter 3. For single crystal aluminum, the cutting surface is parallel to the $\{\bar{1}10\}$ crystal plane. The scanning electron micrographs of the microtomed chips are shown in Fig. 7.1. In Figs. 7.1(a) – (f), the most representative free surface characteristic of the chip morphology is the highly heterogeneous plastic flow, manifested as the periodic folds on the free surface of the chip aligned perpendicular to the cutting direction. This feature was quite prevalent and found in the cutting with all the material systems studied in this work at different starting conditions and even a wide range of cutting scales (100 nm to 3 $\mu$m). These observations are quite consistent with those made by Black [21] and Phillips [22].

When cutting with polycrystalline metals, the folds are found to rarely traverse across the entire cutting width, which is likely due to the interference by the local grain structure. It is common to see a fold vanishing halfway along the cutting width direction or two/multiple small folds merging into a larger one (see arrows in Figs. 7.1(a) – (d)). In contrast, folds in single crystal aluminum ($\alpha = 40^\circ$) are much more uniform. Fig. 7.1(e) shows the single crystal aluminum chip with $t_0 = 3$ $\mu$m at low magnification, where most of the furrows are seen to traverse across the cutting width. With the grain structure effect eliminated, the folds are seen to be extremely uniform in size and distribution, as illustrated in Fig. 7.1(f). Therefore, grain structure is not a requirement for fold formation. Even in the case of polycrystalline materials, it should be noted that the fold size is about 1 $\mu$m or less, which is 1 to 2 orders of magnitudes smaller than the grain size (e.g., copper grain size $\sim 37$ $\mu$m). This again suggests that the formation of folds and fold spacing are relatively insensitive to the effects of the grain structure or grain boundary.

The surface instability features also demonstrate high self-similarity under different deformation sizes. Figs. 7.1(c) and (d) are the fold distributions in aluminum at two different depths of cut (500 nm and 2 $\mu$m). The fold morphologies are seen to be highly similar despite the different spacing of the folds. Fig. 7.2(b) shows the transmission electron micrograph (TEM) of a chip collected from a cutting experiment with polycrystalline aluminum using a diamond knife ($\alpha = 40^\circ$) at $t_0$ = 20 nm. The fact that similar fold distribution can be clearly seen even at a such small deformation

size suggests a continuum-level mechanism for fold formation that is insensitive to the material microstructure.

Interestingly, the fold spacing and distribution are also found to be very sensitive to small defects on the cutting edge. Fig. 7.2(a) shows a deep groove along the cutting direction caused by small defect on the cutting edge. The folds inside the groove are seen to be much more closely spaced and have having smaller amplitude compared to folds outside the groove.

Scanning electron micrographs although quite helpful for observing the fold morphology, fail to provide any information about the fold amplitude. Atomic force microscopy (AFM) was applied to extract the 3D profile of the chip free surface. Figs. 7.3(a) and (b) show the 3D surface maps and selected line scans of the microtomed aluminum chips ($\alpha = 40^\circ$) at two different depths of cut (100 nm and 1 $\mu$m). The 3D scans of the chips at two different depths of cut can be seen to be quite similar, except for fold spacing and amplitude. The fold amplitude of the chip produced at 1 $\mu$m depth of cut chip is substantially larger than the other one. The fold amplitude (as defined by the average distance between peaks and valleys) at 1 $\mu$m depth of cut is about three times that at 100 nm depth of cut. Similarly, the spacing of folds at $t_0$ = 1 $\mu$m is about twice as much as that at $t_0$ = 100 nm. This suggests non-linear scaling of fold spacing and amplitude with respect to the depth of cut. It should be noted that the amplitude obtained from this AFM surface mapping method underestimates the actual fold amplitude as will be shown later using PIV analysis.

### 7.3.2 Characterization of the fold spacing

SEM is primarily used to characterize the fold spacing in polycrystalline copper ($\alpha = 15^\circ$ and $0^\circ$) and single crystal aluminum ($\alpha = 40^\circ$) as a function of depth of cut. A detailed description of the image analysis procedure used to acquire the mean value and the statistical distribution of the spacing between two adjacent folds is given in Fig. 7.4. For this analysis, the SEM images are taken such that their brightness and contrast are well adjusted to clearly distinguish one fold from another across the vertical direction (Y-axis). Such image was then divided into several (usually 5) horizontal sections. For each section, the average grayscale values for the pixels having the same X-coordinate are calculated and plotted against the horizontal position (namely X-axis), as shown in Fig. 7.4(b). This enabled quantitative analysis of the fold spacing. For example, the number of folds in each section can be now easily obtained by counting the number of peaks, whereas

spacing is taken as the difference in the horizontal positions (in $\mu$m) of two adjacent peaks. It was found that roughly 100 fold spacing values can be extracted from a single image, and at least two good quality SEM images were used in our study for each cutting condition of fold spacing to better quantify the uncertainty and statistical distribution. As an example, Fig. 7.4(c) shows the histogram for the fold spacing in copper ($\alpha = 15^\circ$, $t_0 = 500$ nm), which can be considered as normally distributed. Similar histograms were obtained for each cutting condition, with the mean ($\mu$) and standard deviation ($\sigma$) of the fold spacing calculated, such that the range [$\mu$ - $\sigma$, $\mu$ + $\sigma$] covers roughly 2/3 of all the observations. For the histogram shown in Fig. 7.4(c) (copper, $\alpha = 15^\circ$, $t_0 = 500$ nm), a mean spacing of 285 nm and a standard deviation of 65 nm were obtained.

The mean and standard deviation values for the fold spacing for copper ($\alpha = 15^\circ$ and $\alpha = 0^\circ$) and single crystal aluminum ($\alpha = 40^\circ$) obtained using the above method are summarized in Fig. 7.5(a). Fig. 7.5(b) shows the corresponding results, presented in the normalized form (i.e., spacing/$t_0$ vs. $t_0$). It is quite clear that the dependence of spacing on the depth of cut is highly non-linear. For example in polycrystalline copper ($\alpha = 15^\circ$), increasing $t_0$ from 100 nm to 1 $\mu$m results in an increase in fold spacing by only a factor of 2 (from 200 to 400 nm). A similar trend can be also seen at $\alpha = 0^\circ$, and also for crystal aluminum ($\alpha = 40^\circ$).

This non-linear scaling of the fold spacing is qualitatively similar to the non-linear scaling of the cutting forces (i.e. size effect of specific energy) discussed in earlier chapters. The relation between the non-linear scaling of fold spacing and the size effect will be described later.

### 7.3.3 Dynamics of fold development

In Section 7.3.1, the general characteristics of the surface folds are summarized. The surface folds observed in metal cutting at small scales share remarkable similarities with the Type 1 Chip in cutting at more conventional length scales, in terms of both their wrinkled-type morphology and their occurrence only in soft ductile metals. The fact that ultramicrotomy experiments are conducted under very low cutting speeds also supports an instability mechanism that is not thermally driven. To explore a unified chip formation/instability mechanism across the ultramicrotomed chips and the regular Type 1 chips, cutting experiments were carried out with OFHC copper (annealed at 1000 °C for 4 hours) at cutting depths that are 2 – 3 orders higher than in ultramicrotomy.

These length scales ($t_0 \sim 50$ – $100$ $\mu$m) have also allowed us to directly observe the plastic flow dynamics in addition to measuring cutting forces.

Fig. 7.6 shows a sequence of 6 frames showing formation of a single surface fold during cutting. The time interval between these frames is approximately 50 ms. A band of streaklines (blue color band with white boundary) is overlapped on the frames to visualize how a thin layer of surface material evolves as it passes through the deformed zone. The thickness of this surface layer on the uncut portion of the material is 20 $\mu$m. The process of folding starts at a point near the free surface ahead of the tool. This point is referred to as a pinning point (point $O$ in frame B) hereafter. With the progress of cutting, $O$ moves towards a previous pinning point $O'$ and the material between $OO'$ buckles to result in a curved segment with midpoint $P$ as the 'apex' point (frames (c)-(f)). This process repeats itself which results in chip morphology characterized by periodic folds at the free surface. As a consequence of this repetitive folding and buckling of adjacent material layers into sinusoidal-shaped layers, a significantly thick chip is formed. For example, the chip thickness $t_c$ is 6-7 times $t_0$. It is observed from the PIV analysis that the length of the streakline does not remain constant during folding, but increases by a factor of $\sim 2$. In other words, the process of folding is characterized by simultaneous buckling as well as (permanent) stretching of the material. It is this combination of two processes that contributes to large chip thickness increase with respect to $t_0$.

It is important to note that periodic folding is not confined to the chip free surface, but actually extends into the chip thickness. For example, see Fig. 7.7(a) where it is evident from the streaklines that the folds travel deep into the chip. The 'fan shaped' deformation zone (as highlighted by the region of high strain rate) ahead of the tool that extends toward the free surface is also evident from this figure.

Fig. 7.7(b) shows the 3D profile of the free surface of the chip, as captured using three-dimensional optical profilometry method. The surface morphology can be seen to be very similar to those of microtomed chips in Fig. 7.3. This indicates a common buckling driven instability across different length scales ranging over 3 orders of magnitude. Lastly, it should be noted that although the topography maps can be used to calculate the spacing between the adjacent folds, as shown in Fig. 7.7(b), they cannot capture the fold amplitude. This is because the folds travel deep inside the chip as can be seen from Figs. 7.6 and 7.7(a). Therefore, the topography maps provide

only a partial picture of the folding and an accurate assessment of the amplitude of the fold can be made only through *in situ* or chip cross-sectional imaging.

### 7.3.4 Plastic buckling model for surface folding

The *in situ* high-speed imaging and PIV analyses have provided strong evidence that the formation of the surface folds in cutting of ductile metals like copper is a result of periodic material buckling. The similar free surface morphologies between the chips generated in cutting at conventional length scales and the microtomed chips suggest that a similar mechanism likely also exists at much smaller scales.

In the following, the formation of surface folds at sub-$\mu$m to nanometer scales is modeled using the buckling framework, with a view to explain several key experimental observations, including the non-linear scaling of fold spacing with respect to cutting depth.

In view of direct observations of plastic buckling and periodic folding, the process of fold formation is modeled as shown in Fig. 7.8. In this schematic, the main assumption is that the thin material layer comprised of several pinning points undergoes periodic and sequential buckling to result in a 'sinusoidal' folded structure. The initial distance $\delta_0$ between two adjacent pinning points is assumed to be equal, regardless of the grain or microstructural effects in the polycrystalline materials (Fig. 7.8(a)). This is not only inspired by PIV observations where folds form sequentially with approximately equal pinning point distances, but also by the 'evenly' distributed folds observed from the scanning electron micrographs taken from a variety of material systems under diverse cutting conditions. When a load is applied, the part of the beam confined between the two adjacent pinning points where load is applied is deformed to a sinusoidal-shaped fold followed by a series of morphologically similar folds forming in a sequential and orderly manner. The final shape resulting form this periodic buckling is shown in Fig. 7.8(b). The deformed sinusoidal shape is characterized by the spacing $\delta$ (defined as the distance between two adjacent troughs) and amplitude $a$ (assumed to be the difference between the final chip thickness $t_c$ and the initial depth of cut $t_0$). It should be also noted that the final length of the deformed sinusoidal profile differs from (larger than) the initial length by a factor $\beta$, the so-called stretch factor ($\sim 2$ for the case of cutting of annealed copper shown in Fig. 7.6).

For the perfect sinusoidal profile shown in Figs. 7.8(b) and (c), the initial distance between

the pinning points $\delta_0$ can be represented in terms of the fold spacing $\delta$ and the stretch factor $\beta$ as follows:

$$\delta_0 = \frac{\int_0^{\delta} \sqrt{1 + (\frac{(t_c - t_0)\pi}{\delta} \cos(\frac{2\pi}{\delta} x))^2} dx}{\beta} \tag{7.1}$$

Guided by the previous studies [18, 20, 61, 19], $\delta_0$ – the effective undeformed length of the beam at the point of fold/buckle initiation – is taken as the size of the yielding zone, as shown in Fig. 7.9. In this schematic, the yielding zone (zone where stresses exceed the material's yielding stress) is shown as a gray color area, where the maximum length of the yielding zone along the cutting direction is assumed to be the original undeformed beam length ($\delta_0$) between two pinning points. To predict $\delta_0$, we use the Flamant's solution [126] for semi-infinite elastic body loaded at its surface by two point (orthogonal) forces ($F_c$ and $F_t$), where the boundary of the plastically yielding zone is obtained by identifying the region where stresses exceed the material's yield stress. Say $F_c$ is the tangential force along the horizontal axis (x) and $F_t$ is the normal force along the vertical axis (z), the stress state for this system is given by ($\sigma_x$ and $\sigma_z$ are normal stresses, and $\tau_{xz}$ is the shear stress):

$$\sigma_x = \frac{2F_t}{\pi} \frac{x^2 z}{(x^2 + z^2)^2} + \frac{2F_c}{\pi} \frac{x^3}{(x^2 + z^2)^2} \tag{7.2}$$

$$\sigma_z = \frac{2F_t}{\pi} \frac{z^3}{(x^2 + z^2)^2} + \frac{2F_c}{\pi} \frac{xz^2}{(x^2 + z^2)^2} \tag{7.3}$$

$$\tau_{xz} = \frac{2F_t}{\pi} \frac{xz^2}{(x^2 + z^2)^2} + \frac{2F_c}{\pi} \frac{x^2 z}{(x^2 + z^2)^2} \tag{7.4}$$

Noth that $F_c$ and $F_t$ are the normalized forces in N/mm (normalized with respect to the cutting

depth). The span of the yielding zone can be now obtained using the von Mises yield criterion: $\sigma_v = \sqrt{\sigma_x^2 - \sigma_x\sigma_z + \sigma_z^2 + 3\tau_{xz}^2}$, where $\sigma_v$ is the material's yield stress. Fig. 7.10 shows the yielding zone predictions in ultramicrotomy of polycrystalline copper ($\alpha = 15^\circ$) at two cutting depths: $t_0$ = 200 nm and 1 $\mu$m. The boundary of the yielding zone is demarcated by dark grey-colored points. In these calculations, the material's yield stress $Y$ was taken as $\approx$ Hardness/3 ($\approx$ 366 MPa) and $F_c$ and $F_t$ are forces measured experimentally. It can be seen that the shape of the yielding zone in both the cases are similar. $\delta_0$ for the case of 1 $\mu$m cutting depth is about 3 $\mu$m, which is about 3 times the corresponding $\delta_0$ at $t_0$ = 200 nm.

The predictions for the plastic yielding zone size $\delta_0$ at different depths of cut $t_0$ are shown in Fig. 7.11. It can be seen that in all the three cases: copper ($\alpha = 15^\circ$ and $\alpha = 0^\circ$) and single crystal aluminum ($\alpha = 40^\circ$), the dependence of $\delta_0$ on $t_0$ is non-linear. It was found that this non-linear relationship between $\delta_0$ and $t_0$ can be fitted by a power-law: $\delta_0 = ct_0{}^p$, where $c$ is a proportional constant and $p$ is the power. Using the Gauss-Newton algorithm to fit the power-law to the experimental data, a $c$ value of 2.87 and a $p$ value of 0.71 was obtained for copper at $\alpha = 15^\circ$. The corresponding $p$ values for copper at $\alpha = 0^\circ$ and single crystal aluminum were 0.87 and 0.52, respectively.

With the above model for estimating the undeformed beam length (or plastic zone size) $\delta_0$, the model is now complete as it enables prediction of the fold spacing ($\delta$) as a function of material property (hardness), cutting/thrust forces, chip thickness ratio, and the stretch factor $\beta$.

The proposed model is first validated using the results presented in Figs. 7.6 and 7.7, where the distance between the pinning points as well as the stretch factor information is directly available from the PIV analysis. For example, the mean distance between the pinning points at the time of buckle formation is found from PIV analysis to be 340 $\mu$m, whereas the predicted $\delta_0$ from the measured forces ($F_c$: 113 N/mm, $F_t$: 25 N/mm) and yielding model is 383 $\mu$m. Similarly, the fold spacing predicted using Eq. 7.1 (taking $\beta$ to be 2) is 69 $\mu$m, which is close (within 15%) to the PIV-measured average fold spacing of 60 $\mu$m. Given the various assumptions involved in the model, these predictions are very satisfactory.

The proposed model is also capable of predicting the non-linear relationship between the fold spacing $\delta$ and $t_0$ shown in Fig. 7.5. Fig. 7.12(a) shows the predictions of fold spacing $\delta$ at different depths of cut $t_0$, estimated using Eq. 7.1 and the power-law fits for $\delta_0$ as shown in Fig. 7.11.

In these predictions, the stretch factor $\beta$ was taken as 1.1, 2.6, and 3.2 respectively for single aluminum ($\alpha = 40°$) and copper at $\alpha = 15°$ and $\alpha = 0°$. Stretch factors are selected based on the following three criteria: (1) the predicted non-linear trend between $\delta$ and $t_0$ is close to the experimentally observed ones shown in Fig. 7.12(a); (2) there exists a solution for $\delta$ at all the depths of cut; and (3) $\delta$ at larger depth of cut is greater than that at small depth of cut. From Fig. 7.12(a), it can be seen that the model predicts non-linear dependence between $\delta$ and $t_0$ for all three cutting conditions, similar to our experimental observations. It is also observed that the single crystal aluminum ($\alpha = 40°$) has the largest $\delta$ when compared to copper, quite consistent with the SEM measurements. However, it should be noted that the predicted $\delta$ values are several times higher than the actual measurements. A possible reason for this lies in our use of $t_c - t_0$ as an estimate for fold amplitude in Eq. 7.1. From the *in situ* analyses using PIV, it was observed that the actual amplitude can differ from this estimate. This aspect requires further study. Even though the predicted fold spacings are much higher than observed values, the normalized $\delta/t_0$ values are quite consistent with the experimental observations. For copper ($\alpha = 15°$), the predicted $\delta/t_0$ at 100 nm is three times the value at 1 $\mu$m, in-line with the experimental trend shown in Fig. 7.5. Similarly, for copper ($\alpha = 0°$) and aluminum ($\alpha = 40°$), the predicted trends of $\delta/t_0$ vs. $t_0$ are qualitatively the same as the experimental data.

## 7.4 Discussion

The ultramicrotomy experiments conducted with copper (polycrystalline) and aluminum (polycrystalline and single crystal) using glass/diamond knives, coupled with the electron microscopy and AFM characterization of the microtomed chips, have enabled us to study the chip free surface morphology, surface folding and scaling behavior of the surface folds with respect to the depth of cut. Besides the observation of surface folding phenomenon in multiple material systems and in both polycrystalline and single crystal samples, an important observation from the study is the similarity between folds characteristics of microtomed chips ($t_0 \sim$ 100 nm to 1 $\mu$m) and the classical Type 1 chip that is produced at a much larger length scale. The common fold characteristics across different length scales (from nano to mesoscale) include high periodicity, smooth sinusoidal shape, alignment of folds perpendicular to the cutting direction and their universal occurrence in soft ductile metals even at extremely low speeds. Taken together with our PIV observations as

well as the previous reports [18, 19, 20, 61] illustrating the role of plastic buckling in Type 1 chip formation, this strongly suggests a unified buckling-based surface instability mechanism for fold formation across varied length scales (tens of nm to more than one hundred $\mu$m).

In literature [18, 20], it has been shown (using *in situ* experiments) that the initiation of surface fold in Type 1 chip formation is driven by microstructural considerations. In particular, a grain boundary that is located ahead of the primary deformation zone is shown to act as a pinning point needed for initiating a buckle. In other words, the distance between the pinning points (or undeformed beam length) and thereby fold spacing in this case are governed by the average grain size. In contrast, our results show that the fold spacing in chips produced using ultramicrotomy at small length scales is several orders smaller than the workpiece sample grain size. For example, in the case of copper ($\alpha = 15^{\circ}$) the fold spacing is in the range of 200 to 500 nm (depending on the cutting depth), two orders smaller than the average grain size for the sample (37 $\mu$m). Firstly, this clearly suggests that microstructural-level defects such as grain boundaries are not a requirement for the initiation of surface buckling/folding. This conclusion is further supported by experimental observations of multiple folds forming within a single grain as well as fold formation in single crystal samples; for instance, the periodic folds observed in single crystal aluminum are seen to be morphologically identical to those observed in polycrystalline chips. Secondly, the results also show that in the absence of microstructural features or in situations where the microstructural length scales are much greater than the other length scales associated with the problem (e.g., cutting depth, size of the plastic zone, etc.), the initiation and development of the fold is not driven by the grain structure but by continuum-level plasticity considerations. The model presented in the study supports the view that the distance between pinning points for these situations is determined by the size of the plastically yielded zone. It is only when grain size becomes comparable to the plastic zone size that microstructure begins to influence folding both in terms of fold spacing as well as spatial distributions of folds across the chip thickness/width.

A simple continuum-level framework that simplifies the fold geometry as a sinusoidal curve is presented to model fold formation and evolution. It is important to note that the model presented here assumes that buckling has already occurred, that is, it does not provide any information about the critical criterion for buckling. However, it does provide a simple analytical framework to describe the dependence of fold spacing or wavelength as function of the material property (hard-

ness/yield strength) and cutting parameters such as forces and chip thickness. For example, it has been shown that the model captures the non-proportional variation of fold spacing with respect to the cutting depth that has been observed experimentally based on SEM imaging (Fig. 7.4). This non-proportional scaling of fold spacing with $t_0$ in fact arises from the size effect discussed in earlier chapters. This may be illustrated using the Flamant's solution for the stress field where it can be shown that the size of the yielding zone (as defined by the maximum length of this zone along the cutting direction) can be shown to be given by $\delta_0 = \frac{F_c+\sqrt{{F_c}^2+{F_t}^2}}{Y\pi}$ (see APPENDIX B). The fact that the cutting and thrust forces in cutting at small scales exhibit a highly non-linear scaling with the cutting depth (the size effect) means that $\delta_0$ also varies non-linearly with respect to $t_0$. This has been in fact confirmed by the yielding zone predictions and can be also seen from Figs. 7.10 and 7.11; a 5-fold increase in $t_0$ from 200 nm to 1 $\mu$m results in $\delta_0$ increase only by a factor of $\sim 1.5$. In the plastic buckling model shown in Fig. 7.8, a fold forms within the area confined by the yielding zone, whose spacing and amplitude is directly determined both by initial distance between the pinning points as well as the chip thickness ratio. Since the chip thickness ratio is largely insensitive to the depth of cut for a given rake angle [32, 33], it should be evident that it is the non-linear scaling of the plastic zone size and forces that is responsible for the observed dependence of fold spacing on $t_0$. Besides establishing a common mechanism for fold formation across length scales, the work therefore also reveals new connections between disparate phenomena of size effect and surface folding.

A brief comparison of our results pertaining to surface folding and plastic buckling with other buckling-based instability mechanisms – elastic buckling and viscous buckling – is in order. Elastic buckling is first systematically studied by Euler, which is described as the buckling of a long slender column under a uniaxial compression load when the applied load exceeds a critical value [126]. In the case of a simple beam that is fixed on one end while the other is subjected to axial compression, buckling is characterizing by bending of the beam between the two pinning points in a sinusoidal form, quite akin to the assumptions made in the present study. Compression of a thin elastic film attached to a compliant substrate (e.g., silicon on PDMS substrate) is another interesting case of elastic buckling where multiple buckles initiate and evolve simultaneously as the load is increased. Results [127] show that the buckle spacing or wavelength for this case is proportional to the thickness of the elastic film, in contrast to the present case. It is also important

to note that in elastic buckling, the shape change is reversible where as in our case, not only the material is permanently folded into sinusoidal-type profile but also undergoes plastic stretching during the folding process.

Interestingly, a qualitatively similar buckling phenomenon also exists in viscous fluids. The viscous buckling is first investigated by Taylor [128] where it was shown that a viscous fluid filament passing through a small orifice under the effect of gravity can buckle or coil upon encountering a rigid plate, given the critical conditions are satisfied. The dynamics of this buckling process, where buckles form sequentially and in a periodic manner (as opposed to simultaneously), resembles plastic buckling demonstrated here. Since Taylor's work, the buckle characteristics in viscous fluids have been shown to primarily depend on three factors, namely the diameter of the orifice, height of the orifice from the bottom plate, and viscosity of the fluid [129, 130]. In particular, the filament height/diameter ratio governs buckle formation (higher the ratio, more likely the viscous filament will form buckle) as well as the buckling frequency, where larger height/diameter ratios are shown to result in higher buckling frequency (equivalently, smaller buckling wavelength or spacing). Similarly, in the absence of gravitational effects, it was found that more closely-spaced buckles form in the case of thinner viscous fluid layers [131]. These observations are qualitatively similar to plastic buckling in cutting, where the distance between the pinning points and fold spacing decrease upon reducing the cutting depths, i.e., folds form more frequently at a smaller wavelength as the cutting depth is decreased. Whether or not any quantitative relationships exist between the plastic, elastic and viscous buckling phenomena remains an open question.

## 7.5 Conclusion

In this chapter, a surface instability mechanism that results in the formation of periodic folds on the chip free surface in small scale cutting of metals is investigated. This phenomenon is shown to be prevalent in various soft and ductile material systems (both polycrystalline and single crystalline samples) regardless of the underlying microstructural features and even under extremely low cutting speed (i.e., quasi-static deformation conditions). The results demonstrate that the deformation process in cutting of soft metals is intrinsically unstable because of the proximity of the free surface.

Based on observations of the fold characteristics – including their rounded morphology, sen-

sitivity to deformation on the cutting edge, similarity with the conventional Type 1 chip, and dependence of fold spacing and amplitude on the cutting depth – a plastic buckling-based instability mechanism is established for the fold formation. This continuum-level picture of surface instability mechanism is free of temperature effects and is in contact to various mechanisms postulated earlier for unstable/heterogeneous plastic fold during chip formation. Based on *in situ* observations of chip formation, a geometric model is proposed to capture the evolution of fold development post-buckling. The model is shown to qualitatively explain the non-linear dependence of fold spacing with respect to the cutting depth. This non-linearity in fact arises from the size dependence of cutting forces on the depth of cut.

Overall, findings from the study highlight the possibility of a unified framework (based on periodic surface plastic buckling) to model fold formation in soft metals over a wide range of length scales (from nanometer to millimeter scales).

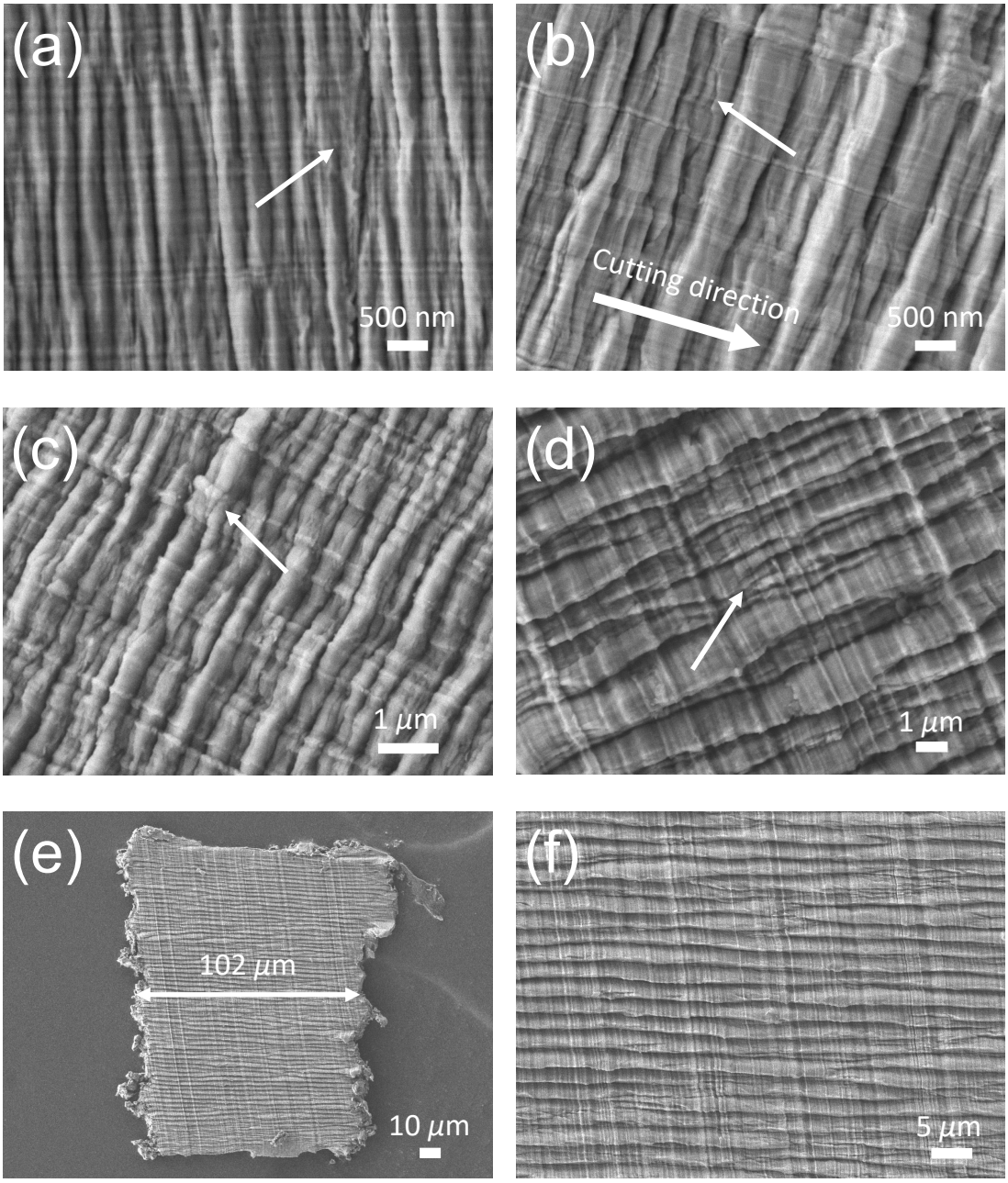


Figure 7.1. SEM images showing the free surface morphology of microtomed chips. Periodic folds distributed perpendicular to the cutting direction are observed in cutting with various metals at different conditions. (a) Polycrystalline copper chip at $t_0 = 500$ nm and $\alpha = 15°$. (b) Polycrystalline copper chip at $t_0 = 2$ $\mu$m and $\alpha = 40°$. (c) Annealed polycrystalline aluminum chip at $t_0 = 500$ nm and $\alpha = 40°$. (d) Annealed polycrystalline aluminum chip at $t_0 = 2$ $\mu$m and $\alpha = 40°$. (e) and (f) Single crystal aluminum chip at $t_0 = 3$ $\mu$m and $\alpha = 40°$ with uniformly distributed folds across the cutting width captured at low (e) and high (f) magnifications.

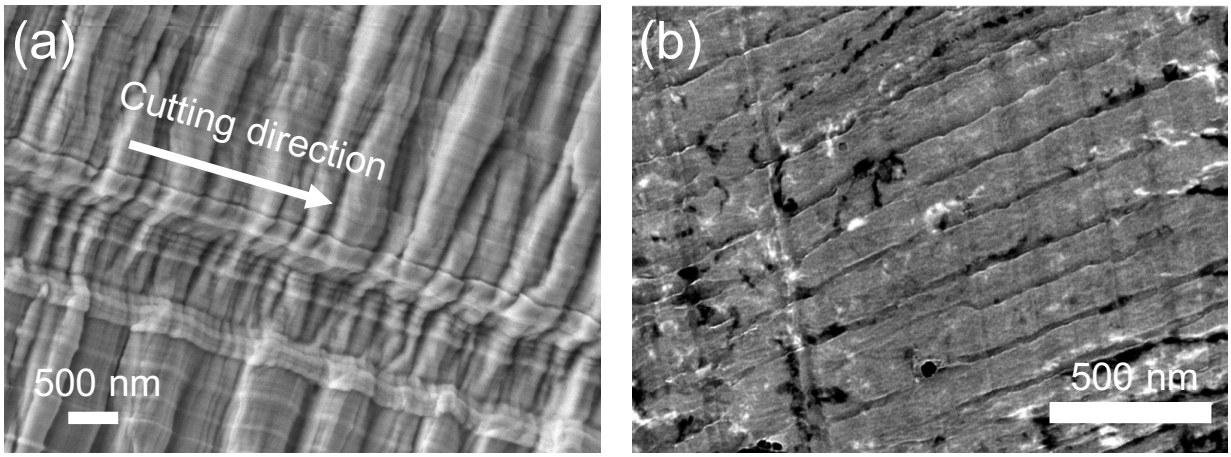


Figure 7.2. (a) SEM image showing the sensitivity of folds on cutting edge imperfection. Significantly different sizes of folds can be seen within and outside the defect (groove). (b) Bright-field TEM image of polycrystalline aluminum chip ($t_0 = 20$ nm, $\alpha = 40°$) generated using a sharp diamond knife. Periodic fine-scale contrast observed in the images is associated with the chip thickness change due to surface folds.

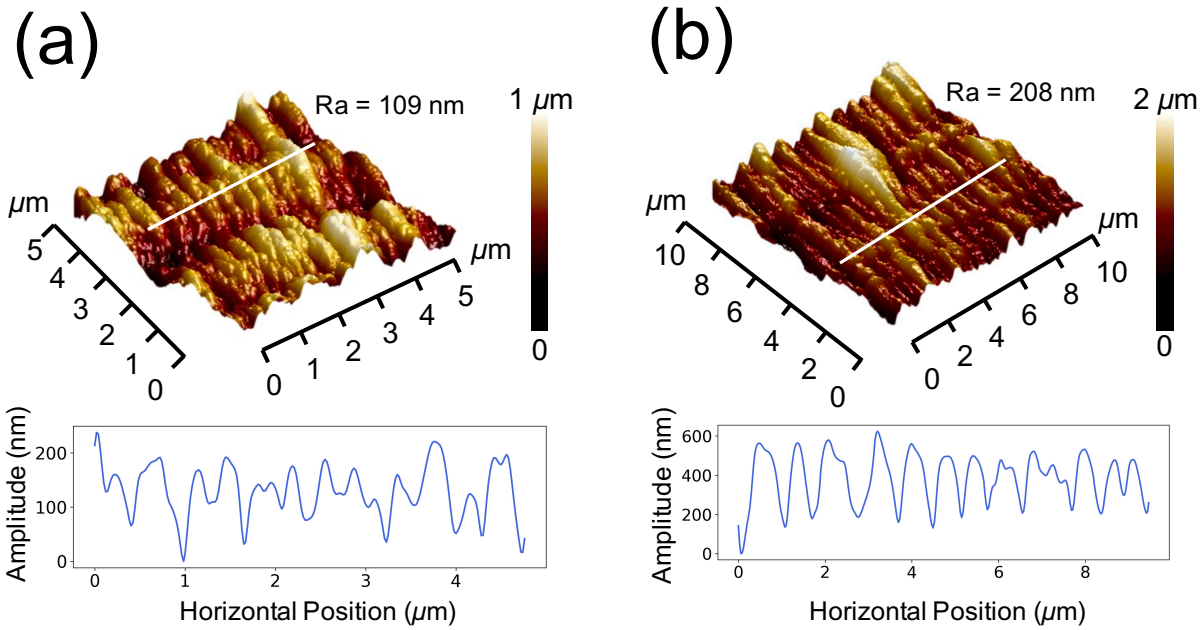


Figure 7.3. AFM characterization of chip free surface. (a) $t_0 = 100$ nm and $\alpha = 40°$, (b) $t_0 = 1$ $\mu$m and $\alpha = 40°$. Material system: annealed polycrystalline aluminum.

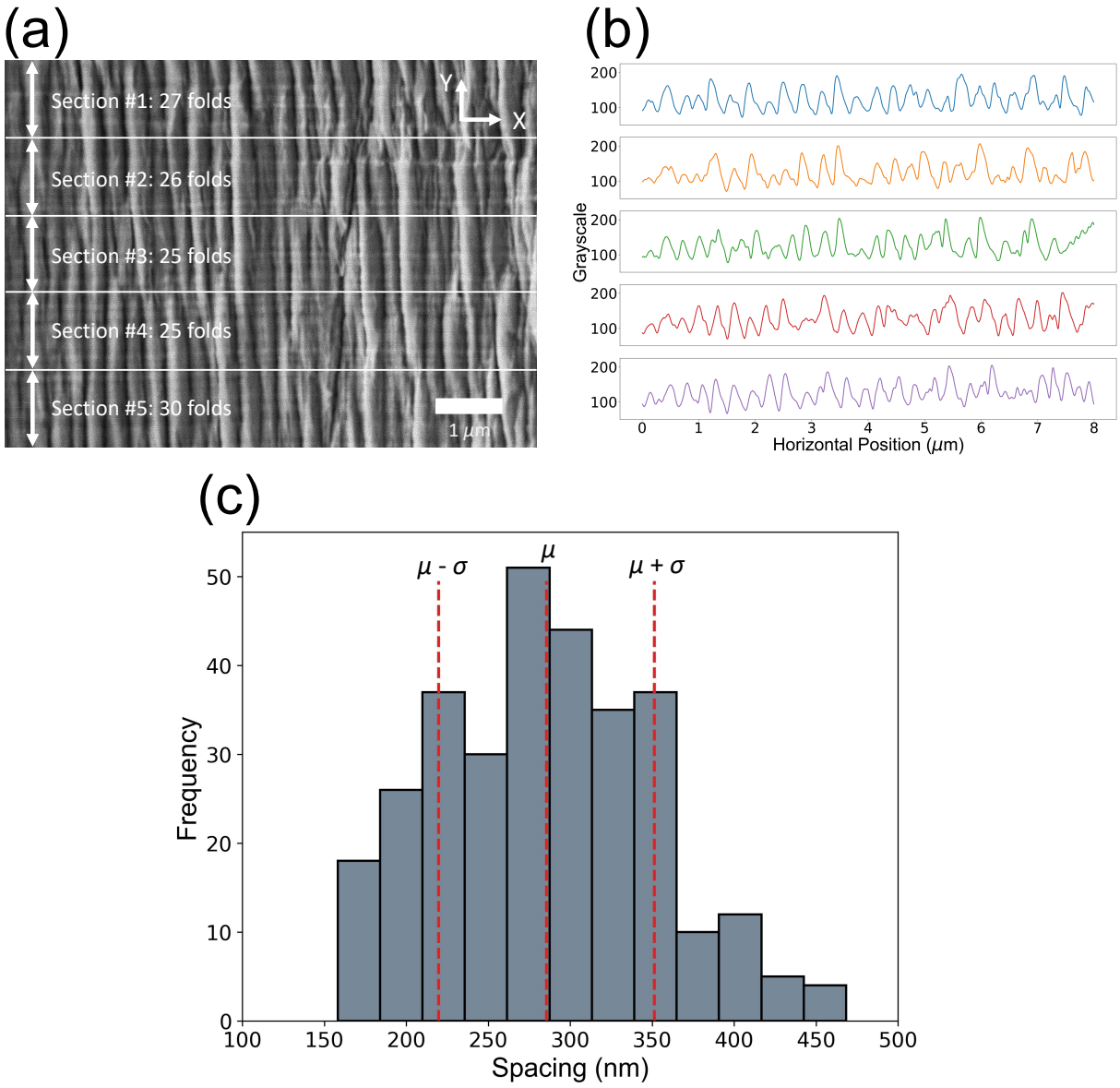


Figure 7.4. Characterization of fold spacing. (a) A representative SEM image (copper, glass knife, $\alpha = 15°$, $t_0 = 500$ nm) that was divided into five sections along the Y-axis. (b) Shows the average grayscale values plotted as a function of horizontal position along X axis in each section. The periodic sinusoidal features correspond to individual folds. (c) Frequency distribution of spacing (calculated as the horizontal position difference between two adjacent peaks) showing an approximate normal distribution. $\mu$ represents the mean fold spacing and $\sigma$ is the standard deviation.

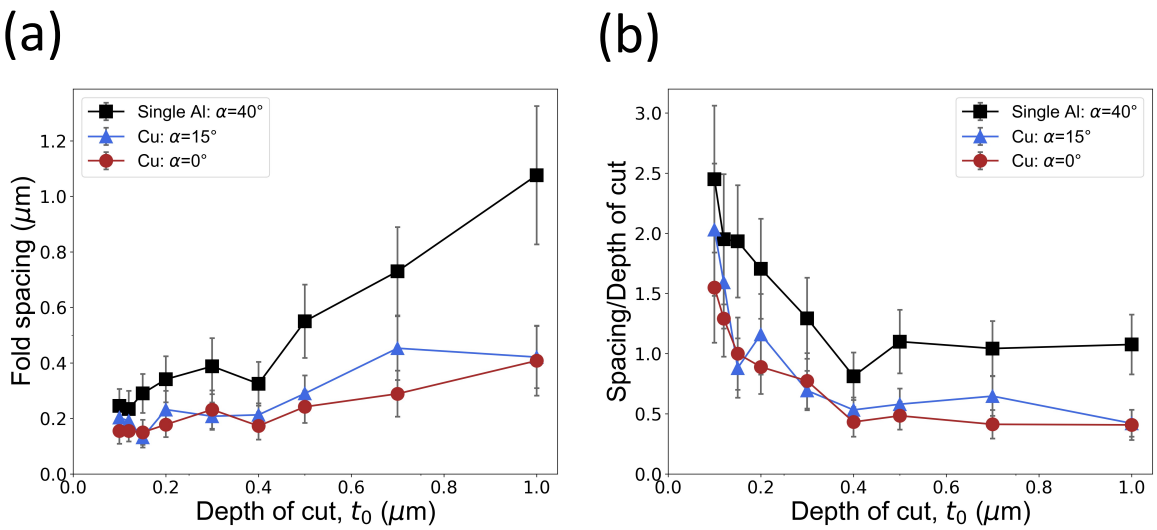


Figure 7.5. The dependence of fold spacing on depth of cut in polycrystalline copper ($\alpha = 15°$, $\alpha = 0°$) and single crystal aluminum ($\alpha = 40°$). (a) Fold spacing vs. depth of cut, (b) normalized plot showing fold spacing/depth of cut vs. depth of cut.

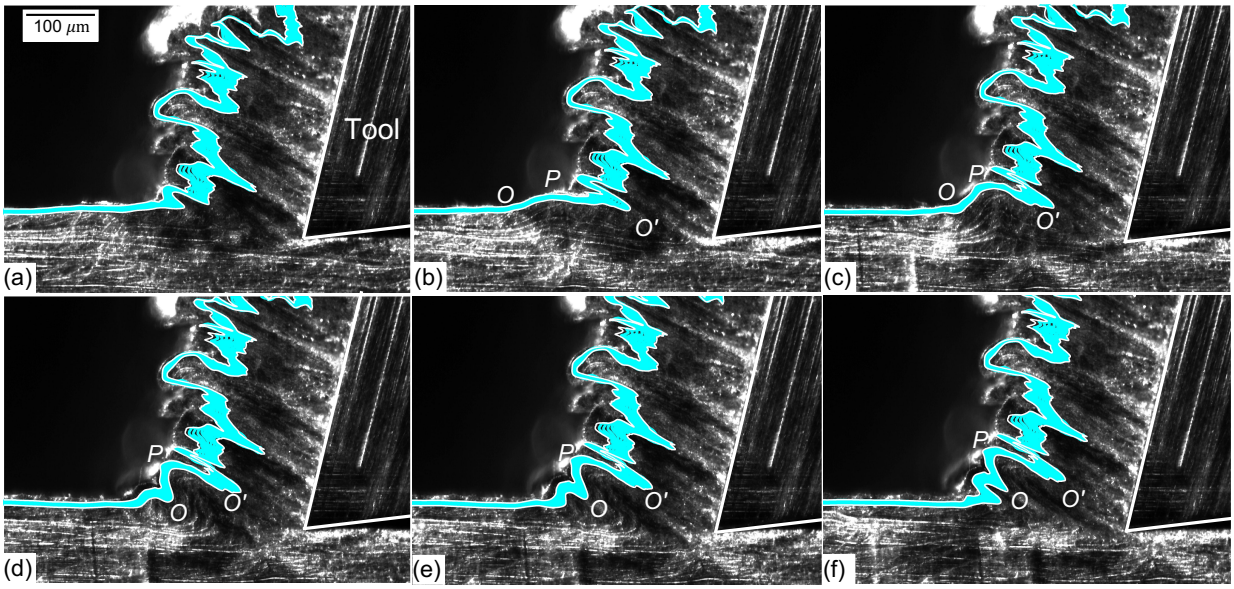


Figure 7.6. Sequence of high-speed images showing the dynamics of folding. A band of streaklines (blue color with white boundary) is superimposed on the image to highlight the phenomenon. Folding starts with buckle formation between two pinning points $O$ and $O'$, followed by folding of the material around the midpoint $P$. This results in a chip that is 6 - 7 times thicker than $t_0$.

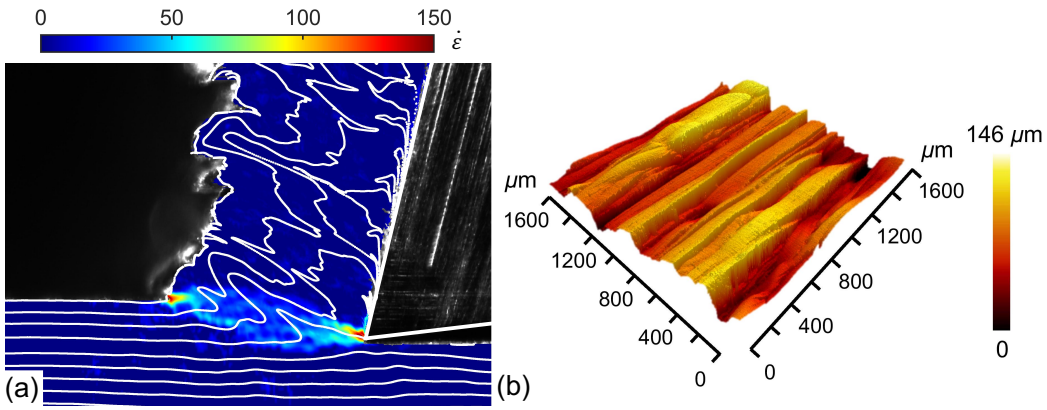


Figure 7.7. (a) Strain rate field map highlighting the 'fan shaped' deformation zone ahead of the tool. The superimposed streaklines show that the folds are not confined to the surface but extend deep into the chip. (b) 3D topography map showing chip free surface morphology that is very similar to that observed in chips produced using ultramicrotomy (e.g., see AFM maps in Fig. 7.3).

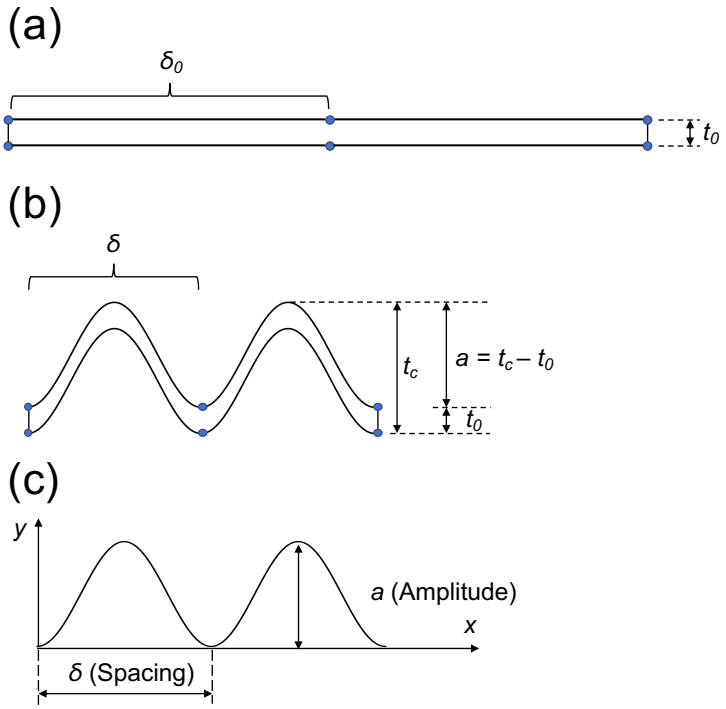


Figure 7.8. Geometric model for plastic buckling. (a) Undeformed beam with evenly distributed "pinning points". (b) Final sinusoidal shape of buckled beam. (c) Sinusoidal profile with a spacing of $\delta$ and and amplitude of $a = t_c - t_0$.

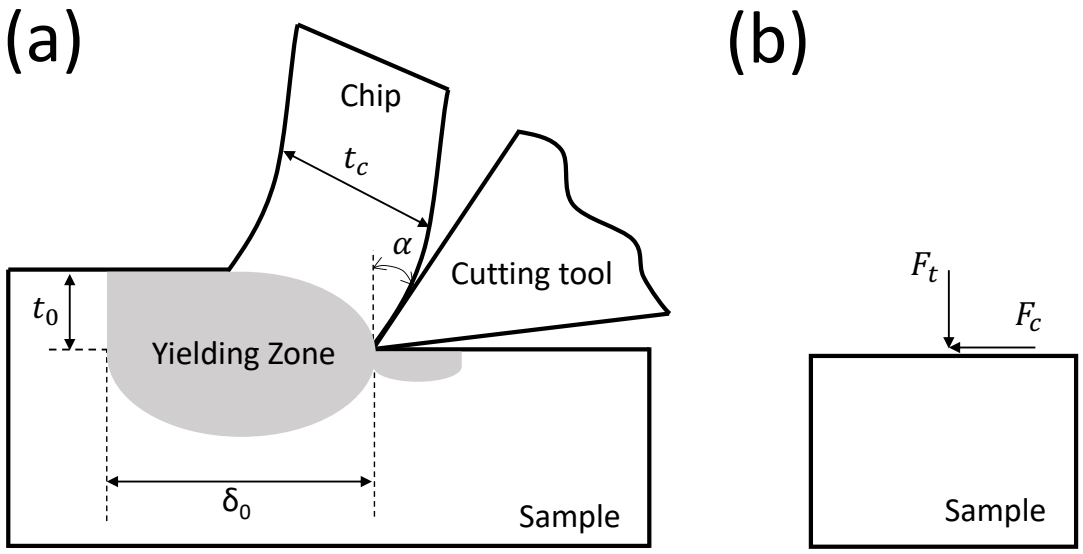


Figure 7.9. (a) Schematic showing the plastic yielding zone (shaded in gray color) in plane-strain cutting. (b) Simiplification of the cutting process as an elastic half-plane loaded by two point (orthogonal) forces $F_c$ and $F_t$.

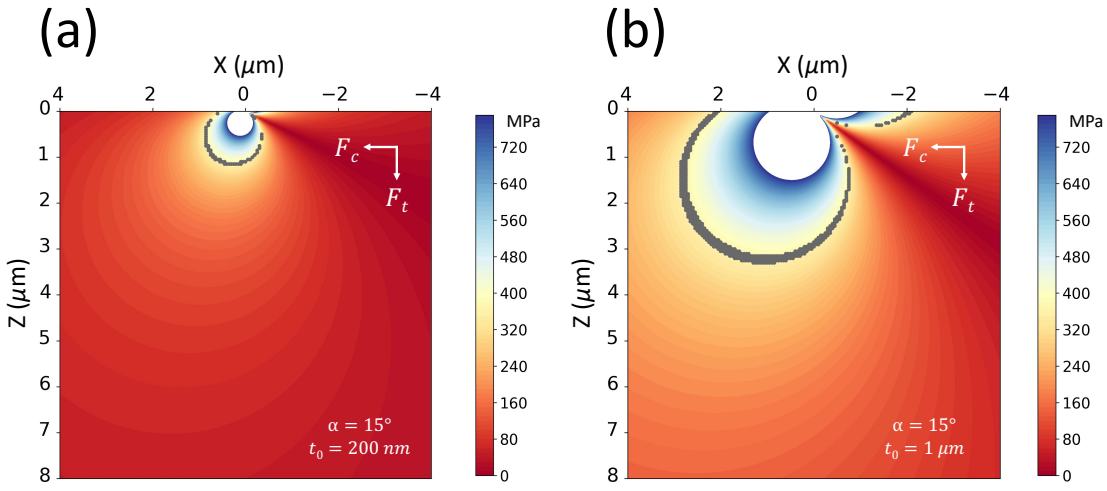


Figure 7.10. Yielding zone prediction in cutting of copper calculated using Flamant's approximation of concentrated cutting and thrust forces. (a) $\alpha = 15°$, $t_0 = 200$ nm. (b) $\alpha = 15°$, $t_0 = 1$ $\mu$m. The boundary of the yielding zone is shown by individual grey-colored markers. The point of force application coincides with (x, y) = (0, 0).

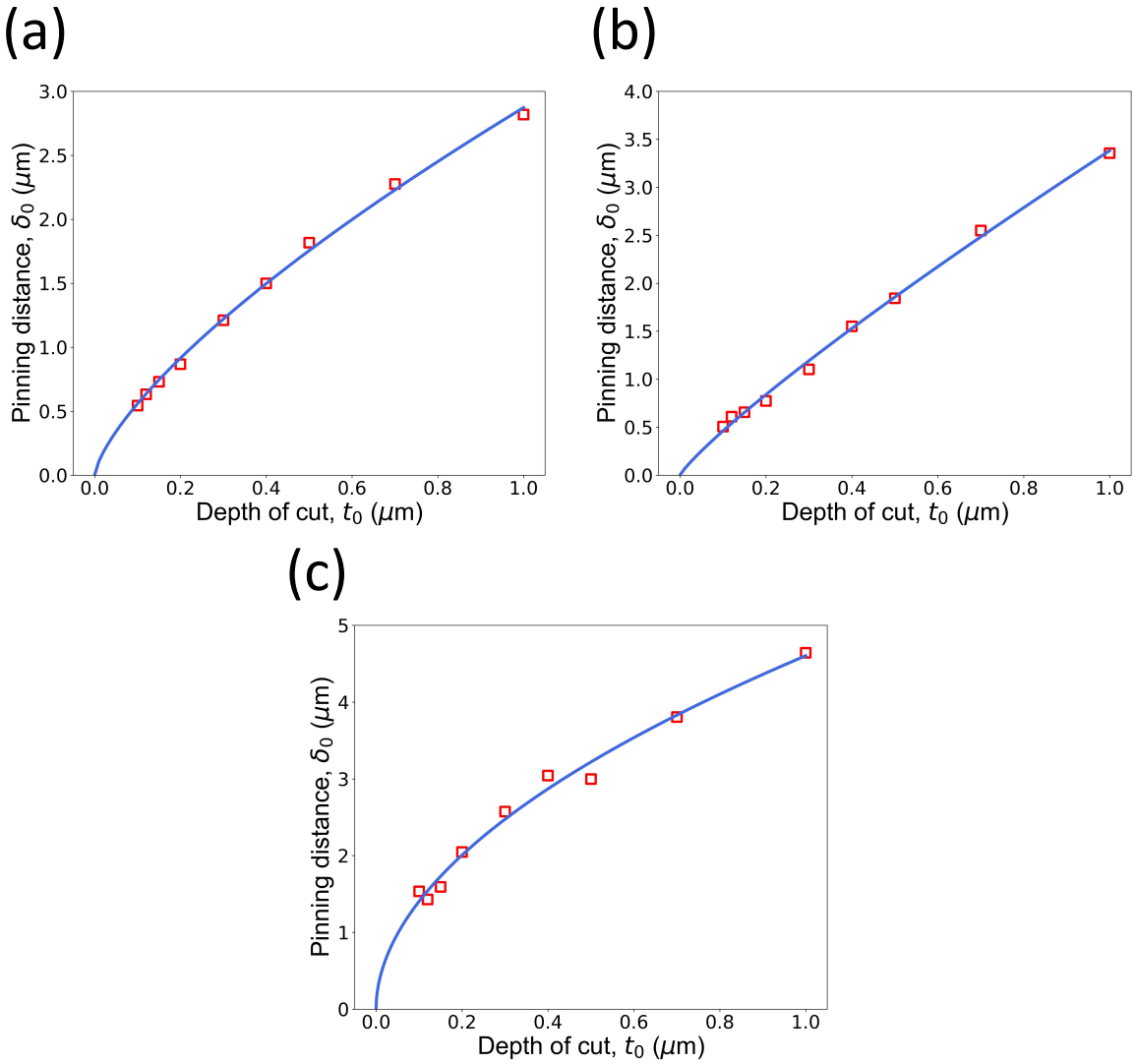


Figure 7.11. Estimated plastic yielding zone size ($\delta_0$) for (a) polycrystalline copper ($\alpha = 15°$), (b) polycrystalline copper ($\alpha = 0°$), and (c) single crystal aluminum ($\alpha = 40°$). Blue curves are the power-law fits to the data.

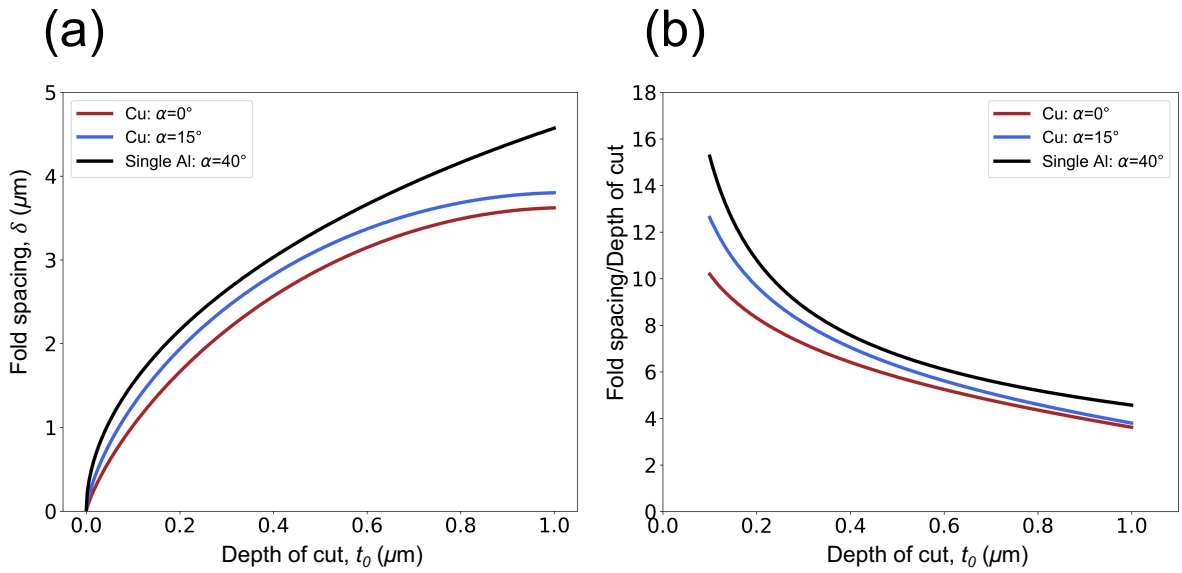


Figure 7.12. Plots showing the predicted fold spacing for all three conditions: Cu ($\alpha = 0°$ and $\alpha = 15°$) and single crystal aluminum ($\alpha = 40°$). (a) $\delta$ vs. $t_0$, and (b) $\delta/t_0$ vs. $t_0$.

# 8. SUMMARY

## 8.1 Conclusion

In this study, a novel instrumented ultramicrotomy technique was developed to carry out cutting experiments at the small scale (sub-$\mu$m to nanometer scale cutting depths) under well-defined conditions. This method, together with the use of atomically sharp glass and diamond knives as cutting tools, enabled precise and systematic measurements of cutting forces and energy under ideal two-dimensional plane strain conditions and in the absence of cutting edge radius effects. These unique experimental features were utilized to understand the mechanics aspects associated with cutting of soft ductile metals at the small scale, including size effect, scale dependence of tool-chip contact friction, and surface plastic instabilities involved during chip formation. These studies were made with a variety of metallic systems (copper, aluminum and zinc), both in polycrystal and single crystal forms, over a range of depths of cut (30 nm to 3 $\mu$m) and rake angles. The effects of tool surface contamination on these phenomena were also explored by coating the tool surface with a thin layer of lubricant or surface films.

Characterization of the forces and specific energy in cutting of different material systems shows that the size effect, which is characterized by up to 5-fold increase in the specific energy with decreasing depth of cut, is likely universal and occurs even in the absence of cutting edge radius effects. This effect primarily arises from non-proportional reduction of the tool-chip contact frictional energy with decreasing depth of cut, whereas the plastic deformation energy associated with the shear zone scales proportionally with the depth of cut. The non-proportional reduction of the frictional energy was experimentally shown to be because of non-proportional scaling of the tool-chip contact area with respect to the cutting depth. In other words, the size effect arises as a result of competition between friction (which scales with area) and plastic deformation resistance (which scales with volume). It is possible that the same underlying phenomenological principle could also contribute to the size-effect in other domains like nanoindentation hardness testing. The experimental results also emphasize that simple extrapolation of cutting force data from higher cutting depths to sub-$\mu$m regimes is inaccurate and leads to significant errors. Various theories for the size effect were evaluated in light of the experimental data and it is shown that the majority of them can

be rejected.

The non-linear scale dependence of tool-chip contact area is interpreted from the standpoint of adhesion and modeled quantitatively using a contact mechanics incorporating surface attraction forces at the tool-chip contact. Additional support for this viewpoint comes from our cutting experiments with lubricants and surface contaminants which drastically reduce adhesion at the tool-chip contact and lead to a significant reduction in the size effect. The chip "pull-off" force measurement technique presented in the study also provides unequivocal evidence for adhesive attractive forces at the tool-chip contact, while enabling a novel experimental approach to quantify the work of adhesion at plastic contacts. Taken together, the study highlights the important role of surface attraction forces and adhesion in determining the contact area and friction at small scales not only in cutting but for plastic sliding contacts in general. Although adhesion is well-studied and appreciated for the case of elastic contacts (both static and sliding), its role in plastic sliding contacts has not received adequate attention.

## 8.2 Implications

It is appropriate to conclude the dissertation with a brief discussion of implications of our work. Several reports exist in the literature about how the hardness of the material increases with a decrease in the indentation depth – the so-called indentation size effect [37, 38] – with most claiming strain-gradient plasticity or the increased difficulty of inducing dislocation slip in a small volume as the underlying mechanisms for this effect. In the light of our findings, and given that indentation testing involves both plastic deformation and friction components analogous to that in cutting, a question arises as to whether the size effect mechanism demonstrated in our study that is based on non-proportional scaling of the friction component offers an alternative and a simpler explanation for the size dependence in indentation. The fact that the size effect in sliding indentation experiments [39] – wherein the friction component is comparable to that of plastic deformation – is considerably higher than in regular indentation tests indeed supports this picture. In addition, it should be possible to verify this viewpoint, say, by altering the extent of the friction component by using lubricants or contaminants that reduce friction or by using sharper indenters which promote relative sliding at the indenter-sample contact (thereby, friction component).

Secondly, the present study calls attention to the need for incorporating adhesion effects into

machining models when cutting depths are in the micro/nano-meter range. Although the pristine and intimate nature of tool-chip contact (factors which promote adhesion) has been well-known [109, 110], it is surprising that adhesive forces have received little consideration to date in machining studies. The fact that adhesion is highly sensitive to the tool-chip contact "cleanliness" has important implications for processes like grinding, polishing and micro/ultraprecision machining where material removal occurs at a small scale. It is worth recalling here that our results show that the size effect can be effectively suppressed using innocuous lubricants or surface contaminants that reduce friction and adhesion at the tool-chip contact. Therefore, significant improvements in the performance of these processes (e.g., reduction in specific energy and stickiness/material build-up at abrasive edges) may be possible by suitably altering the contact condition. The current study has focused on cutting of nominally pure metallic systems at low speeds. It would be of value to study cutting behavior of multi-phase engineering alloys under the high-speed regimes. This will help assess the generality, or lack thereof, of the present observations pertaining to the size effect and the role tool-chip contact condition plays in governing this effect over a broader class of materials and cutting conditions.

Thirdly, the instrumented ultramicrotomy technique, coupled with simple shear nature of deformation in cutting, offers much scope for fundamental investigations of the mechanical behavior of metals at small scales. Among these is the possibility of obtaining clean measurements of critical resolved shear stress over a range of micron and sub-micron length scales. When compared to conventional small-scale testing methods (e.g., micro-compression/tensile testing), ultramicrotomy is much easier to implement in practice and does not require laborious specimen preparation, while allowing multiple measurements to be made in a short time. Preliminary experiments with aluminum have shown that sections produced at cutting depths in the range of 10 - 80 nm are electron transparent and can be directly observed under the TEM without additional sample preparation; this can help provide additional insight into atomic-level mechanisms governing plasticity at small scales. Diamond knives that are characterized by a very sharp cutting edge (radius $<$ 5 nm), and single crystals or large polycrystals with well-defined crystal orientations, should be well-suited for these types of measurements. Similarly, the pristine and two-dimensional nature of tool-chip contact in cutting, where the real area of contact is equal to the apparent area of contact, offers unique opportunities for using orthogonal cutting for studying sliding contact friction and

adhesion over a range of material combinations, sliding speeds and contact sizes that are hard to replicate using conventional techniques. Although the suggestion of using tool-chip contact for fundamental studies of friction was made by Shaw more than 70 years ago [132], it still remains unexplored.

It is hoped that further developments to the experimental platform will enable these explorations.

# REFERENCES


[1] M. C. Shaw, *Metal Cutting Principles*. Oxford, UK: Clarendon Press, 1996.

[2] D. Sagapuram, H. Yeung, Y. Guo, A. Mahato, R. M'Saoubi, W. D. Compton, K. P. Trumble, and S. Chandrasekar, "On control of flow instabilities in cutting of metals," *CIRP Annals*, vol. 64, no. 1, pp. 49–52, 2015.

[3] D. Sagapuram, A. Udupa, K. Viswanathan, J. B. Mann, R. M'Saoubi, T. Sugihara, and S. Chandrasekar, "On the cutting of metals: A mechanics viewpoint," *Journal of Manufacturing Science and Engineering*, vol. 142, no. 11, pp. 110808:1–19, 2020.

[4] S. Yadav, G. Feng, and D. Sagapuram, "Dynamics of shear band instabilities in cutting of metals," *CIRP Annals*, vol. 68, no. 1, pp. 45–48, 2019.

[5] K. Viswanathan, S. Yadav, and D. Sagapuram, "Shear bands in materials processing: Understanding the mechanics of flow localization from Zener's time to the present," *Applied Mechanics Reviews*, vol. 72, no. 6, p. 060802, 2020.

[6] T. Atkins, *The Science and Engineering of Cutting: the Mechanics and Processes of Separating, Scratching and Puncturing Biomaterials, Metals and Non-metals*. Butterworth-Heinemann, 2009.

[7] D. A. Lucca, R. L. Rhorer, and R. Komanduri, "Energy dissipation in the ultraprecision machining of copper," *CIRP Annals*, vol. 40, no. 1, pp. 69–72, 1991.

[8] W. R. Backer, E. R. Marshall, and M. C. Shaw, "The size effect in metal cutting," *Transactions of ASME*, vol. 74, no. 1, pp. 61–72, 1952.

[9] T. Moriwaki, "Machinability of copper in ultra-precision micro diamond cutting," *CIRP Annals*, vol. 38, no. 1, pp. 115–118, 1989.

[10] S. Malkin, "Grinding of metals: Theory and application," *Journal of Applied Metalworking*, vol. 3, no. 2, pp. 95–109, 1984.

[11] K. Nakayama and K. Tamura, "Size effect in metal-cutting force," *Journal of Engineering for Industry*, vol. 90, no. 1, pp. 119–126, 1968.

[12] D. Dinesh, S. Swaminathan, S. Chandrasekar, and T. N. Farris, "An intrinsic size-effect in machining due to the strain gradient," in *Proceedings of 2001 ASME International Mechanical Engineering Congress and Exposition*, pp. 1–8, 2001.

[13] S. S. Joshi and S. N. Melkote, "An explanation for the size-effect in machining using strain gradient plasticity," *Journal of Manufacturing Science and Engineering*, vol. 126, no. 4, pp. 679–684, 2004.

[14] A. G. Atkins, "Modelling metal cutting using modern ductile fracture mechanics: Quantitative explanations for some longstanding problems," *International Journal of Mechanical Sciences*, vol. 45, no. 2, pp. 373–396, 2003.

[15] J. W. Christian, *The Theory of Transformations in Metals and Alloys. Part I*. Oxford, UK: Pergamon Press, 2002.

[16] A. G. Atkins and Y. W. Mai, *Elastic and Plastic Fracture: Metals, Polymers, Ceramics, Composites, Biological Materials*. West Sussex, UK: Ellis Horwood Limited, 1985.

[17] K. Kendall, *Molecular Adhesion and its Applications: The Sticky Universe*. New York, NY: Springer Science & Business Media, 2007.

[18] A. Udupa, K. Viswanathan, Y. Ho, and S. Chandrasekar, "The cutting of metals via plastic buckling," *Proceedings of the Royal Society A: Mathematical, Physical and Engineering Sciences*, vol. 473, no. 2202, p. 20160863, 2017.

[19] H. Yeung, K. Viswanathan, A. Udupa, A. Mahato, and S. Chandrasekar, "Sinuous flow in cutting of metals," *Physical Review Applied*, vol. 8, no. 5, p. 054044, 2017.

[20] A. Udupa, K. Viswanathan, and S. Chandrasekar, "Pattern formation on free surfaces via plastic buckling and periodic folding," *EPL (Europhysics Letters)*, vol. 129, no. 4, p. 46001, 2020.

[21] J. T. Black, "On the fundamental mechanism of large strain plastic deformation: Electron microscopy of metal cutting chips," *Journal of Engineering for Industry*, vol. 93, no. 2, pp. 507–526, 1971.

[22] R. Phillips, "Diamond knife ultra microtomy of metals and the structure of microtomed sections," *British Journal of Applied Physics*, vol. 12, no. 10, pp. 554–558, 1961.

[23] S. Ramalingam and J. T. Black, "An electron microscopy study of chip formation," *Metallurgical Transactions*, vol. 4, no. 4, pp. 1103–1112, 1973.

[24] B. F. V. Turkovich and J. T. Black, "Concerning the dislocation theory of microtomed chips," in *Proceedings of the 1972 Region 1 Conference, October 12 and 13, 1972, Newport, Rhode Island*, p. 216, 1972.

[25] T. Moriwaki and E. Shamoto, "Ultraprecision diamond turning of stainless steel by applying ultrasonic vibration," *CIRP Annals*, vol. 40, no. 1, pp. 559–562, 1991.

[26] K. Iwata, T. Moriwaki, and K. Okuda, "Precision machining of stainless steel with CBN tool," *Bulletin of the Japan Society of Precision Engineering*, vol. 21, no. 2, pp. 134–135, 1987.

[27] Y. Furukawa and N. Moronuki, "Effect of material properties on ultra precise cutting processes," *CIRP Annals*, vol. 37, no. 1, pp. 113–116, 1988.

[28] D. A. Lucca, Y. W. Seo, and R. Komanduri, "Effect of tool edge geometry on energy dissipation in ultraprecision machining," *CIRP Annals*, vol. 42, no. 1, pp. 83–86, 1993.

[29] P. Albrecht, "New developments in the theory of the metal-cutting process: Part I. The ploughing process in metal cutting," *Journal of Engineering for Industry*, vol. 82, no. 4, pp. 348–357, 1960.

[30] E. G. Thomsen, "Deformation work absorbed by the workpiece during metal cutting," *Transactions of ASME*, vol. 75, no. 5, pp. 591–603, 1953.

[31] J. A. Williams and N. Gane, "Some observations on the flow stress of metals during metal cutting," *Wear*, vol. 42, no. 2, pp. 341–353, 1977.

[32] G. Feng and D. Sagapuram, "Size effect and friction in cutting of metals on the small scale," *CIRP Annals*, vol. 69, no. 1, pp. 77–80, 2020.

[33] G. Feng and D. Sagapuram, "A strong basis for friction as the origin of size effect in cutting of metals," *International Journal of Machine Tools and Manufacture*, vol. 168, p. 103741, 2021.

[34] D. Tabor, "Surface forces and surface interactions," vol. 58, no. 1, pp. 2–13, 1977.

[35] K. L. Johnson, *Contact Mechanics*. London, England: Cambridge University Press, 1987.

[36] J. N. Israelachvili, *Intermolecular and Surface Forces*. Academic Press, 2015.

[37] W. C. Oliver, R. Hutchings, and J. B. Pethica, "Measurement of hardness at indentation depths as low as 20 nanometers," in *Microindentation Techniques in Materials Science and Engineering* (P. J. Blau and B. R. Lawn, eds.), (Philadelphia, PA), American Society for Testing and Materials, 1984.

[38] Q. Ma and D. R. Clarke, "Size dependent hardness of silver single crystals," *Journal of Materials Research*, vol. 10, no. 4, pp. 853–863, 1995.

[39] N. Gane and J. Skinner, "The friction and scratch deformation of metals on a micro scale," *Wear*, vol. 24, no. 2, pp. 207–217, 1973.

[40] D. C. Drucker, "An analysis of the mechanics of metal cutting," *Journal of Applied Physics*, vol. 20, no. 11, pp. 1013–1021, 1949.

[41] C. Arcona and T. A. Dow, "An empirical tool force model for precision machining," *Journal of Manufacturing Science and Engineering*, vol. 120, no. 4, pp. 700–707, 1998.

[42] P. W. Wallace and G. Boothroyd, "Tool forces and tool-chip friction in orthogonal machining," *Journal of Mechanical Engineering Science*, vol. 6, no. 1, pp. 74–87, 1964.

[43] M. D. Uchic, D. M. Dimiduk, J. N. Florando, and W. D. Nix, "Sample dimensions influence strength and crystal plasticity," *Science*, vol. 305, no. 5686, pp. 986–989, 2004.

[44] J. R. Greer and J. T. M. De Hosson, "Plasticity in small-sized metallic systems: Intrinsic versus extrinsic size effect," *Progress in Materials Science*, vol. 56, no. 6, pp. 654–724, 2011.

[45] A. Misra and I. Finnie, "On the size effect in abrasive and erosive wear," *Wear*, vol. 65, no. 3, pp. 359–373, 1981.

[46] B. Epstein, "Statistical aspects of fracture problems," *Journal of Applied Physics*, vol. 19, no. 2, pp. 140–147, 1948.

[47] M. C. Shaw, "A yield criterion for ductile metals based upon atomic structure," *Journal of the Franklin Institute*, vol. 254, no. 2, pp. 109–126, 1952.

[48] A. G. Evans and J. W. Hutchinson, "A critical assessment of theories of strain gradient plasticity," *Acta Materialia*, vol. 57, no. 5, pp. 1675–1688, 2009.

[49] N. N. Zorev, *Metal Cutting Mechanics*. Oxford, England: Pergamon Press, 1966. pp. 76–78.

[50] M. Masuko, "Fundamental research on metal cutting. 1st Report. A new analysis of cutting forces," *Transactions of the Society of Mechanical Engineers (Japan)*, vol. 19, pp. 32–39, 1953.

[51] M. Sarwar and P. J. Thompson, "Cutting action of blunt tools," in *Proceedings of the Twenty-second International Machine Tool Design and Research Conference*, pp. 295–304, 1981.

[52] Y. Guo, C. Saldana, W. D. Compton, and S. Chandrasekar, "Controlling deformation and microstructure on machined surfaces," *Acta Materialia*, vol. 59, no. 11, pp. 4538–4547, 2011.

[53] J. J. Gilman, *Chemistry and Physics of Mechanical Hardness*, vol. 5. Hoboken, NJ: John Wiley & Sons, 2009.

[54] K. Nakayama, "On the formation of "saw-toothed chip" in metal cutting," *Proceedings of International Conference on Production Engineering*, p. 572–577, 1974.

[55] M. E. Merchant, "Mechanics of the metal cutting process. I. Orthogonal cutting and a type 2 chip," *Journal of Applied Physics*, vol. 16, no. 5, pp. 267–275, 1945.

[56] W. C. Rice, "The formation of continuous chips in metal cutting," *The Engineering Journal, Engineering Institution of Canada*, vol. 44, p. 41, 1961.

[57] D. Sagapuram, K. Viswanathan, A. Mahato, N. K. Sundaram, R. M'Saoubi, K. P. Trumble, and S. Chandrasekar, "Geometric flow control of shear bands by suppression of viscous sliding," *Proceedings of the Royal Society A: Mathematical, Physical and Engineering Sciences*, vol. 472, no. 2192, p. 20160167, 2016.

[58] D. Sagapuram, K. Viswanathan, K. P. Trumble, and S. Chandrasekar, "A common mechanism for evolution of single shear bands in large-strain deformation of metals," *Philosophical Magazine*, vol. 98, no. 36, pp. 3267–3299, 2018.

[59] S. Yadav and D. Sagapuram, "Nucleation and boundary layer growth of shear bands in machining," *Journal of Manufacturing Science and Engineering*, vol. 141, no. 10, 2019.

[60] R. Komanduri and R. H. Brown, "On the mechanics of chip segmentation in machining," *Journal of Engineering for Industry*, vol. 103, no. 1, pp. 33–51, 1981.

[61] K. Viswanathan, A. Udupa, H. Yeung, D. Sagapuram, J. B. Mann, M. Saei, and S. Chandrasekar, "On the stability of plastic flow in cutting of metals," *CIRP Annals*, vol. 66, no. 1, pp. 69–72, 2017.

[62] A. S. Vandana and N. K. Sundaram, "Simulation of sinuous flow in metal cutting," *Tribology Letters*, vol. 66, no. 3, pp. 1–13, 2018.

[63] W. M. Stobbs, J. S. Kallend, and J. A. Williams, "Deformation behaviour of copper in ultramicrotomy," *Acta Metallurgica*, vol. 24, no. 12, pp. 1083–1093, 1976.

[64] M. Ahlers and L. F. Vassamillet, "Deformation of some fcc metals by ultramicrotomy," *Journal of Applied Physics*, vol. 39, no. 8, pp. 3592–3596, 1968.

[65] K. Iwata, T. Moriwaki, and K. Okuda, "Ultra-high precision diamond cutting of copper," *Memoirs of the Faculty of Engineering*, vol. 31, pp. 93–102, 1984.

[66] S. Asai and A. Kobayashi, "Observations of chip producing behaviour in ultra-precision diamond machining and study on mirror-like surface generating mechanism," *Precision Engineering*, vol. 12, no. 3, pp. 137–143, 1990.

[67] D. A. Lucca, Y. W. Seo, and R. L. Rhorer, "Energy dissipation and tool-workpiece contact in ultra-precision machining," *Tribology Transactions*, vol. 37, no. 3, pp. 651–655, 1994.

[68] D. A. Lucca, Y. W. Seo, R. L. Rhorer, and R. R. Donaldson, "Aspects of surface generation in orthogonal ultraprecision machining," *CIRP Annals*, vol. 43, no. 1, pp. 43–46, 1994.

[69] T. Moriwaki, N. Sugimura, and S. Luan, "Combined stress, material flow and heat analysis of orthogonal micromachining of copper," *CIRP Annals*, vol. 42, no. 1, pp. 75–78, 1993.

[70] T. Moriwaki, A. Horiuchi, and K. Okuda, "Effect of cutting heat on machining accuracy in ultra-precision diamond turning," *CIRP Annals*, vol. 39, no. 1, pp. 81–84, 1990.

[71] T. Nishiguchi, Y. Maeda, M. Masuda, M. Sawa, and K. Uehara, "Mechanism of micro chip formation in diamond turning of Al-Mg alloy," *CIRP Annals*, vol. 37, no. 1, pp. 117–120, 1988.

[72] R. L. Rhorer, "A method for orthogonal cutting experiments with diamond tools," in *Ultraprecision Machining and Automated Fabrication of Optics*, vol. 676, pp. 111–115, International Society for Optics and Photonics, 1987.

[73] T. Sugano, K. Takeuchi, T. Goto, Y. Yoshida, and N. Ikawa, "Diamond turning of an aluminum alloy for mirror," *CIRP Annals*, vol. 36, no. 1, pp. 17–20, 1987.

[74] N. Ikawa, S. Shimada, and H. Morooka, "Technology of diamond tool for ultraprecision metal cutting," *Bulletin of the Japan Society of Precision Engineering*, vol. 21, no. 4, pp. 233–238, 1987.

[75] D. A. Lucca, Y. W. Seo, and R. L. Rhorer, "Energies in the ultra-precision machining of ductile materials," in *Proceedings of the 1992 NSF Design and Manufacturing System Conference, Altanta Georgia*, pp. 123–129, 1992.

[76] P. H. Cohen and M. Lovell, "Friction between deformable surfaces in machining," in *IIE Annual Conference. Proceedings*, p. 1173, Institute of Industrial and Systems Engineers (IISE), 2007.

[77] P. N. Blake and R. O. Scattergood, "Chip topography of diamond turned ductile metals," in *Ultraprecision Machining and Automated Fabrication of Optics*, vol. 676, pp. 96–103, International Society for Optics and Photonics, 1987.

[78] L. M. Clareborough and G. J. Ogilvie, "Machining – theory and practice," ch. Development of the macrostructure of metals by machining, pp. 110–122, Metals Park, Ohio: American Society for Metals, 1959.

[79] I. Ogura, "Ultra-microtomy for electron microscopic observation of metal structures," *Journal of the Second College of Engineering, Nihon University, Series B*, no. 6, pp. 43–49, 1965.

[80] M. L. Ericson and H. Lindberg, "A method of measuring energy dissipation during crack propagation in polymers with an instrumented ultramicrotome," *Journal of Materials Science*, vol. 31, no. 3, pp. 655–662, 1996.

[81] R. T. Allison and J. F. V. Vincent, "Measuring the forces acting during microtomy by the use of load cells," *Journal of Microscopy*, vol. 159, no. 2, pp. 203–210, 1990.

[82] A. Atkins and J. F. V. Vincent, "An instrumented microtome for improved histological sections and the measurement of fracture toughness," *Journal of Materials Science Letters*, vol. 3, no. 4, pp. 310–312, 1984.

[83] M. L. Ericson and H. Lindberg, "Design and potential of instrumented ultramicrotomy," *Polymer*, vol. 38, no. 17, pp. 4485–4489, 1997.

[84] T. R. Matzelle, H. Gnaegi, A. Ricker, and R. Reichelt, "Characterization of the cutting edge of glass and diamond knives for ultramicrotomy by scanning force microscopy using cantilevers with a defined tip geometry. Part II," *Journal of Microscopy*, vol. 209, no. 2, pp. 113–117, 2003.

[85] R. H. Doremus, "Cracks and energy: Criteria for brittle fracture," *Journal of Applied Physics*, vol. 47, no. 5, pp. 1833–1836, 1976.

[86] O. D. S. Ferreira, E. Gelinck, D. de Graaf, and H. Fischer, "Adhesion experiments using an afm—parameters of influence," *Applied Surface Science*, vol. 257, no. 1, pp. 48–55, 2010.

[87] P. E. Senseny, J. Duffy, and R. H. Hawley, "Experiments on strain rate history and temperature effects during the plastic deformation of close-packed metals," *Journal of Applied Mechanics*, vol. 45, no. 1, pp. 60–66, 1978.

[88] F. P. Bowden and D. Tabor, *The Friction and Lubrication of Solids*, vol. 2. Oxford University Press, 1964.

[89] E. M. Kopalinsky and P. L. B. Oxley, "Size effects in metal removal processes," in *In the Proceedings of the 3rd Conference on Mechanical Properties at High Rates of Strain*, pp. 389–396, 1984.

[90] D. Tabor, "Junction growth in metallic friction: The role of combined stresses and surface contamination," *Proceedings of the Royal Society of London. Series A. Mathematical and Physical Sciences*, vol. 251, no. 1266, pp. 378–393, 1959.

[91] J. S. Courtney-Pratt and E. Eisner, "The effect of a tangential force on the contact of metallic bodies," *Proceedings of the Royal Society of London. Series A. Mathematical and Physical Sciences*, vol. 238, no. 1215, pp. 529–550, 1957.

[92] A. Ovcharenko, G. Halperin, and I. Etsion, "In situ and real-time optical investigation of junction growth in spherical elastic–plastic contact," *Wear*, vol. 264, no. 11-12, pp. 1043–1050, 2008.

[93] M. E. Merchant, "Friction and adhesion," in *Interdisciplinary Approach to Friction and Wear* (D. H. Buckley, ed.), Cleveland, Ohio: NASA, 1968.

[94] D. Maugis, *Contact, Adhesion and Rupture of Elastic Solids*, vol. 130. Springer Science & Business Media, 2013.

[95] L. H. Lee, "The chemistry and physics of solid adhesion," in *Fundamentals of Adhesion*, pp. 1–86, Springer, 1991.

[96] K. L. Johnson, K. Kendall, and A. D. Roberts, "Surface energy and the contact of elastic solids," *Proceedings of the Royal Society of London. Series A. Mathematical and Physical Sciences*, vol. 324, no. 1558, pp. 301–313, 1971.

[97] V. M. Muller, B. V. Derjaguin, and Y. P. Toporov, "On two methods of calculation of the force of sticking of an elastic sphere to a rigid plane," *Colloids and Surfaces*, vol. 7, no. 3, pp. 251–259, 1983.

[98] M. D. Pashley, "Further consideration of the DMT model for elastic contact," *Colloids and Surfaces*, vol. 12, pp. 69–77, 1984.

[99] S. K. R. Chowdhury and H. M. Pollock, "Adhesion between metal surfaces: the effect of surface roughness," *Wear*, vol. 66, no. 3, pp. 307–321, 1981.

[100] A. R. Savkoor and G. A. D. Briggs, "The effect of tangential force on the contact of elastic solids in adhesion," *Proceedings of the Royal Society of London. Series A. Mathematical and Physical Sciences*, vol. 356, no. 1684, pp. 103–114, 1977.

[101] J. Golden and G. W. Rowe, "Radio-isotopes in scientific research," in *1st UNESCO Conference, Paris*, p. 343, 1957.

[102] D. Maugis and H. M. Pollock, "Surface forces, deformation and adherence at metal micro-contacts," *Acta Metallurgica*, vol. 32, no. 9, pp. 1323–1334, 1984.

[103] M. D. Pashley and D. Tabor, "Adhesion and deformation properties of clean and characterized metal micro-contacts," *Vacuum*, vol. 31, no. 10-12, pp. 619–623, 1981.

[104] J. Skinner and N. Gane, "Sliding friction under a negative load," *Journal of Physics D: Applied Physics*, vol. 5, no. 11, p. 2087, 1972.

[105] I. Green, "Poisson ratio effects and critical values in spherical and cylindrical Hertzian contacts," *Applied Mechanics and Engineering*, vol. 10, no. 3, p. 451, 2005.

[106] ASM Handbook, "Properties of wrought aluminum and aluminum alloys," *ASM International Handbook Committee*, vol. 2, pp. 62–122, 1990.

[107] K. S. Siow, A. A. O. Tay, and P. Oruganti, "Mechanical properties of nanocrystalline copper and nickel," *Materials Science and Technology*, vol. 20, no. 3, pp. 285–294, 2004.

[108] D. Tabor, *The Hardness of Metals*. Oxford University Press, 1951.

[109] J. G. Horne, *The chip-tool interface in metal cutting*. PhD thesis, University of Cambridge, 1978.

[110] V. Madhavan, S. Chandrasekar, and T. N. Farris, "Direct observations of the chip-tool interface in the low speed cutting of pure metals," *Journal Tribology*, vol. 124, no. 3, pp. 617–626, 2002.

[111] E. M. Trent, "Metal cutting and the tribology of seizure: I. Seizure in metal cutting," *Wear*, vol. 128, no. 1, pp. 29–45, 1988.

[112] P. K. Wright, J. G. Horne, and D. Tabor, "Boundary conditions at the chip-tool interface in machining: comparisons between seizure and sliding friction," *Wear*, vol. 54, no. 2, pp. 371–390, 1979.

[113] D. H. Buckley, *Surface Effects in Adhesion, Friction, Wear, and Lubrication*, vol. 5. Elsevier, 1981.

[114] D. S. Grierson, E. E. Flater, and R. W. Carpick, "Accounting for the JKR–DMT transition in adhesion and friction measurements with atomic force microscopy," *Journal of Adhesion Science and Technology*, vol. 19, no. 3-5, pp. 291–311, 2005.

[115] C. M. Mate and R. W. Carpick, *Tribology on the Small Scale: a Modern Textbook on Friction, Lubrication, and Wear*. Oxford University Press, USA, 2019.

[116] F. Rusu, M. Pustan, C. Bîrleanu, R. Müller, R. Voicu, and A. Baracu, "Analysis of the surface effects on adhesion in mems structures," *Applied Surface Science*, vol. 358, pp. 634–640, 2015.

[117] E. D. Doyle, J. G. Horne, and D. Tabor, "Frictional interactions between chip and rake face in continuous chip formation," *Proceedings of the Royal Society of London. A. Mathematical and Physical Sciences*, vol. 366, no. 1725, pp. 173–183, 1979.

[118] M. D. Pashley, J. B. Pethica, and D. Tabor, "Adhesion and micromechanical properties of metal surfaces," *Wear*, vol. 100, no. 1-3, pp. 7–31, 1984.

[119] J. B. Pethica and D. Tabor, "Contact of characterised metal surfaces at very low loads: Deformation and adhesion," *Surface Science*, vol. 89, no. 1-3, pp. 182–190, 1979.

[120] N. Gane, P. F. Pfaelzer, and D. Tabor, "Adhesion between clean surfaces at light loads," *Proceedings of the Royal Society of London. Series A. Mathematical and Physical Sciences*, vol. 340, no. 1623, pp. 495–517, 1974.

[121] F. P. Bowden and D. Tabor, *Friction: An Introduction to Tribology*. London, UK: Heinemann, 1973.

[122] S. Yadav and D. Sagapuram, "Nucleation properties of isolated shear bands," *Proceedings of the Royal Society A*, vol. 476, no. 2241, p. 20200529, 2020.

[123] S. Yadav and D. Sagapuram, "In situ analysis of shear bands and boundary layer formation in metals," *Proceedings of the Royal Society A*, vol. 476, no. 2234, p. 20190519, 2020.

[124] R. J. Adrian and J. Westerweel, *Particle Image Velocimetry*. No. 30, Cambridge University Press, 2011.

[125] M. Raffel, C. E. Willert, J. Kompenhans, *et al.*, *Particle Image Velocimetry: A Practical Guide*, vol. 2. Springer, 1998.

[126] A. E. H. Love, *A Treatise on the Mathematical Theory of Elasticity*. Cambridge University Press, 2013.

[127] C. M. Stafford, C. Harrison, K. L. Beers, A. Karim, E. J. Amis, M. R. VanLandingham, H. C. Kim, W. Volksen, R. D. Miller, and E. E. Simonyi, "A buckling-based metrology

for measuring the elastic moduli of polymeric thin films," *Nature Materials*, vol. 3, no. 8, pp. 545–550, 2004.

[128] G. I. Taylor, "Instability of jets, threads, and sheets of viscous fluid," in *Applied Mechanics*, pp. 382–388, Springer, 1969.

[129] M. F. Tome and S. McKee, "Numerical simulation of viscous flow: buckling of planar jets," *International Journal for Numerical Methods in Fluids*, vol. 29, no. 6, pp. 705–718, 1999.

[130] J. O. Cruickshank and B. R. Munson, "Viscous fluid buckling of plane and axisymmetric jets," *Journal of Fluid Mechanics*, vol. 113, pp. 221–239, 1981.

[131] J.-O. Arnbom, "Experimental buckling of competent viscous sheets in a less competent viscous matrix," *Geologiska Föreningen i Stockholm Förhandlingar*, vol. 98, no. 4, pp. 348–354, 1976.

[132] M. C. Shaw, "The metal cutting process as a means of studying the properties of extreme pressure lubricants," *Annals of the New York Academy of Sciences*, vol. 53, no. 4, pp. 962–978, 1951.

[133] Y. Mu, M. Liu, and Y. Zhao, "Numerical investigation on the elastic–plastic transition of a cylindrical coating/substrate composite under normal compression," *RSC Advances*, vol. 7, no. 25, pp. 15527–15535, 2017.

# APPENDIX A

# YIELDING PRESSURE OF A CYLINDRICAL WORKPIECE COMPRESSED AGAINST A RIGID SURFACE

This appendix includes the mathematical approach (proposed by Green [105]) to derive the yielding pressure at the contact zone of the soft half cylindrical workpiece when it is compressed against a rigid flat surface under plane strain deformation.

**Notation**

- $P$: applied normal load (normalized with respect to contact length)
- $b$: contact length
- $\nu$: Poisson's ratio of the cylindrical workpiece
- $E$: Young's modulus of the cylindrical workpiece
- $Y$: yielding strength of the cylindrical workpiece
- $R$: radius of the cylindrical workpiece
- $\sigma_v$: von Mises stress
- $\sigma_x, \sigma_y, \sigma_z$: normal stress tensors
- $\tau_{xy}, \tau_{yx}, \tau_{xz}, \tau_{zx}, \tau_{yz}, \tau_{zy}$: shear stress tensors
- $\epsilon_x, \epsilon_y, \epsilon_z$: normal strain tensors
- $x, y, z$: coordinates

**Mathematical formulation**

According to the Hertzian solution [35], the contact pressure $p(x)$ along x-axis ($|x| \leq b$, see Fig. A.1) is expressed as:

$$p(x) = \frac{p_m(b^2 - x^2)^{1/2}}{b}, \tag{A.1}$$

where $p_m$ is the maximum contact pressure at $x = 0$ and $b$ is the contact length that are expressed as:

$$p_m = \frac{2P}{\pi b} \tag{A.2}$$

and

$$b = 2\Big[\frac{PR(1-\nu^2)}{\pi E}\Big]^{1/2} \tag{A.3}$$

Because of plane strain deformation ($\epsilon_z = 0$), the shear stress tensors $\tau_{xz} = \tau_{zx} = \tau_{yz} = \tau_{zy} = 0$. In addition, the shear stress components $\tau_{xy} = \tau_{yx} = 0$ on the axis of symmetry (axis $x = 0$, where the contact pressure also reaches a maximum). Based on the Hooke's law for plane strain deformation, the normal stress tensors are related by $\sigma_z = \nu(\sigma_x + \sigma_y)$. Therefore, the stress tensors along the y-axis ($x = 0$) are as follows [35]:

$$\sigma_x = -\frac{p_m}{b}\Big[\frac{b^2 + 2y^2}{(b^2 + y^2)^{1/2}} - 2y\Big] \tag{A.4}$$

$$\sigma_y = -\frac{bp_m}{(b^2 + y^2)^{1/2}} \tag{A.5}$$

$$\sigma_z = \nu(\sigma_x + \sigma_y) \tag{A.6}$$

$$\tau_{xy} = \tau_{yx} = \tau_{xz} = \tau_{zx} = \tau_{yz} = \tau_{zy} = 0 \tag{A.7}$$

von Mises stress is given as:

$$\sigma_v = \sqrt{\frac{1}{2}[(\sigma_x - \sigma_y)^2 + (\sigma_y - \sigma_z)^2 + (\sigma_z - \sigma_x)^2]} \tag{A.8}$$

Therefore, after plugging in the expressions for $\sigma_x$, $\sigma_y$, and $\sigma_z$ in Eqs. A.4 - A.6, it can be shown that the ratio of $\frac{\sigma_v}{p_m}$ is a function of $\nu$ and $\frac{y}{b}$ [133] expressed as:

$$\frac{\sigma_v}{p_m} = \frac{\sqrt{2}}{2}\Bigg(\Big(2(y/b) - \frac{2(y/b)^2}{((y/b)^2+1)^{1/2}}\Big)^2 + \Big(2(\nu-1)(y/b) + \frac{1-2\nu+(2-2\nu)(y/b)^2}{((y/b)^2+1)^{1/2}}\Big)^2 + \Big(2\nu(y/b) + \frac{1-2\nu-2\nu(y/b)^2}{((y/b)^2+1)^{1/2}}\Big)^2\Bigg)^{\frac{1}{2}} \tag{A.9}$$

The location where $\sigma_v$ reaches a maximum is obtained by replacing $\frac{y}{b}$ with $\zeta_0$ in equation A.9, taking the derivative with respect to $\zeta_0$, and setting it to zero [133]:

$$\begin{aligned}
&\Big(\zeta_0 - \frac{{\zeta_0}^2}{({\zeta_0}^2+1)^{1/2}}\Big)\Big(2 - \frac{4\zeta_0({\zeta_0}^2+1)^{1/2} - 2{\zeta_0}^3/({\zeta_0}^2+1)^{1/2}}{{\zeta_0}^2+1}\Big) + \\
&\Big(2(1-\nu)\zeta_0 + \frac{2(\nu-1){\zeta_0}^2 + 2\nu - 1}{({\zeta_0}^2+1)^{1/2}}\Big)\Big((1-\nu) + \frac{2(\nu-1)\zeta_0({\zeta_0}^2+1)^{1/2} - (2(\nu-1){\zeta_0}^2 + 2\nu - 1)\zeta_0/2({\zeta_0}^2+1)^{1/2}}{{\zeta_0}^2+1}\Big) + \\
&\Big(\frac{1-2\nu{\zeta_0}^2-2\nu}{({\zeta_0}^2+1)^{1/2}} + 2\nu\zeta_0\Big)\Big(\frac{-2\nu\zeta_0({\zeta_0}^2+1)^{1/2} - (1-2\nu{\zeta_0}^2-2\nu)\zeta_0/2({\zeta_0}^2+1)^{1/2}}{{\zeta_0}^2+1} + \nu\Big) = 0
\end{aligned} \tag{A.10}$$

The relation between $\zeta_0$ and $\nu$ expressed by Eq. A.10 can be approximated by a parabolic function (given $\nu$ in a range from 0.2 to 0.5) as follows:

$$\zeta_0 \approx 0.220 + 2.335\nu - 2.411\nu^2 \tag{A.11}$$

Therefore, the max value of $\frac{\sigma_v}{p_m}$ can be calculated by plugging Eq. A.11 into Eq. A.9 (replace $\frac{y}{b}$ with the $\zeta_0$ expressed in Eq. A.11). This results in an expression for $(\frac{\sigma_{eq}}{p_m})_{max}$ as a function of $\nu$, say $f(\nu)$. The complicated $f(\nu)$ function can be expressed (given a $\nu$ value from 0.2 to 0.5) in a simplified form as:

$$f(\nu) \approx \frac{1}{1.164 + 2.975\nu - 2.906\nu^2} \tag{A.12}$$

From Eqs. A.2 and A.3, $\frac{Y}{p_m}$ can be expressed as:

$$\frac{Y}{p_m} = Y\Big[\frac{\pi R(1-\nu^2)}{PE}\Big]^{1/2} \tag{A.13}$$

Since at yielding, $(\frac{\sigma_v}{p_m})_{max} = \frac{Y}{p_m}$, this gives,

$$Y\Big[\frac{\pi R(1-\nu^2)}{PE}\Big]^{1/2} = f(\nu) \tag{A.14}$$

Therefore, the critical value of the applied load ($P_c$) when material starts to yield can be calculated from Eq. A.14 as:

$$P_c = \frac{\pi R Y^2(1-\nu^2)}{Ef(\nu)^2} \tag{A.15}$$

Defining $C_k = \frac{1}{f(\nu)} = 1.164 + 2.975\nu - 2.906\nu^2$, $P_c$ can be written as:

$$P_c = \frac{\pi R Y^2(1-\nu^2){C_k}^2}{E} \tag{A.16}$$

Plugging Eq. A.16 into Eq. A.3, the critical contact length $b_c$ at yielding is then:

$$b_c = 2\Big[\frac{P_c R(1-\nu^2)}{\pi E}\Big]^{1/2} = 2\frac{RY(1-\nu^2)C_k}{E} \tag{A.17}$$

Replacing the $b$ with $b_c$ and $P$ with $P_c$ in Eq. A.2, the expression for the critical stress at the contact when the workpiece starts to yield is:

$$p_{mc} = C_k Y = (1.164 + 2.975\nu - 2.906\nu^2)Y \tag{A.18}$$

Therefore, given the Poisson's ratio and yield strength of the cylindrical workpiece, the yielding pressure at the contact can be estimated.

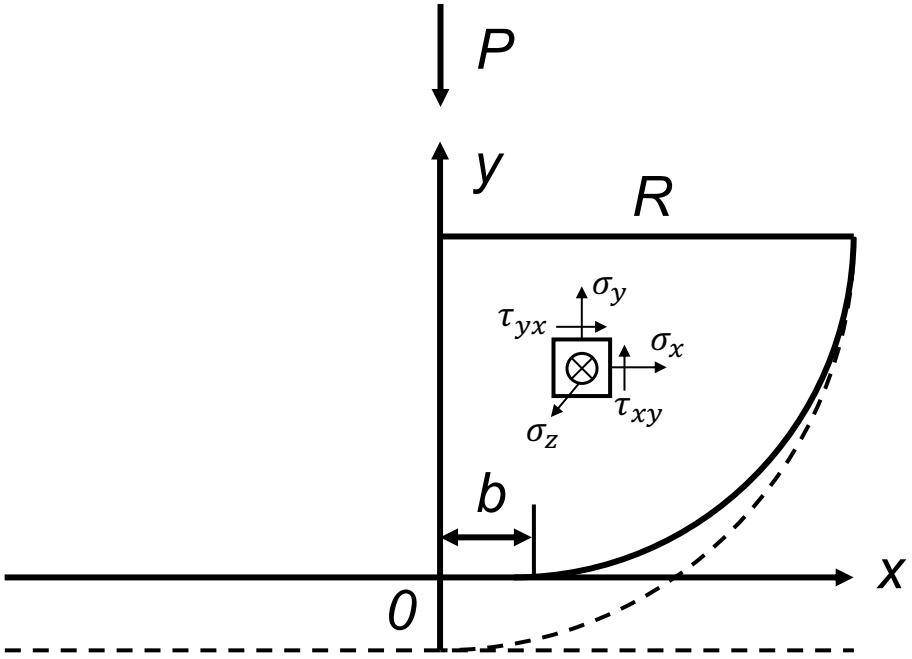


Figure A.1. Schematic showing the contact between a soft cylindrical workpiece and a rigid flat surface under the normal load $P$ (reproduced from Mu et al. [133] with permission).

# APPENDIX B

## PLASTIC YIELD ZONE SIZE IN METAL CUTTING UNDER CONCENTRATED LOADS

This appendix includes the mathematical derivation for the analytical form of the plastic yield zone size (along the cutting direction) in metal cutting under concentrated cutting ($F_c$) and thrust ($F_t$) forces.

**Notation**

- $F_c$: cutting force (normalized with respect to cutting width)
- $F_t$: thrust force (normalized with respect to cutting width)
- $\sigma_v$: von Mises stress
- $Y$: yielding stress of the material (workpiece)
- $\sigma_x, \sigma_y, \sigma_z$: normal stress tensors
- $\tau_{xy}, \tau_{yx}, \tau_{xz}, \tau_{zx}, \tau_{yz}, \tau_{zy}$: shear stress tensors
- $x, y, z$: coordinates

**Mathematical formulation**

For 2-dimensional plane strain deformation,

$$\sigma_y = \tau_{xy} = \tau_{yx} = \tau_{yz} = \tau_{zy} = 0 \tag{B.1}$$

Based on the Flamant's solution [126] for semi-infinite elastic body loaded at its surface by two point (orthogonal) forces ($F_c$ and $F_t$), the stress state for the system is given by ($\sigma_x$ and $\sigma_z$ are normal stresses, and $\tau_{xz}$ is the shear stress, see Fig. B.1):

$$\sigma_x = \frac{2F_t}{\pi}\frac{x^2 z}{(x^2+z^2)^2} + \frac{2F_c}{\pi}\frac{x^3}{(x^2+z^2)^2} \tag{B.2}$$

$$\sigma_z = \frac{2F_t}{\pi}\frac{z^3}{(x^2+z^2)^2} + \frac{2F_c}{\pi}\frac{xz^2}{(x^2+z^2)^2} \tag{B.3}$$

$$\tau_{xz} = \frac{2F_t}{\pi}\frac{xz^2}{(x^2+z^2)^2} + \frac{2F_c}{\pi}\frac{x^2z}{(x^2+z^2)^2} \tag{B.4}$$

von Mises stress for 2-dimensional plane strain deformation is:

$$\sigma_v = \sqrt{\sigma_x^2 - \sigma_x\sigma_z + \sigma_z^2 + 3\tau_{xz}^2} \tag{B.5}$$

Plugging Eqs. B.2, B.3, and B.4 into Eq. B.5 and rearranging the terms, the von Mises stress can be expressed as:

$$\sigma_v = \frac{2}{\pi(x^2+z^2)^2}\sqrt{{F_t}^2z^2 + 2F_tF_cxz + {F_c}^2x^2} \tag{B.6}$$

Therefore,

$$\sigma_v = \frac{2(F_tz + F_cx)}{\pi(x^2+z^2)} \tag{B.7}$$

$$(\sigma_v\pi)x^2 - 2F_cx + (\sigma_v\pi z^2 - 2F_tz) = 0 \tag{B.8}$$

From Eq. B.8, the boundary (in $x$ - $z$ space) of plastic zone is obtained by setting $\sigma_v = Y$, which results in:

$$(Y\pi)x^2 - 2F_c x + (Y\pi z^2 - 2F_t z) = 0 \tag{B.9}$$

The maximum length of the plastic zone in the $x$-direction is obtained by first represent $x$ in terms of $z$ and then find the $z$ that maximize $x$:

$$x = \frac{F_c + \sqrt{{F_c}^2 - Y\pi(Y\pi z^2 - 2F_t z)}}{Y\pi} \tag{B.10}$$

Since the term $Y\pi z^2 - 2F_t z$ is minimum when $z = \frac{F_t}{Y\pi}$, this results in the solution for $x_{max}$ as:

$$x_{max} = \frac{F_c + \sqrt{{F_c}^2 + {F_t}^2}}{Y\pi} \tag{B.11}$$

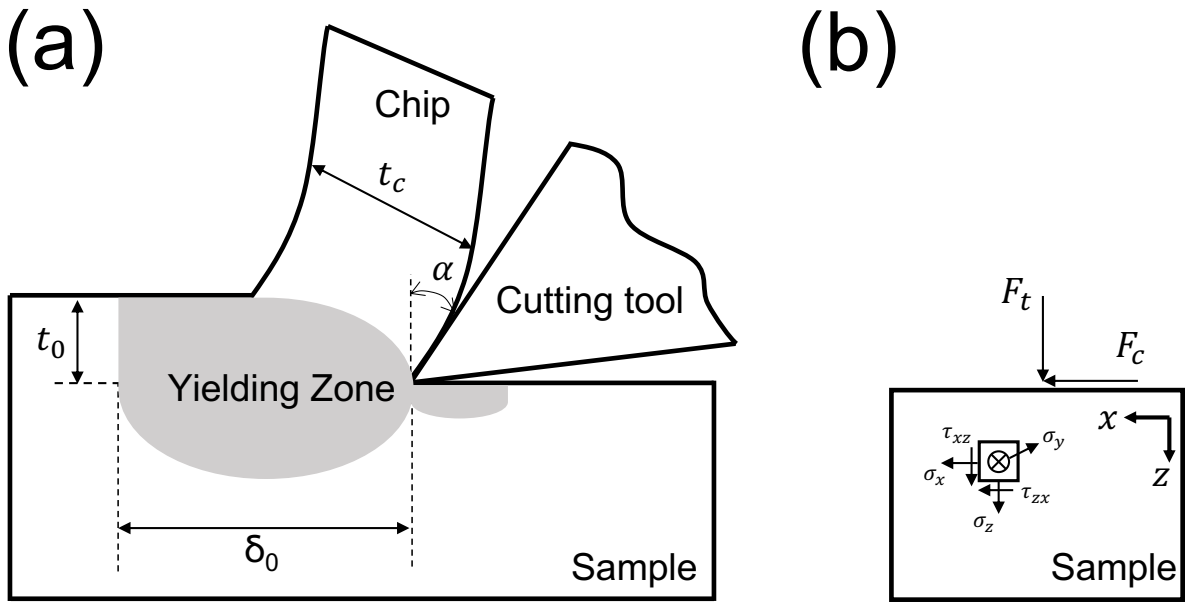


Figure B.1. (a) Schematic showing the plastic yielding zone (shaded in gray color) in plane-strain cutting. (b) Simiplification of the cutting process as an elastic half-plane loaded by two point (orthogonal) forces $F_c$ and $F_t$.